THE
PHYSICAL REVIEW
A journal of experimental and theoretical physics established by E. L. Nichols in 1893

SECOND SERIES, VOL. 70, NOS. 3 AND 4 AUGUST 1 AND 15, 1946

Radioactivity of Be^{10}

EDWIN M. MCMILLAN
Radiation Laboratory, Department of Physics, University of California

AND

SAMUEL RUBEN*
Department of Chemistry, University of California, Berkeley, California

(Received April 22, 1946)

The formation of radioactive Be^{10} by the (d, p) reaction from beryllium has been observed. The assignment of the activity to beryllium is the result of very careful chemical separations. Be^{10} emits negative electrons with an upper limit of 560 ± 50 kev (end point in Al $=180\pm20$ mg/cm^2). The half-life is very long; data are given from which its value could be computed if the yield were known.

I. INTRODUCTION

IT has been known for a long time that the nucleus Be^{10} is formed in the reaction:[1]

$$Be^9+H^2\rightarrow Be^{10}+H^1, \qquad (1)$$

and that its mass is such as to make it unstable against β-decay into B^{10}. Several attempts have been made to observe the activity of this substance. The first was by McMillan.[2] A beryllium target which had been used as a neutron source with 2- to 3-Mev deuterons in the 37″ cyclotron for about a year (no record of total bombardment) ending June, 1935, was put into a Lauritsen electroscope; a very long period β-activity was found, with low energy as shown by absorption in Al. This energy was later measured by Libby and Lee,[3] who gave the value 13 ± 5 kev as its upper limit. It was later shown by O'Neal and Goldhaber[4] that H^3, with β-energy 15 kev, formed in a Be target by the reaction:

$$Be^9+H^2\rightarrow Be^8+H^3, \qquad (2)$$

is occluded in the metal to a considerable extent. Therefore, we can safely attribute the activity observed above to H^3 rather than Be^{10}.

A second attempt to observe the Be^{10} activity was made by Pollard.[5] He bombarded a Be target with 60-microampere hours of 3.1-Mev deuterons, and observed (again without chemical separation) an activity having an upper limit of 0.75 Mev (range of β-particles $=250\pm30$ mg/cm^2 in Al). No mention was made of a soft component; the H^3 radiation would not have been observed unless the counter window were extremely thin. This activity may have come

* Died in a laboratory accident on September 29, 1943, while engaged in war research. The unfortunate death of Dr. Ruben, and the absence of the other author from Berkeley during the war years, account for the delay in the publication of this work.

[1] Oliphant, Kempton, and Rutherford, Proc. Roy. Soc. **A150**, 241 (1935).

[2] E. M. McMillan, Phys. Rev. **49**, 875 (1936).

[3] W. F. Libby and D. D. Lee, Phys. Rev. **55**, 245 (1939).

[4] R. D. O'Neal and M. Goldhaber, Phys. Rev. **57**, 1086 (1940).

[5] E. Pollard, Phys. Rev. **57**, 241 (1940).

from a contamination, since no chemical separation was made.

A third attempt to find the Be^{10} activity was made by Bretscher,[6] using the postulated reaction:

$$B^{10}+n\rightarrow Be^{10}+H^{1}. \quad (3)$$

In this case, Be was separated chemically, and no activity was found. Using Pollard's half-life (380 years) Bretscher found for the above reaction the abnormally small cross section of $<2\times10^{-28}$ cm^2; it is probable from the work reported in this paper that the half-life is much longer.

The availability of large currents at high energies from the Berkeley cyclotrons has enabled us to pursue a more rigorously controlled search for the elusive Be^{10} activity, with the results reported below.

II. TARGETS USED

All the Be targets used in this investigation had been employed as neutron sources. Their history is given below:

Target *A*: Bombarded with 16-Mev deuterons in 60" cyclotron; no record of amount of bombardment.

Target *B*: Old target used in 37" cyclotron at 8 Mev; no record of amount of bombardment.

Target *C*: Three pieces of Be, each $1''\times1''\times\frac{1}{16}''$, soldered to water cooled copper plate. Bombarded with 12,000-microampere hours of 16-Mev deuterons, during period April 8 to August 28, 1940, in 60" cyclotron. This figure comes from beam integrator readings, and is fairly accurate.

III. CHEMICAL SEPARATION OF Be

The treatment was essentially the same for all the samples. It consisted of two parts: a rough purification to get out the bulk of the contamination, and a specific beryllium separation using the solubility of the basic acetate $Be_4(C_2H_3O_2)_6O$ in chloroform. In the rough purification, the following steps were taken:

1. Target dissolved in HCl, solution boiled to drive out volatile components.
2. Pt, Cu, and Sn carriers precipitated by H_2S in slightly acid solution.
3. Mg, Mn, Fe, Co, Ni, Zn carriers precipitated in conc. NaOH (under these conditions Be stays in solution).
4. $PO_3^{=}$ and $SO_4^{=}$ carriers precipitated by Ba, in alkaline solution. (All filtrations were repeated until the filtrates were clean and colorless.)
5. Last filtrate neutralized, $Zn(NO_3)_2$ added (to prevent Zn being carried down, since Zn can go through the basic acetate procedure in small amounts), and $Be(OH)_2$ precipitated with NH_4OH. This precipitate was washed very thoroughly with water. Its activity was found in all cases to be very small compared to that of the original sample, showing the abundance of contamination activities.

The basic acetate procedure was as follows:

1. Dissolved the $Be(OH_2)$ in glacial acetic acid, boiled just to dryness, added more acetic acid, boiled down again, repeated. This converted the $Be(OH)_2$ to the basic acetate.
2. Dissolved in chloroform, discarding undissolved residue. Filtered to take out any suspended particles.
3. Washed chloroform solution with water in separatory funnel three times.
4. Evaporated chloroform, dissolved residue in HNO_3, precipitated $Be(OH)_2$ with NH_4OH.
5. Calcined $Be(OH)_2$ to convert to BeO. (The activity was always reduced by an appreciable amount in the basic acetate procedure, showing that the first part of the purification alone was not good enough).

IV. COUNTING TECHNIQUE

Counts were made in screen wall counters, of the kind described in reference 3. The samples were applied in the form of BeO on the inside surface of brass cylinders, which slide so that the sample is either around the counter or away from it. Readings were made by alternating sample and background counts a number of times, to eliminate drift effects. Two counters were used:

	screen		*sample*		*solid angle factor*
	length	*diam.*	*length*	*diam.*	
large	8 cm	2.5 cm	8 cm	6.2 cm	0.14
small	8 cm	2.5 cm	6.3 cm	4.8 cm	0.21

The Al absorbers were wrapped around the counter screen. The background averaged about 120 counts/min.; all the readings given have the background subtracted. The errors given with the counting rates are mean errors calculated from the counting statistics.

V. RESULTS

1. Sample A-1

This sample consisted of 0.65 g of Be, etched to a depth of 1 mm from the part of the surface

[6] E. Bretscher, Nature 146, 94 (1940).

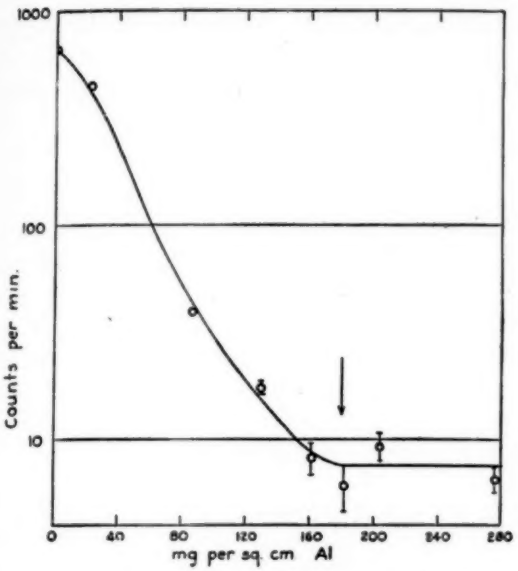

FIG. 1. Absorption of Be^{10} beta-rays in aluminum.

of target *A* showing most evidence of strong bombardment. After chemical purification (done April 4–5, 1940), 500 mg of BeO (36 percent of original sample) remained, which was put into the large counter. The counting rate was 530±20 counts per minute, or a specific activity of 350±13 disintegrations per second per gram Be.

This sample was then taken out, put through the basic acetate procedure a second time, reintroduced into the counter (250 mg BeO) where it gave a rate of 280±4 counts per minute, or a specific activity of 370±5 disintegrations per second per gram Be. The agreement of this value with the first count, after the sample had been subjected to a very specific Be separation, with such thorough washing that half of the sample was lost, is a very strong indication that the activity observed here is actually carried by an isotope of Be.

Some Al absorption points were also taken on this sample, both before and after the second purification; the data are not included, since better values were obtained on a stronger sample, but they served as confirmation that the same activity was being observed.

2. Sample A-2

This consisted of the rest of the surface of target *A*, etched off to a depth of about 1 mm. After purification (April 18, 1940), 1500 mg of BeO were obtained and placed in the large counter, giving a rate of 1320±30 counts per minute. This sample was used to get a good absorption curve of the β's in Al, shown in Fig. 1. The value with no absorber may be a little low because of self-absorption; the sample had a thickness of about 8 mg/cm, including a little paraffin that had to be added as a binder to keep this thick layer from peeling off.

This absorption curve indicates a γ-ray, with an intensity of the order of a quantum per β-disintegration (by comparison with Na^{22}). As a further check of the assignment of the γ-ray to Be, a second basic acetate purification was carried out. The specific γ-ray activity was not changed appreciably. It is, therefore, probable that the γ-ray comes from a Be isotope.

The β-ray activity of this sample (950 g BeO remained after the second purification) was then followed in the large counter. The rates observed were:

July 17, 1940 — 914±20 counts per minute,
October 18, 1940 — 860±40 counts per minute,
December 27, 1941 — 890±20 counts per minute,

showing no change outside the mean error during 17 months.

3. Sample A-3

This consisted of the rest of target *A*. After purification its activity, measured on a Lauritsen electroscope, was small compared to that of *A*-1+*A*-2, although its weight was greater. This serves to show that the activity is concentrated in the surface of the target, and is therefore a deuteron rather than a neutron effect.

4. Check Sample

Some old pieces of various materials that had had long bombardments in the 60″ cyclotron (Al window, Fe target, MgO target, brass holder), with an activity before purification ten times that of target *A*, were dissolved together with some inactive Be and subjected to the chemical purification. The resulting sample was inactive.

5. Sample B

This consisted of a thin layer scraped off the surface of target *B*. It was purified April 13,

1940, and showed the highest specific activity of all the samples. 110 mg BeO in the large counter gave:

Absorber	*Rate*
21.7 mg/cu²A	2030±80 counts/min.
148 mg/cu²A	23.4±4 counts/min.
278 mg/cu²A	21.6±3 counts/min.

These values are seen to be in agreement with sample *A*-2, if a small allowance for self-absorption in the latter is made.

This sample was used to study the γ-ray. Ninety mg of the BeO in the small counter, covered with 169 mg/cm² of lead, gave a counting rate equal to half the background. Absorption of the recoil electrons in Al showed an energy of 400±100 kev. The most important observation was that the γ-rays decayed; 7½ months after the first measurement, the γ-activity had practically disappeared.

6. Sample C

In this case the whole target *C* (5.7 g Be) was dissolved. After the chemical purification (September 7–23, 1940) 6.3 g of BeO remained, or 40 percent of the original amount. One hundred ninety mg of this material were put into the small counter, where they gave 1310±50 counts per minute. The specific activity is therefore 1460±56 disintegrations per second per gram Be. The total activity in the target was then 9200 ±350 disintegrations per second.

VI. DISCUSSION

1. β-Particle Activity

There seems to be no doubt that this activity must be assigned to an isotope of Be; by far the most probable assignment is to Be^{10}. The end point in Al is 180±20 mg/cm², corresponding to an upper limit energy of 560±50 kev.

2. γ-Ray Activity

The observed decay of the γ-ray shows that it does not come from the β-emitter. Its most probable source is Be^{7}, formed by deuteron impact on Li impurity in the target. This substance gives γ-rays alone, of energy 485 kev and half-life 43 days.

3. Energy Relations

The energy available in the β-decay of Be^{10}, as computed from Allison's[7] values of the masses of Be^{9} and B^{10}, and Oliphant, Kempton, and Rutherford's[1] value of the energy output in reaction (1), is 580±240 kev. This is in agreement with the observed energy of 560±50 kev.

4. Half-Life

The half-life of the β-emitter could be determined only if the yield were known. Since this information is lacking, the result of the measurement on sample *C* can be expressed in the following way:

Number of deuterons in 12,000 microampere hours = 2.7×10^{20}.

Yield in active atoms per deuteron = Y.

Total disintegration rate = 9200±350 per second.

Then:

$$\text{Half-life} = \frac{2.7\times10^{20}Y}{9200}\times\frac{0.693}{3.16\times10^{7}}$$

$$= 6.4\times10^{8}Y \text{ years.}$$

Any reasonable guess for the thick-target yield of reaction (1) at 16 Mev thus leads to a very long half-life.

ACKNOWLEDGMENTS

We wish to express our gratitude to the Research Corporation, the Rockefeller Foundation, and the National Advisory Cancer Council, whose financial support of the cyclotron program made this work possible.

[7] S. K. Allison, Phys. Rev. **55**, 624 (1939).

The Disintegration of Na^{24} and P^{32}

KAI SIEGBAHN
Research Institute for Physics, Academy of Sciences, Stockholm, Sweden
(Received April 1, 1946)

The disintegration of Na^{24} and P^{32} has been studied by means of a β-spectrometer of the lens type. The γ-radiation of Na^{24} consists of only two γ-lines incascade, the energies of which have been determined as 1.380 and 2.758 Mev. $E\beta_{max}$ for Na^{24} is 1.390 Mev and for P^{32} 1.712 Mev. In order to obtain β-spectra without secondary electrons, exceedingly thin foils and very small quantities of active materials have been used. With these precautions it appears that the electron distributions follow the allowed form of β-spectra. However, Na^{24} and P^{32} are empirically forbidden spectra of the first and second order, respectively. According to the theory of forbidden spectra developed by Uhlenbeck and Konopinski, the distribution for at least P^{32} would differ from the allowed one.

INTRODUCTION

Na^{24} and P^{32} are among the artificially active elements that, for various reasons, have been most frequently studied. The most important reasons are naturally the high activity and the convenient half-life periods obtained by bombardment of Na and P with deuterons. Furthermore, the problem of the disintegration of Na^{24} and P^{32} has a special relevancy to the β-theory, as the study of their energy-distribution curves in the β-disintegrations, which are forbidden of the 1st and 2nd order, respectively, may yield important information regarding the nature of the matrix elements occurring in the expressions for the disintegrations.

So far no results have been obtained that agree sufficiently well to permit a theoretical interpretation with any degree of certainty. In the case of Na^{24}, further complications are introduced by the γ-radiation accompanying the β-disintegration.

γ-LINES OF Na^{24}

Opinions still seem to differ regarding both the number of γ-lines and their energies. The first determination of Na^{24} γ-lines was carried out by Richardson and Kurie[1] by studying the Compton effect from Al in a Wilson chamber. They obtained three well-defined lines at 0.95, 1.93, and 3.08 Mev. This result was confirmed by a later investigation by Richardson[2] who found, using the same method, 1.01, 2.04, and 3.00 Mev. Later investigations with the spectrographic method, however, did not give concordant results. Japanese workers[3] first obtained the energy values 0.80, 1.49, and 2.97 Mev. Later investigations indicated[4] that only two lines existed, namely at 1.38 and 2.76 Mev. Since this result differs remarkably from the Wilson chamber determinations, the γ-lines of Na^{24} have been subjected to further investigations by other methods. M. Goldhaber, G. S. Klaiber, and G. Scharff-Goldhaber[5] have determined with the aid of the photo-neutron method, using the processes $Be^9(\gamma, n)Be^8$ and $D^2(\gamma, n)H^1$ (applicable only for γ-radiation of energy higher than the threshold values for the reactions concerned, i.e., 1.62 and 2.18 Mev), the upper γ-energy value as 2.87 Mev.

P. G. Kruger and W. E. Ogle,[6] using another

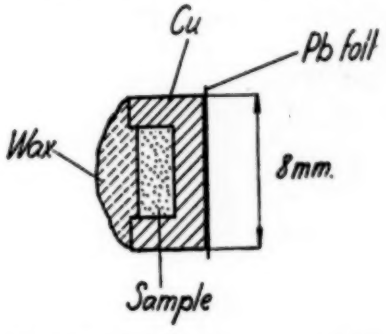

FIG. 1. The radiator for γ-ray studies.

[1] J. R. Richardson and F. N. D. Kurie, Phys. Rev. **50**, 999 (1936).
[2] J. R. Richardson, Phys. Rev. **53**, 124 (1938).
[3] S. Kichuchi, Y. Watase, J. Itch, E. Takeda, and S. Yamaguchi, Proc. Phys. Math. Soc. Japan **21**, 260, 381 (1939).
[4] L. G. Elliott, M. Deutsch, and A. Roberts, Phys. Rev. **63**, 386 (1943).
[5] M. Goldhaber, G. S. Klaiber, and G. Scharff-Goldhaber, Phys. Rev. **65**, 61 (1944).
[6] P. G. Kruger and W. E. Ogle, Phys. Rev. **67**, 273 (1945).

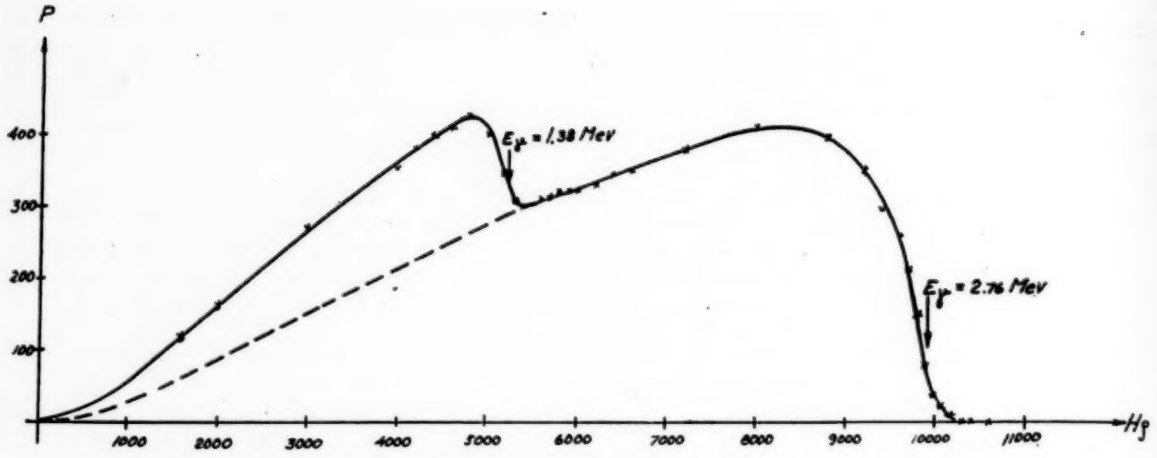

FIG. 2. Secondary electron spectrum expelled from a Cu radiator by the γ-rays of Na^{24}. The curve is in the undivided form.

method, have recently obtained a result differing significantly from those of earlier determinations. They studied the pair formation in a Wilson chamber. Out of 200 pairs, 56 were accepted for measurement. No less than seven γ-lines were reported, namely at 3.24, 2.89, 2.76, 2.68, 2.56, 1.38, and 1.26 Mev. As an explanation of these, the β-spectrum is considered to be complex, consisting of three components.

In order to investigate the γ-radiation from Na^{24}, the present author has employed a technique permitting accurate energy determinations on the γ-radiation from samples with γ-activities as low as a few μC per γ-line.[7] A similar technique has been described by Deutsch, Elliott, and Evans.[8] The active sample is placed in a small, cylindrical radiator of the form shown in Fig. 1. The wall is so thick that all β-radiation is absorbed. The thickness may be calculated with the aid of Feather's formula for the range of the β-radiation, $R=0.543E-0.160$ g/cm^2, where E is the energy of the γ-radiation in Mev. The Compton electrons formed in the radiator by the γ-radiation are then studied in the β-lens spectrograph of high light intensity, described earlier by the present author.[9] In order to limit the size of the radiator, copper is used, which has a high density but a low atomic number. The photo-effect will thus appear only at very low energies. After the Compton spectrum has been recorded, a thin lead foil (0.02−0.2 mm) is placed in front of the radiator, and the distribution of the photo- and Compton electrons is registered. By subtracting one of the two curves from the other, the photo-effect in the thin lead foil is obtained as the essential part of the remainder.

Figure 2 shows a recording of the Compton distribution in the copper radiator. The numbers of impulses counted per unit time (P) are here

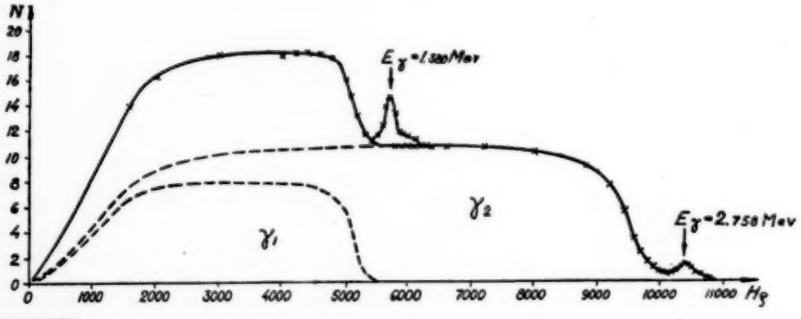

FIG. 3. Secondary electron spectrum expelled from a Cu radiator covered with a 0.02-mm Pb-foil by the γ-rays of Na^{24}.

[7] K. Siegbahn, Phil. Mag. (1946), in print.
[8] M. Deutsch, L. G. Elliott, and R. D. Evans, Rev. Sci. Inst. **15**, 178 (1944).
[9] K. Siegbahn, Arkiv. f. mat., astr. o. fysik **28A**, No. 17 (1944).

plotted as ordinates, and not the intensities over constant $H\rho$-intervals. In order to obtain these latter values, we must divide P by the corresponding value of $H\rho$. Figure 2 clearly shows that there are two well-defined γ-lines. It is easy enough, using this method of plotting, to extrapolate the Compton distribution of the highest energy to zero energy (the broken line in the figure).

Figure 3 shows the distribution obtained with a 0.02-mm thick Pb foil placed in front of the radiator. The intensities over constant $H\rho$-intervals have here been chosen as ordinates. It is here also clear that only two γ-lines exist. Quite a small possibility for the existence of more than two γ-lines naturally remains, if the two γ-lines should happen to be closer together than what the spectrograph would resolve. The resolving power of the spectrograph amounted, on this occasion, to somewhat more than 3 percent, which, however, is in good concordance with the half-breadth value of the two lines, determined as $\sim$3.5 percent. It therefore seems rather unlikely that any of the photo-lines is complex.

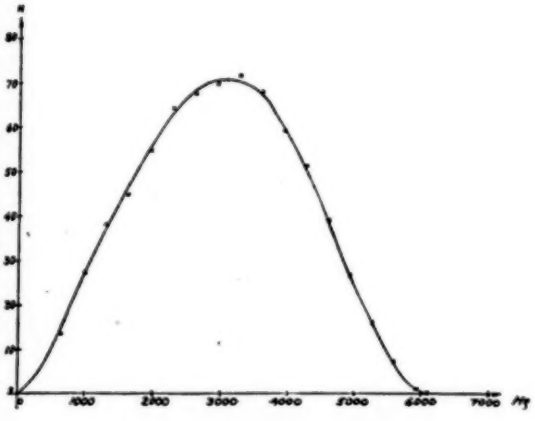

FIG. 4. The β-spectrum of Na^{24}.

The energies of the γ-lines are obtained with great accuracy from the corresponding K-photo-lines as 1.380 and 2.758 Mev, in perfect concordance with the above-quoted work of Elliott, Deutsch, and Roberts.[4]

The energies may obviously be obtained direct from the Compton distributions. It has been proved, in investigations of several other γ-lines employing this method, that γ-energy values may be obtained that very well agree with the results from the photo-lines, if measurements are made on the inflection points at the edge of the undivided Compton distribution (Fig. 2). When this procedure is employed, the γ-energies are

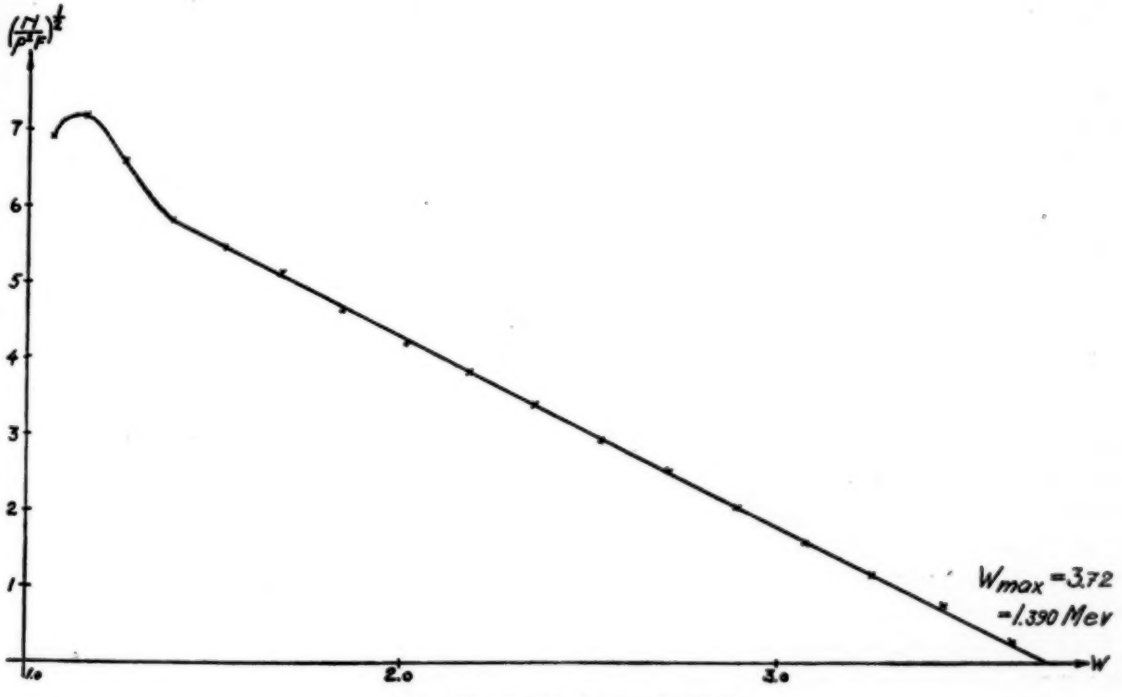

FIG. 5. The Fermi diagram for Na^{24}.

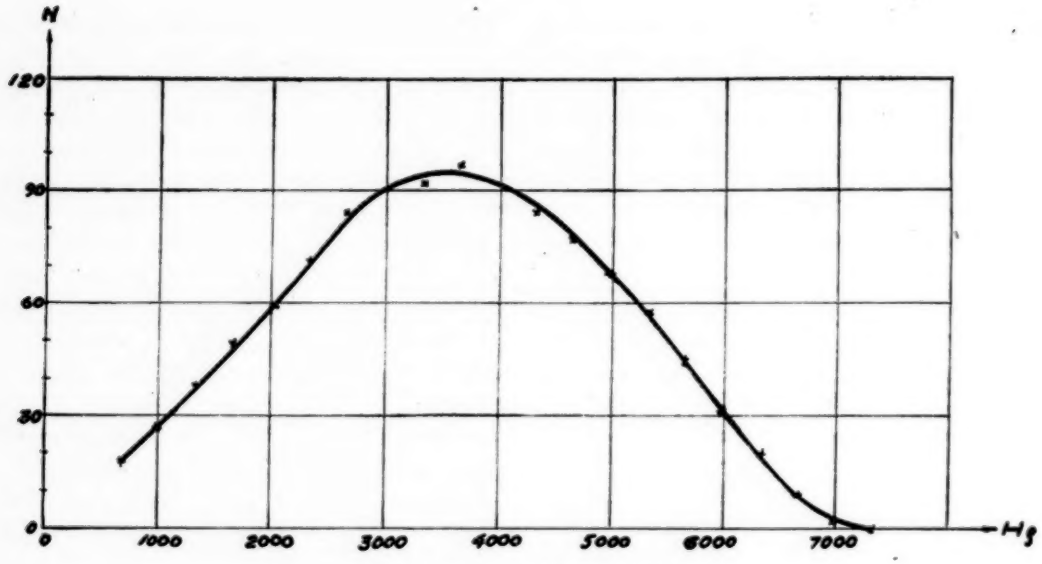

FIG. 6. The γ-spectrum of P^{32}.

determined as 1.38 and 2.76 Mev. Kruger and Ogle report, among other lines, a weak γ-radiation of 3.24 Mev (originating from one electron-positron pair). Though searching carefully for possible weak γ-lines above 2.76 Mev, the present author could not establish the presence of such.

THE β-SPECTRUM OF Na^{24}

The β-spectrum of Na^{24} has been studied by several authors with the aid of the β-spectrograph. Of these, Lawson's measurement is probably the most accurate.[10] Lawson used 3.5 mg substance per cm^2 on a substratum of 7.4 mg/cm^2. According to the experience of the present author, even such small quantities may cause a deformation in the spectrum, owing to secondary effects in the sample itself and in the substratum. Accordingly, the irradiation was performed in the 32" cyclotron of this institute, so that the activity of the sodium sample became very high. A highly diluted drop of the sample was then allowed to evaporate on a backing foil, about 0.1 μ thick and suspended on a small ebonite ring of 2 cm internal diameter. Owing to the high light intensity of the spectrograph, the quantity of dry substance, in the order ~0.1 mg, was sufficient to give good intensity in the registration of the β-spectrum. The result of an experimental series is shown in Fig. 4. A Fermi analysis of the spectrum (Fig. 5) gives as the upper limit $W_{max}=1.390\pm0.005$ Mev.

In spite of the fact that Na^{24}, according to its place in the Sargent diagram, is a forbidden transition of the 1st order, the spectrum is of the allowed type, as is seen from the diagram. As a matter of fact, the Fermi curve is absolutely straight as far down as an energy <0.2 Mev, where a small peak appears. It is interesting to observe here that the more carefully the secondary radiation is eliminated, the nearer the curve approaches a straight line. The curve in Lawson's diagram deviates from a straight line at about 0.6 Mev. Judging from these two measurements, an extrapolation down to a negligible secondary

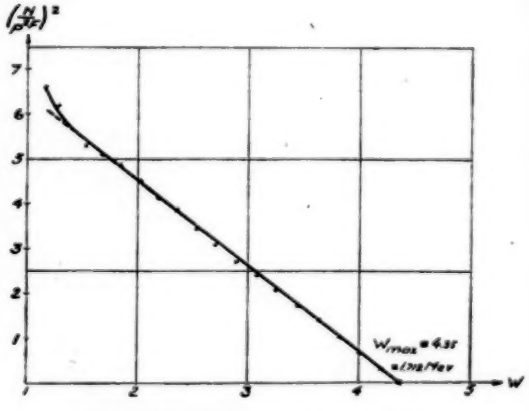

FIG. 7. The Fermi diagram for P^{32}.

[10] J. L. Lawson, Phys. Rev. 56, 131 (1939).

radiation would very probably give a straight line throughout the energy range.

THE β-SPECTRUM OF P^{32}

The same impression is obtained by studying the β-spectrum of P^{32}. Here also, the optimum conditions are realized in respect of high specific activity. Furthermore, no γ-radiation, which might contribute to a secondary radiation, is present. Figure 6 shows the recording of the β-spectrum, the weight of the substance and substratum being approximately the same as for Na^{24}. Figure 7 is the corresponding Fermi diagram, from which the upper limit can be determined as 1.712 ± 0.008 Mev. The Fermi diagram consists in this case of a straight line as far down as an energy <0.1 Mev. The recording of the β-spectrum of phosphorus by Lawson, who used a sample weighing about 3 mg/cm², deviates from the straight line at about 0.8 Mev. It seems therefore probable that, under ideal conditions, the curve will follow a straight line along its whole course.

DISCUSSION

The Term Scheme of Na^{24}

The Fermi analysis of the Na^{24} β-spectrum shows quite clearly that the transition is simple and not complex. This interpretation is also supported by the experiments concerning the number of β-γ-coincidences per registered number of β-particles as a function of the β-energy, carried out by Langer, Mitchell, and McDaniel[11] and also by Feather and Dunworth,[12] who find the coincidence number to be independent of the β energy. Konopinski[13] has suggested, in order to explain the deviation from the straight line in the Fermi analysis of Lawson's recording,[10] the possibility of internal conversion lines. Despite the fact that Mg^{24}, the end-product of the β-emission, is a light nucleus, the possibility for internal conversion is not quite excluded, provided that the γ-radiation has a high multipole character. The difference in spin between the excited levels and the ground state in Mg^{24} must

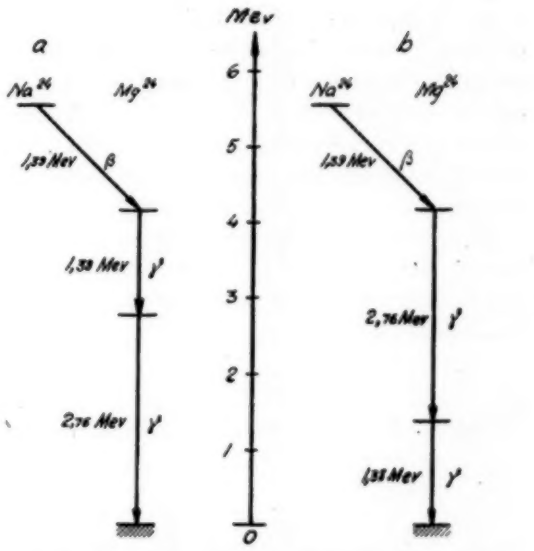

FIG. 8. Nuclear level scheme for the disintegration of Na^{24}.

actually be fairly large, for the direct β-transition from Na^{24} to the ground state of Mg^{24} is so strictly forbidden that no β-radiation with this energy can be observed, in spite of the fact that the energy release should be considerably greater. This possibility, however, must be rejected, judging from the present investigation, since the deviation from the straight line in the Fermi diagram has a tendency, when the secondary radiation is weaker, to disappear completely, and since no γ-line below 1.37 Mev has actually been encountered.

As the β-spectrum is simple and only two γ-lines are emitted, the term scheme should have a simpler appearance than that suggested by Kruger and Ogle.[6] The two alternatives possible are shown in Fig. 8. The order of sequence of the two γ-lines in cascade is, of course, impossible to determine from the present experimental material.

The mass of Na^{24} may be obtained from the term scheme and the spectroscopically determined mass of Mg^{24}. If the latter be assumed to be 23.99300 ± 0.00038, the mass of Na^{24} is obtained as $23.99300 + 1.074.10^{-3} \times 5.53 = 23.99893 \pm 0.00045$.

According to the term scheme, the two γ-lines must have the same intensity. The ratio of the "γ-efficiencies" of the radiator for the two γ-energies may thus be obtained directly by dividing the areas of the two Compton distribu-

[11] L. M. Langer, A. C. Mitchell, and P. W. McDaniel, Phys. Rev. **56**, 962 (1939).
[12] N. Feather and J. V. Dunworth, Proc. Camb. Phil. Soc. **34**, 442 (1938).
[13] E. J. Konopinski, Rev. Mod. Phys. **15**, 209 (1943).

tions. It does not appear to be excluded that an efficiency curve for copper, applicable to γ-GM tubes in, for instance, coincidence measurements, can be constructed in this way with the aid of additional γ-energies. At low energies, the contribution from the photo-effect (<0.5 Mev) should naturally be taken into account. The γ-sensitivities of the radiator at 2.76 and 1.38 Mev are in the ratio $\sim 2.65:1$, according to Fig. 3. This value is larger than would be expected from the efficiency curves for copper γ-tubes reported in the literature. No definite conclusion, however, can be drawn in this matter until the influence of the geometrical factors on the γ-efficiency of the radiator has been more closely investigated.

THE FORM OF THE β-SPECTRA AND β-THEORY

The β-theory of forbidden transitions has been developed by E. J. Konopinski and G. E. Uhlenbeck[14] (cf. also E. J. Konopinski[15]). In contradistinction to the theory of allowed transitions, that of forbidden transitions gives different expressions for the energy distribution, depending on which of the five forms of interaction (scalar, polar, tensor, axial, pseudoscalar) is supposed to apply. Thus a study of Na^{24} (empirically first forbidden) and P^{32} (empirically second forbidden) might decide in principle which form of interaction is the correct one. Uhlenbeck and Konopinski give their result in the form of an energy-dependent factor C, which, when multiplied by the allowed Fermi function, will give the energy distribution for forbidden transitions. This factor is dependent on which assumption is made regarding the above-mentioned forms of interaction, and also on whether the forbidden transition is of the first or second order. It is interesting to consider whether the rather surprising result, that Na^{24} and P^{32} are spectra of the allowed type, is compatible with the above-mentioned theory. The condition for this is that the factor C may be rendered energy-independent by suitable assumptions regarding the relative magnitudes of the nuclear matrix elements in C. Starting with Na^{24} (following the notation of Uhlenbeck and Konopinski), the factors C_{1S} and C_{1P} can never be independent of energy and are hence rejected. C_{1V}, C_{1T}, and C_{1A} are energy-independent, if the matrix elements $|\int \alpha|^2$, $|\int \alpha|^2$, and $|\int \gamma_5|^2$, respectively, are considerably larger than other matrix elements, such as $|\int r|^2$, $|\int \sigma \times r|^2$, etc. According to U. and K., such a relation between the relevant matrix elements is conceivable.

It is considerably more difficult, however, to combine the allowed type of the P^{32} spectrum with an energy-independent factor C_2. Actually none of the various forms of interaction gives a factor C_2 that is energy-independent, as each matrix element occurs multiplied by energy functions. The possibility certainly remains that the different energy functions of each factor may together, by choosing matrix elements of suitable magnitudes, be made approximately energy-independent along a large interval of energy. A numerical investigation* shows, however, that C_2 cannot, even approximately, be made energy-independent for all choices of relative magnitudes for the matrix elements. Moreover, it seems unlikely that various special assumptions need be made in order to obtain, from rather complicated expressions, the simple form of energy distribution found in the experiments with both Na^{24} and P^{32}. A possibility, not to be excluded, is that both Na^{24} and P^{32} actually are allowed as regards both spin and parity but forbidden by other rules of selection. It is also possible that further forms of interaction are to be taken into consideration.

[14] E. J. Konopinski and G. E. Uhlenbeck, Phys. Rev. **60**, 308 (1941).
[15] E. J. Konopinski, Rev. Mod. Phys. **15**, 209 (1943).

* The author wants to thank Dr. Svartholm for valuable discussion on this point.

The Disintegration of I^{128}

KAI SIEGBAHN AND NJÅL HOLE
Nobelinstitutet för Fysik, Vetenskapsakademien, Stockholm, Sweden

(Received April 4, 1946)

The β- and γ-radiations of the 25-min. activity of I^{128} have been investigated by means of a β-spectrograph and a special technique for the γ-determination. The disintegration is shown to be complex. The main transition (93 percent) occurs to the ground level in X^{128} with the release of 2.02-Mev energy. A faint γ-ray of 0.428 Mev is found, corresponding to an excited level in X^{128}.

IF iodine is irradiated with slow neutrons, an activity with the half-life of 25 min. is produced. As this element has only one stable isotope with the mass number 127, the activity must be assigned to I^{128}. The active isotope is quite easily obtained and, in spite of its somewhat short half-life, has frequently been used in tracer work. For this and other reasons it is of importance to acquire exact knowledge of the disintegration.

The half-life has been accurately determined by Hull and Seelig,[1] who found the value 24.98 ± 0.02 min. Some disagreement seems to exist concerning the occurrence of a γ-radiation. Thus Bacon, Grisewood, and van der Merwe[2] obtained with the Wilson chamber technique a highly complex β-spectrum with upper limits 1.05 and 2.10 Mev. However, they were unable to detect any γ-radiation. Livingood and Seaborg,[3] by means of absorption measurements, estimated the γ-radiation to have the energy 0.4 Mev. On the other hand, Roberts and Irvine,[4] with the aid of γ-sensitive GM counters, could detect no γ-radiation in the order of 0.1 γ-ray per β-ray.

500-ml ethyl iodide was irradiated with slow neutrons from the 32″ cyclotron of this institute for about one hour. The active iodine was extracted by shaking the ethyl iodide with an aqueous solution of sodium bisulphite and potassium carbonate and was then precipitated as Ag I. Preliminary experiments showed that the active sample emitted a very faint γ-radiation of small energy. The half-life of the γ-radiation was about 25 min. and could thus be attributed to the I^{128} isotope.

Since the previous investigations diverged rather strikingly as regards both the energy limit and the form of the β-spectrum, we found it advisable to make a new determination of the spectrum with the more accurate β-spectrograph technique. The active powder was spread out over an area of $\phi=8$ mm on a thin zaponlac foil (0.5μ) which was suspended over a circular ebonite frame, the diameter of which was 2 cm. The powder was covered with 0.1μ zaponlac foil. The sample could be quickly brought into the spectrograph by means of a lock device. The β-spectrograph, which is of the lens type with a high transmission factor, will be described elsewhere.[5]

Figure 1 shows the β-spectrum obtained. The appearance of the spectrum shows no definite complexity owing to its rather symmetric form. For the purpose of obtaining the most accurate upper limit of the spectrum, the Fermi diagram is given in Fig. 2. The diagram is slightly curved, partly owing to the fact that the amount of substance was not of negligible weight. The value of E_{max} from this curve is 2.02 Mev.

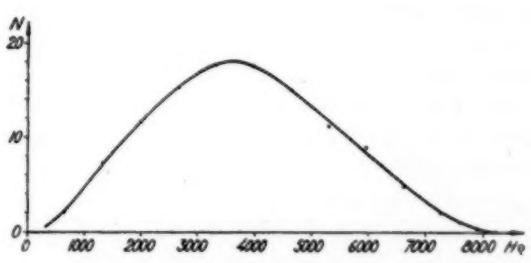

FIG. 1. The β-spectrum of I^{128}.

[1] D. E. Hull and H. Seelig, Phys. Rev. **60**, 553 (1941).
[2] R. H. Bacon, E. N. Grisewood, and C. van der Merwe, Phys. Rev. **59**, 531 (1941).
[3] G. T. Seaborg and J. J. Livingood, Phys. Rev. **54**, 775 (1938).
[4] A. Roberts and J. W. Irvine, Phys. Rev. **53**, 609 (1938).
[5] Kai Siegbahn, in print.

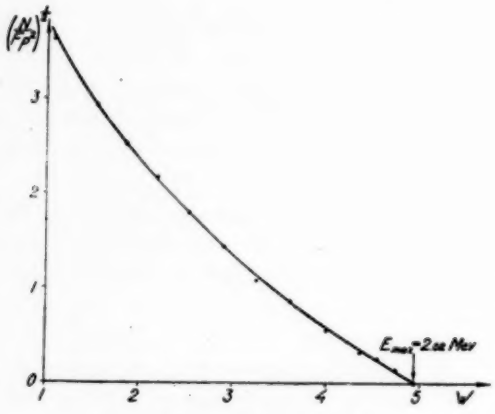

FIG. 2. The Fermi plot of I^{128}.

In the preliminary absorption measurements the existence of a weak γ-radiation was established. To obtain more precise information about the energy of the γ-radiation a measurement was made by means of the photo-Compton method. The photo- and Compton electrons expelled from a suitable radiator in which the sample was placed were investigated in the lens spectrograph. The radiator consisted of a cylindrically formed copper cap ($\phi=8$ mm, $l=6$ mm), the wall thickness of which was sufficient to absorb completely the β-spectrum. In front of the copper cap a Pb foil of 0.1 mm was placed. Owing to the faintness of the γ-radiation a large amount of active sample had to be used. Nevertheless, the whole activity amounted to only about 0.5μC Ra γ-equivalence.

The distribution of the secondary electrons thus formed is shown in Fig. 3. To give an impression of the sensitivity of the method the number of impulses per min. in the GM counter is plotted along the ordinate axis instead of the intensity ($P/H\rho$). In the figure may be seen a continuous distribution with a small drop in intensity before a pronounced peak. This continuous distribution is due to the Compton effect in the copper.

The high peak is explained by the K-photo-effect in the lead foil and the lower peak is the corresponding L-photo-line. Obviously we are concerned here with only one γ-line. The energy of this is obtained with good accuracy from the K-photo-line by adding the K-binding energy in Pb (0.088 Mev) to 0.340 Mev. As an effective check on this result the same γ-energy can be determined from the L-photo-line. By adding the L-binding energy (0.016 Mev) to the energy of this photo-line we obtain $E\gamma=0.429$ Mev, which gives strong evidence of the correctness of the value calculated above for the γ-energy. The search for other γ-lines with higher energies than this gave negative results.

The presence of this γ-ray requires a complexity in the β-spectrum. Since the γ-radiation is of small intensity, its emission in cascade with a simple β-transition is eliminated.

The usual method of determining the relative intensities of the β-transitions is impracticable here. This is caused by the fact that the two β-components differ only slightly in energy. The accurate resolution of the Fermi curve into two components is still more complicated by the small magnitude of the β-component of lower energy.

The degree of complexity was therefore determined in another way.

If two I^{128} samples, the relative intensities of which are known, are measured under the same geometrical condition, one with a β-counter and the other with a γ-counter, the number of γ-quanta per electron can be determined, provided that the net efficiency factor of the counter for the γ-energy concerned is known. This factor can be determined by making an analogous measurement with an active isotope, where a γ-radiation of the same energy is emitted in a known proportion to the β-radiation. This is the case[6] with Au^{198} where the β-spectrum is known

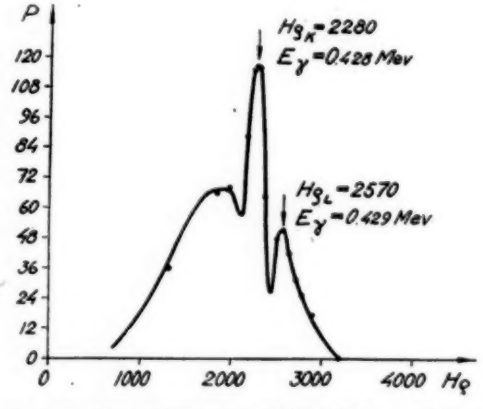

FIG. 3. Secondary electrons expelled from a radiator by the faint γ-radiation of I^{128}.

[6] Kai Siegbahn, "Slow neutron-induced activity in Au," Proc. Roy. Soc. (1946), in print.

to be followed by a γ-ray of $E\gamma = 0.401$ Mev in cascade, i.e., about the same energy as for I^{128}

We first measured the γ-intensity from a large amount of active I^{128} in a standard arrangement. A small accurately known part of the total sample was allowed to decay for a period sufficiently long to give an activity that could be measured in the β-counter in the same arrangement. The time for the decay was measured. This permitted a recalculation of the activity to the same time as employed in the γ-intensity investigation. The net efficiency factor for the γ-counter was then determined by placing a thin activated Au foil in the same standard arrangement. The results of these measurements showed that 7 γ-quanta were emitted per 100 β-particles.

The disintegration scheme for I^{128} may now be obtained from the results of the above determinations of the β- and γ-components. The term scheme is uniquely established as shown in Fig. 4. The partial half-lives t_1 and t_2 for the two transitions are 21,400 and 1600 sec., respectively. Following the notation of Konopinski[7] the corresponding ft-values may be calculated. We then find $(ft)_1 = 4.1 \times 10^6$ and $(ft)_2 = 0.78 \times 10^6$. Both transitions must evidently be placed in the $1B$-group, which means that they are both forbidden and of the same order, i.e., the first.

By using the selection rules for the β-decay proposed by Gamow-Teller[8] some information may be gained concerning the spins and parities of the various levels. X^{128} contains an even number of protons and neutrons and the ground state may therefore be assumed to have zero spin and even parity. A first forbidden transition

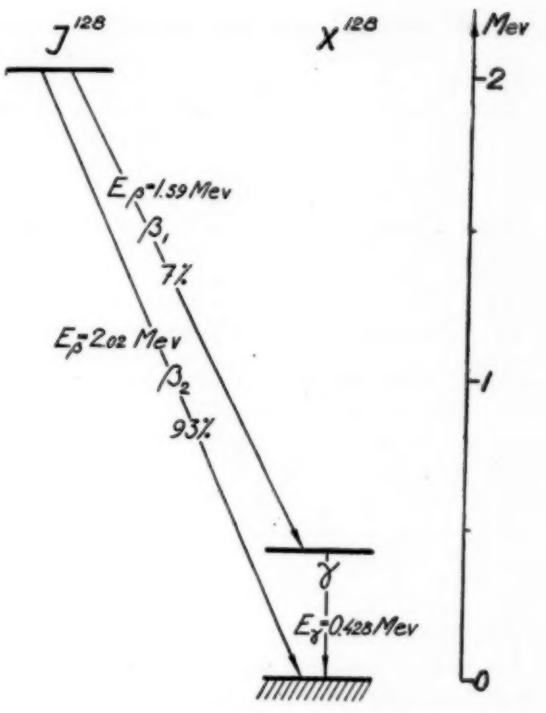

FIG. 4. The term scheme for the disintegration of I^{128}.

is accompanied by a parity change; consequently the ground state in I^{128} must have odd parity and the excited state in X^{128} even parity. The spin relations cannot be so uniquely established. According to the selection rules I^{128} may have spin = 1 or 2 while the spin in the excited state of X^{128} may be 0 or 1 or 2. The spin 0 of the latter level would imply a γ-transition to the ground level with a spin change $0 \rightarrow 0$. This is highly forbidden and should give a very high coefficient of internal conversion. Since this is not the case, we can exclude this possibility.

[7] E. Konopinski, Rev. Mod. Phys. **15**, 209 (1943).
[8] G. Gamow and E. Teller, Phys. Rev. **49**, 895 (1936).

PHYSICAL REVIEW VOLUME 70, NUMBERS 3 AND 4 AUGUST 1 AND 15, 1946

Neutron Beam Spectrometer Studies of Boron, Cadmium, and the Energy Distribution from Paraffin*

JAMES RAINWATER AND WILLIAM W. HAVENS, JR.
Columbia University, New York, New York

(Received August 23, 1945)†

A slow neutron velocity selector has been developed for use with the Columbia University cyclotron. By the method of arc modulation, neutron production is usually confined to intervals of (10–200) microseconds out of a (1000–10,000) microsecond cycle. Neutrons slowed down in paraffin are detected by BF_3 proportional counters. Excellent collimation is obtained by using an extensive B_4C and Cd collimating system. Experiments were conducted principally at a 5.4-meter source detector distance. A special selector system counts all the neutrons detected and also selectively counts those detected in an adjustable timed interval after the cyclotron burst. The slow neutron energy distributions from paraffin "source" slabs were shown to be of a modified Maxwellian form with an asymmetrical high energy "tail." Data for the resonance absorption by Cd were well matched by a one-level Breit-Wigner formula having $E_0=(0.180\pm0.008)$ ev, $\Gamma=(0.112\pm0.005)$ ev, $\sigma_0=(7{,}800\pm800)\times10^{-24}$ cm²/atom. The results of measurements with several boron filters over the range of 0.01 ev to over 100 ev were well matched by the $1/v$ relation, $\sigma_B=(118\pm4)E^{-\frac{1}{2}}\times10^{-24}$ cm²/atom.

INTRODUCTION

THE variation with energy of the interaction of slow neutrons with nuclei supplies much of the detailed knowledge of the energy levels of these nuclei. Absorption bands are found at low neutron energies which give a picture of the levels of the compound nucleus in the vicinity of the binding energy of the neutron (8 Mev). When the energy of the neutron is in the thermal region, the wave-length of the neutron is of the same order of magnitude as the spacing between the atoms in molecules thus giving rise to interference and diffraction effects which offer important information concerning the structure of matter.

Experiments which have been carried out with slow neutrons usually depend on an arrangement in which fast neutrons produced in the course of nuclear disintegrations, such as take place in a cyclotron or in a radium-beryllium source, are slowed in paraffin or some other hydrogenous material to attain partial thermal equilibrium. Use of slow neutron detectors of the radioactive, ionization chamber, or proportional counter type, then permits absorption measurements to be made using the resultant energy distribution. These experiments have the disadvantage of using a wide distribution of neutron velocities. Although the distribution can be varied by controlling the temperature of the paraffin source and introducing absorbing filters such as Cd, the method does not give a sharply defined monochromatic neutron beam. In addition to the dependence of the energy distribution of the neutrons upon the temperature of the paraffin source there is also a dependence on the amount of paraffin used, the geometry of the system, and the energy of the fast neutrons used. These factors make difficult the proper evaluation of such experiments.

The use of resonance absorbers as detectors permits measurements to be made with neutrons of sharply defined energies corresponding to the resonance energies of the levels responsible for the slow neutron absorption.[1–4] When only one main absorption level is present, the energy of this level is usually determined by measuring the absorption cross section of a boron filter first for these resonance energy neutrons and then for the thermal energy neutrons removed by a cadmium filter. If boron is assumed to

* Submitted by James Rainwater in partial fulfillment of the requirements for the degree of Doctor of Philosophy in the Faculty of Pure Science, Columbia University, New York, New York. Publication assisted by the Ernest Kempton Adams Fund for Physical Research of Columbia University.

† The experimental work on this paper was completed prior to 1943, but publication was voluntarily withheld at the request of the Manhattan District until the date indicated.

[1] H. A. Bethe, Rev. Mod. Phys. 9, 113–161 (1937).
[2] H. B. Hanstein, Phys. Rev. 59, 489 (1941).
[3] W. J. Horvath and E. O. Salant, Phys. Rev. 59, 154 (1941).
[4] H. Feeny, C. Lapointe, and F. Rasetti, Phys. Rev. 61, 469 (1942).

TABLE I. Fundamental relations important in the measurements described in this paper.

$E\rightarrow$	1 Mev	0.1 Mev	0.01 Mev	1000 ev	100 ev	10 ev	1 ev	0.1 ev	0.01 ev	0.001 ev
V in meters/sec.	1.38×10^7	4.38×10^6	1.38×10^6	437,500	138,400	43,750	13,840	4375	1384	438
Microsec./meter	.0723	.229	.723	2.29	7.23	22.9	723	229	723	2286
Microsec./5.4 meters	.390	1.24	3.90	12.4	39.0	124	390	1235	3900	12,350
λ in A	.0003	.001	.003	.0091	.0286	.0905	.286	.905	2.86	9.05
Collisions required to cascade from 7 Mev	2	4	7	9	11	14	16	18	21	23
Assumed cm m.f.p.	4	1.3	.8	.7	.7	.7	.7	.4	.2	.2
Microsec. time required to cascade	.005	.01	.03	.06	.2	.7	2	4	9	20

absorb according to a $1/v$ law and if the effective energy of the thermal neutrons is assumed to be kT, the energy at resonance can be determined. Since the effective energy of the "thermal" neutrons used in such determinations is probably greater than kT (see below), this method usually gives too low a value for the resonance energy but a reasonably correct comparison of different levels.

The resonance absorption method can be used with high accuracy only in the special case in which there is a single resonance level involved. Also the properties of any element cannot be investigated over a continuously variable interval but can only be investigated at the energy values where suitable detection levels occur. These qualifications greatly limit the use of this method in determining the interesting properties of many of the nuclear levels.

Direct methods for obtaining monochromatic neutrons involve some sort of timing device whereby neutrons having different times of flight between source and detector can be separated. The times of flight of the neutrons, together with other pertinent data, are listed in Table I for different neutron energies.

When a steady source of neutrons is used, the only basic method possible is the use of a mechanical velocity selector. The first slow neutron velocity selector was the mechanical device of Dunning, Pegram, Fink, Mitchell, and Segré,[5] which was later improved by Fink.[6] This device used rotating disks with Cd sectors to pass bursts of slow neutrons from a radon beryllium source to a nearby ionization chamber detector similarly shielded by a second rotating disk with Cd sectors. The energy of the neutrons passed or discriminated against by the selector system depended on the separation of the disks and their speed of rotation and relative phase. Mechanical considerations limiting the possible speed of rotation confined the operation of the selector to the region of thermal energies. Because of the relatively large, fast neutron backgrounds inherent in such systems, the resolution could be made only moderately high. This method has one main advantage over other methods in that the time of starting of the slow neutron burst is definitely known within the limits of the resolution. This factor will be discussed later.

Another method was employed by Alvarez[7] with the Berkeley cyclotron. In this method the output of the cyclotron was modulated by supplying the plate voltage of the oscillator providing the D voltage with rectified but unfiltered 60-cycle high voltage. Since the efficiency of the cyclotron decreases rapidly with decreasing D voltage, most of the beam production was limited to the time when the D voltage was near the peak of the cycle. By placing the detector at different distances from the paraffin-surrounded target and counting the neutrons which arrived between the bursts at the source, the effects of neutrons of corresponding velocities could be observed. The arrangement employed was limited to energies below 0.025 ev. With half-wave rectification, the "on-time" was reduced to 20 percent of the cycle, which represents comparatively poor resolution, but eliminates the fast neutron background.

Experiments in which direct accelerating sources were modulated were conducted by Fertel, Gibbs, Moon, Thompson, and Wynn-

[5] Dunning, Pegram, Fink, Mitchell, and Segré, Phys. Rev. **48**, 704 (1935).
[6] G. A. Fink, Phys. Rev. **50**, 738 (1936).
[7] L. W. Alvarez, Phys. Rev. **54**, 609 (1938).

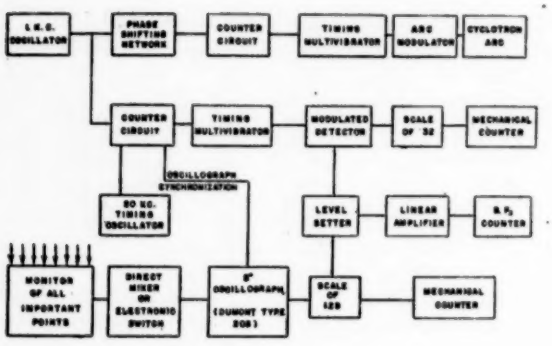

FIG. 1. Fundamental operating parts of the neutron beam spectrometer circuits.

Williams[8] and others, wherein the ion current was modulated and counts at a distant detector were recorded on an oscillograph as a function of time after the burst. The results of these experiments were not completely satisfactory because of the extremely low intensities obtained and because of the difficulties met with in the particular experiments conducted. This method has been used with good results by J. H. Manley, L. J. Haworth, and E. A. Luebke[9] who measured the lifetime of thermal neutrons in water and performed other experiments.

The present work is similar to that conducted by C. P. Baker and R. F. Bacher[10] using the Cornell cyclotron which was modulated by controlling the accelerating voltages of the ion source. Timed bursts of 50 to 100 microseconds duration could be produced with a 400-cycle repeat time. This work gave high resolution compared to the work previously mentioned as the "on-time" could be reduced to 8 percent of the total cycle. The distances employed, 1.5 and 3 meters, permitted experiments with neutron energies up to several electron volts and the resonance curves of several elements were studied. The accuracy of these measurements was limited by the low neutron intensities used, by background effects due to incomplete shielding from stray neutrons, and by the effect of the delayed emission of thermal neutrons from the thick paraffin "source" employed.

[8] Fertel, Gibbs, Moon, Thompson, and Wynn-Williams, Proc. Roy. Soc. 175, 316 (1940).
[9] J. H. Manley, L. J. Haworth, and E. A. Luebke, Phys. Rev. 61, 152 (1942).
[10] C. P. Baker and R. F. Bacher, Phys. Rev. 59, 332 (1941).

The work described in this paper was undertaken to investigate more fully the possibilities of the modulated neutron-beam method with the Columbia cyclotron. The principal advantages of the present work include much higher intensities, better shielding from stray neutrons, thinner paraffin sources to minimize the uncertainty in the time of emission of neutrons from the paraffin, greater working distances, and, therefore, effectively higher resolution. Also, a more complete and flexible electronic control of the timing system was obtained over a wide range of neutron energies.

APPARATUS DESCRIPTION

Neutron Source

The neutron bursts are produced by modulating the accelerating voltage on the arc of the cyclotron. Arc currents of 1 to 2 amperes rise and fall in times shorter than 5 microseconds. The arc is modulated by a bank of 12 type 6L6 tubes which is controlled by appropriate pulses from the modulation system. The width of the pulses can be varied continuously from less than 10 microseconds to 1000 microseconds out of a total cycle period of 1000 to 10,000 microseconds. The cyclotron is operated with an internal beryllium target on a probe placed for maximum stability in a position corresponding to a beam of about 8-Mev energy. Instantaneous beam currents utilized are of the order of 50 to 200 microamperes which give fairly high neutron intensities.

Timing Circuits

The fundamental arrangement employed in controlling the cyclotron and detector is shown in Fig. 1. A thousand-cycle oscillator of the "transitron" type was calibrated by using a scaling circuit and a clock to determine the fundamental timing frequency. The output of this oscillator was divided into two parts.

One part was fed to a circuit which converted the sine wave output to a square wave. This square wave then operated a counter circuit which could be set to respond to any number of cycles from 1 to 10 to give a corresponding frequency reduction in the fundamental timing cycle. This gave flexibility in changing the

timing cycle, so that the optimum value could be used for any experiment performed. The output of this counter circuit triggered a special multivibrator circuit. This produced the fundamental modulation pulse which could be varied from 10 to 1000 microseconds in width. The output of this circuit activated the "level-setters" on the detectors so that only neutrons detected within the duration of the pulse would be recorded as "timed counts."

The other part of the oscillator output was fed to a phase-shifting condenser output. The sine wave could be shifted in phase continuously by any desired amount. The phase shift was linear with angle of rotation of the phase-shifting condenser with one revolution of the phase-shifting condenser corresponding to 1000 microseconds, or one cycle, phase shift in the wave. The output of this condenser went to another counting circuit and timing multivibrator. The output of this timing multivibrator was then fed to a low impedance power output circuit, then over a line to a power amplifier which was in series with the exciting voltage generator of the arc of the cyclotron.

Arc Modulation

To investigate the sharpness of the arc modulation, an amplifier circuit was arranged to respond only to current pulses through the arc so the current pulse in the arc circuit could be studied on an oscillograph screen. These pulses were as sharp as could be expected in view of the amplifier circuit constants. The voltage pulses to "fire" the arc tended to produce an opposite effect so that when there was no arc, negative pulses were seen on the screen in place of the normal positive pulses. When the filament current was increased to the value where the arc would strike, the current pulses reversed the direction of the pulses to a positive value several times the previous size. This afforded an excellent check on the operation of the arc. The pulse observed rose and fell in about 5 microseconds. The limitation was probably, to a considerable extent, in the frequency response of the amplifier itself.

The time required for the voltage pulse to the arc to rise was determined by the sharpness of the grid signal applied to the power amplifier and by the rate at which the initial current could charge the r-f filtering condenser on the arc. Since this filtering capacitance was 0.004 microfarad and the initial currents were of the order of 1 ampere, the time required to charge the condenser to the operating voltage of the arc, 200 volts, should be less than 1 microsecond. The rate at which the voltage pulse decreased was determined by the rate at which the 0.004 microfarad condenser was discharged when the tubes ceased conducting. A 500-ohm resistor in parallel with the arc reduced this time to less than 5 microseconds. The manner in which the arc current followed the voltage pulse was less definite, but the time of firing was less than 5 microseconds, and probably less than one microsecond.

The arc source used was an enclosed capillary type, fairly well shielded from the main r-f voltage on the dees, so that the stopping of the ion production should be quite clean. Supplementary sources of ions should be relatively ineffective. A study of the results shows there can be no very large error from this source. This is best shown by the experimental resolution curve of Fig. 3 together with the fact that the neutron production dropped to zero when no modulation pulses "fired" the arc.

Monitoring of Circuit Operation

In order to keep check on the operation of the circuits, a buffer triode was attached to each essential point of the circuit. A special switching

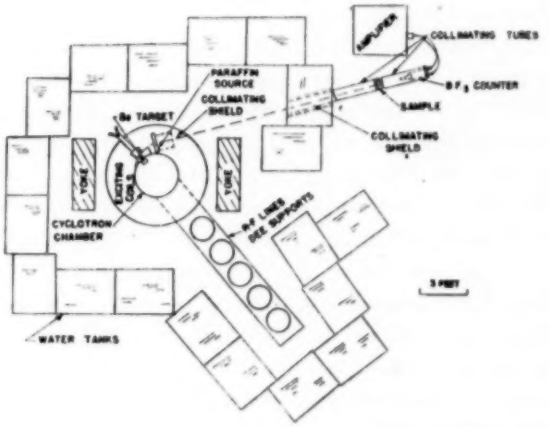

FIG. 2. Room plan showing the cyclotron, the water tank shielding the collimating system, and the slow neutron "source," sample, and detector positions.

arrangement permitted—(a) direct examination of the wave form at any point; (b) the direct addition of two wave forms in a mixer circuit; (c) the simultaneous observation of three points by use of two synchronized electronic switches of special design.

Timing Measurements

A 20-kilocycle transitron oscillator synchronized to the same point from which the oscillograph synchronization was obtained permitted all timing measurements to be made directly in units of cycles or fractions of cycles of the 20-kilocycle wave. A 5″ Dumont Type 208 oscillograph was used for all measurements. Parts of the pattern could be expanded to give 50 microseconds-per-inch spread so that measurements could be made to 5 microseconds or better.

Floor Plan of the Cyclotron Enclosure

The geometry of the paraffin and the collimating arrangement is shown in Fig. 2 for the work at 5.40 meters distance between the effective slow neutron source and the detector. The cyclotron chamber is located between the 36-inch diameter pole pieces of the magnet. The target was a piece of beryllium on a probe placed about 15″ from the center of the chamber.

Slow Neutron Sources

The effective source of slow neutrons was a vertical paraffin slab placed on the case of the magnet coils to slow down the fast neutrons produced at the target. While the thickness of the paraffin slab could be varied to give the best neutron distribution for a given experiment, other considerations made it more desirable to use one standard thickness. Experiments investigating the relative slow neutron intensity from the source slab as a function of slab thickness had indicated that a maximum was obtained for a 4.5-cm slab while with cadmium over the slab the maximum occurred for a 2.5-cm slab. Since the consideration of the delayed emission of thermal neutrons (see below) suggested as thin a source as possible, a compromise value was employed.

For most of the experiments a source consisting of a 2.6-cm thickness of paraffin in a 0.25-in. thick plywood box was used. Because of its low density and hydrogen content the total 0.5-in. thickness of plywood present was equivalent to only about 0.3-cm paraffin.

Collimation and Shielding

The collimation and shielding employed are shown in Fig. 2. The cyclotron was surrounded by thick water tanks to reduce the external radiation to a minimum. In one of these tanks a central slot was provided through which the collimated path was taken. A B_2O_3 cadmium collimating shield was placed in the slot and the space to the sides was filled in with boxes containing a 30 percent boric acid, 70 percent paraffin mixture. A similar small collimating section was placed in front of the paraffin slab to reduce the effect of neutrons scattered from the water tanks.

The final collimation for each detector was provided by two 36-inch collimating tubes in a line placed outside the enclosure. These tubes were 5-inches O.D. and 3.25-inches I.D. lined with cadmium. The 0.75-inch thickness between the inner and outer walls was filled with dried boron oxide in the first tubes and with dried boron carbide in the second tubes containing the counters. The counters were mounted in brass tubes and the electrical connections were brought out through cadmium shields. In this manner excellent shielding from stray neutrons was obtained.

In order to investigate the completeness of the collimation the following experiments were carried out. Thick cadmium (0.43 g/cm^2) was placed between the collimating tubes in the sample position and a reduction of total intensity from 100 to 7 in arbitrary units was obtained. When the timing was set for the peak of the neutron distribution coming from paraffin, the intensity of the timed neutrons was reduced from 100 to 0.79 when Cd was placed over the source and was reduced from 100 to 0.43 when Cd was placed over the tube (see Fig. 8) thus showing that essentially all the neutrons counted came from the slab of paraffin which served as the effective source. A thick boron carbide filter placed in the sample position reduced the total intensity from 100 to 1, illustrating the effective-

ness of the shielding obtained with the collimating tubes and the smallness of the total fast neutron background.

Detection

Proportional counters normally filled to a pressure of 30 cm of BF_3 were used to detect the neutrons. The counters were enclosed in an envelope of soft glass of low boron content with a copper screen cylinder 5 cm in diameter and 20 cm long as the negative electrode and a tungsten wire (0.01 cm diameter) as the positive electrode. The proportional region of these counters was very broad. They could be used anywhere between 2400 and 3500 volts. The "Geiger region" at which the counter responded equally to beta-particles was reached at about 4000 volts.

Proportional counters have several advantages over ionization chambers in this type of work in that (a) the pulses are usually of shorter duration; (b) the amplification required is much less, and, therefore, they are much less subject to r-f and other types of pick-up; (c) there is less response to gamma-radiation. The disadvantages of a proportional counter include the somewhat greater non-uniformity of pulse sizes, the tendency of the gas amplification to drift because of temperature changes in the counter, and the lower sensitivity.

The output of the proportional-counter, linear-amplifier was fed to a level-setter which was set at approximately $\frac{1}{4}$ the height of the highest neutron pulses, to insure that only neutrons were counted. This was further tested by timed counts with a Cd filter in the region of 200 micro-seconds/meter.

The change in gas amplification due to temperature changes was found to be very slow when the counters were compared with each other and with ionization chamber systems around the cyclotron. Any error due to this source was eliminated entirely by referring the number of neutrons counted in a timed interval to the total number of neutrons counted in the total interval of time. In this manner a change in the efficiency of counting would represent an equal change in both values and cancel. Since such changes are relatively slow, this is not considered a serious source of error even when comparison measurements with two counters were made to obtain the total cross section.

The output of the proportional counter was fed to a twin channel 5-stage linear amplifier. Previous work with proportional counters had shown that if the low frequency response of the amplifiers was maintained the pulse would rise sharply and then gradually drop again to zero. Since the effective on-time of the detector modulation also includes the counter pulse width above the level-setter height, it was desirable to narrow the pulse width as much as possible. To reduce the low frequency response of the amplifier the input resistor of the first tube was reduced to 25,000 ohms and the time constants of the coupling of successive stages were kept small. Inverse feedback by pairs was used to make the total gain of the amplifier almost independent of line voltage and other fluctuations. The fifth stage of the amplifier used a type of 6L6 tube to provide low impedance output. The output of the amplifier was fed over low impedance transmission lines to the cyclotron control room some distance away where the counting circuits and the modulation equipment were operated.

CALIBRATION OF THE INSTRUMENT

When the results of experiments performed with the instrument are to be evaluated, it is first necessary to evaluate all the factors and uncertainties inherent in the instrument and the method which will influence the results. The factors involved here are discussed below.

1. Path Length for Timed Flight

The distance measured was from the front surface of the paraffin source slab to the center of the proportional counter. If the effective starting point were some distance below the paraffin surface, this would represent a source of error. For transmission measurements at 5.4 meters a source consisting of 2.6-cm paraffin in a box of $\frac{1}{4}''$ plywood was used so this effect would be small.

The effect of the 20-cm counter length is to broaden the resolution of the instrument. For a 5.4-meter path this effect gives a maximum uncertainty in a velocity measurement of ± 1.85 percent. When the uncertainty is converted to a

time of flight uncertainty, this represents a total extra resolution broadening of 3.7 percent of the measured time of flight. Since the probability of detecting a slow neutron directed along the length of the counter is only a few percent, the displacement of the effective center of the counter towards the near end is always negligible.

2. Measurement of the Time Interval Between the Cyclotron and Detector On-Time Intervals

The frequency of the 1000-cycle oscillator establishing the fundamental timing was measured occasionally with a scaling-circuit and a clock and was seldom found in error more than 0.1 percent. The timing measurements were in terms of a synchronized 20-kc oscillator and were probably known always to within 5 microseconds.

3. Over-All Time Lag of the System

The effective time-of-flight of the neutrons from the paraffin source to the detector will be less than the measured spacing between the cyclotron and detector on-time intervals because of time lags in the neutron production and detection. First there is a time interval of the order of 5–10 microseconds required for the deuterons to be accelerated in the cyclotron before striking the target. Then a negligible time is required for the neutrons to slow to energies of the order of a few electron volts and escape (see Table I). Since a detected neutron will be counted in a timed interval if the resultant pulse height is above the level-setter position during any portion of the detection interval there will also be an effective detection time lag, from the time the neutron is captured by a boron nucleus in the counter to the time when the resultant pulse reaches the center of its interval above the level-setter height.

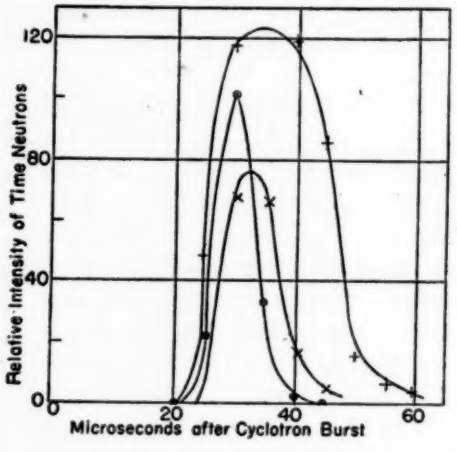

FIG. 3. Experimental resolution curve. Data taken 8 cm from the paraffin "source." ○ = counter in B_4C shield with a pulse sharpener. + = counter in B_4C shield without the pulse sharpener. × = with Cd shielding with a pulse sharpener.

The over-all time lag of the instrument may be directly determined by measuring the slow neutron intensity from the paraffin source slab as a function of cyclotron and detector on-time spacing with the detector near the source. The results of these measurements are shown in Fig. 3.

The counter was mounted in a cylindrical B_4C-Cd shield with an opening in the side facing the source slab. In one set of measurements a B_4C-Cd plug was placed in the slot to eliminate all but the highest energy slow neutrons. In the second set the plug was removed and Cd filtration was employed. Although the counter was placed as close to the source as possible in these measurements, the effect of 8-cm distance from the front of the source to the counter axis shows up as a 5-microsecond shift. This represents the time of flight of the slower neutrons above the Cd cut-off region over this short distance.

In two of the measurements a special pulse sharpening circuit was employed to minimize the effect of the pulse width when the cyclotron and detection on-time were reduced to an extreme minimum. Comparisons with and without the sharpening circuit clearly show the effect of the pulse width on the effective resolution. In the other experiments described in this paper this pulse sharpener was not employed as such extreme resolution was not required. Figure 3 shows better than any other experiment the sharpness of the source modulation starting and stopping.

When the sharpening circuit was not employed, the resulting intensity function appeared flat on top rather than triangular as only the pulse width was important. When the source and detection on-time widths are equal, the resolution function is more nearly the usual triangular shape.

From Fig. 3 it is seen that the basic delay time is 30 microseconds to which must be added half the pulse width. Accordingly 35 microseconds was deducted from all measurements when the sharpening circuit was not employed.

4. Thermal Emission Delay

Neutrons slowed in paraffin will continue to suffer collisions in the paraffin until they escape or are captured. This results in a continued emission of thermal neutrons from the paraffin slab for a considerable time after the production of fast neutrons has ceased. This delayed emission will decay with a mean life for decay determined by the thickness of the paraffin for diffusion and by the mean lifetime for capture of a neutron in paraffin of about 180–200 microseconds. Applying simple diffusion theory to this problem it is found that the diffusion of thermal neutrons from the source should roughly be proportional to the square of the paraffin thickness for thin samples and limited by the mean life for capture for thicker slabs. Using probable values for the diffusion coefficient and the mean life for capture in paraffin the predicted mean lives for decay for the two sources measured have been calculated.

For the main measurements a paraffin source consisting of 2.6 cm of paraffin enclosed in a box of $\frac{1}{4}$-inch thick plywood was used. The effective source thickness for diffusion, after the effect of the plywood and the necessary zero correction at edges were considered, was taken as 3.2 cm. The predicted mean life for decay for this thickness was 43 microseconds. The second source used consisted of a 6.2-cm thickness of paraffin in a box of $\frac{1}{4}$-inch thick plywood corresponding to 6.8-cm effective diffusion thickness. The predicted mean life for decay from this thickness was about 100 microseconds.

In order to measure experimentally the effective decay time of the thermal emission from these slabs measurements were made with the counter next to the source. The collimating arrangement mentioned above was used with the opening next to the slab. After making these measurements it was at once apparent that the time required for the thermal neutrons to travel the few centimeters distance to the counter was sufficiently great to render the results meaningless.

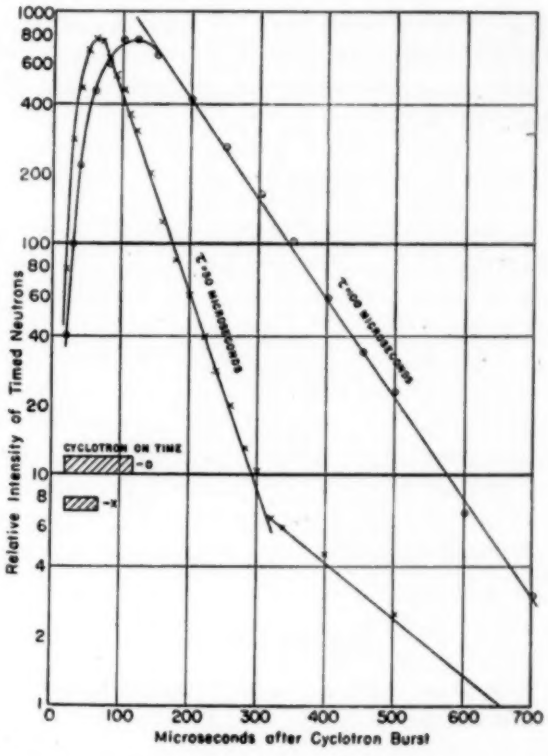

FIG. 4. Thermal neutron delayed emission from paraffin "source" slabs. Data taken next to the source with a tiny BF_3 counter. × = 2.6 cm thick paraffin in a box of $\frac{1}{4}$" thick plywood. ○ = 6.2 cm thick paraffin in a box of $\frac{1}{4}$" thick plywood.

To reduce the path length still farther a tiny BF_3 counter 1 cm in diameter was used in contact with the slab. The results of these measurements are shown in Fig. 4. For the measurements with the thin source a cyclotron on-time of 50 microseconds and a detector on-time of 15 microseconds were employed. There was an exponential rise in intensity during the cyclotron on-time and then an exponential decay of intensity after production had ceased. Although a decay time of 50 microseconds seems clearly indicated from Fig. 4, the results of different measurements gave values between 43 and 50 microseconds. In these and other measurements with thinner slabs there seemed evidence that the measured time tended to be too large so a value of (45±5) microseconds was selected as the effective decay time for this source.

The measurement of the thicker source gave a more extended straight line logarithmic plot with a decay time of 100 microseconds. This value

agrees exactly with the predicted value but differences obtained in different measurements indicate that this value should be expressed as (100±10) microseconds.

Timing Correction

As a result of the factors mentioned above a deduction of 35 microseconds was made from all time-of-flight measurements. In the thermal energy region an additional deduction was made equal to the mean decay time for the emission of thermal neutrons from the source. In the intermediate region a fractional deduction was made as an approximate method of bridging the gap between the thermal and higher energy regions. Fortunately, as may be seen from Figs. 6 and 7, this transition is relatively abrupt on a time-of-flight basis.

Resolution Width

The total resolution width for times-of-flight below the thermal region was taken as the sum of the cyclotron and detector on-times, the detector pulse width, and 3.7 percent of the corrected time-of-flight. In the thermal region an additional width equal to the mean decay time for the delayed emission of thermal neutrons from the source was added. Although the true effect of the delayed emission is more complex, this was considered to be the best approximation. When the effect of the resolution function on the measurements was considered, a triangular shape was always assumed. Although the true shape was quite complex and varied, it was always roughly triangular in shape and this was considered to be the best simple approximation. When a resolution triangle is indicated on a curve a width equal to the sum of the first three factors mentioned above is shown. The 3.7 percent effect and the delayed emission effect should thus be added to the width indicated for analysis.

THE EFFECT OF THE RESOLUTION WIDTH

When the timing is set for a measurement on neutrons of time-of-flight t_1, the effect of a triangular resolution function of width $2a$ will be to make the actual region of measurement lie between (t_1-a) and (t_1+a). In a measurement of the intensity distribution function from the source, I, or of the transmission function of a sample, T, the resolution width will have no effect only if these quantities are constants. When I and T are smoothly increasing or decreasing functions of the time of flight of the neutrons, there will be a distorting effect which may be expressed as a change in I or T at the point t_1. It is also permissible to regard this effect as one of changing the effective weighting over the resolution function to give the true value of I or T for a slightly different time of flight $(t_1+\alpha)$ where $|\alpha|<a$. This latter method has seemed preferable for the analysis in this paper.

If both I and T may be approximated by exponentially increasing or decreasing functions between (t_1-a) and (t_1+a) and $\Delta I/I$ and $\Delta T/T$ are the fractional changes in I and T between (t_1-a) and (t_1+a), it may be shown that α is approximately given by

$\alpha_1=(a/24)(\Delta I/I)$ for a measurement of I,
$\alpha_2=(a/24)(\Delta T/T+2\Delta I/I)$ for a measurement of T.

Since these fractional changes are usually small as compared with unity, the effective timing shift is usually quite small and is not corrected for in the analysis of the data.

When I or T pass through a sharp maximum or minimum, the averaging effect changes the measured value by an amount proportional to the curvature of the function and the square of the resolution width. A correction for this effect has been made only in the case of the cadmium resonance where a numerical integration method was employed as described below.

EXPERIMENTAL PROCEDURE

A. Intensity Measurements

After the cyclotron had been running stably for a period of time the modulator was turned on. The desired timing cycle was set and the desired cyclotron on-width and detector on-width set with respect to the 20-kilocycle oscillator. Then the number of counts coming in the timed interval was recorded using a standard number of total or untimed counts (taken with the same counter) to define the counting interval. In this manner the ordinate of the intensity *vs.* time-of-flight curve was referred to the total area under

the curve, thereby automatically eliminating any drifts that would take place. In the intensity or open-beam measurement the series of timed intensity values obtained in this manner provides all the data necessary to give the intensity *vs.* time-of-flight curve of the neutron distribution emerging from the paraffin source.

B. Transmission Measurements

In making transmission measurements with a neutron source of constant strength it is necessary only to count for *equal intervals of time* with the sample in the beam ("in" count) and with no sample in the beam ("out" count). The ratio of the two counts then gives the experimental value of the true transmission of the sample. When a source of varying intensity is employed the equal intervals of *time* are replaced by equal "intervals" of *neutron production* at the source. To measure equal intervals of cyclotron neutron production an extra BF_3 counter situated in the cyclotron enclosure was used as a monitor. In order to establish a procedure for using this extra "monitor," however, the factors involved in possible alternative procedures were examined. It should first be noted that the procedure of adjusting the counting intervals to that necessary to obtain a standard number of total detector counts as was employed in making the intensity *vs.* time-of-flight measurements will give only a *relative* transmission value when the ratio of the timed counts for the in and the out runs is taken. This is because the counting rate for the total or "untimed" counts with the sample in the beam is reduced by a factor equal to the average transmission of the sample for the particular total neutron flux distribution involved. Thus if this method were used it would also be necessary to determine the factor which would convert the *relative* transmission values to an absolute basis.

A direct method of obtaining the proper counting intervals would be to use the interval required to obtain a standard number of monitor counts as a reference as the monitor counting rate is not affected by the position of the sample. The ratio of the timed counts with sample in to that with sample out counting for intervals of equal monitor counts would then give the transmission directly. This procedure was not employed, however, because of the disadvantage that two counters are now involved and any drifts in their relative efficiencies between an in and an out run would directly introduce an additional error in the result. In the intensity measurements this effect was eliminated by comparing the number of timed counts to the total counts on the *same* counter. It was desired to retain this feature in the transmission measurements, if possible, so the procedure described below was finally adopted.

After the desired time-of-flight had been set, the out measurement was made by recording the number of timed counts q_1 and the number of monitor counts Q_3 obtained for a standard number of total detector counts Q_1. Similarly for an in run the number of timed counts q_2 and the number of monitor counts Q_4 were recorded for a standard number of total detector counts Q_2. Although Q_1 and Q_2 were in general chosen differently according to the reasoning discussed below, the value of Q_1 was the same for all out runs and Q_2 was the same for all in runs. The ratio q_2/q_1 gives a value proportional to the transmission at the point. Using the monitor counts as a reference the transmission, T, is given by $T=(q_2/q_1)(Q_3/Q_4)$. Since the ratio (Q_3/Q_4) is subject to the objection discussed above, however, the monitor ratio was first averaged over the entire run before it was applied as a correction factor to convert the relative transmission values to an absolute basis. The averaging effect and statistical accuracy introduced by a long series of alternating in and out runs thus minimizes the errors introduced in determining the monitor ratio such that the final uncertainty in a transmission value is almost entirely dependent on the uncertainties in the ratio (q_2/q_1). Since q_1 and q_2 are not affected by drifts in the counter efficiency, this freedom from the effect of drifts in counter sensitivity has largely been retained in the transmission measurements.

SAMPLES—GENERAL CONSIDERATIONS

In choosing the samples, two effects have to be taken into consideration. First, the statistical accuracy in determining the points, and, second, the resolution of the apparatus. When the transmission is a slowly varying function of the time-of-flight, the effect of the resolution of the apparatus is small and will not influence the

choice of the sample; so, in this region of a transmission curve, the sample which will give the best statistical accuracy should be used.

A relation may be obtained to give as a function of T, the transmission of the sample, the statistical uncertainty of the cross section for a fixed total counting time, t. The effect of the timed counts alone is considered in the analysis below.

Let N = counts in time t with sample out of the beam ("out position"); then NT = counts in time t with sample in the beam ("in position").

Let X = fraction of total interval t devoted to the in position; then

$N_1 = XNT$ = counts received for in position,

$N_2 = (1-X)N$ = counts received for out position,

$\alpha = \Delta N_1/N_1 = 1/(XNT)^{\frac{1}{2}}$

= fractional uncertainty in N_1,

$\beta = \Delta N_2/N_2 = 1/[(1-X)N]^{\frac{1}{2}}$

= fractional uncertainty in N_2,

$T = N_1/N_2[(1-X)/X]^{\frac{1}{2}}$

= transmission of the sample,

$$\frac{\Delta T}{T} = (\alpha^2+\beta^2)^{\frac{1}{2}} = \frac{1}{(NT)^{\frac{1}{2}}}\left[\frac{1}{X}+\frac{T}{(1-X)}\right]^{\frac{1}{2}}$$

= fractional uncertainty in T,

$T = \epsilon^{-n\sigma}$,

σ = cm²/atom of the type considered,

$\sigma = -(1/n)\log T$,

n = atoms/cm² in the beam,

$$\frac{\Delta\sigma}{\sigma} = \left|\frac{\left(-\frac{1}{n}\frac{\Delta T}{T}\right)}{\left(-\frac{1}{n}\log T\right)}\right| = \frac{-\Delta T}{T\log T} = \phi(X, T).$$

To make $\phi(X, T)$ a minimum with respect to X the term $[1/X+T/(1-X)]$ in $\Delta T/T$ must be made a minimum. This gives

$X = 1/(1+\sqrt{T})$ for $\phi(X, T)$ a minimum.

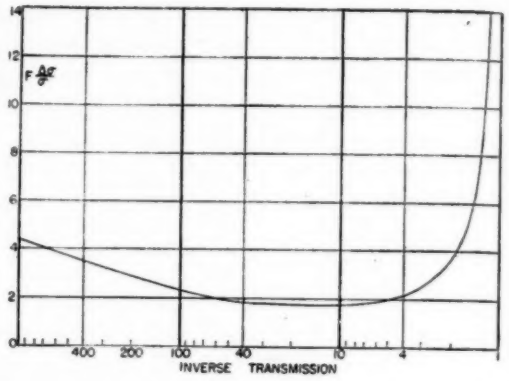

FIG. 5. Statistical error function. As a guide in choosing the optimum sample thickness this curve gives the relative statistical uncertainty in a cross section measurement as a function of the reciprocal of the transmission of the sample for a fixed counting time.

Then $\Delta T/T = (1+\sqrt{T})/(NT)^{\frac{1}{2}}$ and we obtain

$$\left(\frac{\Delta\sigma}{\sigma}\right)_{X\,\min} = \frac{-(1+\sqrt{T})}{(NT)^{\frac{1}{2}}\log T} = \frac{F(T)}{\sqrt{N}}. \qquad (1)$$

The function $F(T) = -(1+\sqrt{T})/(T^{\frac{1}{2}}\log T)$ has been plotted in Fig. 5. It is seen to have an extremely broad and flat minimum which, for practical purposes, is constant between about $T=0.01$ and $T=0.25$. Solving for the value of T at the minimum gives

$$-\log\sqrt{T} = (1+\sqrt{T})$$

as the relation to be solved. This gives

$$T = e^{-2.556} = 0.0761$$

from which

$$F_{\min}(T) = 1.79.$$

The effect of choosing X slightly different from the optimum value $X=1/(1+\sqrt{T})$ is also not critical in its effect on the final uncertainty. In practice X would be chosen as some convenient value near the optimum value.

Near a resonance point the transmission varies rapidly as the energy of the neutron approaches the resonance energy. The apparatus effectively averages the transmission over a time interval Δt where the efficiency of detection approximately follows a simple triangle law. If the Breit-Wigner one-level formula is assumed to hold for the cross section in the vicinity of the resonance point, the

predicted experimental transmission will be given by

$$T_{\text{exp}} = \int_{t-(\Delta t/2)}^{t+(\Delta t/2)} f(t) \times \exp\left\{-n\sigma_0(E_0/E)^{\frac{1}{2}} \Big/ \left[1+\left(\frac{E-E_0}{\Gamma/2}\right)^2\right]\right\} dt, \quad (2)$$

where

$f(t)$ is the normalized triangular resolution function,
σ_0 is the actual value of the cross section at exact resonance,
Γ is the width of the nuclear resonance line,
n is the number of absorbing atoms per square centimeter.

The predicted experimental value of the cross section at the maximum will be given by

$$\sigma_0' = -(1/n) \log T_{\text{exp}}. \quad (3)$$

Samples for Investigating Resonances

Since the experimental data should give some quantitative indication of the actual value of the cross section at the peak of the resonance curve, the number of atoms of absorbing material per square centimeter should not be large. The thicker the sample, the larger the correction factor will have to be in order to obtain the actual cross section at the peak from the observed cross section at the peak. This effect can be seen very easily if the problem is simplified by assuming that the cross section rises sharply from zero to a value σ at a time of flight t_0, is constant between t_0 and t_0+a, and then drops again to zero. If the resolution width is twice the width of this idealized line and the resolution efficiency is assumed to be constant over the interval $2a$, then the predicted minimum experimental transmission will be

$$T_{\text{exp}} = \tfrac{1}{2}[1+e^{-n\sigma}] = \exp(-n\sigma_{\text{exp}}). \quad (4)$$

From this equation it is seen that if $n\sigma$ is very small, then $\sigma_{\text{exp}}=\sigma/2$, but if $n\sigma$ becomes very large, then $n\sigma_{\text{exp}} \rightarrow \log 2$. In this simplified case the best predicted experimental value that could be obtained would be $\frac{1}{2}$ the actual value of the cross section at the maximum and as the number of atoms/cm² was increased the experimental cross section would approach the relation $1/n \log 2$, which is not related to σ.

Therefore, thin samples should be used in order to have the experimental value of $n\sigma_{\text{exp}}$ as sensitive as possible to variation in the actual value of $n\sigma$. The correction due to the resolution of the apparatus should also be kept small because of uncertainties in the knowledge of the exact resolution function to be used due, for example, to the small uncertainty in the fundamental timing width settings. Taking both the statistical error and the resolution error into consideration, the transmission of the sample at resonance should be about 0.3 to 0.5, this being near the upper end of the flat part of the error curve of Fig. 5.

In the cadmium measurements, two different samples of rolled Cd were used. The main measurements used a sample of 43.3 mg/cm² while supplementary measurements employed a 219 mg/cm² sample.

In the boron measurements four different samples were used because of the large range of cross-section values to be studied. In the region where the cross section was low, two thick samples of B_2O_3 were used. To prepare these samples the B_2O_3 was baked for 48 hours at 140°C to make sure that all the water was removed. The dry B_2O_3 was then packed tightly in aluminum containers to give 1.092 g/cm² of B_2O_3 and 0.418 g/cm² of aluminum for one and 2.464 g/cm² B_2O_3 and 0.418 g/cm² of aluminum in the other.

For lower energies where the cross section was higher, a thinner sample was desired so another sample containing 0.310 g/cm² of B_2O_3 and 0.418 g/cm² of aluminum was prepared in a manner similar to the others.

For the lowest energies studied as a further check on the procedure, a third sample was used which consisted of several layers of Pyrex glass totaling 0.965 g/cm². Analysis of this type of glass has shown that it contains 12.9 percent B_2O_3, the remaining part being mainly SiO_2. The consistency of the results with the three different samples is a good check on all the samples as the regions studied always overlapped considerably.

THE SLOW NEUTRON ENERGY DISTRIBUTION FROM THE PARAFFIN SOURCE SLABS

The exact form of the slow neutron distribution from a paraffin source is of considerable interest

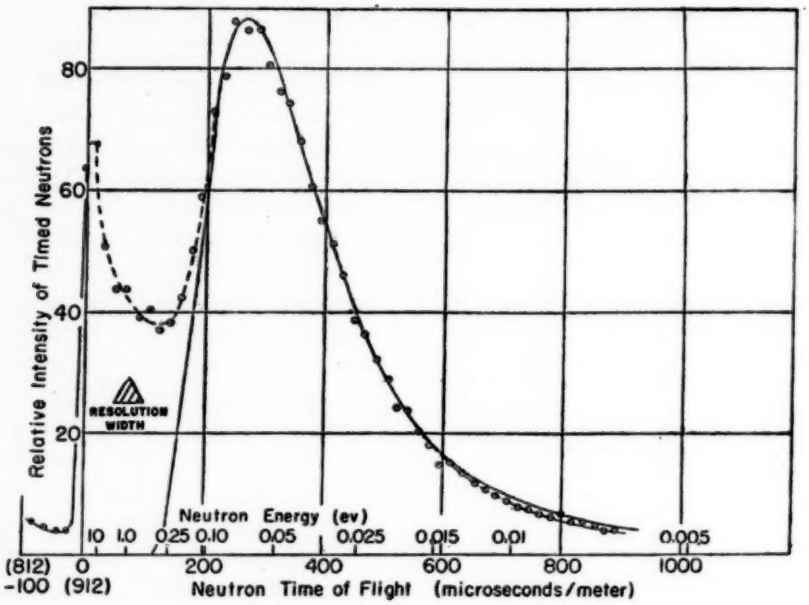

FIG. 6. The slow neutron distribution from the "thin" paraffin "source" slab. (2.6 cm thick paraffin in a box of $\frac{1}{4}$" thick plywood.) O = experimental curve. — = v^4 theoretical curve for 430°K.

as the mechanism of the establishment of thermal equilibrium between the neutrons and the paraffin is involved. Since this apparatus is particularly suited to such measurements the distributions from two source slabs were studied. This investigation was carried out to determine the shape of the emerging energy distribution also as an indication of the relative intensities to be expected in making cross-section measurements for different neutron times of flight. As a result of these and other intensity measurements, the standard source slab was chosen as one containing 2.6 cm thickness of paraffin in a box of $\frac{1}{4}$-inch thick plywood. As a "thick source" for these measurements, a 6.2-cm thickness of paraffin in a box of $\frac{1}{4}$-inch thick plywood was used.

The results of the measurements on these sources are given in Figs. 6 and 7. The source-detector distance employed was 5.4 meters and the cyclotron and detection on-time widths were both 100 microseconds. For the thin source a 5000-microsecond cycle was used and for the thick source an 8000-microsecond cycle was used to decrease the relative intensity of neutrons overlapping from previous cycles. In Figs. 6 and 7 the results have been corrected for the dead time and delayed thermal emission effects and the results reduced to a one-meter basis. In each case the approximate number of timed counts taken in obtaining a point may be obtained by multiplying the ordinate by 160. The uncertainty in the value of the timed counts is best shown, however, by the magnitude of the deviations of the points from a smooth curve.

The value of the dead time correction is shown in Fig. 3 to be about 35 microseconds. The delayed thermal emission from these slabs has been discussed above and is shown in Fig. 4. The effective source thicknesses were also discussed at that time.

Theoretical Considerations

The distributions in Figs. 6 and 7 are well matched by Maxwellian type curves of a corrected form for temperatures somewhat above the paraffin temperature. The expected form of the curves may be seen from the following discussion.

If it is assumed that the neutrons in the paraffin source are in complete thermal equilibrium with the paraffin, the number with velocities between v and $v+dv$ will be proportional to

$$N_0(v)dv = v^2 \exp(-mv^2/2kT)dv, \qquad (5)$$

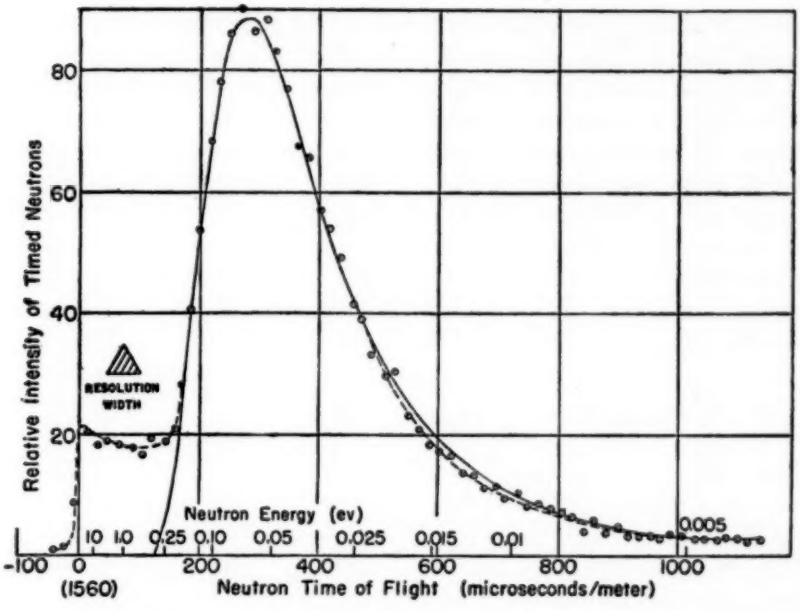

FIG. 7. The slow neutron distribution from a "thick" paraffin "source" slab. (6.2 cm thick paraffin in a box of $\frac{1}{4}$" thick plywood.) O = experimental curve. — = v^4 theoretical curve for 390°K.

where T here is used to represent the absolute temperature. If a constant mean free path is assumed, this density function will also be maintained for the neutrons emerging from the paraffin. The flux distribution, however, will contain an extra v factor to give a v^3 type distribution. Since the detector employed utilizes the $B(n, \alpha)$ reaction which is proportional to $1/v$, and the counter efficiency is always small enough to maintain this efficiency relation, the velocity distribution of neutrons detected by the BF_3 counter should be the same as $N_0(v)$.

When some parameter ϕ, other than v, is used to express the form of the distribution, we have, considering only absolute magnitudes,

$$F(\phi)d\phi = N_0(v)dv = [dv/d\phi N_0(v)]d\phi. \quad (6)$$

In these measurements equal intervals of time-of-flight, t, of the neutrons over a path of length, l, are used to give

$$F(t)dt = [N_0(v)dv/dt]dt = v^2/1N_0(v)dt,$$

or

$$F(t) = C_1 v^4 \exp(-mv^2/2kt)$$
$$= C_2 t^{-4} \exp(-ml^2/2kTt^2). \quad (7)$$

It is thus seen that the form of the predicted experimental curve should be of the v^4 or t^{-4} variety due to the above factors. This curve will thus correspond in shape neither to the neutron density, v^2, or flux, v^3, distributions from paraffin. It may easily be shown however that the value of the ordinate of the curve at any point corresponds to the *flux* distribution from paraffin expressed in equal logarithmic or fractional intervals of any of the parameters such as velocity, energy, or time-of-flight. The value of the ordinate thus corresponds to a dimensionless representation of the *flux* distribution from the paraffin. It should be noted that this is true independent of the form of the distribution function.

After the correction has been made for the delayed emission of thermal neutrons from the paraffin, the true distribution should differ from Eq. (7) for several reasons. The first of these is the fact that the mean free path of slow neutrons in paraffin continuously decreases as the energy decreases or the time of flight increases. This has the effect of making it easier for the faster neutrons to escape and thus has an effect which may roughly be described as an additional v^α factor where α is small and positive.

The second reason has to do with the fact that the neutrons initially are of several Mev energy and are slowed by successive collisions in the

paraffin. Since some of these "cascading" neutrons of all energies escape from the paraffin before reaching thermal equilibrium, a high energy tail above the thermal region will be added and a contribution to the thermal energy region will again be present which will asymmetrically favor the high energy side of the distribution. It may be noted that the existence of such a tail was shown experimentally in the first velocity selector experiments of Dunning *et al.*[5]

For a thick paraffin source the probability is small that a cascading neutron will escape after a given collision before making another. It may be shown theoretically that in such a case, in a region of constant mean free path, the flux distribution should be constant for equal logarithmic intervals of the measuring parameter. For thinner sources the curve above the thermal region should be a decreasing function of the time-of-flight where the negative exponent of t is proportional to the probability that a cascading neutron will escape immediately after a given collision. For the thick source where this probability is small the curve, Fig. 7, is nearly flat above the thermal region. For the thin source, Fig. 6, the intensity drops rapidly as the thermal region is approached. In both cases there will be a contribution of the cascading neutrons to the thermal region which will be more complicated than the corresponding contribution above the thermal region.

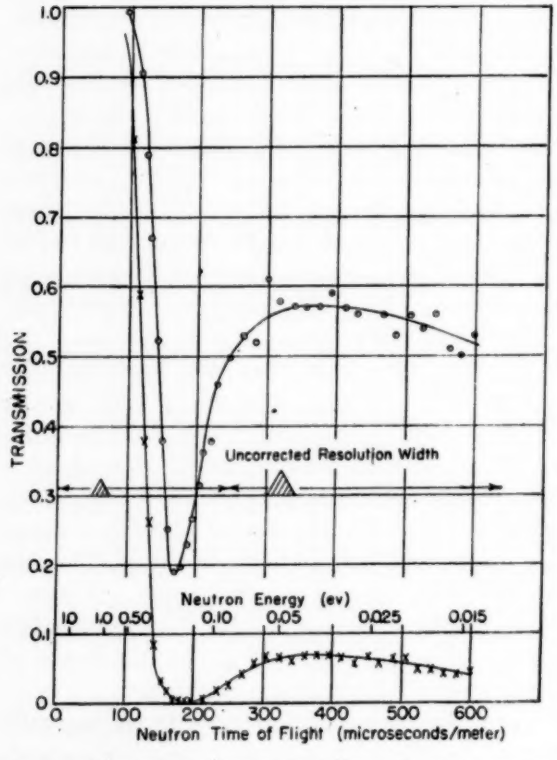

FIG. 8. Cadmium transmission curves. ○ =43.3 mg/cm² Cd sample. × =219 mg/cm² Cd sample.

The third factor which will cause the observed distribution to differ from Eq. (7) involves the mechanism of energy exchange between the neutrons and the paraffin. At thermal energies the quantum effects associated with the paraffin structure limit the probability that a low energy neutron will undergo a collision involving only a small change in energy. This has the effect of requiring a very large number of collisions to approach thermal equilibrium closely. Before this occurs many of the thermal neutrons, depending on the emission delay time, will escape in only partial thermal equilibrium and the high energy side of the distribution will again be emphasized.

Since the thermal distributions, Figs. 6 and 7, would be expected to favor higher energy neutrons relative to a curve of the form of Eq. (7) for the temperature of the paraffin source, it was considered to be of interest to see how well it could be matched by a curve of this type for a slightly higher temperature. The curve of Fig. 6 is seen to be in excellent agreement with the theoretical curve for 430°K while Fig. 7 is well matched by a theoretical curve for 390°K. These correspond, respectively, to increases of 43 and 30 percent above the absolute temperature of the paraffin slabs.

CADMIUM RESONANCE ABSORPTION

The results of the cadmium absorption measurements are given in Figs. 8 and 9. The distance employed for the time-of-flight measurements in this case was 5.4 meters with the standard thin paraffin source slab. Cyclotron and detection on-time intervals of 50 microseconds each were used for times-of-flight of less than 240 microseconds/meter where the resolution effects would be serious. For times-of-flight greater than 240 microseconds/meter the intensity and resolution functions change slowly so on-times of 100 microseconds each were employed. All data were corrected for the over-all dead time.

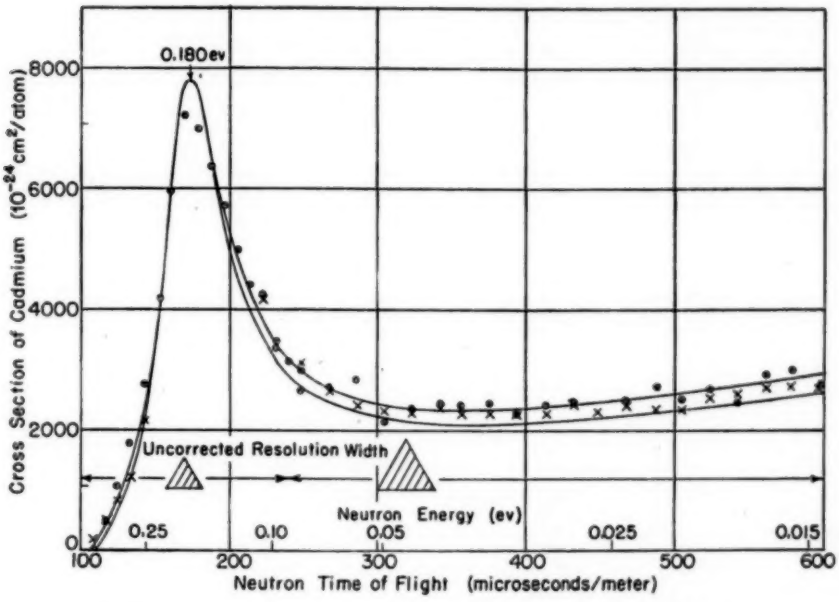

FIG. 9. Cadmium resonance cross section curve. This shows the total slow neutron cross section of Cd as a function of the time-of-flight of the incident neutrons. ○ = experimental points for a 43.3 mg/cm² sample. × = experimental points for a 219 mg/cm² sample. — = theoretical curves for $E_0 = 0.180$ ev; $\sigma_0 = 7800 \times 10^{-24}$ cm²/atom; $\Gamma = 0.114$ ev—upper curve; $\Gamma = 0.108$ ev—lower curve.

The delayed thermal emission correction of 45 microseconds was not applied suddenly but was gradually added over the region between 700 and 1500 microseconds for 5.4 meters or 125 and 265 microseconds on the one-meter basis. The gradation was chosen by reference to Fig. 6 from which the ratio of thermal to cascading neutrons can be estimated with fair accuracy. Since the total correction amounts to only 8.3 microseconds, and the uncertainty in the correction factor is certainly much less than this, the total error due to this factor is probably less than 2 microseconds/meter.

For a single sample which could be used over the entire region of interest a 43.3 mg/cm² sheet of rolled Cd was employed. To give supplementary information near the "transmission edge" and for energies below the peak a 219 mg/cm² sample was used. The transmission curves for these two samples are shown in Fig. 8. The cross sections corresponding to these measured transmissions are given in Fig. 9 together with two reference Breit-Wigner one-level curves.

The procedure employed in matching the experimental points in Fig. 9 to a best fitting theoretical curve was one of trial and error. In the region above 240 microseconds/meter the effect of the resolution is negligible so these values were considered to be reliable within the accuracy of the measurement. In the region of the peak, however, the effect of the resolution width is to make the measured transmission greater than the true transmission by averaging the "true transmission" curve over a region given by the resolution function. In the region of the peak the resolution width was taken as 30 microseconds/meter including the cyclotron and detector on-times, the effect of the counter length, and a partial thermal delay width.

A numerical integration near the peak employing a theoretical Breit-Wigner transmission curve and a 30 microsecond/meter resolution width indicated that the correction at the peak should be about 8 percent. Thus the value of σ_0 chosen for the calculation was $\sigma_0 = 7800 \times 10^{-24}$ cm²/atom. Since the asymmetric effect of the $1/v$ factor in the Breit-Wigner formula moves the maximum of the cross-section curve to the right of the resonance time-of-flight (Fig. 9), the best value of the resonance time-of-flight was determined by a matching process to be $t_0 = 170$ microseconds/meter corresponding to $E_0 = 0.180$ ev.

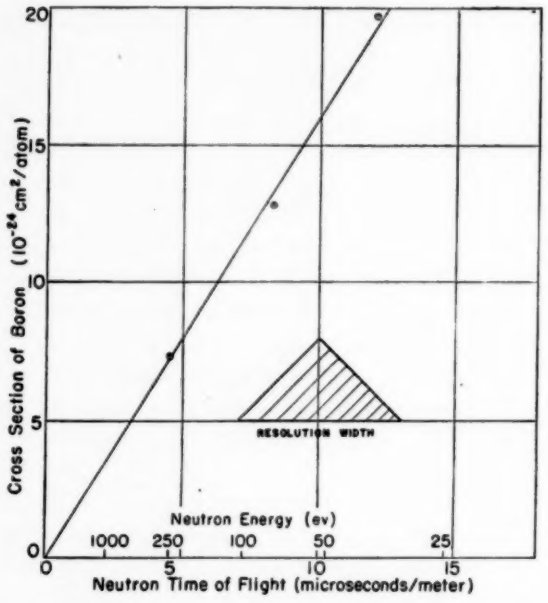
Cross Section of Boron (10^{-24} cm²/atom)
RESOLUTION WIDTH
Neutron Energy (ev)
1000 250 100 50 25
0 5 10 15
Neutron Time of Flight (microseconds/meter)

FIG. 10. Boron cross section curve for higher energies. O = experimental points. — = straight-line relation $\sigma = 118E^{-\frac{1}{2}} \times 10^{-24}$ cm²/atom.

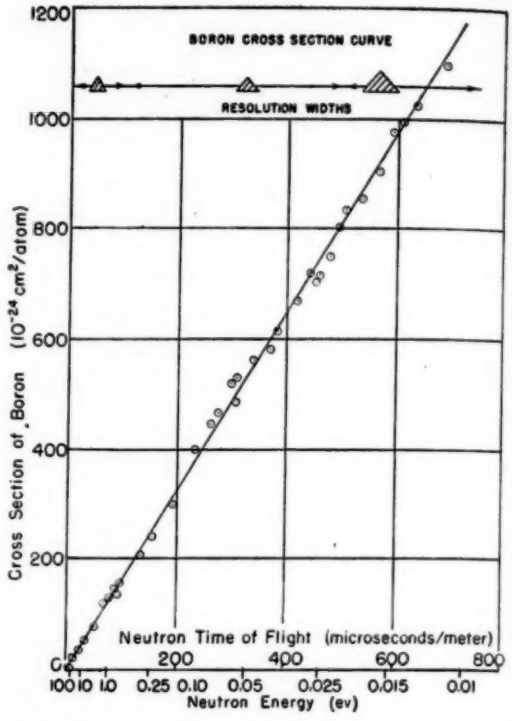
BORON CROSS SECTION CURVE
RESOLUTION WIDTHS
Cross Section of Boron (10^{-24} cm²/atom)
Neutron Time of Flight (microseconds/meter)
200 400 600 800
100 10 1.0 0.25 0.10 0.05 0.025 0.015 0.01
Neutron Energy (ev)

FIG. 11. Boron cross section curve. O = experimental points. — = straight-line relation $\sigma = 118E^{-\frac{1}{2}} \times 10^{-24}$ cm²/atom.

In Fig. 9 close matching theoretical curves for two values of Γ have been shown. These indicate the best value of Γ and also show the sensitivity of the agreement for times of flight above 240 microseconds/meter.

Considering all the possible sources of error which may be involved in such measurements as described above, the final results for Cd may be stated as follows:

$\sigma_0 = (7800 \pm 800) \times 10^{-24}$ cm²/atom,
$\sigma_{min} = (2300 \pm 150) \times 10^{-24}$ cm²/atom near 0.04 ev,
$\Gamma = (0.112 \pm 0.006)$ ev,
$E_0 = (0.180 \pm 0.008)$ ev.

The agreement of the experimental results with the Breit-Wigner curve of Fig. 9 is very gratifying as such an extended experimental comparison has not been made for this theory before. Since Cd is used as a standard filtering material for slow neutron measurements an accurate knowledge of the resonance parameters should prove useful.

In the above analysis no effort was made to assign the effect to a single isotope and an average value for normal Cd was given. If it is assumed that the capture cross section is caused by an odd isotope whose abundance is 13 percent, the effective cross section becomes $\sigma_0 = 60{,}000 \times 10^{-24}$ cm²/atom. This gives $\Gamma_N = 1.86 \times 10^{-3}$ ev or 0.62×10^{-3} ev depending on the angular momentum of the resulting nucleus.

BORON RESULTS

The results of the measurements with the boron absorbers are given in Figs. 10 and 11. The samples employed have already been described above. The measurements were taken with a source-detector distance of 5.2 meters for some of the points and 5.4 meters for the others, always using the standard thin paraffin source slab. In all cases the dead time correction was made and the delayed thermal emission correction was applied as discussed above. The times of flight were then reduced to a one-meter basis for plotting.

For measurements above the Cd cut-off region a total cycle period of 1000 microseconds was used. For the highest energy measurements shown in Fig. 10 the cyclotron and detection on-time intervals were reduced to about 15 microseconds each to give a total resolution width of

about 6 microseconds/meter. For the measurements below 100 microseconds/meter the total resolution width was 20 microseconds/meter plus 3.7 percent of the time-of-flight due to the counter length.

For the remainder of the measurements a 5000-microsecond cycle was used with cyclotron and detection, on-time widths of 100 microseconds each below 500 microseconds/meter and 150 microseconds each above 500 microseconds/meter. In calculating the total resolution width above 200 microseconds/meter the delayed thermal emission width of 45 microseconds and the 3.7 percent effect due to the counter length must be added to the sum of the cyclotron and detection on-time intervals.

The results for the main part of the boron measurements are shown in Fig. 11 and it is seen that, over the region studied, the experimental points are well matched by the $1/v$ relation

$$\sigma_B = 118\times10^{-24}E^{-\frac{1}{2}} \text{ cm}^2/\text{atom},$$

where E is expressed in electron volts. Since it was considered desirable to extend the measurements to higher energies, the resolution was reduced to a minimum and a 2.464 g/cm² sample of B_2O_3 was used. Since the scattering cross sections of oxygen and aluminum are an important fraction of the total cross section for energies above 100 ev, it is probably only fortuitous that the straight lines formed by the points pass through the origin rather than being shifted upwards or downwards. Also it is seen that the resolution width, although reduced to a very small absolute value, is not small compared to the measured times-of-flight. The fact that the intensity and the transmission are relatively slowly varying functions of the time of flight in this region probably makes the points in Fig. 10 more significant on a time-of-flight basis than the rapid rate of change of the energy scale would indicate.

The results were corrected for the effect of the oxygen and aluminum present for the B_2O_3 samples and the SiO_2 present in the Pyrex samples. For oxygen the value of 4.1×10^{-24} cm²/atom was used[11] and for silicon the value 2.5×10^{-24} cm²/atom. This value of the cross section for silicon was used rather than a value for SiO_2 because the measured cross sections of SiO_2 are usually too low because of structural effects which should not be important in Pyrex.[11,12] For aluminum the cross section was assumed to be 1.5×10^{-24} cm²/atom. Small uncertainties in these corrections are not serious over most of the region because of the large boron cross section. They become most important for the values in Fig. 10. It should also be noted in this respect that the effect of a constant cross section is only to displace the straight line vertically without changing its slope.

These time-of-flight measurements give a clear experimental check on the $1/v$ law for boron within the experimental accuracy over a large energy range. It is fortunate that the results do demonstrate that boron follows a $1/v$ law as the interpretation of a great deal of experimental work has been based on this assumption.

The results of these measurements together with an estimate of the over-all uncertainty present may be given as:

$$\sigma_B = (118\pm4)E^{-\frac{1}{2}}\times10^{-24} \text{ cm}^2/\text{atom},$$

where E is the neutron energy in electron volts. This equation gives directly the $1/v$ proportionality factor for boron and should be of value in resonance-detector measurements for determining the positions of the energy levels without the necessity of making the customary comparison with thermal neutrons, of somewhat undefined effective energies. Since the lack of this knowledge has been one of the major sources of uncertainty in previous energy determinations, this should permit re-examination of earlier measurements.

The writers wish to express their appreciation of the interest taken in this problem by Professor J. R. Dunning, who originally suggested the problem and without whose active interest and stimulating discussions the work could not have been carried out. The Ernest Kempton Adams Fellowship Fund has aided materially in providing the special equipment for this work.

[11] Henry Carroll, Phys. Rev. **60**, 702 (1941).

[12] Whitaker, Bright, and Murphy, Phys. Rev. **57**, 551 (1940).

The Slow Neutron Cross Sections of Indium, Gold, Silver, Antimony, Lithium, and Mercury as Measured with a Neutron Beam Spectrometer*

WILLIAM W. HAVENS, JR. AND JAMES RAINWATER
Columbia University, New York, New York

(Received August 23, 1945)†

The variations of the slow neutron transmissions of In, Au, Ag, Sb, Li, and Hg have been investigated as a function of the time-of-flight of the incident neutrons for a 5.4-meter path by use of a neutron beam spectrometer. A method of analysis is developed for determining E_0 and $\sigma_0\Gamma^2$ for resonances above 1 ev based on the experimental transmission curves and the Breit-Wigner theory. The positions of the levels located, listed in order of importance for each element, are: In, (1.44±0.04) ev; Au, (4.8±0.2) ev; Ag, (5.11±0.2) ev, (13.7±1) ev, and (43±5) ev; Sb, (6.3±0.5) ev, (19.2±1.0) ev, and indications of other unresolved levels in the region of 50 to 500 ev; Li, only a $1/v$ cross section; Hg, a negative level at (−2.0±0.2 ev) and indications of unresolved positive levels above 25 ev. In the thermal region, the Ag, Sb and Li cross-section curves can be resolved into the sum of a constant term and a $1/v$ term. If E is the neutron energy in ev, these are: Ag: $[(9.05\pm0.10)E^{-\frac{1}{2}}+(6.6\pm0.5)]\times10^{-24}$ cm²/atom; Sb: $[(0.64\pm0.02)E^{-\frac{1}{2}}+(4.2\pm0.3)]\times10^{-24}$ cm²/atom; Li: $[(11.5\pm0.2)E^{-\frac{1}{2}}+(1.7\pm0.2)]\times10^{-24}$ cm²/atom; LiF was used in the Li measurements and a value 2.5×10^{-24} cm²/atom has been deducted for the F. The Hg cross section below 5 ev was well matched by the relation $(64\pm3)E^{-\frac{1}{2}}(1+E/2.0)^{-1}\times10^{-24}$ cm²/atom.

IN a previous paper[1] a neutron beam spectrometer system for use with the Columbia University cyclotron was described and the various instrument corrections were analyzed and evaluated.

This neutron spectrometer system uses the method of arc modulation in which the accelerating voltage for the ion source arc is modulated by a bank of hard vacuum tubes controlled by elaborate electronic timing circuits. The neutron production can be confined to intervals of 10–200 microseconds out of a 1000–10,000 microsecond cycle. Neutrons slowed down in a paraffin "source" slab are detected by a BF_3 proportional counter which for most measurements is 5.4 meters from the paraffin. Excellent collimation is obtained by using extensive B_4C and Cd shields. A special selector system counts all neutrons detected and also selectively counts those detected during an adjustable time interval after the cyclotron burst.

Investigations of other problems have been made and certain improvements in the apparatus have been carried out.

APPARATUS IMPROVEMENTS

In the previous paper it was shown that with this system there was an over-all delay time of 35 microseconds involved between the cyclotron arc pulse and the detection of the highest energy neutrons when the detector was close to the source. This time delay was therefore subtracted from all timing measurements made to obtain the actual time-of-flight of the neutron over the measured path. The measurement of this time delay was made with the BF_3 counter placed in a thick B_4C shield at an effective distance of 8 cm from the paraffin source slab. The cyclotron and the detector modulation "on-times" were made as narrow as possible and the number of counts recorded by the detector were plotted as a function of the time spacing between the cyclotron arc pulse and the timed detection intervals. These measurements were made with and without a "pulse sharpener" after the "level-setter" in the detector amplifier circuit. This pulse sharpener circuit decreased the time width of the pulses sent from the level-setter to the timed counting circuit. The results of these measurements showed that there was an effective broadening of the order of 10–15 μsec. due to that portion of the neutron counter pulse width above the level-setter height when the pulse

* A Thesis submitted by William W. Havens, Jr. in partial fulfillment of the requirements for the degree of Doctor of Philosophy in the Faculty of Pure Science, Columbia University, New York. Publication assisted by the Ernest Kempton Adams Fund for Physical Research of Columbia University.

† The experimental work on this paper was completed prior to 1943, but publication was voluntarily withheld at the request of the Manhattan District until the date indicated.

[1] J. Rainwater and W. W. Havens, Jr., Phys. Rev. 70, 136 (1946).

sharpening circuit was not used after the level-setter. This broadening, due to the width of the pulses from the neutron counter, also introduces some uncertainty in the time-of-flight measurements. It should be noted that the use of the pulse sharpening circuit after the level-setter does not influence that portion of the detector pulse width between the start of the pulse and the time when the pulse reaches a height sufficient to trip the level-setter. If this portion of the pulse width is large, the over-all time delay is correspondingly increased while differences in the width for different pulses introduces an additional resolution broadening. This is true even if the pulses leaving the level-setter are made extremely sharp. This condition may be improved by sharpening the detector pulses before they reach the level-setter height. In order to accomplish this purpose the amplifier circuit was modified to "sharpen" the pulses. The input resistor of the amplifier was reduced to 5000 ohms and the time constant of the coupling circuit between the second and third amplifier stages was greatly reduced. The measurements described above were repeated with the results shown in Fig. 1. This graph shows that the delay time using the pulse sharpening circuit is now 23 μsec. while only a slight broadening to 25 μsec. was introduced when the sharpening circuit was omitted. Therefore a delay time of 25 μsec. was subtracted from all timing measurements.

A METHOD OF ANALYSIS FOR THE MEASUREMENTS OF RESONANCE ABSORPTION LEVELS AT ENERGIES ABOVE 1 ev

In the analysis of the cadmium absorption employed in the previous paper, it was found that the experimental results could be well matched to a one-level Breit-Wigner curve over an energy range wide compared to the level width. The greatest deviation between the experimental results and the theoretical curve occurred in the region of exact resonance where a method of correcting for the resolution of the instrument was applied. In this case the correction was small, amounting to about 8 percent of the total cross section assumed for the best fit to the Breit-Wigner formula.

In the present investigations measurements were made on the transmission of indium, gold, silver, and antimony, all of which are characterized by having relatively much sharper resonance levels at higher energies than the resonance level of cadmium.[2–13]

Typical forms of such experimental transmission curves can be seen in Figs. 4, 5, 7, 9, 11, and 13 where some of the results of the measurements described in this paper are presented. These transmission curves are characterized by a sharp asymmetric dip with a clearly defined minimum and a width somewhat greater than the resolution width of the instrument. The position of the minimum in the transmission curve when corrected for asymmetric effects gives the time of flight, t_0, of the resonant neutron and from this the resonant energy E_0 can be calcu-

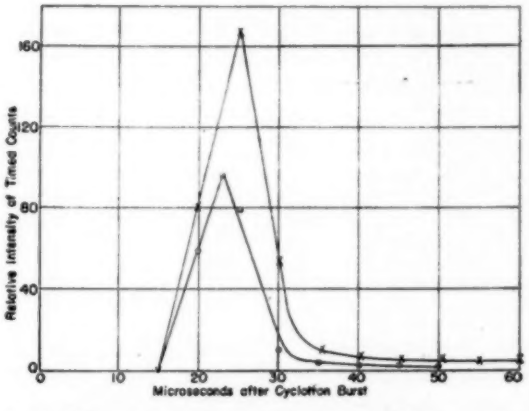

FIG. 1. Experimental resolution curve. These measurements were taken with a BF_3 counter in a thick B_4C shield with the counter axis 8 cm from the front of the paraffin source slab. The relative timed intensity is given as a function of the time between the cyclotron arc pulse and the timed detection pulse. The over-all delay time and the sharpness of the resolution are well illustrated. Circles represent the pulse sharpener in the circuit, the crosses without the pulse sharpener.

[2] H. A. Bethe, Rev. Mod. Phys. 9, 113–161 (1937).
[3] Dunning, Pegram, Fink, and Mitchell, Phys. Rev. 48, 265 (1935).
[4] Goldsmith and Rasetti, Phys. Rev. 50, 328 (1936).
[5] G. A. Fink, Phys. Rev. 50, 738 (1936).
[6] E. Amaldi and E. Fermi, Phys. Rev. 50, 899 (1936).
[7] M. Goldhaber and G. Briggs, Proc. Roy. Soc. London (A) 162, 127 (1937).
[8] H. Von Halban and P. Preiswerk, Nature, 905 (1936).
[9] H. Von Halban and P. Preiswerk, Helv. Phys. Acta 9 (318) (1936).
[10] Hornbostel, Goldsmith, and Manley, Phys. Rev. 58, 18 (1940).
[11] C. P. Baker and R. F. Bacher, Phys. Rev. 59, 332 (1941).
[12] Feeny, Lapointe, and Rasetti, Phys. Rev. 61, 469 (1942).
[13] H. Volz, Zeits. f. Physik 121, 232–234 (1943).

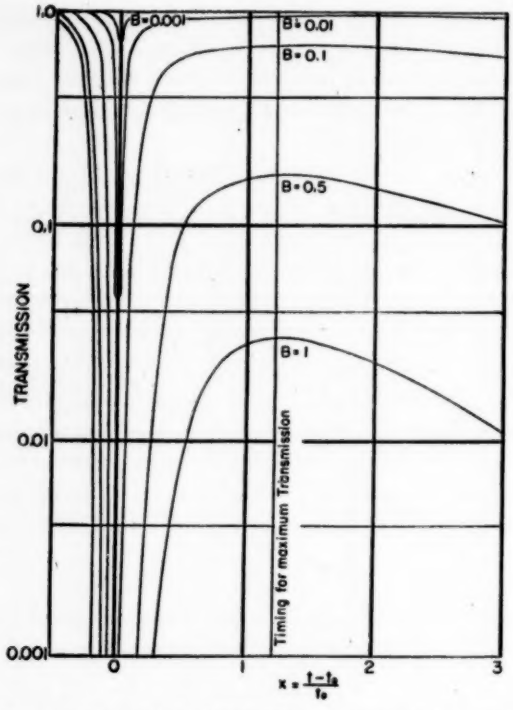

FIG. 2. Theoretical Breit-Wigner transmission curves. These transmission curves are calculated from the Breit-Wigner one-level formula using a neutron time-of-flight scale. The shapes of the curves are given for different effective sample thicknesses, $B=n\sigma_0\Gamma^2/4E_0^2$, as a function of $x=(t-t_0)/t_0$ where t_0 is the time-of-flight of a neutron at the resonance energy.

lated. If the Breit-Wigner one-level formula is assumed to hold for the cross section in the vicinity of the resonance, it is of interest to evaluate the capture cross section at exact resonance, σ_0 and the half-width of the level, Γ, as defined by the formula

$$\sigma(E)=\frac{\sigma_0\Gamma^2(E_0/E)^{\frac{1}{2}}}{\Gamma^2+4(E-E_0)^2}. \tag{1}$$

Since the experimental results are first obtained in the form of a transmission curve for the sample as a function of the time-of-flight of the incident neutrons, the most satisfactory method of analysis will be that in which the best match is made between this curve and a transmission curve calculated from the Breit-Wigner formula and corrected for the resolution effects of the instrument.

The transmission of a sample for neutrons of energy E is given by the formula

$$T_c=e^{-N\sigma(E)}, \tag{2}$$

where N=atoms/cm² of the absorbing material in the beam and σ is the cross section in cm² atom as given in formula (1).

If t represents the time-of-flight of the neutron with energy E and t_0 represents the time-of-flight for neutrons of resonant energy E_0 and we define the parameters x, λ, and B such that

$$x=\frac{t-t_0}{t_0}, \quad \lambda=\frac{\Gamma}{2E_0}, \quad B=N\sigma_0\lambda^2, \tag{3}$$

then the transmission of the sample as a function of these dimensionless parameters will be given by

$$T_c(x)=\exp-\frac{B(x+1)}{\lambda^2+[x(x+2)/(x+1)^2]^2}. \tag{4}$$

This dimensionless representation has certain advantages in that a table of values of

$$\frac{x+1}{\lambda^2+[x(x+2)/(x+1)^2]^2}$$

can be calculated as a function of the parameter x for several values of λ^2. Using this table of values the transmission of a sample for any value of B can be read directly from a single setting of the slide rule. Thus an easily applied system of analysis is established for the study of any resonance level at any time of flight. Also the fact that $x=0$ at exact resonance permits easier examination of the form of the function near the resonance time of flight.

In order to obtain a satisfactory dip in the experimental transmission curve when studying a sharp level, it is always necessary to choose an absorber of such a thickness that $N\sigma_0$ or B/λ^2 is large compared to unity. This corresponds to the condition that T be effectively zero at exact resonance. For values of x sufficiently far from exact resonance that T is appreciably different from zero, the λ^2 term in the denominator of the exponent is small compared to the second term in the denominator so that Eq. (3) may be replaced by the approximate relation

$$T_c=\exp\left[-B\frac{(x+1)^5}{x^2(x+2)^2}\right]. \tag{5}$$

In nuclear physics resonant absorbers are usually described as "thick" if $N\sigma_0$ is large com-

pared to unity and as "thin" if $N\sigma_0$ is small compared to unity. In the measurement of sharp levels with a neutron beam spectrometer it is always necessary that $N\sigma_0$ be large compared to unity in order to obtain a satisfactory dip in the measured transmission at resonance. Since according to the usual terminology this means that thick absorbers are always used, it is necessary to employ a different criterion for referring to the effective absorber thickness. This will be done in terms of the types of experimental transmission curves which are obtained. In Eq. (4) if $B \ll 1$ there is a sharp dip in T at exact resonance with a rapid recovery on either side of the resonant time of flight. A sample will be considered "very thin" if the recovery of T to approximately unity occurs in an interval of the same order of magnitude or smaller than the resolution width of the apparatus. If the interval between the resonant time of flight and the recovery to approximately unit transmission is larger than the resolution width of the apparatus, then the sample will be considered thin. If $0.05 < B < 0.3$ the measurements on the sample may be extended from the vicinity of resonance to the thermal energy region and the shape of the curve at energies different from the resonant energy may be studied. Samples in this region may be referred to as "medium thick." If $0.3 < B < 1$, then the sample will be referred to as thick, and if $B > 1$ then the sample will be referred to as "very thick." The thick and very thick samples are useful in studying the cross section in the region near $t = 2.2t_0$ where a maximum in the transmission curve occurs.

In Fig. 2 Eq. (3) has been plotted for five values of B with $\lambda^2 = 3 \times 10^{-3}$ illustrating the five conditions described above.

Determination of B from the Experimental Data

The area under the curve $y = (1 - T_c)$ will be given by the integral

$$F(B) = \int_a^b [1 - T(x)]dx. \qquad (6)$$

The area under this curve will be a function of the parameter B and will increase as B increases. For the purpose of this analysis the limits $x = -0.3$ and $x = 0.5$ were selected to consider only the region near the peak, where most of the effect due to the resonance occurs. It is impossible to locate the area under the total curve since as $x \to \infty$ the integral diverges due to the $E^{-\frac{1}{2}}$ factor in the Breit-Wigner formula. If the approximate value of T given by Eq. (4) is inserted in Eq. (5), the area under the curve $(1 - T)$ will be given by

$$F(B) = \int_{-0.3}^{+0.5} \left[1 - \exp\left(-B\frac{(x+1)^5}{x^2(x+2)^2}\right)\right]dx. \qquad (7)$$

The relation $F^2(B)/B$ has been plotted as a function of B in Fig. 3. This fraction approached π as B approaches zero.

Actually the area under the experimental curve $(1 - T)$ is not given accurately by the above formula because the experimental transmission at any one point is not the actual transmission of the samples at that time-of-flight but is the transmission of the sample integrated over the resolution width of the apparatus. However, it may be shown that the effect of the resolution width of the apparatus in causing the area under the experimental curve to differ from the area under the actual transmission curve is only a small edge correction. If $f(x)$ corresponding to $(1 - T_c)$ is a function whose area is confined to a region small compared to the range of integration, we may write

$$I_0 = \int_{x_1}^{x_2} f(x)dx = \int_{-\infty}^{\infty} f(x)dx. \qquad (8)$$

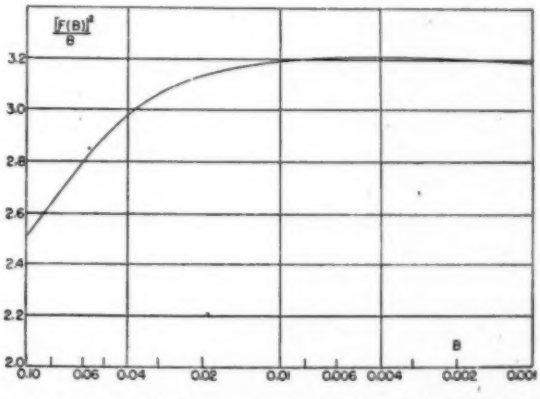

FIG. 3. Theoretical curve for determining the "effective" absorber thickness, B, from the area, $F(B)$, Eq. (7), between the experimental transmission curve and unit transmission, between the limits of $t = 0.7t_0$ and $t = 1.5t_0$. For a very thin absorber $F^2(B)/B = \pi$.

If a "smearing function" $\varphi(u)$ is now introduced (corresponding to the resolution function of the apparatus) where $\varphi(u)=0$ for $|u|>a$ and

$$\int_{-a}^{+a}\varphi(u)du=1$$

where $a\ll(x_2-x_1)$, then

$$I=\int_{-\infty}^{\infty}\left\{\int_{-a}^{a}f(x+u)\varphi(u)du\right\}dx \qquad (9)$$

represents the corresponding integral when the resolution is not infinitely sharp. By integrating first with respect to x Eq. (8) reduces to

$$I=I_0\int_{-a}^{a}\varphi(u)du=I_0.$$

In comparing the area over the experimental transmission curve with that over $T_C(x)$, however, the range of integration is not infinite and does not vanish at the limits of integration x_1 and x_2. A more extended analysis shows that the difference $(I-I_0)$ depends only on the difference of the odd derivatives of $T_C(x)$ at x_1 and x_2 if $\varphi(u)$ is symmetric. Thus the principal effect is caused by the difference in the slopes $[f'(x_2)-f'(x_1)]$ and the correction is always small for the limits of integration chosen.

The area method of analysis is used only in obtaining the first approximation of the parameter B. In the final procedure the transmission curve calculated from the assumed value of B is integrated numerically over the resolution width of the apparatus and the value of the parameter which gives the best match between the calculated transmission curve and the experimental results is chosen. Therefore any error introduced in this part of the analysis will not affect the final results.

Other Factors Affecting the Transmission

The above analysis assumes that all the neutrons that do not reach the detector have been captured by the sample according to the Breit-Wigner one-level formula. However, it is also possible for neutrons to be removed from the beam by nuclear scattering or by some more complex molecular scattering and interference phenomena. Therefore, the decrease in the transmission due to these effects must also be taken into consideration.

When the resonance occurs at an energy appreciably above the thermal region, the cross section in the thermal region should consist of a $1/v$ capture term and another term which should be approximately constant over the energy region considered, and which will take into account all the other factors involved. Since the $1/v$ term gives a linear logarithmic plot on the time-of-flight basis, it is easy to resolve such a straight-line logarithmic plot into the sum of a constant term and a straight line through the origin. If the nuclear scattering cross section and the molecular and interference effects depend strongly on the energy of the incident neutron over the energy range measured, and if the variation in the scattering term is not negligible compared to the capture term, then the conclusions of this part of the analysis will be correspondingly reduced in significance. However, inspection of the results given in Fig. 10, for example, shows that the cross section in the thermal region can here be considered as consisting of a fixed term and a $1/v$ term and that in this case the other effects are sufficiently small in themselves or cancel each other in such a manner that the over-all effect is negligible.

METHOD OF MATCHING AN EXPERIMENTAL TRANSMISSION CURVE TO A MOST PROBABLE THEORETICAL CURVE BASED ON THE BREIT-WIGNER FORMULA

The material is first studied by investigating the transmission of a medium thick sample over the entire range of the apparatus with moderate resolution. This most quickly locates the regions of particular interest for closer investigation with higher resolution. These particular regions are then investigated more thoroughly with high resolution and with a different sample thickness if indicated.

The procedure used in analyzing the data for a definite sample will vary somewhat according to the particular properties of the sample itself but a few generalizations may be set up which usually represent the procedure employed.

1. A logarithmic plot of the transmission of the sample is made in the thermal energy region

for times-of-flight appreciably greater than t_0. The true transmission curve in this region is assumed to give a straight-line logarithmic plot and the best straight line through the experimental points is found by the method of least squares. This straight line is extrapolated to zero time-of-flight and the intercept at $t=0$ is taken to represent the transmission value, T_0, corresponding to the constant term in the total cross section.

2. The data in the vicinity of the resonance peak are plotted on a linear scale after the transmission at each point has been divided by T_0, the value of the intercept of the straight line obtained from the logarithmic plot of the transmission in Part 1.

3. The position of the minimum of the experimental transmission curve near the resonance is determined and a slightly lower time-of-flight value is chosen as t_0 because of the asymmetry of the transmission curve. The corrected transmission curve in the region of the resonance as obtained in Part 2 is then replotted in terms of the dimensionless parameter $x=(t-t_0)/t_0$.

4. The area above the transformed transmission curve from Part 3 between $x=-0.3$ and $x=0.5$ is then measured and an approximate value of B is obtained by the use of the graph given in Fig. 3.

5. Tables of values of T_c (theoretical transmission curves) are then computed using the exact relationship in Eq. (3) for several different values of B starting with the value of B found in Part 3 and with different values of λ^2 for each B. The transmission curve calculated for each separate value of B and λ^2 is then numerically integrated over the resolution function $\varphi(u)$ for several values of x to give T_t where

$$T_t=\int_{-a}^{a} T(x+u)\varphi(u)du, \qquad (10)$$

and $\varphi(u)$ is assumed to be triangular of width $2a$.

6. The shapes of several of these predicted curves are compared with the curves plotted in Part 2 and the set of values of B and λ^2 which gives the best fit is selected.

7. In the illustrations of these resonance absorption curves the curve obtained in Part 6 is then multiplied by the transmission due to the constant cross section and the calculated transmission curve is shown with the experimental results.

This procedure may of course be modified if the sample used is so thin that the decrease in transmission due to the constant cross section is negligible compared with the experimental error involved. In this case steps 1, 2, and 7 may be eliminated and steps 3, 4, 5, and 6 will be all that are necessary.

This method of analysis admittedly places great stress on both the theory and the experimental results, but it was felt that it would be of interest to see how good a match between a theoretical curve and the experimental results could be obtained. This method also has the advantage of reducing to a minimum all errors which would be introduced by more approximate methods of analysis. If two or more thicknesses of the same material are measured, the values of B and λ^2 obtained for one thickness of the absorber may be used to predict the transmission curve for the other absorber thicknesses to obtain an independent check on the uncertainties involved in the location of the parameters.

Paraffin Source and Source Detector Distance

The paraffin slab used as source of slow neutrons consisted of a 2.6-cm thickness of paraffin enclosed in a box of $\frac{1}{4}''$ thick plywood. The effective delayed emission time for thermal neutrons (times of flight of greater than 200 μsec/meter) was found to be about 45 μsec. The detector used was a BF_3 proportional counter in which the outer electrode was 20 cm long. The source detector distance was 5.4 meters measured from the detector side of the paraffin source slab to the center of the proportional counter. Thus an effective resolution broadening of 3.7 percent of the measured time-of-flight of the neutron was introduced because of the length of the counter. In the final analysis all results were reduced to the time-of-flight of the neutrons for one meter and the time-of-flight is usually expressed in μsec./meter.

These transmission measurements are always plotted on the time-of-flight basis because the resolution width of the apparatus is constant in this type of plot. If any other scale were used (velocity or energy) the result would give no

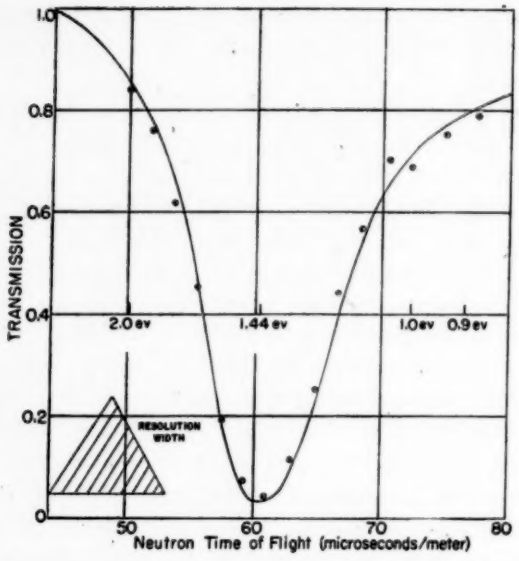

FIG. 4. The slow neutron transmission of 0.193 g/cm² of indium. The experimental points (circles) are compared with a calculated transmission curve (full line) based on the Breit-Wigner formula and the resolution function of the apparatus. The theoretical curve is for $E_0=1.44$ ev, $\sigma_0\Gamma^2=210\times10^{-24}$ (ev)² cm²/atom with $\Gamma=0.09$ ev.

indication of that portion of the transmission curve which the resolution width of the apparatus integrated over in order to determine the transmission of the sample at one point.

INDIUM

Two different samples were used for the indium transmission measurements. The thin sample contained 0.193 g/cm² of metallic indium and the thick sample contained 5.02 g/cm² of the metal. These samples were obtained from the Indium Company of America and were the purest indium that could be furnished by this company.

The results of the transmission measurements on the thin indium sample are given in Fig. 4 where the transmission is plotted as a function of the time-of-flight of the incident neutron for one meter. Each point represents the average of at least 8 separate pairs of measurements with the sample "in" and "out" of the beam. The over-all statistical accuracy of each point should be better than 5 percent. The resolution width of the apparatus is shown in the lower left corner of the figure. The total resolution width, which includes the cyclotron "on-time," detector on-time, counter pulse width, and the effect of the length of the counter, was taken to be 9 μsec./meter for the analysis given below.

Since the sample was thin, the scattering could not cause a difference in the transmission of more than 2 percent, therefore the data on this sample was analyzed according to the procedure given above assuming that the scattering had a negligible effect on the transmission.

The transmission minimum occurs at 60.2 μsec./meter so this value was chosen as t_0 for a first approximation. The area under the curve $(1-T)$ was calculated between 42 μsec./meter and 90 μsec./meter. The value $B=0.026$ was found from the theoretical curve given in Fig. 3. With this value of B the transmission at $t=t_0$ was calculated for several different values of λ^2. The value of λ^2 that gave the best agreement with the experimental transmission at the minimum of the curve was $\lambda^2=1\times10^{-3}$. The solid curve shown with the experimental points in Fig. 4 is the calculated transmission curve for $B=0.026$, $\lambda^2=1\times10^{-3}$, $t_0=60.2$ μsec./meter and an assumed resolution width of 9 μsec./meter. This corresponds to $\sigma\Gamma^2=210\times10^{-24}$ (ev)² cm²/atom and $\Gamma=0.09$ ev.

Although there seems to be satisfactory agreement between the theoretical curve and the experimental points in Fig. 4, the agreement is not completely indicated until the sensitivity of the agreement to variations in the parameters is shown. The shape of the theoretical transmission curve depends on the resolution width of the apparatus and the choice of the dependent parameters B and λ^2. The value of B can be determined to a fair degree of accuracy by the area method described above. As a check on this method, the transmission of the sample when $|t-t_0|\gg0$ is only very slightly affected by λ^2 and the resolution width of the apparatus. With the value of $B=0.026$, the calculated transmission at the edge of the resonance curve agrees fairly well with the experimental results.

The determination of the value of λ^2 is more difficult because it depends on the transmission of the sample at the minimum of the transmission curve where the correction due to the resolution width of the apparatus will also be a maximum. Therefore a small uncertainty in the value of the resolution width of the apparatus will cause

a large uncertainty in the value of λ^2 chosen to give a best fit.

In order to determine the magnitude of the effect of the resolution width of the apparatus on the choice of the value of λ^2 for best fit, the transmission at the minimum of the transmission curve was calculated as a function of the width of the level for several different resolution widths. The results of these calculations are given in Fig. 5. If the outside limit of error on the determination of the resolution width is taken as 1 μsec./meter, an estimate of the uncertainty in Γ, introduced by the uncertainty in the resolution width, can be made. From the curves given in Fig. 5 the value of Γ can only be said to lie between 0 ev and 0.16 ev. Thus this method of measuring the value of Γ will not give a very accurate value because of the uncertainty in the value of the resolution width.

Since the value chosen for B will also influence the choice of Γ for the best fit, the over-all uncertainty permits only an upper limit of 0.2 ev to be set on Γ.

In order to check the measurements made with the thin sample (0.193 g/cm²) the transmission of the thick sample was measured in the thermal region. If only one level is assumed to be effective in the very low energy region, then the parameter B should determine the transmission in the thermal region. Since the parameter λ should have negligible effect at energies other than those in the immediate vicinity of the resonance peak, the parameter B can be located by use of Eq. (4), from the thick sample measurements.

When a thick sample is used, the changes produced in the transmission by a variation in B will be very large and consequently greater sensitivity can be obtained in the location of this parameter than in the measurements with a thin sample.

The calculated transmission curves in the thermal region using three different values of B for the thick sample, corresponding to the values $B=0.022$, 0.026, 0.034, for the thin sample are plotted logarithmically in Fig. 6 together with the experimental points for the transmission in this region. Since the ratio of the thicknesses for the two samples was 26, the values of B employed are also 26 times as large giving $B=0.572$, 0.676, 0.884.

The curve determined by the experimental points seems to follow the general shape of the theoretical curve very well thus indicating that only one level could be considered important in determining the thermal cross section. The experimental points seem to be slightly higher than the theoretical curve for $B=0.676$, thus indicating that the value chosen for B from the

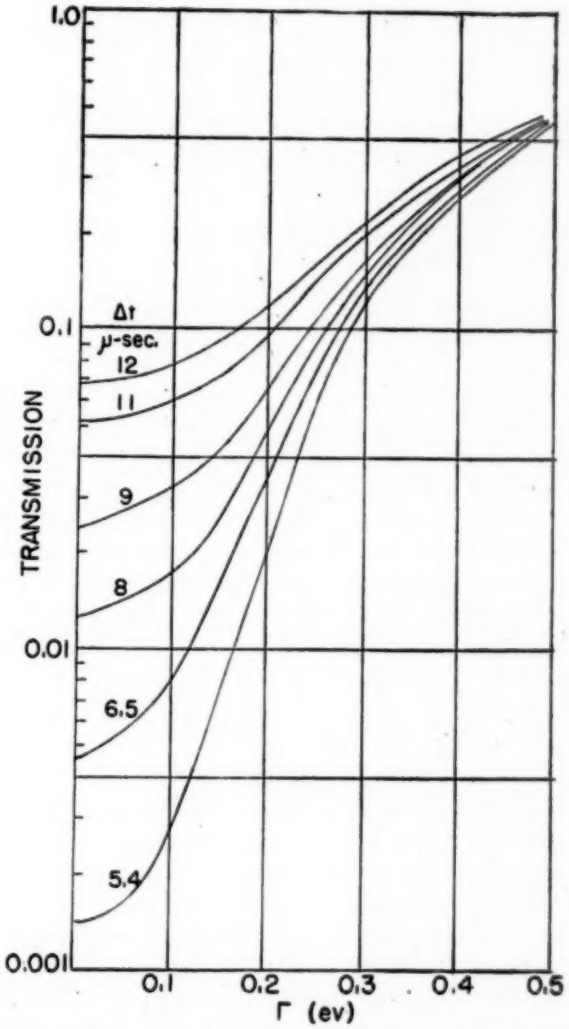

FIG. 5. The effect of Γ and the width of the resolution function on the transmission of the sample at the 60.2 μsec./m minimum of the indium transmission curve. The transmission at the minimum of the indium transmission curve has been calculated as a function of the width of the resonance level for several different resolution widths in order to show the effect that the resolution width of the apparatus has on the determination of the Γ from the experimental data.

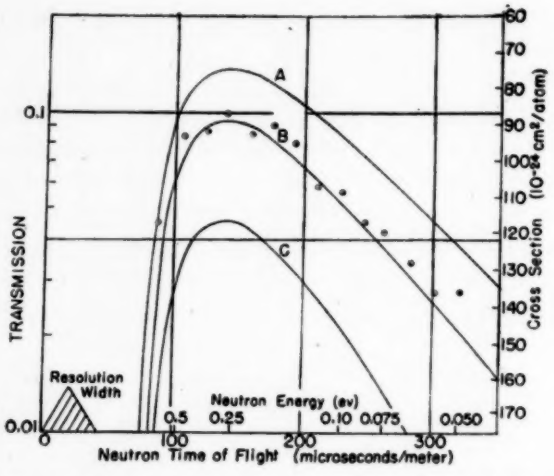

FIG. 6. The slow neutron transmission of 5.02 g/cm² of indium. The value of the effective sample thickness, B, is best determined for a thick sample from the maximum of the transmission curve between the resonance and the thermal region. The theoretical curves (full lines) are for the values of the parameters located from the measurements on the thin indium. Curve A: $B=0.572$ or $\sigma_0\Gamma^2=177\times10^{-24}$ cm² (ev)². Curve B: $B=0.676$ or $\sigma_0\Gamma^2=210\times10^{-24}$ cm² (ev)². Curve C: $B=0.884$ or $\sigma_0\Gamma^2=274\times10^{-24}$ cm² (ev)².

experimental results on the thin sample was slightly large. This would be further accentuated by the fact that the constant cross section has not been taken into consideration.

The method for determining the constant cross section described above cannot be applied accurately in the case of indium because the resonance level occurs at too low an energy. Therefore, the assumption that the capture cross section is directly proportional to the time-of-flight would not be valid until the energy was below about 0.07 ev. Measurements were not carried much below this energy because of the extremely low transmission of the sample which was available.

If the value for the constant cross section of indium is arbitrarily chosen as being the same order of magnitude as for silver and antimony, and less than that for nickel, a value for σ (const.) between 4×10^{-24} and 10×10^{-24} cm²/atom would be appropriate. Choosing the upper value will shift the theoretical curves in Fig. 6 down by the factor 0.77. In this case the value of B chosen would not be lower than 0.572 as this curve, when lowered the required amount, still lies observably above the experimental points.

Taking into account all the factors involved, the final results can be given as

$E_0=(1.44\pm0.04)$ ev,
$\sigma_0\Gamma^2=(210\pm60)\times10^{-24}$ cm² (ev)²,
$\Gamma<0.2$ ev ($\Gamma=0.09$ ev),
$\sigma_0>5200\times10^{-24}$ cm²/atom
($\sigma=26{,}000\times10^{-24}$ cm²/atom).

GOLD

In studying the transmission of gold as a function of the time-of-flight of the incident neutrons two different thicknesses of gold foils were used. The first contained 0.2100 g/cm² and the second contained 0.856 g/cm². Both of these samples were fine gold obtained from Handy and Harman of New York City, who state that the purity is better than 99.999 percent. Since both of these samples can be classed as thin, no discussion of the measurements on the thinner of the two samples seems necessary as more accurate data can be secured using the thicker sample. The results of the measurements on the thinner sample are introduced to show the self-consistency of the results for two different sample thicknesses.

The results of the transmission measurements for the two gold samples are given in Fig. 7. The upper curve, of course, is for the thinner

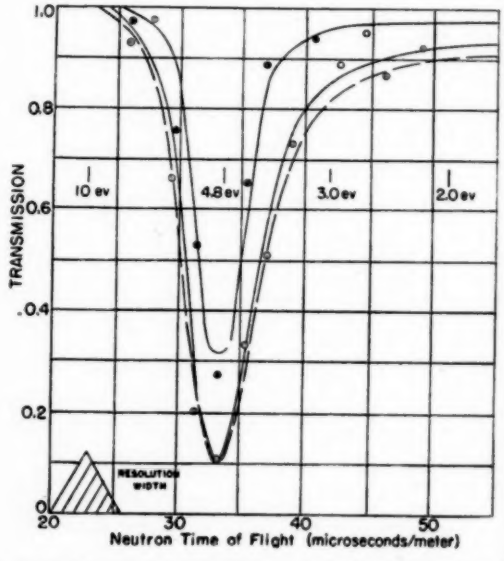

FIG. 7. The slow neutron transmission of 0.210 g/cm² and 0.856 g/cm² of gold. The solid curves are based on the Breit-Wigner formula and the resolution function of the apparatus with $\sigma_0\Gamma^2=600\times10^{-24}$ cm² ev²/atom and $\Gamma=0$. The dashed curve is for $\sigma_0\Gamma^2=655\times10^{-24}$ cm² ev²/atom and $\Gamma=0.5$ ev. ⊙—Experimental points for 0.856 g/cm² sample: ⊗—Experimental points for 0.210 g/cm² sample.

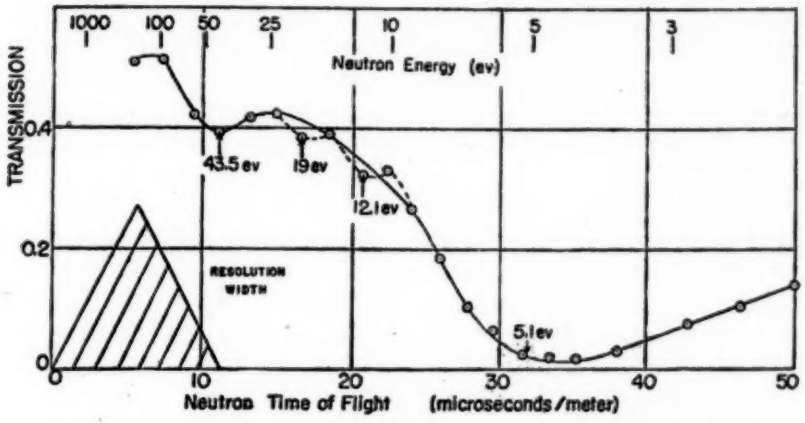

FIG. 8. The slow neutron transmission 19.8 g/cm² of silver. This is a typical preliminary transmission curve using a thick sample to explore a wide energy range as a basis for further investigations using appropriate sample thicknesses. With this sample thickness, the principle resonance at 5.1 ev is flattened to extend over a considerably wider range than is desirable for accurate analysis.

sample. The resolution width of the apparatus is shown in the lower left-hand corner of the figure. The position of the minimum in both curves seems to occur at about 33.5 microseconds/meter. Since the resolution width of the apparatus is fairly wide compared to the width of the resonance line, the value of $t_0=33$ microseconds/meter was chosen as a first approximation for the resonant time-of-flight.

The analysis described above was applied to the data for the thicker sample and the values of the parameter which gave the best fit to the experimental points were $B=0.017$, $\lambda^2=0$. Because of the relatively poor resolution used here, it is not surprising that the value for the width of the line should come out zero. This only means that no lower limit can be set for the width of the line although it is possible to set an upper limit as previously described. This upper limit was taken as $\lambda^2=3\times10^{-3}$. With this value of λ^2 and the value of $B=0.022$ which gave the transmission at the minimum point the dashed theoretical transmission curve in Fig. 7 was definitely too low at the edge of the resonance dip. The two solid curves in the graph represent the theoretical curve for the two different samples with $B=0.017$, $\lambda^2=0$ for the thicker sample and $B=0.0042$, $\lambda^2=0$, as corresponding values for the thinner sample. The values for the thinner sample are equal to the ones for the thicker sample when multiplied by the thickness ratio so a direct comparison of the consistency of the results for the two thicknesses may be made.

The values for the physical constants corresponding to these values of the parameters and their uncertainties are:

$$E_0=(4.8\pm0.2)\text{ ev},$$
$$\sigma_0\Gamma^2=(600\pm80)\times10^{-24}\text{ (ev)}^2\text{ cm}^2,$$
$$0<\Gamma<0.5\text{ ev},$$
$$\sigma_0>2400\times10^{-24}\text{ cm}^2.$$

The Breit-Wigner theory of neutron capture sets an upper limit on the cross section at resonance as $\sigma_0\leq\pi\lambda^2$, where $2\pi\lambda$ is the wavelength of the resonant neutron (2).

Since gold has only one isotope

$$\sigma_0\leq178{,}000\times10^{-24}\text{ cm}^2$$

therefore $\Gamma>0.06$ ev.

Feeney, Lapointe, and Rasetti[12] reported from indirect measurements that there were some indications of more than one resonance level in the gold spectrum, but no indication of another level within the range of the instrument was found in these investigations. The energy of the gold resonance found by them was quite different from the value reported here. However, the discrepancy seems to lie in the value of the effective thermal energy which was assumed in the boron absorption method employed by that group.

If their value for the boron absorption at the energy of the resonance is used together with the

energy dependence of the boron cross section as determined in the previous paper[1] then the difference between their value and the one found here is not appreciable.

SILVER

The selection of a sample for the study of the resonance absorption of neutrons by silver offers a more complex problem than for indium or gold because silver was known to have more than one level present for neutron energies of the order of a few electron volts. Therefore, the trial and error method was applied in the selection of the sample. All the silver samples were purchased from Handy and Harman and were the purest silver obtainable. There was no copper impurity detectable.

Since previous experience had indicated that a thick absorber was good for the preliminary study, a 19.8 g/cm² disk of metallic silver was used. The transmission of this sample as a function of the time of flight of the incident neutron is shown in Fig. 8 with the resolution width of the apparatus indicated in the lower left-hand corner of the figure. It is immediately obvious from this curve that one level is predominant as far as this type of measurement is concerned. The predominant level has its maximum absorption at 32 microseconds/meter. Another level can easily be detected at 11 microseconds/meter, and others might be present at about 17 and 21 microseconds/meter but no definite conclusions are warranted from this data. The transmission of this sample is so low near the 32 microsecond/meter resonance and the effects of this level are so strong that little more can be said from these results.

Because the one level at 32 microseconds/meter is so predominant on the time-of-flight basis, the transmission of a *thin* absorber will be affected by this level only, in the vicinity of this level, and the effects of the other levels will be negligible. Therefore transmission measurements were made using a thin sample containing 1.043 g/cm², in the vicinity of 32 microseconds/meter. The highest resolution consistent with useful intensity was employed in these measurements, the results of which are given in Fig. 9. The shape of the curve looks very much like the curve obtained for the gold transmission measurements, indi-

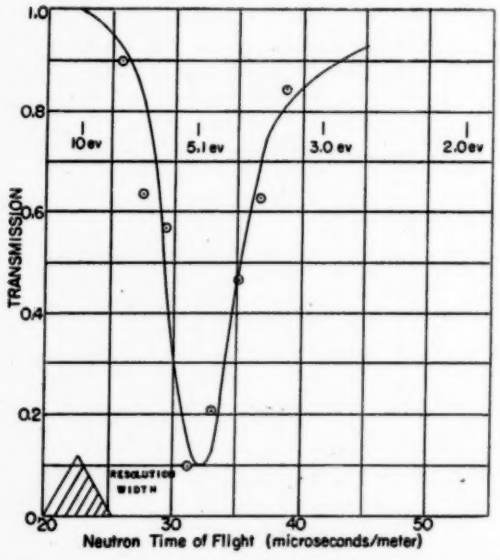

FIG. 9. The transmission of 1.046 g/cm² of silver. This is a "thin" sample, used to study the main resonance at 5.1 ev. The solid curve is a calculated transmission curve for one level at $E_0=5.1$ ev with $\sigma_0\Gamma^2=300\times10^{-24}$ cm² ev²/atom and $\Gamma=0$.

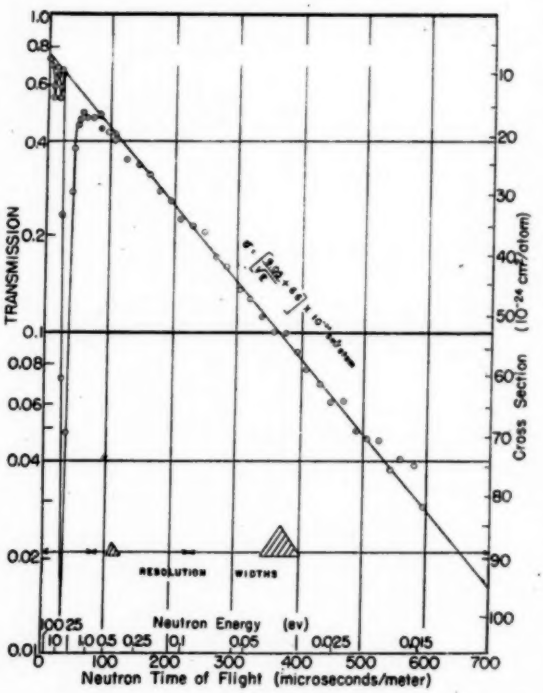

FIG. 10. The slow neutron transmission of 7.84 g/cm² of silver. A sample of intermediate thickness was best for a study of the entire region of investigation. The transmission curve, except for the resonance region, can easily be resolved into the sum of a constant cross section and a $1/v$ term. The relative sharpness of the levels for this type of measurements is also well illustrated.

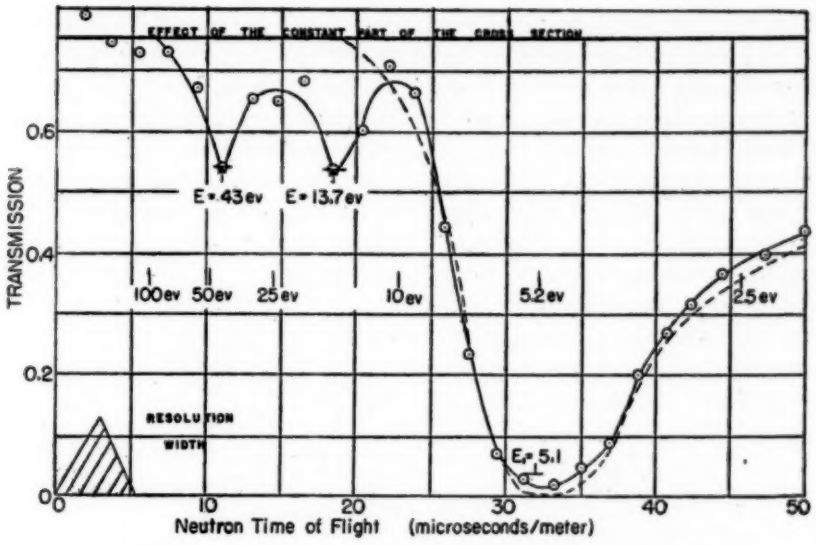

FIG. 11. The slow neutron transmission of 7.84 g/cm² of silver in the resonance region. The high energy portion of the previous plot is expanded to show resonances at 43 ev, 13.7 ev, and 5.1 ev. The dashed curve is a calculated curve for one level based on the parameters located from the transmission of the 1.046 g/cm² sample. The "strengths" of the two higher energy levels obtained from the magnitude of the transmission dips in this figure are $\sigma_0\Gamma^2 = 380\times10^{-24}$ cm² ev²/atom for the level at 43 ev and $\sigma_0\Gamma^2 = 14\times10^{-24}$ cm² ev²/atom for the level at 13.7 ev. The constant cross section factor was located from Fig. 10.

cating that little error is introduced by assuming only the one level to be effective in this region. The standard method of analysis was applied to this data, assuming that only the one level was effective in producing this absorption and that the constant cross section was unimportant. The theoretical curve given in Fig. 9 along with the experimental points is for $B=0.017$, $\lambda^2=0$. As was also true in the case of gold, the effects of small changes in λ^2 are negligible when the relative resolution is as low as in this case. No attempt has been made to set an upper limit on λ^2 because of the assumptions made as to the magnitude of the effects of the other levels and of the constant cross section. Therefore $\sigma_0\Gamma^2 = 300\times10^{-24}$ (ev)² cm² was taken as the effective "strength" of this level and $t_0=32$ microseconds/meter was taken as the resonant time-of-flight. This corresponds to a resonant energy $E_0=(5.1\pm0.2)$ ev.

A preliminary run on the thin sample in the thermal region gave sufficient data to indicate the thickness of the sample which would give best results in this region. Therefore, the thick sample was cut approximately in half and a sample containing 7.84 g/cm² was used for the rest of the measurements on silver.

The results of the transmission measurements with this sample are given in Figs. 10 and 11. In Fig. 10 the transmission is plotted logarithmically as a function of the time-of-flight of the incident neutron over the full range of the measurements taken. The resolution width of the apparatus was varied for different portions of the curve, as indicated by the triangles given at the base of the figure. In Fig. 11 the region between 0 and 50 microseconds per meter has been expanded on a linear plot to show the region in which the resonance levels are detected.

The full method of analysis described above was applied to the data on this sample. The straight line which *best fits* the experimental points on the logarithmic plot has its intercept at $T=0.75$. This corresponds to a constant term in the cross section of silver of approximately 6.6×10^{-24} cm²/atom. The equation of this straight line as a function of the energy of the incident neutron is

$$\sigma_0=(9.05E^{-\frac{1}{2}}+6.6)\times10^{-24}\ \text{cm}^2/\text{atom},$$

where E is in electron volts.

Assuming the constant part of the cross section for silver to be 6.6×10^{-24} cm² as determined from

the data given in Fig. 10 and assuming that $\sigma_0\Gamma^2=300\times10^{-24}$ (ev)^2 cm^2 for the level at 5.1 ev as determined from the data given in Fig. 9, the form of the transmission curve was calculated in the vicinity of 32 microseconds/meter. This curve is the dashed curve in Fig. 11. The calculated curve seems to agree fairly well with the experimentally determined points.

In the measurements using the 7.84 g/cm^2 sample with the highest resolution obtainable the two less noticeable levels in this type of measurements which had been tentatively located using the 19.8 g/cm^2 sample were confirmed. Although from the appearance of the curve it may seem that too much stress has been placed on the points at 11.1 and 19.4 microseconds per meter, the values of the transmission shown in Fig. 11 by the points are each the average of at least eight separate pairs of measurements and have a statistical accuracy of better than 3 percent. Also these levels were tentatively located with the thicker sample so that their reality seems plausible. An approximate value of B was determined for each of these levels. The accuracy of this value is probably accurate to about a factor of 2 because of the relatively poor resolution of the instrument in this region and the confusion due to several levels.

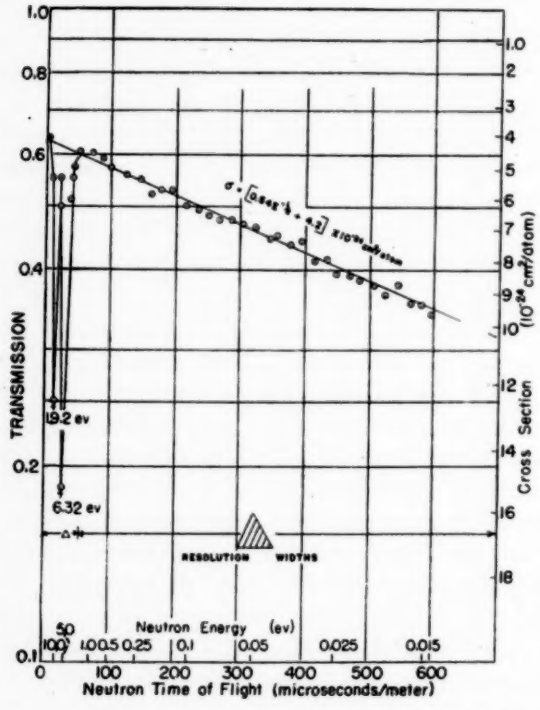

FIG. 12. The slow neutron transmission of 22.41 g/cm^2 of antimony. This shows the transmission of antimony throughout the entire region of investigation and shows the method of locating the constant cross section and the $1/v$ curve in the thermal region. The relative position of the resonances is also indicated.

Taking into consideration all of the facts involved in the measurements on silver the final results may be given as

$$E_1=(5.1\pm0.2)\text{ ev},$$
$$\sigma_1\Gamma_1^2=(300)\times10^{-24}\text{ (ev)}^2\text{ cm}^2/\text{atom}.$$
$$E_2=(13.7\pm1)\text{ ev},$$
$$\sigma_2\Gamma_2^2=(14)\times10^{-24}\text{ cm}^2\text{ (ev)}^2/\text{atom}.$$
$$E_3=(43\pm5)\text{ ev},$$
$$\sigma_3\Gamma_3^2=(380)\times10^{-24}\text{ cm}^2\text{ (ev)}^2/\text{atom}.$$
$$\sigma_{\text{thermal}}=\{(9.05\pm0.30)E^{-\frac{1}{2}}+(6.6\pm0.5)\}\times10^{-24}\text{ cm}^2/\text{atom}$$

where E is in ev.

ANTIMONY

For the measurements on antimony the heaviest sample available was used in order to give sufficient neutron absorption in the thermal region and at the resonances for accurate measurements to be made. The sample used contained 22.41 g/cm^2 of metallic antimony. Even then the lowest transmission at the minimum of a resonance dip was only 18 percent. This sample was cast by the Mackay Laboratories from antimony metal of the analytical reagent grade.

The results of the transmission measurements on antimony are shown in Figs. 12 and 13. The resolution width of the apparatus was considerably different for the resonance energy region than for the thermal region as is indicated at the bottom of Fig. 12. The results given in Fig. 13 show very definite dips in the transmission at 16.5 microseconds/meter and at 28.7 microseconds/meter. There also seems to be a broad dip in the transmission between 0 and 10 microseconds/meter with its center at about 6 microseconds/meter. This dip in the transmission at the lower time-of-flight might be caused by one very broad level at 6 microseconds/meter but, for reasons mentioned below, it is probably caused by many levels spread out over this energy region which are too narrow and too closely spaced to be resolved in these measurements. The minima at 16.5 microseconds/meter and at 28.7 microseconds/meter correspond to energies of 19.2 ev

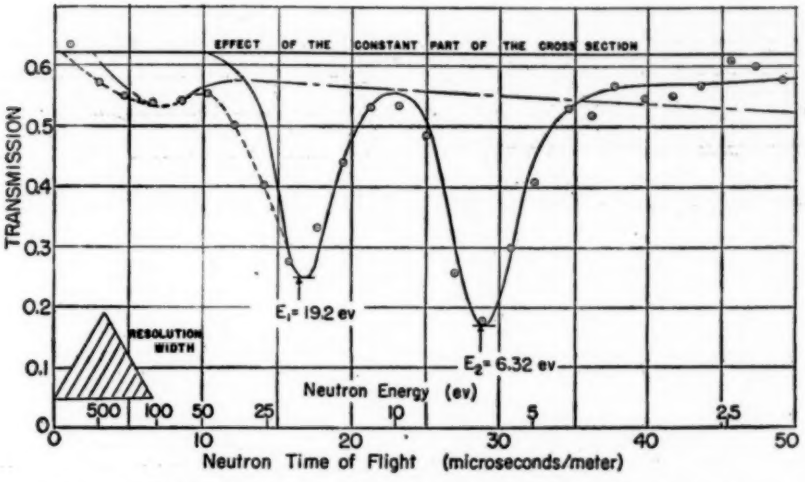

FIG. 13. The transmission of 22.41 g/cm² of antimony in the resonance region. The two main resonances and indications of others at higher energies are seen from the dips in the transmission below the value due to the constant term located from Fig. 12. The solid curve is a calculated transmission curve for two independent levels at 19.2 and 6.3 ev with $\sigma_0\Gamma^2=210\times10^{-24}$ cm² ev²/atom for the level at 19.2 ev and with $\sigma_0\Gamma^2=20\times10^{-24}$ cm² ev²/atom for the level at 6.3 ev. The dot-dashed curve is an attempted fit for the high energy dip assuming a single level with $E_0=145$ ev and $\Gamma=92$ ev. The effect of this level would be much too large in the thermal region and too small in the resonant region indicating the probability of many interfering levels.

and 6.3 ev, respectively. A timing of 6.0 microseconds/meter corresponds to an energy of 145 ev.

The standard method of analysis was applied to the results of the transmission measurements in the thermal region and the intercept of the straight line was located as $T=0.64$. The equation of the straight line which best fits the experimental results in the thermal region given in Fig. 12 is

$$\sigma_{\text{thermal}}=\{(0.64\pm0.02)E^{-\frac{1}{2}}+(4.2\pm0.4)\}\times10^{-24}\ \text{cm}^2/\text{atom}$$

where E is in electron volts.

The constant term in the cross section for antimony was therefore taken as 4.2×10^{-24} cm²/atom and the best values of B were located for the 16.5 and 28.7 microsecond/meter resonances assuming each to be a single independent level. The separate calculated transmission curves for the two levels were then multiplied together to give an over-all theoretical transmission curve for the two levels. This curve was then numerically integrated over the resolution function of the apparatus to give the solid curve shown in Fig. 13. In all cases the value of λ was assumed to be zero and no attempt was made to set an upper and lower limit on Γ. Since the resolution width of the apparatus is relatively broad in this energy region, the sensitivity of the shape of the transmission curve to variations in B is not large. When the additional effect of small uncertainties in the determination of the constant part of the cross section is considered, the over-all accuracy of the value selected for the parameter B is probably accurate to about a factor of 2.

An attempt was made to fit a calculated transmission curve to the experimental results in the vicinity of 6 microseconds/meter assuming that only one broad level is present. The dot-dash curve in Fig. 13 shows the calculated transmission due to a level at 145 ev with a width of 92 ev. The area between this curve and the line $T=0.64$, which corresponds to unity transmission for capture, is seen to be much less than this same area for the experimental curve in the region between 4.2 and 9.0 microseconds/meter. Therefore the value of B required for one level to give the observed area would have to be even larger than that chosen. The area of the absorption dip in the resonance region has a different dependence on the parameter B than the corresponding absorption in the thermal region. The area of the absorption dip in the resonance region depends

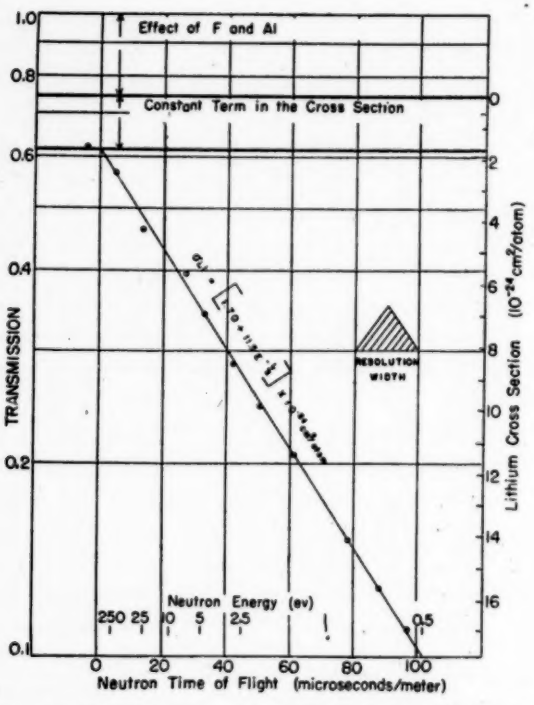
Effect of F and Al
Constant Term in the Cross Section
TRANSMISSION
Lithium Cross Section (10⁻²⁴ cm²/atom)
RESOLUTION WIDTH
Neutron Energy (ev)
250 25 10 5 2.5 0.5
Neutron Time of Flight (microseconds/meter)

FIG. 14. The slow neutron transmission of 4.85 g/cm² of lithium fluoride. The logarithmic plot of the transmission of lithium can easily be resolved into a straight line with $\sigma=(1.7+11.5E^{-\frac{1}{2}})\times10^{-24}$ cm²/atom if the cross section of fluorine is assumed to be constant at 2.5×10^{-24} cm²/atom. The high energy region is emphasized in this plot.

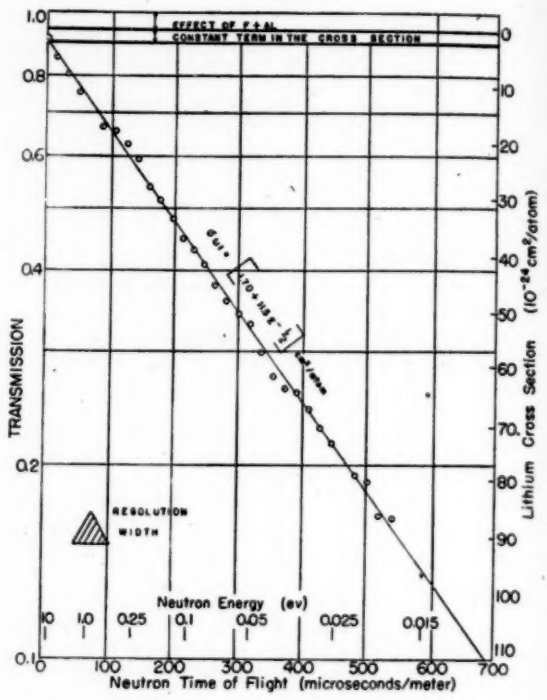

FIG. 15. The slow neutron transmission of 0.862 g/cm² of lithium fluoride. The *same* $1/v$ and constant term in the cross section have been taken for the straight line drawn in this plot as were taken for the much thicker sample used in Fig. 14. A much wider range is covered showing good agreement with the results on the thicker sample.

on $\sqrt{B}$ while the corresponding absorption in the thermal region depends on B itself. When the effects of several levels are combined in the resonance region the total area under the absorption curve will be proportional to the sum of the $\sqrt{B}$ terms for each level with slight chance of interference if the levels do not overlap appreciably. In the thermal region the area under the absorption curve increases as the sum of the separate B values therefore the increase in absorption in the thermal region will be relatively much slower than the corresponding increase in absorption in the resonance region. In addition the interference effects between several levels could be very pronounced in the thermal energy region which is quite a distance from the resonance energy region of all the levels. Suppose, for example, there are four levels of equal strength which together produce a specified area for absorption in the resonance region. Then the corresponding absorption in the thermal region will be at most one-half as much as that which would occur if only one level had been responsible for the total resonance absorption. Interference effects between the levels might then further reduce the relative thermal absorption to much less than the value one half.

The predicted absorption in the thermal region due to only the two easily resolved levels at 16.5 and 28.7 microseconds/meter is approximately the same as the experimentally observed absorption. The predicted absorption in the thermal region due to only the one level at 6.0 microseconds/meter is several times larger than that actually observed. Therefore, considering all the factors involved, it seems quite likely that the transmission dip in the vicinity of 6 microseconds/meter is caused by several unresolved levels which probably interfere considerably in the thermal region.

The results of the transmission measurements on antimony may be summarized as

$$E_1=(19.2\pm1.0)\text{ electron volts }\sigma_1\Gamma_1^2$$
$$=(210)\times10^{-24}\text{ (ev)}^2\text{ cm}^2,$$

$E_2 = (6.3 \pm 0.2)$ electron volts $\sigma_2 \Gamma_2^2$
$= (20) \times 10^{-24}$ (ev)^2 cm^2,

$\sigma_{\text{thermal}} = [(0.64 \pm 0.02)(E)^{-\frac{1}{2}} + (4.2 \pm 0.3)]$
$\times 10^{-24}$ cm^2/atom.

Other levels above 50 ev not resolved.

LITHIUM

Lithium fluoride was the substance used as an absorber for the transmission measurements on lithium. This salt was tightly packed in an aluminum container such that there were 4.85 g/cm^2 of LiF and 0.418 g/cm^2 of aluminum in the beam for the thicker sample and 0.862 g/cm^2 of LiF and 0.418 g/cm^2 of aluminum in the beam for the thinner sample. The lithium fluoride was obtained from the City Chemical Corporation and was of analytical reagent grade. The salt was dried at 120°C for 48 hours before being packed in the container.

The results of the transmission measurements on these two samples are given in Figs. 14 and 15. The experimental points can easily be fit to a straight line on a logarithmic plot. This straight line has its intercept at $T = 0.905$ for the 0.862 g/cm^2 sample and at $T = 0.614$ for the 4.18 g/cm^2 sample. If the cross section of aluminum is assumed to be 1.5×10^{-24} cm^2/atom and that of fluorine 2.5×10^{-24} cm^2/atom[4,5] and these cross sections are assumed constant over the energy interval studied, then the absorption due to the aluminum and the fluorine will be equivalent to a reduction in the transmission to $T = 0.938$ for the 0.862 g/cm^2 sample and to $T = 0.826$ for the 4.85 g/cm^2 sample. The experimental results then indicate that the slow neutron cross section of lithium follows a $1/v$ law and may be expressed as:

$\sigma_{\text{Li}} = [(11.5 \pm 0.2)(E)^{-\frac{1}{2}} + (1.7 \pm 0.2)]$
$\times 10^{-24}$ cm^2/atom,

where E is expressed in electron volts.

The cross sections of aluminum and fluorine in the thermal region are known to be small and almost entirely due to scattering. The variation of their cross sections over the energy region considered should be small and thus introduce negligible error in the determination of the slope of the line which best fits the experimental results.

However, the determination of the constant term in the expression for the cross section of lithium is directly dependent on, and of the same order of magnitude as, the cross section for the aluminum and fluorine. Therefore, this value depends directly on the assumed values of the cross sections of aluminum and fluorine. The effect of the absorption of the aluminum is the same for both samples and is equivalent to a reduction in the transmission to $T = 0.986$; therefore a 10 percent error in the assumed aluminum cross section will introduce an error of less than 0.7 percent in the determination of the constant term in the expression for the cross section from the results on the 4.85 g/cm^2 sample. However, the absorption due to the fluorine increases with the sample thickness in the same proportion as that of the lithium. The cross section of fluorine is known quite well[5] and a 5 percent error in the assumed cross section will change the value of the constant cross section by about 7 percent which is well within the precision stated.

The constant term in the expression for the

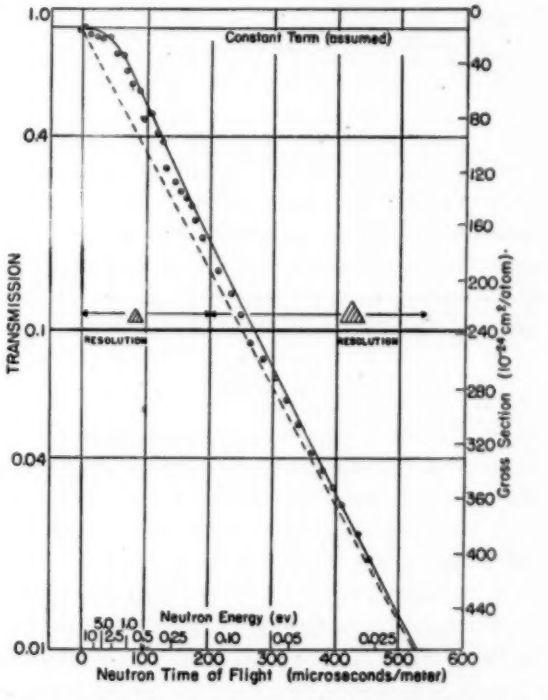

FIG. 16. The slow neutron transmission of 3.25 g/cm^2 of mercury. The solid curve in the figure is a theoretical transmission curve for a negative level at -2.0 ev. The dotted line represents the corresponding $1/v$ line determined from these data. The constant term in the cross section was taken from Figs. 17 and 18.

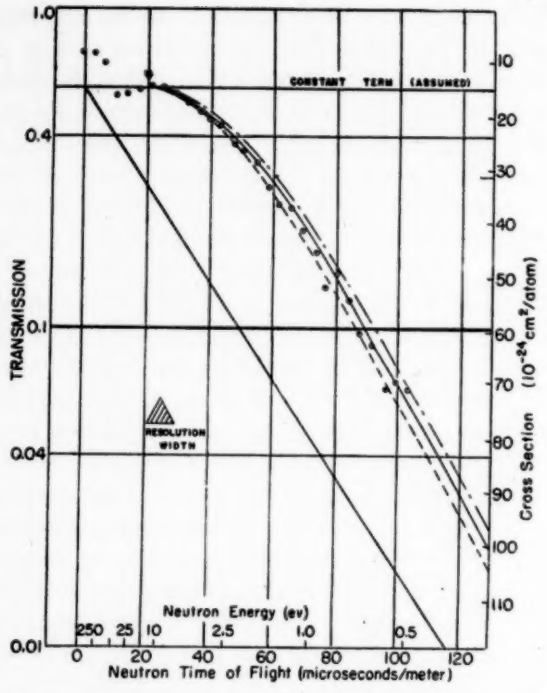

FIG. 17. The slow neutron transmission of 12.9 g/cm² of mercury. The curves shown in this figure are theoretical transmission curves based on the $1/v$ factor determined from Fig. 16. Dashed curve: $E_0=-2.25$ ev. Full curve: $E_0=-2.00$ ev. Dot-dash curve: $E_0=-1.75$ ev. Heavy straight line: $\sigma=[15+64E^{-\frac{1}{2}}]\times10^{-24}$ cm²/atom. The constant term in cross section was located by a process of trial and error.

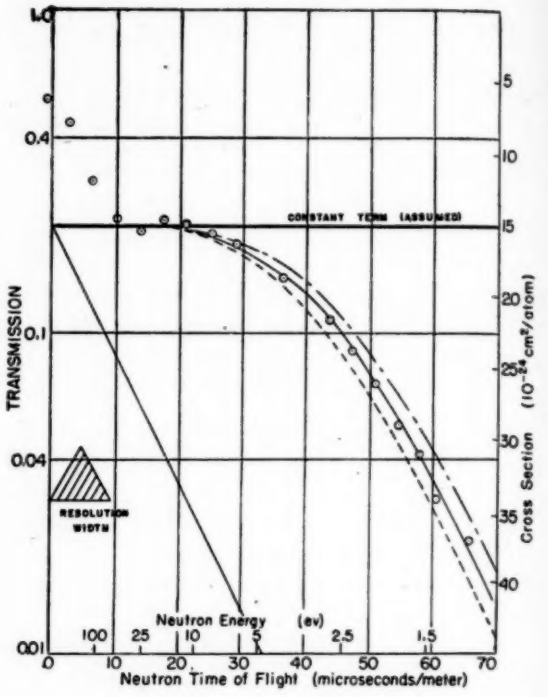

FIG. 18. The slow neutron transmission of 34.4 g/cm² of mercury. The curves shown here are for the same set of theoretical parameters as used in Fig. 17. The close agreement of the curve for $-E_0=-2.0$ ev for the three greatly different sample thicknesses of Figs. 16–18 show that there can be no appreciable systematic errors in the method. The common disagreement with the theoretical curve above 10 ev indicates the existence of positive levels.

cross section of lithium is equal to the capture cross section at approximately 45 ev. If the constant part of the cross section is assumed to be caused only by scattering then this value agrees qualitatively with the order of magnitude calculations given by Bethe.[2]

MERCURY

For the transmission measurements on mercury several brass containers were constructed to hold different thicknesses of liquid mercury. The side walls of all the containers were made of the same thickness brass plate and the slow neutron transmission of all the holders were compared and found to be the same. The use of an empty container on the "out" runs thus eliminates the effect of the container on the results. The mercury was U.S.P. XII redistilled—purchased from the Mallinkrodt Chemical Works.

For the preliminary investigation of the entire transmission curve of mercury, a sample containing 3.25 g/cm² of the liquid was used. The results of these transmission measurements are shown in Fig. 16. It is at once evident from these results that the nature of this transmission curve is qualitatively different from the transmission curves of the other elements studied. For a material with a positive resonance the logarithmic plot of the transmission is a straight line over most of the energy range studied and the actual transmission dips below this straight line in the region of the resonance. In Fig. 16 the logarithmic plot of the transmission also gives an approximately straight line in the region of large timings (low energies) but then it differs from the other curves in that the transmission is much higher than the $1/v$ line in the region of the higher energies. This is the type of transmission curve that would be expected from an element having a resonance level below the binding energy of the neutron. The solid curve that is shown with the

experimental results in Fig. 16 is for a negative energy of -2.0 ev.

For a negative energy level the Breit-Wigner one-level formula for neutron capture is of the form

$$\sigma=\sigma_0\left[\frac{E_0}{E}\right]^{\frac{1}{2}}\frac{\Gamma^2}{\Gamma^2+4(E+E_0)^2},$$

where $-E_0$ is the resonant energy. If $E_0\gg\Gamma$, then the first term in the denominator will always be small compared to the second and consequently can be neglected. The equation may then be written

$$\sigma=\left[\frac{\sigma_0\Gamma^2}{4E_0^{\frac{1}{2}}}\cdot\frac{1}{E^{\frac{1}{2}}}\right]\left[1+\frac{E}{E_0}\right]^{-2}.$$

In this expression the first bracket represents the $1/v$ straight-line term in the cross section. The second bracket is the expression that is of interest in locating the negative resonance energy. If $E\ll E_0$, then the value of the second bracket is approximately unity and the cross section follows a $1/v$ curve. As E/E_0 approaches unity or larger, the cross section becomes appreciably smaller than the $1/v$ relation and gradually changes into a $1/v^5$ dependence.

In matching the experimental results to a theoretical curve of this type three parameters must be evaluated. The first of these is the constant term which must be deducted from the cross section before any other analysis can be applied. The second is the slope of the $1/v$ curve in the thermal region and the last is the energy of the negative resonance level. A trial and error method was applied to the results of the transmission measurements on the 3.25 g/cm² sample. Several theoretical curves with different $1/v$ factors and different negative energy values were calculated and the shapes of these curves were compared with the shape of the experimental curve. By this process it was found that the agreement in the thermal region was very sensitive to a change in the $1/v$ factor but relatively insensitive to a change in the value chosen for the resonant energy. The agreement in the higher energy region (in the vicinity of 30–100 microseconds per meter) is most sensitive to a change in the value chosen for the resonant energy and less sensitive to a change in the $1/v$ factor. Since this region can be studied with much greater accuracy using a thicker sample only the $1/v$ factor was obtained from the results on the 3.25 g/cm² sample. The assumed constant cross section shown in Fig. 16 was located from the thicker sample. The resulting theoretical curve for a negative resonance energy of 2.0 ev is shown in Fig. 16 for comparison with the experimental points. It can easily be seen from these results that the $1/v$ factor cannot be changed by as much as 5 percent without causing the theoretical curve to be appreciably different from the experimental results.

In Figs. 17 and 18 the results of the transmission measurements on a 12.9 g/cm² sample and a 34.4 g/cm² sample are shown for the entire region of investigation of these samples. In Fig. 19 the high energy region for the thicker sample has been expanded to give some indication of the behavior of the transmission in this region. These results clearly show a broad shallow dip in the transmission between 10 and 15 microseconds/meter with a maximum in the transmission near 20 microseconds per meter. The cross section seems to be of the order of 7×10^{-24} cm²/atom in the vicinity of zero time-of-flight. For the purpose of analysis of the

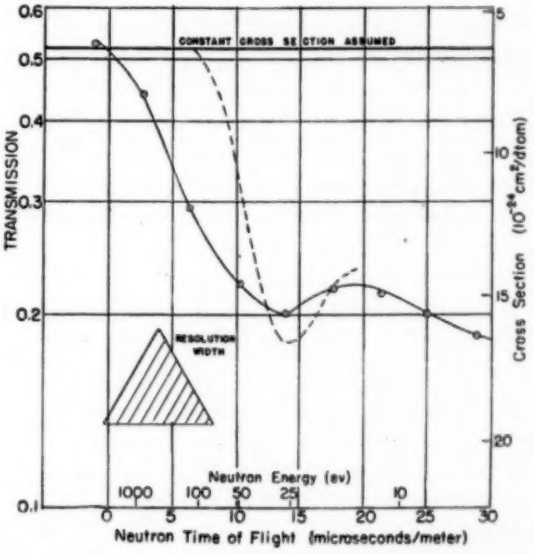

FIG. 19. The slow neutron transmission of 34.4 g/cm² of mercury in the high energy region. The solid curve follows the experimental points indicating resonances above 25 ev. The dotted curve is a theoretical curve for a single level at $E_0=31.4$ ev with $\Gamma=37.8$ ev showing the probable existence of several levels above 25 ev to give the observed broad dip.

negative energy level the shape of the curve for timings below 20 microseconds/meter was assumed to be caused by several levels which interfered with each other in such a manner that their over-all contribution to the cross section for energies below 10 ev could be neglected compared to the effect of the negative level. The possible effects of these positive levels will be discussed further below.

Using the $1/v$ factor located from the results on the 3.25 g/cm² sample several transmission curves were calculated for the two thicker samples, using different values of the resonant energy. The shapes of these curves were compared with the shapes of the experimental transmission curves as shown in Figs. 17 and 18. Since the constant cross section corresponds to a constant distance on a logarithmic transmission plot, the value of the constant cross section which will give the best fit to a theoretical curve can be found by inspection. A preliminary value of $\sigma_{const}=15\times10^{-24}$ cm²/atom was therefore chosen.

When the constant cross section is determined and the $1/v$ term is also located, it is possible to calculate a value of E_0 from each of the experimental points. These calculations were carried out for the results on the 34.4 g/cm² sample. Because of the nature of the dependence of the transmission on the timing only the values of the transmission at timings greater than 30 microseconds/meter were considered. Using a value of $\sigma_c=15\times10^{-24}$ cm²/atom for the constant cross section the calculated values of E_0 were fairly constant giving a value of $E_0=-(1.95\pm0.02)$ ev where the probable error given considers only the internal consistency of the results. This does not indicate the accuracy of the determination but it does show the degree of internal agreement of the calculated values. In order to test the sensitivity of the determination of the negative resonance energy to changes in the chosen value of the constant cross section the values for the resonant energy were again calculated using first a greater and then a smaller value for the constant cross section. If a value of $\sigma_c>15\times10^{-24}$ cm²/atom is used, the calculated numerical value of $|E_0|$ will be small for low times of flight and increase to approach the value of $-E_0=2.0$ ev for larger times of flight. Similarly if the values of $\sigma_c<15\times10^{-24}$ cm²/atom is used, the calculated value of $|E_0|$ will be too large for low times of flight and will decrease to approach the value of $-E=2.0$ ev for larger times of flight. Thus the requirement that the constant term be chosen in such a manner that the calculated value of E_0 does not systematically change with the timing dictates that the constant term to be deducted for the analysis of the negative level be $\sigma_c=15\times10^{-24}$ cm²/atom and the resulting energy of the negative resonance be $-E_0=2.0$ ev.

For reference the calculated transmission curves for $-E_0=1.75$ ev, 2.00 ev and 2.25 ev have been plotted in Figs. 17 and 18 to indicate the sensitivity of the agreement between the theoretical curves and the experimental results to the choice of E_0. In comparing the position of the experimental points and the theoretical curves in Figs. 16–18, it should be noted that the same theoretical values have been used for all the curves and that the values of the parameters were not separately adjusted for each curve to give the best fit. The excellent agreement between the curves for widely different sample thicknesses therefore indicates the absence of appreciable systematic errors and is a valuable check on the significance of the results.

Although the shape of the transmission curves for times-of-flight greater than 20 microseconds/meter are well matched by theoretical curves for a negative level, assuming the above $1/v$ factor, a constant cross section of 15×10^{-24} cm²/atom, and $-E_0=2.0$ ev, the actual relations may be somewhat different from this if the effect of the positive energy levels above 25 ev are considered. In Fig. 19 the experimental points for the 34.4 g/cm² sample for the high energy region are shown. An attempt was made to analyze this resonance by the standard procedure for positive resonances given above, but no satisfactory fit to the experimental results could be obtained. A theoretical transmission curve for a level with a resonant energy of $E_0=31.4$ ev and with a width of 37 ev is shown in Fig. 19 along with the experimental results. Even this very broad level would give a much sharper dip in the transmission than is actually observed. For this reason the broad shallow dip in the transmission in the region from 5 to 18

microseconds/meter is probably caused by several levels above 25 ev which may interfere with each other in such a manner that the net effect in the thermal region is negligible.

A rough estimate of the maximum effect that these positive levels could have on the calculation of the negative resonant energy can be made by using the fact that the transmission curve for the positive level always lies below the $1/v$ curve for $E<E_0$. If a straight line is drawn in Fig. 18 starting with $T=0.53$ at $t=0$ and passing somewhat above the experimental curve in the region of 35 microseconds/meter, this will represent the maximum effect that any positive levels could have on the transmission. Using this procedure a reasonable upper limit for the fraction of the total slope observed in the thermal region due to positive energy levels is of the order of 30 percent. If such an effect were assumed, the corresponding analysis for the negative level would give a value of the $1/v$ factor approximately 70 percent of that used in this analysis. The value of the negative resonance which would then be obtained would be about $-E_0=1.25$ ev. Probably the effect of the positive levels is smaller than this but this is an estimated maximum effect that could be expected.

In conclusion the results for the transmission measurements on mercury can be given with the following qualifications.

If the effect of the negative resonance level is assumed to be predominant for energies below 10 ev, then a good agreement is obtained with a Breit-Wigner one-level curve for

$$-E_0=(2.0\pm0.2)\text{ ev},\quad \Gamma\ll E_0;$$

$$\frac{\sigma_0\Gamma^2}{4E_0^{\frac{1}{2}}}=(64\pm3)\times10^{-24}(\text{ev})^{\frac{1}{2}}\text{ cm}^2/\text{atom},$$

$$\sigma_{\text{const}}=(15\pm1)\times10^{-24}\text{ cm}^2/\text{atom}.$$

In addition there is probably more than one level above 25 ev. The maximum possible effect that the positive levels could have on the negative resonance would be to change the resonant energy to -1.25 ev.

ACKNOWLEDGMENTS

The authors wish to express their appreciation of the active interest taken in this problem by Professor J. R. Dunning without whose active interest and stimulating discussion the investigations could not have been carried out. We also wish to thank Dr. W. E. Lamb and Mr. J. G. Beckerley for the help received in the discussion of some of the problems involved, and to thank the United States Indium Corporation for the loan of the thick indium sample. The Ernest Kempton Adams Fund has also aided materially in carrying out this research.

PHYSICAL REVIEW VOLUME 70, NUMBERS 3 AND 4 AUGUST 1 AND 15, 1946

Calorimetric Experiment on the Radiation Losses of 2-Mev Electrons[1]

W. W. BUECHNER AND R. J. VAN DE GRAAFF
Massachusetts Institute of Technology, Cambridge, Massachusetts

(Received May 21, 1946)

Various investigators report from cloud-chamber experiments that the energy lost in the scattering of 2-Mev beta-rays is several times the loss calculated from the Bethe-Heitler theory. However, other experimenters have found that the production of x-rays in this range agrees with theory. To account for the extra energy loss, Klarmann and Bothe and Champion have suggested the emission of neutrinos as well as x-rays. To test this hypothesis, a 2-Mev beam of electrons was directed on a target immersed in mercury, the assembly acting as a calorimeter. Experiments using beryllium, gold, and mercury targets show that within the experimental error, which is somewhat less than one percent, no energy is carried out of the calorimeter by neutrinos or other penetrating radiation. It thus appears that the production of such radiations cannot account for the large extra energy losses reported from cloud-chamber experiments.

INTRODUCTION

A CONSIDERABLE number of researches with cloud chambers have reported that the energy lost in the scattering of beta-rays by heavy nuclei is several times the radiation loss calculated from the well-established Bethe-Heitler theory. For example, Klarmann and Bothe[2] report that in the energy range from 0.5 to 2.4 Mev the inelastic scattering in krypton and xenon is 2 to 5 times that predicted by the theory. Leprince-Ringuet[3] found indications of 10 times the expected amount for argon in the range 1 to 3 Mev and Laslett and Hurst[4] observed that, for lead, the scattering is high by a factor of 30 for energies from 1.5 to 4.5 Mev. Barber and Champion[5] found 6 times too much inelastic scattering for 1-Mev electrons scattered by mercury. It does not appear that these excess energy losses can be due to the production of x-rays as Arcimovic and Chramov[6] and Petrauskas, Van Atta, and Myers[7] have found experimentally that the production of x-rays in this energy range is in agreement with the theory.

To account for the large extra energy losses which have been reported, Klarmann and Bothe,[2] and Champion[8] have suggested the emission of neutrinos as well as x-rays resulting from the interaction of fast electrons with heavy nuclei. In the case of the continuous beta-ray spectrum, calorimeter experiments performed by Ellis and Wooster[9] and by Meitner and Orthmann[10] have been employed to investigate the energy losses due to neutrino emission. The purpose of the calorimeter experiment described here was to determine whether or not the large energy losses referred to above could be accounted for by the emission of neutrinos or other extremely penetrating radiation.[11]

EXPERIMENTAL PROCEDURE

Figure 1 is a schematic drawing of a calorimetric apparatus constructed to investigate the possibility of such loss by high speed electrons. A 2-Mev electron beam from an electrostatic generator[12] passed downward into a copper tube provided with two targets at the bottom, one of

[1] A preliminary account of this work was presented at the February, 1941 meeting of the American Physical Society, Phys. Rev. **59**, 687 (1941).
[2] H. Klarmann and W. Bothe, Zeits. f. Physik **101**, 489 (1936).
[3] L. Leprince-Ringuet, Ann. de physique **7**, 5 (1937).
[4] L. G. Laslett and D. G. Hurst, Phys. Rev. **52**, 1035 (1937).
[5] A. Barber and F. C. Champion, Proc. Roy. Soc. **A168**, 159 (1938).
[6] L. A. Arcimovic and V. A. Chramov, Comptes Rendus Acad. Sci. U.S.S.R. **7**, 415 (1938).
[7] Petrauskas, Van Atta, and Myers, Phys. Rev. **63**, 389 (1943).
[8] F. C. Champion, Rep. Progress Phys. **5**, 348 (1938).
[9] C. D. Ellis and B. A. Wooster, Proc. Roy. Soc. **A117**, 109 (1927).
[10] L. Meitner and W. Orthmann, Zeits. f. Physik **60**, 143 (1930).
[11] Since the experimental work here reported was completed, we have seen the paper of Ivanov, Walter, Sinelnikov, Taranov, and Abramovich, J. Phys. U.S.S.R. **4**, 319 (1941). These authors describe a somewhat different calorimetric experiment on the radiation losses of fast electrons incident on lead and aluminum. The results of the two experiments are consistent.
[12] Van Atta, Northrup, Van de Graaff, and Van Atta, Rev. Sci. Inst. **12**, 534 (1941).

beryllium and the other of gold. This tube was thermally insulated from the rest of the apparatus by the Micarta studs and Pyrex cylinder shown, and was arranged with a flexible metal bellows so that it could be tipped about a horizontal axis through the center of the diaphragm at the top of the copper tube. Thus the target holder could be shifted slightly by pulling a cord from a well-shielded remote control station, so that either target could be bombarded at will. This insulated target assembly was immersed in 42 kilograms of mercury, held in a container which was thermally insulated from the surroundings. The temperature of the mercury could be measured either with a thermocouple or with a Beckmann differential thermometer viewed through a telescope. The thermometer proved to be the most convenient since it was direct reading and temperature differences could be readily estimated to 0.001°C. A stirring rod was used to assure temperature equilibrium throughout the mass of mercury. The temperature rise due to the rotation of stirring rod was small and reproducible.

There are two alternative methods by which such an apparatus can be used to investigate the possible production of extremely penetrating radiation by the impact of high speed electrons on nuclei. In the first place, the rate of heating in the calorimeter should decrease when the target is shifted from beryllium to gold in the middle of a single run, assuming, as has been suggested, an appreciable amount of energy is carried away by penetrating neutrinos when heavy nuclei are bombarded. It is to be expected, both from the experimental evidence and from general considerations, that energy loss due to neutrinos should be small or non-existent for a light element such as beryllium.

On the other hand, a calorimeter can be used in a more absolute way by calibrating it so that the temperature rise per second is known for any given power input at the target. Then, if the voltage and the current of the beam striking the target are known, it is possible, by comparing the observed temperature rise with that to be expected from the power input, to determine whether any appreciable fraction of this incident energy is carried away by particles or radiations which are able to escape through the mercury of the calorimeter.

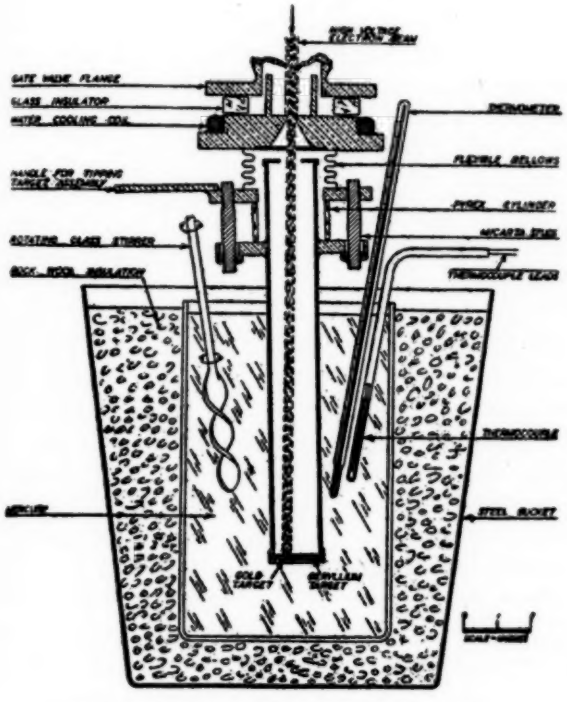

FIG. 1. Schematic drawing of calorimeter.

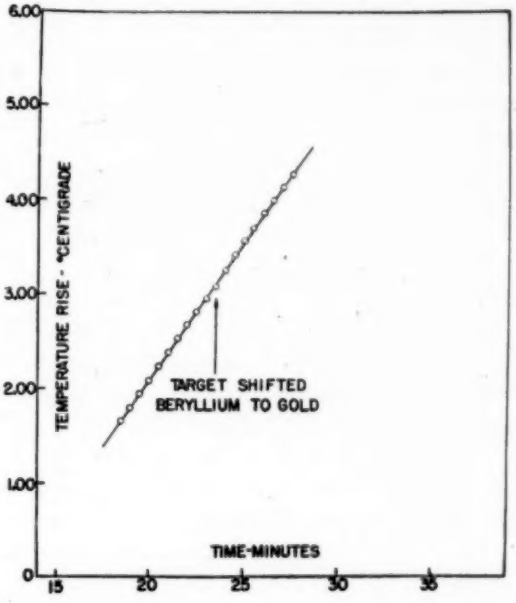

FIG. 2. Calorimeter run at 2 Mev. At the time indicated by the arrow, the target was shifted from beryllium to gold.

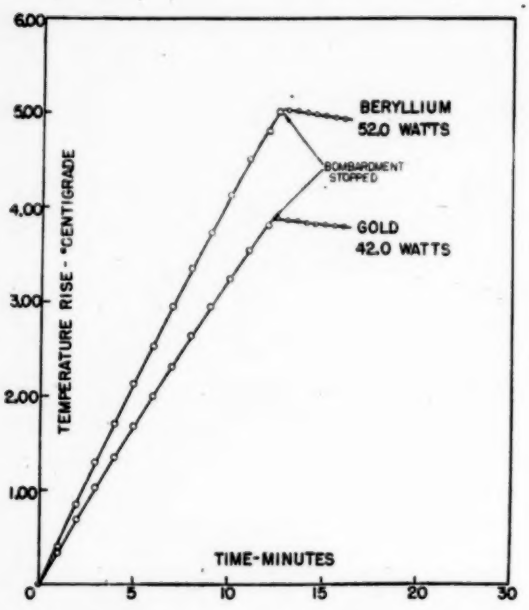

FIG. 3. Two calorimeter runs, both at 2 Mev. For beryllium the current was 26 μa; for gold, 21 μa.

RESULTS

Figure 2 is representative of a number of measurements taken in the way discussed first in the previous section. For this curve the electron energy was 2 Mev, which is in the general energy range for which the cloud-chamber measurements indicate the greatest discrepancy with theory. Since the electron energy was reduced from 2 Mev to zero in the solid targets used, it is evident that the experiment also affords a check on radiation losses at voltages less than the maximum. The temperature rise in the mercury is plotted as a function of time with a steady electron beam of about 10 microamperes. At the time indicated by the arrow, the target holder was shifted so that the element under bombardment was changed from beryllium to gold. There is no perceptible change of slope as there would be if more energy escaped from the calorimeter for one target than the other. This shows that, if there is a difference in the amount of very penetrating radiation produced for heavy elements such as gold as compared to a very light element such as beryllium, it amounts to less than 1 percent of the incident energy. At 2 Mev, this is less than one-fifth of the energy loss to be expected from bremsstrahlung.

Figure 3 shows two curves, representative of a number taken by use of the second method described above, the voltage again being 2 Mev. The power inputs indicated on the two curves are those computed from the voltage and the target currents. When correction is made for the small heat losses from the calorimeter, the temperature rise per watt of bombarding energy is the same for the two targets within the experimental error. This temperature rise per watt also agrees, within the experimental error, with that obtained by a calibration run where the power input was obtained from the I^2R heating of a resistor suitably located in the mercury in place of the target.

DISCUSSION

Experiments on the production of x-rays previously referred to[6,7] show that, in the case of a heavy element like gold, of the order of 5 percent of the bombarding energy is transformed into x-radiation at 2 Mev, in agreement with the predictions of the Bethe-Heitler theory. Cloud-chamber experiments have indicated that the energy losses for the heavy elements are several times those predicted by this theory. If, for definiteness, we assume that the observed cloud-chamber losses are 5 times the bremsstrahlung losses, then about 20 percent of the incident bombarding energy should escape from the calorimeter if the excess losses are to be accounted for by the production of neutrinos. Measurements on the absorption coefficient of 2-Mev x-rays show that only a negligible fraction of the x-rays produced can escape from the calorimeter through the mercury. Because of the small solid angle at the top of the target tube and the predominantly forward direction of the radiation, an even smaller fraction of the x-rays produced will escape upward. Thus, within the experimental accuracy, which is somewhat better than 1 percent, the present calorimeter experiments show that none of the energy of the bombarding electrons is transformed into extremely penetrating radiation which escapes from the calorimeter.

In the work described above, gold was used as a representative heavy element because of its convenient properties. In order to make observations with an element used in cloud-chamber

work, experiments were done with mercury as a target material. Barber and Champion[5] have found about 6 times too much inelastic scattering for mercury. For this purpose, the target holder shown in Fig. 1 was altered and the gold replaced by a thin steel window 0.003 inch thick which allowed the electron beam to bombard the mercury in the calorimeter, the voltage in this case being raised to 2.3 Mev to compensate for the energy lost in the window. As in the case of gold, it was observed that within the experimental error there was no energy carried away by penetrating radiation.

It thus appears that the large energy losses which have been previously reported cannot be accounted for by the suggested emission of neutrinos or other extremely penetrating radiation. As has been referred to in a previous footnote, this result is in accord with the experiments of Ivanov, Walter, Sinelnikov, Taranov, and Abramovich[11] who, employing lead and aluminum targets and a different calorimeter arrangement, find no evidence of neutrino emission and that the radiation losses of electrons in this general energy range are adequately accounted for by the Bethe-Heitler theory.

ACKNOWLEDGMENTS

We are glad to acknowledge the able assistance of Mr. Anthony Sperduto and Mr. E. A. Burrill in making the measurements, and of Mr. E. W. Nickerson in the construction of the apparatus. This work was supported in part by grants from the Research Corporation and the Carnegie Corporation of New York, to whom grateful acknowledgment is made.

PHYSICAL REVIEW VOLUME 70, NUMBERS 3 AND 4 AUGUST 1 AND 15, 1946

The Stability of Electron Orbits in the Synchrotron

N. H. FRANK
Research Laboratory of Electronics, Massachusetts Institute of Technology, Cambridge, Massachusetts

(Received May 21, 1946)

The motion of an electron in a synchrotron (or betatron) is analyzed as its motion in an axially symmetric magnetic field under the action of external torques provided by an r-f field and radiation reaction acting about the axis of symmetry. The process of transition from betatron to synchrotron action is examined in detail and a criterion is established for the condition of "locking-in" of the electrons to the r-f wave which drives them synchronously. The typical stages of synchrotron operation are discussed and it is shown that the requirements for successful, stable operation should not be difficult to realize.

1.

THE theory of the stability of electron orbits in the synchrotron with respect to angular, radial, and vertical oscillations has been treated by a number of authors. The original calculations of McMillan,[1] Veksler,[2] and Blewett[3] are essentially equivalent and comprise what may be termed the quasi-stationary theory. More recently, Schwinger and Saxon[4] have examined the problem in a more refined treatment, providing a quantitative basis for the fundamental assumptions underlying the quasi-stationary theory.[5]

Consider an electron moving in a magnetic field increasing with time, the field being symmetrical about an axis, the z axis. This is the arrangement for a betatron and, as is well known, stable circular motion in a circle of radius r_0 is possible if the magnetic flux linking this orbit is $2\pi r_0^2 B$, where B is the z component of the magnetic field at the orbit. If the fractional increase of the magnetic field in the time of one revolution

[1] E. M. McMillan, Phys. Rev. **68**, 143 (1945).
[2] V. Veksler, J. Phys. U.S.S.R. **9**, 153 (1945).
[3] Unpublished calculations.
[4] Unpublished calculations.

[5] D. M. Dennison and T. H. Berlin have also investigated the stability of electron orbits in a synchrotron operating with a frequency modulated r-f field. Phys. Rev. **70**, 58 (1946).

is very small, a condition satisfied to a high degree of approximation in both the betatron and the proposed synchrotrons, the period of the electronic motion can be written in m.k.s. units as

$$T=(2\pi/ec^2)(E/B), \tag{1}$$

where E is the total energy of the electron (including its rest energy), and B is the z component of the magnetic field at the orbit at the time of this rotation. The radius of the orbit is related to the period by

$$r=\frac{\beta cT}{2\pi}=\frac{\beta E}{ecB}=\frac{E}{ecB}[1-(m_0c^2/E)^2]^{\frac{1}{2}}, \tag{2}$$

where β is the ratio of the electron speed to that of light. In the betatron, the equilibrium radius r_0 is constant and hence the period of electronic motion decreases very slowly with time, approaching a constant value at high energies as β approaches unity. In this high energy range the ratio of energy to magnetic field becomes very nearly constant. The energy is gained, of course, from the e.m.f. induced around the orbit by virtue of the changing magnetic flux through it.

In synchrotron operation, the energy is obtained largely from a radiofrequency voltage existing across one or more gaps. The electrons are driven synchronously by the r-f so that their average rotation period equals that of the r-f. When this condition is established, the orbit radius will swell, according to Eq. (2), as the energy increases. Thus, if any electron gets "locked" into the r-f when its energy is about 2 Mev, $\beta=0.97$, and is then driven synchronously, its mean radius will increase by about 3 percent from its initial to its final high energy value. In addition to this very slow increase of the orbital radius, there will be departures from the mean radius and by (2) from the mean period of rotation. One of the objectives of the theory is the study of these deviations in radius and phase to determine the stability of synchrotron operation. Another is the investigation of the transition from betatron to synchrotron action to establish criteria for the "locking-in" of the electrons relative to the r-f.

The motion of an electron in either a betatron or a synchrotron can be described to a high degree of approximation as its motion in an axially symmetric magnetic field under the action of external torques about the axis of symmetry, the z axis, since both the applied r-f field and radiation forces will exert negligible torque action about any other axis. Using a cylindrical coordinate system, r, θ, z, the equations of motion can be written in the form:

$$\left.\begin{aligned}&\frac{d}{dt}(m\dot{r})=mr\dot{\theta}^2-er\dot{\theta}B_z,\\&\frac{d}{dt}\left(mr^2\dot{\theta}-\frac{e\Phi}{2\pi}\right)=Q_\theta,\\&\frac{d}{dt}(m\dot{z})=er\dot{\theta}B_r.\end{aligned}\right\} \tag{3}$$

Here $m=m_0/(1-v^2/c^2)^{\frac{1}{2}}$ is the relativistic mass, $-e$ the charge on an electron. $\Phi=2\pi\int_0^r rB_z\,dr$ is the magnetic flux linking a circle of radius r and Q_θ is the external torque, defined as the generalized force by $Q_\theta=dW/d\theta$, where dW is the work done by this torque during an angular displacement $d\theta$ of the electron. If the time rate of change of the magnetic field is slow enough to be considered quasi-stationary, the radial and vertical components of the magnetic field are related by $\partial B_r/\partial z=\partial B_z/\partial r$. The energy equation

$$\frac{d}{dt}(mc^2)=\dot{\theta}\left(\frac{e}{2\pi}\frac{\partial\Phi}{\partial t}+Q_\theta\right) \tag{4}$$

follows from (3) by multiplying those equations by $\dot{r}$, $\dot{\theta}$, and $\dot{z}$, respectively, and adding.

For the interval during which the synchrotron is run as a betatron, prior to the application of an r-f field, $Q_\theta=0$ since radiation is negligible in the low energy range, and the stable motion occurs in a circle of constant radius r_0 with an angular velocity given by the first of Eqs. (3) as $\omega=\dot{\theta}_{r=r_0}=eB/m=ec^2B/E$. This is the same as Eq. (1). The second of Eqs. (3) gives the familiar betatron flux relation. The oscillations about the equilibrium orbit are obtained by setting

$$r=r_0+\rho;\quad \dot{\theta}=\omega-\dot{\phi} \text{ and } z=z, \tag{5}$$

inserting these into Eqs. (3), and treating ρ, ϕ, and z small enough so that second and higher order terms in these quantities can be ignored. If the variation of B_z in the neighborhood of r_0

is given by

$$B_z = B(r_0/r)^n \tag{6}$$

and the consequent variation of B_r used, there follow the familiar results of betatron theory. For our purposes, it is sufficient to note that the angular frequencies of the oscillations are of the same order of magnitude as the angular velocity of the electron, and that the vertical z-motion is independent of the radial and angular motions to this order of approximation.

Now let the external torque Q_θ be provided by an r-f field $\mathcal{E}_\theta$ extending over a gap of negligible angular opening at $\theta=0$. A Fourier analysis of this field, which is periodic in θ with a period 2π, gives

$$Q_\theta = -\frac{eV}{2\pi}\sum_{k=-\infty}^{+\infty} \sin(\omega_1 t - k\theta), \tag{7}$$

where V is the peak voltage across the gap and ω_1 the angular radiofrequency. If ω_1 is very nearly equal to the angular velocity $\dot\theta$ of the electron, the only term in the sum which can be effective in doing work on the electron over a time comprising many cycles is that for which $k=1$. Thus, the resolution of the r-f field into traveling waves—and this will be true in general whether the r-f field be created across a single or multiple gaps—brings out the essential fact that only one component wave is essentially in step with the electron motion and all the others give rise to torques which have a rapid variation with time, frequencies of the order of ω_1 and higher, and hence will do no work on the average. The deviations from exact synchronism of the electron motion from the component wave

$$Q_\theta = -\frac{eV}{2\pi}\sin(\omega_1 t - \theta) \tag{7a}$$

will give rise to slow variations in phase and radius of the electronic motion. As will be shown later, the natural frequency of these oscillations is very much smaller than any produced by the remaining component waves or than that of free betatron oscillations. Thus the resultant electron motion can be considered as a superposition of two independent motions:

(a) A relatively high frequency variation of radius and phase, of the order of ω_1, or higher; and

(b) A low frequency, slow change of radius and phase caused by that wave which can drive the electrons synchronously.

For the slow motion (b), one can neglect the acceleration term on the left-hand side of Eq. (3) (and this is the basic assumption of the quasi-stationary theory), insert the expressions (5), (6), and (7a) into this and the second equation of (3) and there follows

$$\frac{\dot\phi}{\omega} = \frac{\omega^2 r_0^2}{c^2}\left(\frac{\rho}{r_0}\right), \tag{8}$$

and

$$\frac{d}{dt}\left(\frac{B\dot\phi}{\omega^3}\right) + \frac{V\sin(\omega_1 t-\theta)}{2\pi c^2(1-n)} = \frac{-r_0^2\dot B}{c^2}\left(\frac{1-\delta}{1-n}\right). \tag{9}$$

Here $\delta = \dot\Phi_0/2\pi r_0^2\dot B$ is the ratio of the time rate of change of the flux linking the betatron orbit to that required for betatron orbit stability and will equal unity as long as the betatron flux condition is satisfied.

2.

We now consider the transition from betatron motion (motion with constant mean radius and slowly increasing angular frequency) to synchronous driving (motion of constant average angular frequency and slowly changing radius). If the betatron angular velocity ω differs at all from the radiofrequency ω_1, there will be a slip of the electron motion relative to the traveling r-f wave and evidently the average energy gain from the r-f wave, averaged over one slip cycle, will be zero. Even if the frequencies differ by as little as one percent it will take only one hundred revolutions to complete such a slip cycle. To obtain synchronous driving, the r-f voltage must be sufficient to stop the slip and "lock" the electrons into synchronism with the wave. Furthermore, this synchronous "locking" should occur before the betatron flux condition is destroyed to insure proper transition from betatron to synchrotron action.

If we set $\psi(=\omega_1 t-\theta)$ equal to the angle between the electron and the r-f wave, the relative angular velocity is, using (5),

$$\dot\psi = \omega_1 - \dot\theta = (\omega_1-\omega)+\dot\phi. \tag{10}$$

$(\omega_1-\omega)$ is the slip angular velocity and $\dot\phi$ is

the perturbation in the angular velocity caused by the r-f field. Inserting (10) into (9) with $\delta=1$, one obtains

$$\frac{d}{dt}\left(\frac{B\dot{\psi}}{\omega^3}\right)+\frac{V\sin\psi}{2\pi c^2(1-n)}=\frac{d}{dt}\left[\frac{B(\omega_1-\omega)}{\omega^3}\right]. \quad (11)$$

The condition for "locking-in" can be then obtained simply if one remembers the exceedingly slow variation of B and ω with time. As a first approximation, we can consider these constant and Eq. (11) becomes the equation of motion of a physical pendulum. The condition for transition from motion with slip to synchronous driving is then the condition for transition from rotatory to oscillatory motion of the pendulum. This gives as the condition for "locking-in"

$$\left|\frac{\omega_1-\omega}{\omega}\right|\leq\left[\frac{4V}{c\lambda(1-n)B}\right]^{\frac{1}{2}}, \quad (12)$$

where λ is the wave-length corresponding to the frequency ω. For the M.I.T. synchrotron design one gets, with $V=1$ kv, $B=400$ gauss $=4\times10^{-2}$ weber/m^2, $n=\frac{3}{4}$ and $\lambda=\pi$ meters,

$$|(\omega_1-\omega)/\omega|\leq0.02,$$

so that synchronous driving sets in when the difference between betatron and r-f frequencies becomes the order of 2 percent. The effect of the slow variation of B and ω with time can be then included as a second approximation. This modifies the inequality (12) by multiplying the right-hand side by the factor $(1+\alpha)$, where

$$\alpha<\frac{\pi c^2\dot{B}(1-n)}{V\omega_1^2}\left(\frac{m_0c^2}{E_1}\right)^2,$$

where E_1 is the electron energy when $\omega=\omega_1$. This term α is a fraction of a percent for the M.I.T. design and is hence quite negligible in this case.

In the preceding discussion, it has been assumed that the r-f voltage had built up to its maximum value without appreciably modifying the betatron angular velocity ω. This will be very nearly true if the inequality (12) is *not* satisfied during the build-up time. If, however, the radio frequency ω_1 does satisfy (12) during the build-up time, "locking-in" will take place at lower than peak voltage. The case of build-up under conditions of exact synchronism $\psi_1=\omega$ (at high enough energies) has been considered in detail by Schwinger and Saxon[6] and they have shown that considerable bunching about zero phase (the equilibrium value of ψ or ϕ) can take place during this time and this bunching is enhanced the longer the build-up time.

3.

Once the electrons have been locked into synchronism with the r-f field, the angular departure ψ of the electron from the traveling r-f wave becomes pure oscillatory. In this synchronous region the total energy of the electron will in general be sufficiently high compared to its rest energy that we can take its speed equal to that of light. Equation (8) can then be replaced by

$$\dot{\phi}\cong\frac{\rho\omega}{r_0}\cong\rho\frac{\omega_1}{r_0} \quad (8a)$$

and Eq. (9) for the phase oscillations takes the form

$$\frac{d}{dt}\left(\frac{B\dot{\psi}}{\omega^3}\right)+\frac{V\sin\psi}{2\pi c^2(1-n)}=\frac{-r_0^2\dot{B}}{c^2}\left(\frac{1-\delta}{1-n}\right)+\frac{d}{dt}\left[\frac{B(\omega_1-\omega)}{\omega^3}\right]. \quad (9a)$$

First consider the range of operation for which saturation has not yet started, so that $\delta=1$. If we neglect the small forcing term $(d/dt)(B[\omega_1-\omega]/\omega^3)$ for the time being and take $\omega\cong\omega_1$ as constant, Eq. (9a) becomes the equation for the free oscillatory motion of a physical pendulum of slowly changing moment of inertia corresponding to the slow increase of magnetic field B with time. For this motion the integral $\oint B\dot{\psi}d\psi$ taken over a period is an adiabatic invariant, i.e., is constant, so that the amplitudes of the oscillations decrease slowly as B increases. The integral can be evaluated in terms of complete elliptic functions and the result is:

$$h[\sin(\psi_m/2]=\text{const.}/B^{\frac{1}{2}} \quad (13)$$

where $h(k)=E(k)-(1-k^2)K(k)$, K and E being complete elliptic functions of the first and second

[6] Unpublished calculations.

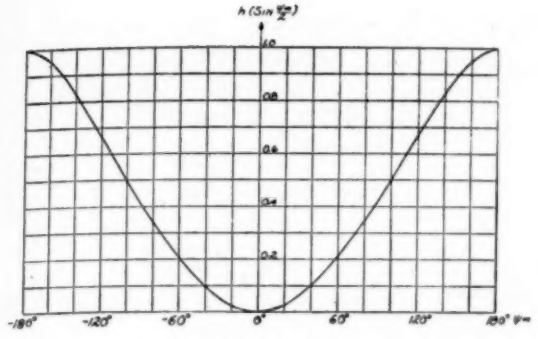

FIG. 1. Plot of $h(\sin \psi_m/2)$ *vs.* ψ_m to be used in conjunction with Eq. (13).

kind, and ψ_m the maximum oscillation amplitude. Figure 1 is a plot of $h[\sin(\psi_m/2)]$ as a function of ψ_m and shows how bunching takes place even for large amplitudes. This may be termed "pre-bunching" as it occurs prior to the onset of saturation.

The neglect of the extremely slow variation of ω at high energies does not change the result appreciably. When included, it indicates a slightly slower rate of decrease of amplitude with increasing magnetic field than is given by Eq. (13) and its effect gets smaller the higher the energy at which this pre-bunching occurs.

The effect of the small forcing term

$$(d/dt)[B(\omega_1-\omega)/\omega^2]$$

is to cause the oscillations to occur about an equilibrium phase slightly different from zero. The position of this equilibrium phase point, which is given to a good degree of approximation by

$$\sin\psi_e=-\frac{2\pi r_0^2(1-n)\dot{B}}{V}\left[2\left(\frac{\omega'-\omega}{\omega'}\right)-\frac{\omega_1-\omega}{\omega_1}\right],$$

with $\omega'=c/r_0$, will change very slowly with time as the betatron frequency ω gradually increases. This slow change occurs coincidently with the slowly changing radius and is accompanied by a small gain of energy of the electrons from the r-f field. Once saturation has started, however, the effect of this forcing term becomes entirely negligible and will be omitted in the remainder of this paper.

During the process of saturation and the consequent destruction of the betatron flux relation, δ changes slowly from unity to something of the order of 20 to 25 percent. During this slow change the equilibrium phase will slowly change according to the relation

$$\sin\psi_e=-(2\pi r_0^2\dot{B}/V)(1-\delta). \tag{14}$$

For small oscillations about this equilibrium phase, one can readily solve Eq. (9a) and finds further decrease of amplitude of oscillation, i.e., further bunching. From the analogy with the motion of a physical pendulum it is clear that this further bunching will occur for large amplitudes also.

After saturation is complete, the equilibrium phase stays essentially fixed until the energy becomes sufficiently large to have radiation reaction play a significant role. In this region, we shall obtain some of the orders of magnitude of the quantities of interest. For this purpose, it is convenient to change the independent variable in Eq. (9a) from time t to number of revolutions N. This choice of independent variable was originally made by Veksler. To the degree of approximation employed in deriving Eq. (9a), one has

$$dt/dN=T\cong T_1=2\pi/\omega_1,$$

where T and T_1 are the periods of the electron motion and the r-f field, respectively. Equation (9a) takes the form, ignoring the small forcing term in $(\omega_1-\omega)$,

$$\left(\frac{B}{\dot{B}T_1}\right)\frac{d^2\psi}{dN^2}+\frac{d\psi}{dN}+\frac{4\pi^2V\sin\psi}{\lambda^2\dot{B}(1-n)}=-2\pi\left(\frac{1-\delta}{1-n}\right), \tag{9b}$$

where $\lambda=cT_1$ is the r-f wave-length.

If one now considers the magnetic field a linear function of the time,

$$B=B_0+\dot{B}t=B_0+\dot{B}NT_1.$$

(9b) becomes finally:

$$(N_0+N)\frac{d^2\psi}{dN^2}+\frac{d\psi}{dN}+\Omega^2\sin\psi=-2\pi\left(\frac{1-\delta}{1-n}\right), \tag{9c}$$

with $N_0=B_0/\dot{B}T_1$ and $\Omega^2=4\pi^2V/(\lambda^2\dot{B}(1-n))$. If now, instead of ψ, we write $\psi+\psi_e$, where ψ_e is the equilibrium phase given by (14) or its

equivalent

$$\sin \psi_e = -\frac{2\pi}{\Omega^2}\left(\frac{1-\delta}{1-n}\right),$$

and consider small deviations ψ from this equilibrium phase, ψ satisfies the homogeneous equation

$$(N_0+N)\frac{d^2\psi}{dN^2}+\frac{d\psi}{dN}+(\Omega^2\cos\psi_e)\psi=0. \quad (9d)$$

The solution of this equation is, with $\cos\psi_e \cong 1$ and $x=2(N_0+N)^{\frac{1}{2}}$,

$$\psi = c_1 J_0(\Omega x)+c_2 N_0(\Omega x).$$

To get the order of magnitudes involved, we take the M.I.T. figures $V=10^3$ volts, $\dot{B}\cong 2\times 10^2$ webers/m²-sec.; $\lambda=\pi$ meters; $n=\frac{3}{4}$ and $B_0\cong 6\times 10^{-2}$ weber/m² corresponding to an energy of about 9 Mev when saturation is complete. Then $\Omega\cong 9$ and $x_0=2\sqrt{N_0}\cong 350$, so that $\Omega x>3000$ and the asymptotic values of the Bessel functions can be used. Then we have

$$\psi=(C/\sqrt{x})\cos(\Omega x-D). \quad (9e)$$

To get the period of small phase oscillations, we have $\Omega(x_2-x_1)=2\pi$, whence

$$\Delta N = N_2-N_1\cong\frac{2\pi}{\Omega}(N_0+N_1)^{\frac{1}{2}}\cong\frac{2\pi}{9}(30{,}000+N_1)^{\frac{1}{2}},$$

so that the number of revolutions per cycle of phase oscillation increases slowly with the total number of revolutions, and is of the order of 200 for $N_1=0$, i.e., when saturation ends.

As Saxon and Schwinger have shown, radiation reaction subsequently results in a further increase in the magnitude of the equilibrium phase and modifies the rate of change of amplitude of oscillation about this point, increasing the bunching action if $n<\frac{3}{4}$ and decreasing it if $n>\frac{3}{4}$.

Because radiation effects become significant only at extremely high energies, the torque Q_θ due to radiation reaction can be written as

$$Q_\theta = -\frac{2}{3}\cdot\frac{e^2}{4\pi\epsilon_0 r}\left(\frac{ecrB_z}{m_0c^2}\right)^4,$$

with $\epsilon_0=(1/36\pi)\times 10^{-9}$ farad/meter, very nearly. Following the same procedure as before, one obtains as the equation for phase oscillations:

$$\frac{2\pi r_0^2(1-n)}{\omega}\frac{d}{dt}(B\dot{\phi})+\frac{e}{3\epsilon_0 r_0\omega}\left(\frac{ecr_0B}{m_0c^2}\right)^4(3-4n)\dot{\phi}$$

$$+V\sin\phi=-2\pi r_0^2\dot{B}(1-\delta)-\frac{e}{3\epsilon_0 r_0}\left(\frac{ecr_0B}{m_0c^2}\right)^4,$$

which leads to an equilibrium phase angle, at very high energies where radiation losses alone practically determine it, given by

$$\sin\phi_e=-\frac{e}{3\epsilon_0 r_0 V}\left(\frac{E}{m_0c^2}\right)^4$$

where $E=ecr_0B$ is the total energy of the electron.

4.

There remains the problem of justifying the neglect of the left-hand side of the first of Eqs. (3) for the slow variations of radius and phase and the assumption that the slow motion can be treated independently of the remaining high frequency motion. To do this simply, consider the motion of an electron of very high energy as given by Eqs. (3) with $\omega=\omega_1=c/r_0$ under the action of the external torque (7a) alone.

By use of (5) and considering only small departures from circular motion, one obtains from the first and second of Eqs. (3) (the z-motion is independent of the radial and angular motion to first order),

$$\frac{d}{dt}\left[\frac{d}{dt}(B\dot{\rho})+B\omega^2(1-n)\rho\right.$$

$$\left.+\omega^2 r_0^2\left(B-\frac{\Phi_0}{2\pi r_0^2}\right)\right]=-\frac{\omega^2 V}{2\pi r_0}\sin(\omega t-\theta)$$

and using the relations $\rho=r_0\dot{\phi}/\omega$ and $\phi=\omega t-\theta$, this becomes

$$\frac{d^2}{dt^2}\left(B\frac{d^2\phi}{dt^2}\right)+\omega^2(1-n)\frac{d}{dt}\left(B\frac{d\phi}{dt}\right)$$

$$+\frac{\omega^3 V\sin\phi}{2\pi r_0^2}=-\omega^3\dot{B}(1-\delta) \quad (15)$$

as the equation determining the phase oscilations. Thus there are two frequencies of phase oscillation under the action of the external

FIG. 2. Schematic sequence of operations of a synchrotron.

torque and they are determined from Eq. (15) by setting B constant and $\sin\phi=\phi$ for small oscillations. These two frequencies ω' and ω'' are then given as the solutions of the biquadratic equation:

$$\omega_0^4-\omega_0^2\omega_r^2+A=0, \tag{16}$$

where $\omega_r^2=\omega^2(1-n)$ and $A=\omega^3V/2\pi r_0^2B$. The roots ω' and ω'' are then

$$\left.\begin{aligned}\omega'^2&=\omega_r^2(\tfrac{1}{2}+\tfrac{1}{2}(1-4A/\omega_r^4)^{\frac{1}{2}})\\ \omega''^2&=\omega_r^2(\tfrac{1}{2}-\tfrac{1}{2}(1-4A/\omega_r^4)^{\frac{1}{2}})\end{aligned}\right\}. \tag{17}$$

Oscillatory motion will occur if $4A/\omega_r^4<1$ or

$$B>2V/\pi r_0^2\omega(1-n)^2,$$

a condition well satisfied for almost any reasonable design parameters. In the case of the M.I.T. design, the magnetic field need be greater than only $\frac{2}{3}$ gauss. Since it is of the order of several hundred gauss when the r-f field goes on, $4A/\omega_r^4$ is very small compared to unity and the two frequencies of phase oscillation become

$$\omega'^2=\omega_r^2=\omega^2(1-n),$$

$$\omega''^2=\frac{A}{\omega_r^2}=\frac{\omega V}{2\pi r_0^2B(1-n)}.$$

Thus it is clear that the root ω'' can be obtained to this high degree of approximation from Eq. (16) with the first term missing. Since this term arose from the radial acceleration term in Eq. (3), the left-hand side of the first of these equations, we have justified the neglect of this term from the outset to get the slow oscillations induced by the r-f field. The high frequency oscillation $\omega'=\omega_r$ is just the betatron radial oscillation frequency and, since this can be obtained from Eq. (16) by neglecting the last term which alone depends on the r-f field, this is unaffected by the presence of this component wave of the r-f field. The higher harmonics of this field whose frequencies are close to ω_r will, of course, modify the high frequency motion but evidently will have no significance for the low frequency motion. Equation (15) with the first term on the left omitted is just Eq. (9a) used to describe the synchronous region of operation.

5.

One can summarize the essential results obtained in this paper schematically with the help of the diagram of Fig. 2. In this the horizontal line represents increasing time but not to any particular scale. The sequence of operations shown in the figure can be described as follows:

Initially, one has pure betatron action during the latter part of which the r-f field is built up. The electrons gain energy by betatron action alone until "locking" into synchronism occurs as indicated. At this point pure betatron action ceases and the synchronous region begins, characterized by a small decrease in radius. Energy is still essentially supplied to the electrons from the betatron induced e.m.f. As this energy increases the radius slowly increases, passing through the betatron equilibrium radius when the betatron frequency equals the radiofrequency. During this time pre-bunching is taking place, and the electrons derive a small additional energy from the r-f field. When saturation begins, the electrons start picking up an appreciable amount of energy from the r-f field, and the equilibrium phase slowly rises to a definite value when saturation is complete. This state of affairs with continually greater bunching persists until radiation effects become important. Then there is a further slow increase of the equilibrium phase, additional energy abstracted from the r-f field to supply radiation losses and a modification of the bunching because of the radiation reaction.

A Note Concerning the Coriolis Contribution to the Energy of a Symmetric Polyatomic Molecule

HARALD H. NIELSEN
Mendenhall Laboratory of Physics Ohio State University, Columbus, Ohio

(Received May 27, 1946)

By a third-order perturbation calculation it is shown that the degenerate Coriolis interaction term in the vibration-rotation energy of a symmetric polyatomic molecule should be written $\mp 2\sum_t \zeta_t l_t K C_v$ rather than $\mp 2\sum_t \zeta_t l_t K C_e$, C_e being equal to $(h/8\pi^2 I_{zz}^{(e)} c)$ and $C_v = C_e - \sum_t (v_t + g_t/2)\Gamma_t$, Γ_t being a constant $\gamma_t + \sum_{t'\sigma'} \zeta_{t\sigma,t'\sigma'}^2 (3\omega_t + \omega_{t'})/(\omega_t^2 - \omega_{t'}^2)$ where γ_t is the usual correction term of the effective reciprocal of inertia.

THE vibration-rotation term value of a symmetric molecule when evaluated by the usual perturbation methods of the quantum mechanics, may, if the centrifugal distortion terms are omitted, be written:

$$(E/hc) = (E_v/hc) + J(J+1)B_v - K^2(B_v - C_v) \mp 2\sum_t \zeta_t l_t K C_e, \quad (1)$$

where (E_v/hc) is the vibration term value of the molecule, $B_v = B_e - \sum_s (v_s + g_s/2)\alpha_s$, $C_v = C_e - \sum_s (v_s + g_s/2)\gamma_s$, B_e and C_e being the reciprocals of inertia $(h/8\pi^2 I_{xx}^{(e)} c)$ and $(h/8\pi^2 I_{zz}^{(e)} c)$, respectively. In the foregoing α_s and γ_s are constants, $I_{xx}^{(e)}$ and $I_{zz}^{(e)}$ the equilibrium values of the principal moments of inertia, and g_s a constant which takes the value of the degeneracy of the vibration frequency ω_s. In (1) ζ_t is the Coriolis coupling factor and l_t is a quantum number of internal angular momentum associated with a two-fold degenerate frequency ω_t. l_t may take the values $v_t, v_t - 1, \cdots, 0$ or 1 where v_t is the total vibration quantum number associated with the vibration frequency ω_t.

It has been suggested by Herzberg[1] that it is reasonable to suppose that the last term in Eq. (1) should be replaced by $2\sum_t \zeta_t l_t K C_v$. It may be shown that the selection rules for the quantum numbers K and l are $\Delta K = \Delta l = \pm 1$. By use of the term value (1) this transition rule leads to the following approximate spacing between two Q branches in a fundamental perpendicular band

$$\Delta\nu = 2[C_v - \zeta_t C_e - B_v], \quad (2)$$

while if the modified form suggested by Herzberg is adopted, the value obtained for $\Delta\nu$ will be seen to be

$$\Delta\nu = 2[C_v(1 - \zeta_t) - B_v]. \quad (3)$$

While the difference between (1) and the modified form suggested by Herzberg, i.e., $2\sum_t \zeta_t l_t K \times (C_v - C_e)$, is of an order of importance smaller than the second in the energy, the difference between (2) and (3) is sufficiently large in many cases to be observed spectroscopically. It is therefore of importance to investigate further what the last term in (1) should be, i.e., whether it should be $\sum_t \zeta_t l_t K C_e$ or $\sum_t \zeta_t l_t K C_v$ or whether it should be some value different from either of these.

Since the difference between (1) and the modification suggested by Herzberg is smaller than second order of approximation, it is necessary to resort to a third-order perturbation calculation. The results for a third-order correction to the energy may be obtained by reference to Born and Jordan[2] or it may quite readily be derived by the usual methods. One quickly verifies that the second- and third-order corrections to the energy are the following

$$E_2 = (v_s, J, K|H_2|v_s, J, K) + \sum_{v_s}' \sum_{K'} \frac{(v_s, J, K|H_1|v_s', J, K')(v_s', J, K'|H_1|v_s, J, K)}{E_{v_s}^0 - E_{v_s}^0}, \quad (4a)$$

[1] G. Herzberg, *Infrared and Raman Spectra* (D. Van Nostrand Company, Inc., New York, 1945), p. 403.
[2] M. Born and P. Jordan, *Elementare Quantenmechanik* (Verlagsbuchhandlung, Julius Springer, Berlin, 1930), p. 197.

$$E_2=(v_s, J, K|H_2|v_s, J, K)+\sum_{v_s'}{}' \sum_{K'} \frac{(v_s, J, K|H_1|v_s', J, K')(v_s', J, K'|H_2|v_s, J, K)}{E_{v_s}{}^0-E_{v_s}{}^0}$$

$$+\sum_{v_s'}{}' \sum_{K'} \frac{(v_s, J, K|H_2|v_s', J, K')(v_s', J, K'|H_1|v_s, J, K)}{E_{v_s}{}^0-E_{v_s}{}^0}$$

$$+\sum_{v_s'}{}' \sum_{K'} \sum_{v_s''}{}' \sum_{K''} \frac{(v_s, J, K|H_1|v_s', J, K')(v_s', J, K'|H_1|v_s'', J, K'')(v_s'', J, K''|H_1|v_s, J, K)}{(E_{v_s}{}^0-E_{v_s}{}^0)(E_{v_s}{}^0-E_{v_s}{}^0)}. \quad (4b)$$

The quantum-mechanical Hamiltonian for a polyatomic molecule has been expanded by Nielsen,[3] but only certain of the terms are of interest here. The terms of importance here are the following:

$$H_0=\cdots(P_z{}^2/2I_{zz}{}^{(e)})+\cdots, \quad (5a)$$

$$H_1=\cdots -ih\sum_t \zeta_t\partial/\partial\chi_t(P_z/I_{zz}{}^{(e)})+\cdots\sum_{ts}\sum_{t's'}{}' \zeta_{tt'}\left[\left(\frac{\omega_{t'}}{\omega_t}\right)^{\frac{1}{2}} q_{ts}p_{t's'}-\left(\frac{\omega_{t'}}{\omega_t}\right)^{\frac{1}{2}} q_{t's'}p_{ts}\right](P_z/I_{zz}{}^{(e)})+\cdots$$

$$-\tfrac{1}{2}\sum_{s''s'''}(h^2/4\pi^2c^2\omega_{s''}{}^2)^{\frac{1}{2}}(c_{s''s'''}/(I_{zz}{}^{(e)})^2)q_{s''s'''}P_z{}^2\cdots+hc\sum_{ts}\sum_{s's''} k_{s''ts}q_{s's''}q_{ts}{}^2+\cdots, \quad (5b)$$

$$H_2=\cdots\sum_{s''s'''}(h^2/4\pi^2c^2\omega_{s''}{}^2)^{\frac{1}{2}}(c_{s''s'''}/(I_{zz}{}^{(e)})^2)q_{s''s'''}(-ih\sum_t \zeta_t\partial/\partial\chi_t)P_z+\cdots$$

$$-\sum_{s''s'''}(h^2/4\pi^2c^2\omega_{s''}{}^2)^{\frac{1}{2}}(c_{s''s'''}/(I_{zz}{}^{(e)})^2)q_{s''s'''}\sum_{ts}\sum_{t's'}{}' \zeta_{tt'}\left[\left(\frac{\omega_{t'}}{\omega_t}\right)^{\frac{1}{2}} q_{ts}p_{t's'}-\left(\frac{\omega_t}{\omega_{t'}}\right)^{\frac{1}{2}} q_{t's'}p_{ts}\right]P_z+\cdots$$

$$-\tfrac{1}{2}\sum_{ts}[(\hbar/2\pi c\omega_t)][C'_{tsts}-(f_{ts}{}^2/I_{zz}{}^{(e)})-(e_{ts}{}^2/I_{yy}{}^{(e)})-(c_{ts}{}^2/I_{zz}{}^{(e)})]q_{ts}{}^2(P_z/I_{zz}{}^{(e)})^2+\cdots, \quad (5c)$$

$$H_3=\cdots\tfrac{1}{2}\sum_{ts}[(\hbar/2\pi c\omega_t)][C'_{tsts}-(f_{ts}{}^2/I_{zz}{}^{(e)})-(e_{ts}{}^2/I_{yy}{}^{(e)})-(c_{ts}{}^2/I_{zz}{}^{(e)})]q_{ts}{}^2$$

$$\times(-ih\sum_t \zeta_t\partial/\partial\chi_t)(P_z/(I_{zz}{}^{(e)})^2)+\cdots. \quad (5d)$$

In the relations (5) P_z is the operator corresponding to the component of angular momentum directed along the body fixed z, $-ih\sum_t \zeta_t\partial/\partial\chi_t$ is the internal angular momentum operator (also directed along z) associated with a twofold degenerate frequency ω_s, and C'_{ssss}, f_{ss}, e_{ss}, and c_{ss} are constants. For a more detailed definition of these the reader is referred to reference 3.

The elements of (5a) are diagonal in all the quantum numbers and these are simply:

$$(K, l_t|H_0|K, l_t)=\cdots-K^2C_e+\cdots. \quad (6)$$

The first term in (5b) is also diagonal in all the quantum numbers and the elements are the following:

$$(K, l_t|H_1|K, l_t)=\mp 2\sum_t \zeta_t l_t K C_e. \quad (7)$$

In evaluating E_2 the diagonal elements of the second term in (5c), the $(v_{ts}, v_{t's'}|v_{ts}\pm 1, v_{t's'}\pm 1)$ elements of the second term in (5b) multiplied into the $(v_{ts}\pm 1, v_{t's'}\pm 1|v_{ts}, v_{t's'})$ elements of the same term and the $(v_{s''}|v_{s''}\pm 1)$ elements of the third term of (5b) multiplied into the $(v_{s''}\pm 1|v_{s''})$ elements of the fourth term are involved and correction terms are obtained with the aid of (4a) which are proportional to K^2. When added to (6) one obtains:[4]

$$\cdots K^2[C_e-\textstyle\sum_t (v_t+1)\gamma_t], \quad (8)$$

where $\gamma_t=\sum_s z_{ts}$ in which

$$z_{ts'}=(Ce^{\frac{1}{2}}/\omega_t)\{C_e{}^{\frac{1}{2}}[C'_{tsts}-(f_{ts}{}^2/I_{zz}{}^{(e)})-(e_{ts}{}^2/I_{yy}{}^{(e)})-(c_{ts}{}^2/I_{zz}{}^{(e)})$$

$$-\sum_{t's'}{}' \zeta_{tt'}{}^2(3\omega_t{}^2+\omega_{t'}{}^2)/(\omega_t{}^2-\omega_{t'}{}^2)]-\sum_{s''s'''}[k_{tts''}(c_{s''s'''}{}^2/I_{zz}{}^{(e)}\omega_{s''})^{\frac{1}{2}}(\omega_t/\omega_{s''})]\}. \quad (9)$$

[3] H. H. Nielsen, Phys. Rev. 60, 794 (1941).

[4] The relation (8) will also contain terms $\sum_s (v_s+\frac{1}{2})\gamma_s$, but with these we are not here concerned so they will be omitted for simplicity.

One comes then to the calculation of the third-order correction. It is quickly verified that only the first and second terms of (4b) yield anything of interest in the evaluation of E_3 for this problem. Inspection of (5c) and (5d) reveals that the coefficients multiplying

$$(-ih\sum_t \partial/\partial\chi_t)P_z$$

and

$$\sum_{t\sigma}\sum_{t'\sigma'}\zeta_{tt'}\left[\left(\frac{\omega_{t'}}{\omega t}\right)^{\frac{1}{2}}q_{t\sigma}p_{t'\sigma'}-\left(\frac{\omega_t}{\omega_{t'}}\right)^{\frac{1}{2}}q_{t'\sigma'}p_{t\sigma}\right]P_z$$

are the same, respectively, as those multiplying P_z^2 in (5b) and (5c). Evaluating the first term in (4b) is, therefore, entirely similar to evaluating the first term in (4a), the $(v_t|v_t)$ elements of (5d) being the same as the $(v_t|v_t)$ elements of the second term in (5c). Evaluating the second term in (4b) is also entirely like evaluating the second term in (4a), the $(v_{s''}|v_{s''}\pm1)$ elements of (5c) multiplied into the $(v_{s''}\pm1|v_{s''})$ elements of the third term of (5b) being the same as the $(v_{s''}|v_{s''}\pm1)$ elements of the second term of (5b) multiplied into the third term of (5b). There are, however, no correction terms here which are proportional to $\sum_t\zeta_t l_t K$ corresponding to the second kind of terms encountered in the former calculation which were proportional to K^2, i.e., there are no terms in E_3 multiplying $\sum_t\zeta_t l_t K$ proportional to the product of the $(v_{t\sigma}, v_{t'\sigma'}|v_{t\sigma}\pm1, v_{t'\sigma'}\pm1)$ elements of the second term in (5b) multiplied into the $(v_{t\sigma}\pm1,\ v_{t'\sigma'}\pm1|v_{t\sigma},\ v_{t'\sigma'})$ elements of the same term which correspond to those which occur in E_2 as coefficients of K^2. These terms are those which give rise in γ_t to the quantities containing the denominators $(\omega_t^2-\omega_{t'}^2)$. The last term in (1) is different from zero only for the values of $s=t$ which correspond to twofold degenerate frequencies where σ takes the values $\sigma=1$ and $\sigma=2$. In such cases the coefficient of $2\sum_t\zeta_t l_t K$, which we shall call c_v, in E is, therefore, the same as that multiplying K^2 except that the components containing $(\omega_t^2-\omega_{t'}^2)$ in the denominator are absent, i.e.,

$$c_v=C_e-\sum_t(v_t+1)\Gamma_t, \tag{10}$$

where

$$\Gamma_t=\gamma_t+\sum_{t'\sigma'}\zeta^2_{t,\sigma;t',\sigma'}(3\omega_t+\omega_{t'})/(\omega_t^2-\omega_{t'}^2).$$

It becomes evident therefore that the correct value of the spacing between two Q branches in a fundamental band is given by a relation of the form (2) where C_e is replaced by c_v rather than by (3). Whether c_v is more closely approximated by C_e or by C_v is difficult to predict; certainly in some cases the terms containing the resonance denominators represent the most important contributions to γ.

Similarly for spherically symmetric molecules, it has been suggested by Dennison[5] that the rotational energy for the first excited state including the Coriolis contribution should be written:

$$E=J(J+1)B'+\epsilon, \tag{11}$$

where ϵ takes the values $2B'\zeta_i(J+1)$, 0 and $-2B'\zeta_i J$, B' being the B value for the excited state, instead of $2B_e\zeta_i(J+1)$, 0 and $-2B_e\zeta_i$J. It has been shown by Shaffer, Nielsen, and Thomas[6] that the rotational energy for a semi-rigid rotator can only approximately be represented by $J(J+1)B_v$. To the extent, however, that it is legitimate to represent the energy of the semi-rigid spherical rotator in this form one may infer also that the coefficient in ϵ should be b' rather than B_e or B' where b' is equal to B' except that the terms containing resonance denominators will be absent.

---

[5] D. M. Dennison, Rev. Mod. Phys. **12**, 209 (1940).
[6] W. H. Shaffer, H. H. Nielsen, and L. H. Thomas, Phys. Rev. **56**, 895 (1939).

Influence of Space Charge on the Bunching of Electron Beams

L. BRILLOUIN
Cruft Laboratory, Harvard University, Cambridge, Massachusetts

(Received April 3, 1946)

A rigorous computation of electron trajectories within plane structures may be made, with the inclusion of space-charge effects, by use of the Llewellyn method of integration. These computations can be used for a discussion of conditions leading to intercrossing trajectories, i.e., bunching. The discussion has been carried out for a conventional plane diode, for a diode wherein electrons are injected with a given initial velocity, for a velocity-modulated beam, for a plane magnetron, and for a plane magnetron with velocity modulation. In the last case it can be proved that trajectories intercross not once but many times thus disentangling themselves after a while, then crossing again and soon.

1. INTRODUCTION AND DISCUSSION OF LLEWELLYN'S METHOD

IN a number of problems of electron tubes, the same question is encountered over and over again: Do electron trajectories cross each other or not? When trajectories do not intercross, the motion retains the "single stream" character, where at each point in space only one velocity vector is found for the moving electrons. Intercrossing of trajectories means "bunching," and a change to "double stream" motion, where two different electron velocities are obtained at some points in space.

The method followed in the present paper is to start from a single stream motion for electrons leaving the cathode, and to use the Llewellyn method of integration, that works all right in that case. One may thus follow the trajectories until some of them intercross and the method ceases to apply and he obtains the rigorous conditions for the first bunching.

We start with a short survey of Llewellyn's method, and assume a plane structure, where all quantities (field, space charge) depend only upon x and t but not upon y or z. We define the total current density (electronic plus displacement) that has an I_x component and in some instances (magnetron problem) an I_y component too. Maxwell's equations tell us that

$$\text{div } I = \partial I_x/\partial x = 0, \qquad I_x(t) \quad (1)$$

hence I_x is a function of t only, but not of x.

$$I_x(t) = -\rho\dot{x} - \epsilon_0(\partial E/\partial t)_x. \quad (2)$$

The sign is such as to yield a positive current when electrons ($\rho<0$) move from the cathode ($x=0$) to the anode ($x=a$). We then write Poisson's relation

$$\epsilon_0(\partial E/\partial x)_t = \rho \quad (3)$$

and compute the rate of change of the field E when we follow the motion of a certain electron

$$\frac{dE}{dt} = \left(\frac{\partial E}{\partial t}\right)_x + \dot{x}\left(\frac{\partial E}{\partial x}\right)_t = -\frac{I_x}{\epsilon_0}, \quad (4)$$

according to Eqs. (2) and (3). This is where the "single stream" assumption is introduced implicitly. In a double stream motion, the space charge density ρ would split into two parts, ρ_1 moving with $\dot{x}_1$ and ρ_2 moving with $\dot{x}_2$; and Eq. (2) should consequently be modified, hence (4) could not hold any more. Let $E_0(t)$ be the field on the cathode. An electron leaving the cathode at t_0 reaches a certain distance $x(t_0, t)$ at time t and the electric field acting upon it at t is

$$E(t_0, t) = E_0(t_0) + \int_{t_0}^{t} \frac{dE}{dt}dt = E_0(t_0) - \frac{1}{\epsilon_0}\int_{t_0}^{t} I_x(t)dt; \quad (5)$$

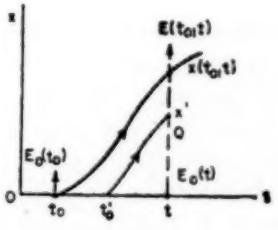

FIG. 1.

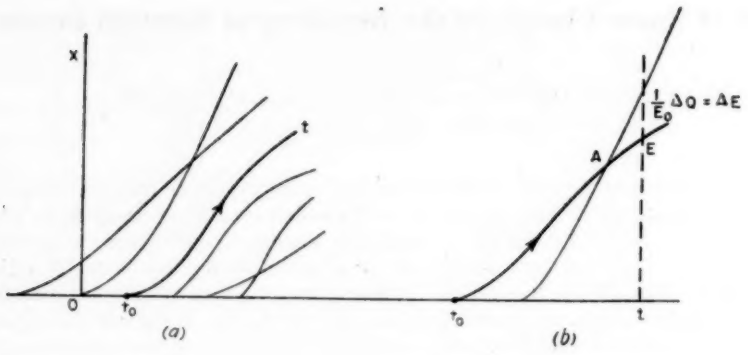

FIG. 2.

a direct integration of (4) is possible on account of (1). The physical content of this formula is explained in Fig. 1. At time t we have a total charge (per square area) Q in the space charge, between cathode ($x=0$) and point x, accordingly

$$\epsilon_0[E(t_0, t)-E_0(t)]=Q. \qquad (6a)$$

Next we note that, between t_0 and t, there has been an increase q of the surface charge density on the cathode

$$\epsilon_0[E_0(t)-E_0(t_0)]=q \qquad (6b)$$

and

$$q+Q=-\int_{t_0}^{t} I_x(t)dt. \qquad (7)$$

Combining (6) and (7), we obtain (5). This physical picture enables one to discuss the *limits of validity* of Eq. (5). Figure 2(a) visualizes a case where the trajectory under consideration does not cross any other one, but some intercrossings take place along other trajectories. This does not change the charges Q or q of Eq. (6), hence formula (5) holds without any trouble. The situation is different for the case of Fig. 2(b), since the intercrossing brings a charge ΔQ in front of our trajectory, hence decreasing the field $E(t_0, t)$ by an amount $(1/\epsilon_0)\Delta Q$

$$E(t_0, t)=E_0(t_0)-\frac{1}{\epsilon_0}\int_{t_0}^{t} I(t)dt-\frac{1}{\epsilon_0}\Delta Q. \qquad (8)$$

In many problems we shall be able to compute or at least to evaluate approximately the amount of charge ΔQ brought by the intercrossing trajectories, hence the field correction, and we will discuss the corresponding change in the shape of the trajectories beyond the crossing point.

Our discussion is based on some general assumptions that shall be stated now.

A. Electron trajectories should not intercross prior to the instant of time when we investigate the motion. For instance, there must be no back-bombardment of the cathode and the motion of electrons leaving the cathode must retain the single stream character.

B. The *flow of electrons from the cathode is uninterrupted.* A few examples of interrupted electronic currents have been previously discussed[1] and they all lead to motions where electron trajectories intersect near the cathode (see Fig. 3). If the current is negative during a time interval t_1t_2, electrons fall back upon the cathode, but there remains always a good many "old" electrons in the space charge at the time when a new emission starts, and a certain amount of overlapping of electron beams seems inevitable. We thus assume that the *electronic part* of the *current on the cathode never becomes negative.*

2. PLANE DIODE WITH SPACE CHARGE

The method discussed in the first section yields, at any time t, the field $E(t_0, t)$ acting upon an electron emitted at t_0, hence the equation of motion

$$\ddot{x}=(e/m)E(t_0, t). \qquad e<0 \quad (9)$$

To specify our problem we assume the following

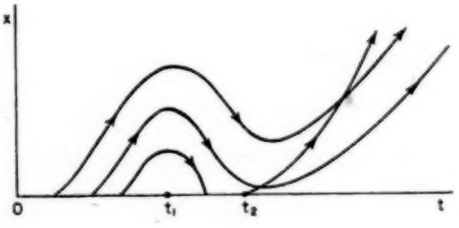

FIG. 3.

[1] L. Brillouin, El. Comm. **22**, No. 1, 110; No. 2, 212.

quantities to be *given:*

$$\begin{cases} \text{I—total current density } I(t) \text{ through the tube,} \\ \text{II—initial electron velocity } v_0(t) \text{ on the cathode } x=0, \\ \text{III—initial electric field } E_0(t) \text{ on the cathode.} \end{cases} \tag{10}$$

The first two assumptions actually correspond to physical data and to measurements made on the tube. The *third* assumption refers to the initial electric field that is *definitely not a measurable quantity.* What we actually measure is the anode voltage, but it is not directly connected with the electric field on the cathode, and we shall find examples of uncertainty, where one given anode voltage may correspond to two (or more) distinct initial fields E_0 according to the type of space-charge distribution obtained inside the tube. We must keep this difficulty in mind for practical applications of the theory.

We now define, according to Eq. (5),

$$\begin{cases} F_0(t) = -\dfrac{e}{m\epsilon_0}\displaystyle\int_0^t I(t)dt, \\ F_1(t) = \displaystyle\int_0^t F_0(t)dt, \\ F_2(t) = \displaystyle\int_0^t F_1(t)dt, \end{cases} \tag{11}$$

$$\frac{e}{m}E(t_0, t) = \frac{e}{m}E_0(t_0) + F_0(t) - F_0(t_0).$$

Integration of (9) using (11) and initial conditions II, III, yield

$$\dot{x}(t_0, t) = F_1(t) - F_1(t_0) + v_0(t_0) + \left[\frac{e}{m}E_0(t_0) - F_0(t_0)\right]\tau,$$

$$x(t_0, t) = F_2(t) - F_2(t_0) + (v_0(t_0) - F_1(t_0))\tau + \left[\frac{e}{m}E_0(t_0) - F_0(t_0)\right]\frac{\tau^2}{2}, \tag{12}$$

$t - t_0 = \tau$ transit time.

The electronic part of the current on the cathode never becoming negative, there is an uninterrupted flow of electrons from the cathode. Electron trajectories will not intercross if electrons emitted at a certain time t_0 never catch up with electrons emitted at $t_0 - dt_0$, a short time before, that is to say if

$$(\partial x/\partial t_0)_{t=\text{const}} < 0. \tag{13}$$

Bunching is obtained when this derivative becomes zero and intercrossing of trajectories when it is positive. Hence we compute

$$\left(\frac{\partial x}{\partial t_0}\right)_t = -\frac{\partial F_2(t_0)}{\partial t_0} - v_0(t_0) + F_1(t_0) + \left(\frac{\partial v_0}{\partial t_0} - \frac{\partial F_1}{\partial t_0} - \frac{e}{m}E_0(t_0) + F_0(t_0)\right)\tau + \left[\frac{e}{m}\frac{\partial E_0}{\partial t_0} - \frac{\partial F_0}{\partial t_0}\right]\frac{\tau^2}{2}.$$

According to (11) terms in $-\partial F_2/\partial t_0$ and $F_1(t_0)$ cancel each other, and so do $\partial F_1/\partial t_0 - F_0(t_0)$ hence

$$\left(\frac{\partial x}{\partial t_0}\right)_t = -v_0(t_0) + \left(\frac{\partial v_0}{\partial t_0} - \frac{e}{m}E_0(t_0)\right)\tau + \frac{ei(t_0)}{2m\epsilon_0}\tau^2, \tag{14}$$

where $i(t_0)$ is the *electronic part* of *the current* on the *cathode* at t_0 [Eq. (2), (11)]

$$i(t_0) = I(t_0) + \epsilon_0\frac{\partial E_0}{\partial t_0} = \epsilon_0\left(-\frac{m}{e}\frac{\partial F_0}{\partial t_0} + \frac{\partial E_0}{\partial t_0}\right). \tag{15}$$

Equations (13) and (14) summarize the whole problem.

In a conventional *diode with hot cathode* electrons are practically emitted with zero velocity and we distinguish between two cases

$$\begin{cases} v_0 = 0, \quad E_0 = 0, \\ \qquad\qquad \text{space charge limited current,} \\ v_0 = 0, \quad E_0 < 0, \quad eE_0 > 0, \\ \qquad\qquad \text{saturation current.} \end{cases} \tag{16}$$

The electronic current $i(t_0)$ on the cathode is always positive (assumption *B*, end of Section 1) hence condition (13) is always satisfied. Electron trajectories travel farther and farther apart when transit time increases.

A similar result holds for a diode wherein electrons are injected with a constant velocity,

$v_0>0$ provided we can be certain that $E_0\leqslant 0-$. This is not a simple question to answer, since E_0 is not directly measurable, as noted at the beginning of this section.

The limiting case of *negligible space charge* is obtained by taking

$$\rho\to 0, \quad i(t)\to 0. \tag{17}$$

All the preceding formulae remain valid, with the following simplification

$$\begin{aligned} I&=-\epsilon_0\frac{\partial E}{\partial t} && \text{in (2)},\\ Q&=0 && \text{in (6a)},\\ F_0(t)&=(e/m)E(t) && \text{in (11)}. \end{aligned} \tag{18}$$

Up to this point, computations are not too difficult because all formulae remain linear in character. The situation changes when one wishes to compute the *voltage*.

$$V(t)=-\int_{x'=0}^{x'=x} E\,dx' = -\int_{t_0'=t}^{t_0'=t_0} E(t_0',t)\left(\frac{dx'}{dt_0'}\right)_t dt_0'. \tag{19}$$

Notations are explained on Fig. 1. This formula is no more linear and contains again our partial derivative (14), which is seen to play an important role in all practical applications of the theory.

The connection between this same derivative and space-charge density ρ at the point $x(t_0, t)$ is obvious

$$\rho dx=i(t_0)dt_0, \quad \text{hence} \quad \rho=\frac{i(t_0)}{(dx/dt_0)_t}. \tag{20}$$

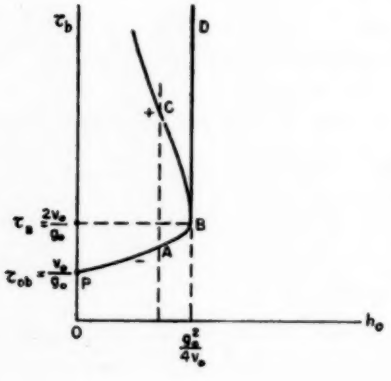

FIG. 4.

The beginning of bunching corresponds to $(dx/dt_0)_t=0$ and ρ infinite.

It should be emphasized that the preceding formulae are strictly rigorous and that the law of variation of current, velocity, and initial field are completely arbitrary, the only restrictions being contained in assumptions A, B of Section 1. It is a very favorable situation that all factors in Eq. (14) have a clear physical meaning, while quantities entering (12) have not.

3. DIODE WITH INITIAL VELOCITY

When the initial velocity of electrons emitted at $x=0$ is not zero, we have to use the complete formula (14)

$$(\partial x/\partial t_0)_t=-v_0+g_0\tau-h_0\tau^2, \tag{21a}$$

$$\left.\begin{aligned} &v_0(t_0)>0 \text{ initial velocity at emission time } t_0,\\ &\tau=t-t_0, \text{ transit time},\\ &g_0=\frac{\partial v_0}{\partial t_0}-\frac{e}{m}E_0(t_0) \quad E_0(t_0) \text{ initial field},\\ &h_0=-\frac{e}{2m\epsilon_0}i(t_0)>0, \quad i(t_0) \text{ electric current at emission}. \end{aligned}\right\} \tag{21b}$$

According to (13) the question to be investigated is whether (21a) remains negative or not. For $g_0<0$ there is no problem, so we must discuss the case $g_0>0$. If space-charge effects can be neglected ($h_0\to 0$), the critical condition corresponds to

$$\tau_{0b}=\frac{v_0}{g_0}, \quad h_0=0, \tag{22}$$

and bunching starts at this transit time τ_{0b}. This represents the bunching condition for a given field and velocity modulation $v_0(t_0)$ at very small electronic current. When the current is increased, bunching occurs when (21a) is zero.

$$\tau_b=\frac{g_0}{2h_0}\pm\left[\left(\frac{g_0}{2h_0}\right)^2-\frac{v_0}{h_0}\right]^{\frac{1}{2}}. \tag{23}$$

There are two roots, one of which (+) becomes infinite when $h_0\to 0$, while the other sign (−) yields the value (22) for $h_0\to 0$. The whole situation is explained on Fig. 4. Bunching becomes impossible when

$$h_0>h_{0b}=g_0^2/4v_0 \tag{24}$$

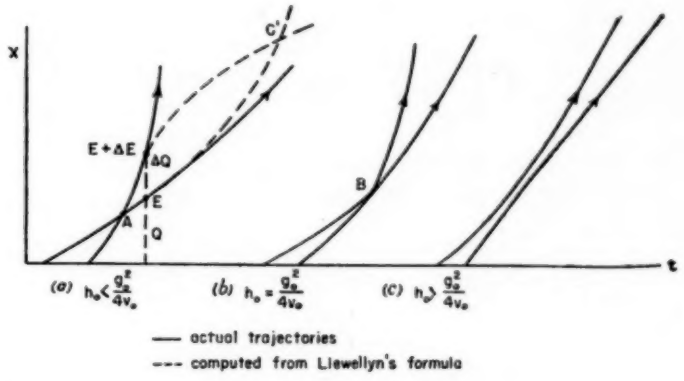

FIG. 5.

and for higher currents, electron trajectories do not intersect any more. The critical value h_{0b} corresponds to $\tau_b = 2\tau_{0b} = 2(v_0/g_0)$. As stated in Section 1, our computation of trajectories rests upon Llewellyn's formula, that in turn supposes single stream motion. Let us now discuss the type of trajectories obtained and how they will be perturbed in the case of intercrossing (Fig. 5).

For small currents ($h_0 < h_{0b}$) the Llewellyn trajectories intersect twice, at points A and C, but the second solution is spurious, as can be proved directly, by looking at Fig. 2b. Let us call E the field acting, at time t on the lower trajectory, the field on the upper trajectory is $E+\Delta E$ with

$$\epsilon_0 \Delta E = \Delta Q. \tag{25}$$

Now, E, Q, ΔE, ΔQ, are all negative, hence

$$|E+\Delta E| > |E|.$$

Furthermore, the upper trajectory corresponds to a larger velocity. Hence the corresponding electron leaves point A with a higher velocity and is acted upon by a stronger field, so it will fly away faster and the electron on the lower trajectory shall never catch up.

When $h_0 \geqslant h_{0b}$, the single stream character remains unperturbed and Llewellyn's trajectories are correct. High space charge provides too strong a repulsion between trajectories that do not intersect any more. We thus have to correct our graph of Fig. 4. The whole (+) branch $B\,C$ is meaningless. Instead, we draw a vertical line $B\,D$ and we conclude that our single stream solution is correct below the curve $PAB\,D$ (and to the right of it). Bunching occurs along PAB, double stream is the rule above $PAB\,D$ (and to the left of it).[2]

Let us take a special example, assuming the electric field E_0 on the first electrode to be zero, and the *velocity modulation* to be sinusoidal.

$$\begin{aligned} v_0 &= u_0(1+b\cos\omega t), \quad 0 \leqslant b \leqslant 1 \\ g_0 &= \partial v_0/\partial t = -u_0 b\omega \sin\omega t. \end{aligned} \tag{26}$$

The critical condition for bunching (24) reads

$$h_{0b} = \frac{(-e)i}{2m\epsilon_0} = \frac{1}{4v_0}\left(\frac{\partial v_0}{\partial t}\right)^2 = \tfrac{1}{4}u_0 b^2\omega^2, \tag{27}$$

since most favorable bunching conditions correspond to

$$\omega t = \pi/2, \quad \sin\omega t = 1, \quad \cos\omega t = 0.$$

Equation (27) yields the maximum current for which bunching may be obtained, and on this limit, bunching occurs after a transit time twice as large as the one found for very small current (Fig. 4).

Another example is found in the case of constant initial velocity v_0, constant injected electronic current i_0, *starting at* $t=0$, and a given field E_0 on the first electrode. It should be noted that in order to maintain a constant field, E_0, it will be necessary to vary the anode voltage in course of time. If the anode voltage is maintained constant, the motion of the space charge will progressively change the initial field E_0. Here we have

$$g_0 = -eE_0/m, \tag{28}$$

and according to (23) no bunching nor inter-

[2] Similar problems have been discussed very carefully by E. Feenberg (Sperry).

crossing ever occurs when

$$g_0^2 > 4v_0 h_0, \quad E_0 < E_{0L} = +\left(\frac{2m}{|e|\epsilon_0} v_0 i\right)^{\frac{1}{2}}. \quad (29)$$

For positive fields above this limit (retarding fields) bunching occurs and we obtain the same transit time values as on Fig. 4.

$$\left.\begin{aligned} E_0 &= \left(\frac{2m}{|e|\epsilon_0} v_0 i\right)^{\frac{1}{2}}, & \tau_B &= 2v_0/g_0, \\ E_0 &\to +\infty, & \tau_{0b} &\to v_0/g_0. \end{aligned}\right\} (30)$$

Intercrossing trajectories appear in this problem just at the moment when the first electrons are stopped, since we have (Eqs. (11), (12))

$$I = i = \begin{cases} 0 & t<0 \\ i_0, & t>0, \end{cases}$$

$$F_0 = -ei_0 t/m\epsilon_0, \quad F_1 = -ei_0 t^2/2m\epsilon_0, \quad (31)$$

$$\dot{x} = -ei_0 t^2/2m\epsilon_0 + v_0 + eE_0 t/m = -(\partial x/\partial t_0)_t, \qquad t_0 = 0.$$

The motion retains the single stream character only for the short time interval 0, τ_b and changes afterward into double stream (Fig. 6).

The theory of space-charge effects between parallel plane electrodes has been very completely discussed by Fay, Samuel, and Shockley.[3] They only consider the static case, when a constant flow of electrons is injected through the first electrode with a given constant velocity v_0, as is the case when this first electrode is a grid with a very fine mesh, at a positive potential $V_1 = -m/2ev_0^2$, in a tube with a hot cathode at potential zero. On Fig. 7, C is the hot cathode working under space-charge limited current conditions. ($x=-1$). The fine grid is at $x=0$ and the different curves represent potential distributions

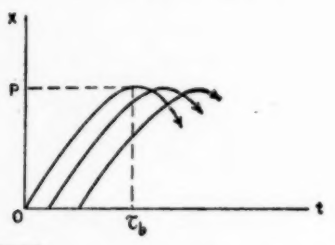

FIG. 6.

[3] C. E. Fay, A. L. Samuel, and W. Shockley, Bell Sys. Tech. J. **17**, 49 (1938); G. Jaffe, Phys. Rev. **65**, 91 (1944).

beyond the grid. The slope of the curves at point A is $-E_0$. Our single stream solution works for all cases (29) when $-E_0 > -E_{0L}$, that is for all curves above the heavy curve A – V.C. The point V.C. represents a virtual cathode. For other curves like OP, the single stream solution works only at the very beginning of the operation. When the first electrons reach point P, their velocity is zero, and electron trajectories start intercrossing each other (Eq. (31), Fig. 6). After a transitory stage, and a rearrangement of trajectories, a stable double stream motion is established, and has been completely discussed by Fay, Samuel, and Shockley. One may also notice on Fig. 7 that some potential curves intercross (point Q, for instance), a very curious feature that proves that a given anode voltage may correspond to two different initial E_0 fields. This is the sort of difficulty that was explained at the beginning of Section 2. For a complete discussion, see again, Fay, Samuel, and Shockley.

4. PLANE MAGNETRON—GENERAL THEORY

The same general method can be applied to the problem of a single anode plane magnetron. The structure is similar to that of the diode, with a plane cathode at $x=0$, plane anode $x=a$, but a magnetic field H is acting along the z axis. The trajectories are no more straight lines parallel to the x axis, but curves in the xy plane, owing to the Lorentz force $\mu_0 e[v \times H]$. The discussion of Section 1 remains unchanged, but the equation of motion (q) is replaced by

$$\begin{aligned} \ddot{x} &= -2\omega_H \dot{y} + (e/m)E(t_0, t), \\ \ddot{y} &= 2\omega_H \dot{x}, \\ \omega_H &= \tfrac{1}{2}\mu_0(-e)H/m, \\ &\quad \text{Larmor's angular velocity.} \end{aligned} \quad (32)$$

Electrons are supposed to leave the plane $x=0$ with a normal initial velocity

$$\dot{x}(t_0) = v_0(t_0), \quad \dot{y}(t_0) = 0. \quad (33)$$

Usual cathodes yield $v_0 = 0$, but we want to include in the discussion the case of an initial velocity $v_0(t_0)$. The second equation (32) is readily integrated

$$\dot{y} = 2\omega_H x;$$

hence,

$$\ddot{x} + 4\omega_H^2 x = (e/m)E(t_0, t). \quad (34)$$

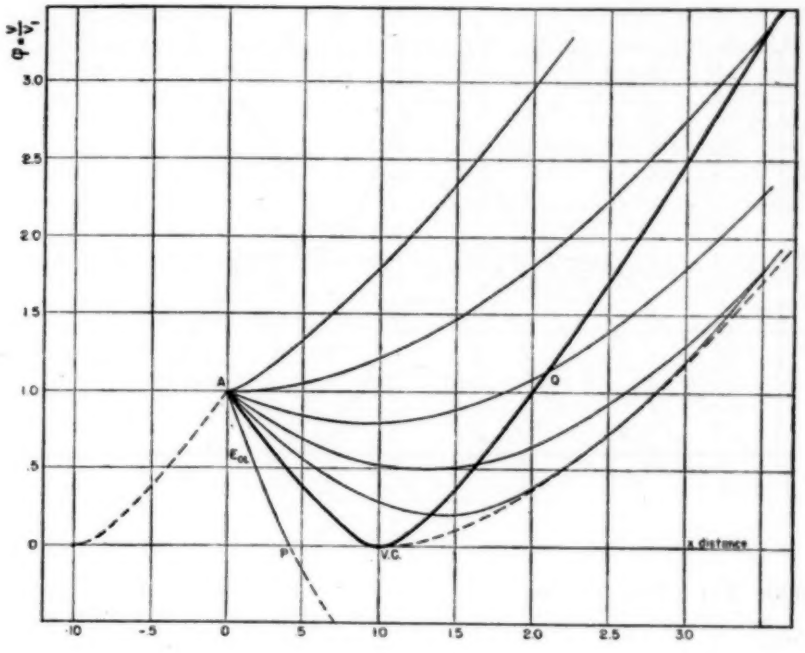

FIG. 7.

This is our fundamental equation, and it applies to any circumstance, whether the motion has the single or double stream character. We shall discuss it in connection with the same general condition (10), (11) assumed in Section 2, that correspond to a single stream motion near the cathode.

Equation (34) represents a harmonic oscillator acted upon by an arbitrary force $(e/m)E(t_0, t)$. To carry on the integration we assume that we have been able to find a function $f(t)$ such as

$$f''+4\omega_H^2 f=F_0(t), \tag{35}$$

and we write the general solution of Eq. (34) for an electron emitted at t_0

$$(e/m)E(t_0, t)=(e/m)E_0(t_0)+F_0(t)-F_0(t_0),$$

$$x(t_0, t)=f(t)-\frac{1}{4\omega_H^2}\left[F_0(t_0)-\frac{e}{m}E_0(t_0)\right]+C\cos 2\omega_H\tau+S\sin 2\omega_H\tau,$$

$$\tau=t-t_0, \quad \text{transit time.} \tag{36}$$

The C, S coefficient must be conveniently chosen in order to satisfy the initial conditions

$$t=t_0, \quad x=0, \quad \dot{x}=v_0;$$

hence,

$$C=-f(t_0)+\frac{1}{4\omega_H^2}\left[F_0(t_0)-\frac{e}{m}E_0(t_0)\right],$$
$$S=\frac{1}{2\omega_H}[v_0(t_0)-\dot{f}(t_0)]. \tag{37}$$

We compute again the derivative (13) and obtain

$$\left(\frac{\partial x}{\partial t_0}\right)_t=-\frac{1}{4\omega_H^2}\left[\frac{\partial F_0}{\partial t_0}-\frac{e}{m}\frac{\partial E_0}{\partial t_0}\right]+\left(\frac{\partial C}{\partial t_0}-2\omega_H S\right)\cos 2\omega_H\tau+\left(\frac{\partial S}{\partial t_0}+2\omega_H C\right)\sin 2\omega_H\tau, \tag{38}$$

where

$$\frac{\partial C}{\partial t_0}-2\omega_H S=\frac{1}{4\omega_H^2}\left(\frac{\partial F_0}{\partial t_0}-\frac{e}{m}\frac{\partial E_0}{\partial t_0}\right)-v_0,$$
$$\frac{\partial S}{\partial t_0}+2\omega_H C=\frac{1}{2\omega_H}\left(\dot{v}_0-\frac{e}{m}E_0(t_0)\right), \tag{39}$$

when (35) is taken into account. We again introduce the electronic part $i(t_0)$ of the current

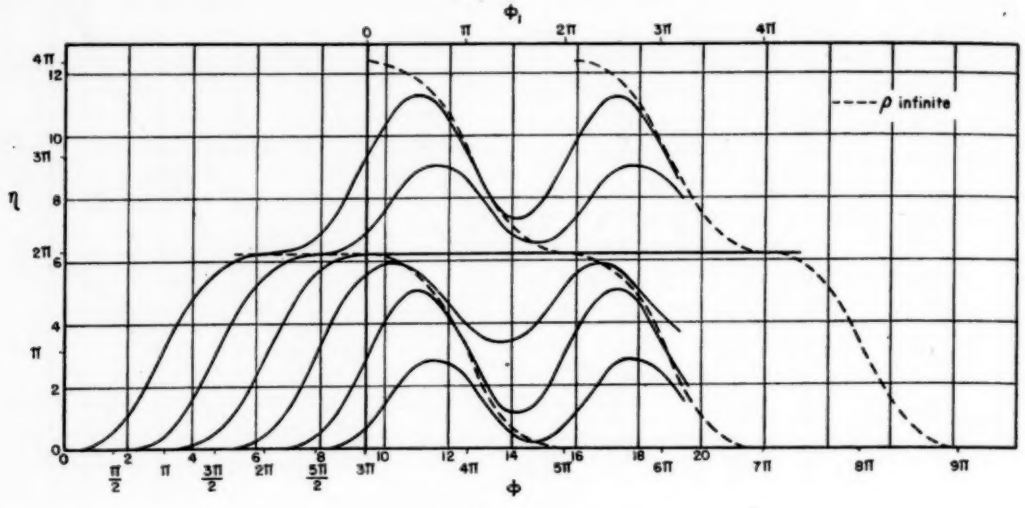

FIG. 8.

on the cathode (Eq. (15)) and find

$$\left(\frac{\partial x}{\partial t_0}\right)_i = \frac{ei(t_0)}{m\epsilon_0 4\omega_H^2}(1-\cos 2\omega_H\tau) + \frac{m\dot{v}_0 - eE_0(t_0)}{m2\omega_H}\sin 2\omega_H\tau - v_0\cos 2\omega_H\tau. \quad (40)$$

Comparing this formula with the previous one (14) for the diode without magnetic field we recognize in both cases the same general features:

All factors have a clear physical meaning.
Equation (14) is obtained on the limit $H\to 0$, $\omega_H\to 0$.
Negligible space charge corresponds to $i\to 0$.

5. SINGLE-ANODE PLANE MAGNETRON, DISCUSSION

In a conventional single-anode plane magnetron, electrons are emitted from the cathode with zero velocity ($v_0=0$) and the last term in (40) drops out. We now have two distinct cases:

I. Space-charge limited current, $E_0=0$.

In this case we are left with the first term only. This term is always negative ($e<0$, $i>0$), and becomes zero when

$$2\omega_H\tau = 2n\pi. \quad (41)$$

This means infinite space-charge density, two electron trajectories just touching each other without intercrossing. The motion always retains the single stream type.

II. Saturation current $E_0<0$, $eE_0>0$.

Expression (40) is negative for small transit time τ, but it will become positive later on, indicating intercrossing trajectories. The first zero of $\partial x/\partial t_0$ occurs between $\pi<2\omega_H\tau<2\pi$, and is just below 2π for small E_0 field. The motion is single stream at the beginning only and turns afterward to double stream.

As an example of case I let us take a rectangular current impulse:

$$i=\begin{cases}0, & t<0,\\ I_0, & 0<t<T,\\ 0, & T<t,\end{cases} \quad (42)$$

and assume space-charge limited current. Our function $F_0(t)$ of Eq. (11) is

$$F_0(t)=\begin{cases}0, & t<0,\\ -eI_0t/m\epsilon_0, & 0<t<T,\\ -eI_0T/m\epsilon_0, & T<t,\end{cases} \quad (43)$$

and we obtain the function $f(t)$ of Eq. (35)

$$f(t)=\begin{cases}0, & t<0,\\ Dt, & 0<t<T,\\ D(T+1/2\omega_H\sin 2\omega_H(t-T)), & T<t,\end{cases} \quad (44)$$
$$D=-(e/m\epsilon_0)(I_0/4\omega_H^2).$$

The sine term in the last formula is needed to insure continuity of f and $\partial f/\partial t$ at $t=T$. We then compute from (36) the trajectories. Electrons are emitted during the time interval

$$0<t_0<T,$$

when current is positive, and electronic emission stops at T, while previously emitted electrons go

on running between cathode and anode.

$$\frac{1}{D}2\omega_H x=\begin{cases}\varphi-\varphi_0-\sin(\varphi-\varphi_0), & 0<t_0<t<T,\\ \Phi-\varphi_0-\sin(\varphi-\varphi_0)+\sin(\varphi-\Phi), & T<t,\end{cases} \quad (45)$$

$$\varphi=2\omega_H t, \quad \varphi_0=2\omega_H t_0, \quad \Phi=2\omega_H T.$$

Figure 8 represents a plot of electron trajectories for the case $\Phi=3\pi$ and shows large undamped oscillation of the border of the space charge. With $\Phi=2\pi$, 4π, $--$, the border of the space charge would remain in a fixed position, but large undamped oscillations would still be observed along the trajectories of electrons inside the space charge. In all cases, the anode voltage, when computed, is found to exhibit oscillations, despite the fact that after T the total current remains identically naught (Eq. (42)). This means that our example corresponds to experimental conditions with an infinite external resistance. In an actual experiment, the anode would be connected to the battery through a large but finite resistance. This would not modify materially the beginning of the discharge, but the oscillations in voltage would draw a small oscillating current from the magnetron, and energy dissipation in the external resistance would progressively damp out the electronic space-charge oscillations. The final result would exhibit no space-charge oscillations, electrons running parallel to cathode and anode.

On the curves of Fig. 8, one recognizes the lines for infinite space charge (dashed lines), according to condition (41)

$$\varphi-\varphi_0=2\omega_H\tau=2n\pi.$$

6. MAGNETRON WITH INITIAL VELOCITY

The problems we want now to discuss are similar to those investigated in Section 3, but for the fact that a transverse magnetic field is added. Let us first rewrite our formula (40) with the same notation as in Eq. (21):

$$\left(\frac{\partial x}{\partial t_0}\right)_t=-v_0\cos\psi+g_0\frac{\sin\psi}{2\omega_H}-h_0\frac{1-\cos\psi}{2\omega_H^2}, \quad (46)$$

$$\psi=\varphi-\varphi_0=2\omega_H\tau.$$

For very small magnetic field, Eq. (46) goes over

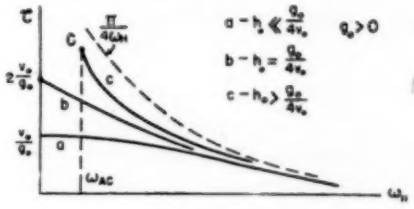

FIG. 10.

to (21)

$$(\partial x/\partial t_0)_t\to-v_0+g_0\tau-h_0\tau^2, \quad \omega_H\to 0. \quad (21)$$

The discussion of the sign of expression (21) and of the critical condition making it zero (first bunching) were given in Section 3. Here, the problem is more complicated since expression (46) contains oscillating functions.

Let us start with the case of negligible *space-charge* and take $h_0=0$. In Section 3 (Eq. (22)) the answer was

$$\left.\begin{array}{l} g_0<0, \quad \partial x/\partial t_0<0 \text{ for all } \tau \text{ values}\\ g_0>0, \quad \partial x/\partial t_0<0 \text{ for } \tau<\tau_{0b}=v_0/g_0\end{array}\right\}\omega_H=0. \quad (47)$$

For non-vanishing magnetic field, the critical transit time is given by

$$\tan\psi_c=(v_0/g_0)2\omega_H, \quad (48)$$

$$\begin{array}{ll} g_0<0, & \pi/2<\psi_c<\pi,\\ g_0>0, & 0<\psi_c<\pi/2.\end{array} \quad (49)$$

The corresponding variation of the critical transit time τ_c as a function of ω_H is explained on Fig. 9. For a large magnetic field, ω_H is large, hence $\tan\psi$ becomes large according to (48), and it has the same sign as g_0. This means

$$\begin{array}{ll} \psi\leqslant\pi/2, & \text{when} \quad g_0>0,\\ \psi\geqslant\pi/2, & \text{when} \quad g_0<0.\end{array}$$

When the current density is not very small, the *space-charge term* in h_0 must be kept in Eq. (46),

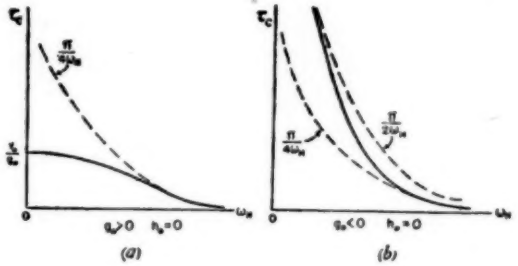

FIG. 9.

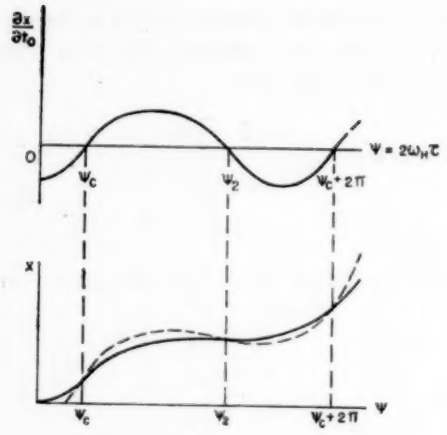

FIG. 11.

FIG. 12.

and the discussion becomes more complicated. An example shall be given a little later. Figure 10 summarizes the results for the case $g_0>0$, and

(a) $h_0 \ll g_0^2/4v_0$, similar to Fig. 9a.

(b) $h_0=g_0^2/4v_0$, critical case for $H=0$, $\omega_H=0$. (50)

(c) $h_0>g_0^2/4v_0$,

In this last case, trajectories never intercrossed when the magnetic field was zero (Section 3). The same situation is obtained for small magnetic field, but when $\omega_H>\omega_e$ bunching reappears and one finds a new curve (c). For large magnetic field, the h_0 term in (46) always becomes negligible on account of its ω_H^{-2} dependence and all three curves (a) (b) (c) are asymptotic to $\pi/4\omega_H$ as on Fig. 9.

Let us discuss carefully this case (c) and investigate the beginning of the curve at point C. According to (50, c) the current is large enough to prevent bunching when the magnetic field is zero (see Section 3, Figs. 4 and 5). The question is now to find the magnetic field for which bunching shall reappear. We rewrite (46) in a similar way to (21)

$$\partial x/\partial t_0=-v+g\tau-h\tau^2=0, \qquad (51)$$

$$v=v_0\cos\psi, \quad g=g_0\sin\psi/\psi, \quad h=2h_0(1-\cos\psi)/\psi^2.$$

Bunching reappears at the moment when Eq. (51) obtains real roots instead of imaginary ones, that is when

$$g^2\geqslant 4hv.$$

Critical conditions (point C) mean

$$g^2=4hv, \quad \tau_c=2v/g=g/2h; \qquad (52)$$

hence,

$$g_0^2\sin^2\psi=8h_0v_0\cos\psi(1-\cos\psi),$$

$$g_0^2(1+\cos\psi)=8h_0v_0\cos\psi, \qquad (53)$$

$$\cos\psi=\frac{g_0^2}{8h_0v_0-g_0^2}, \quad 0<\cos\psi<1.$$

Using now the second relation (52) we obtain

$$\tau_c=2\frac{v}{g}=2\frac{v_0}{g_0}\cot\psi\cdot\psi=2\frac{v_0}{g_0}\cot\psi 2\omega_H\tau_c;$$

hence,

$$2\omega_H\tau_c=\frac{g_0}{2v_0}\tan\psi=2\left(4\frac{h_0^2}{g_0^2}-\frac{h_0}{v_0}\right)^{\frac{1}{2}}. \qquad (54)$$

These relations (53) (54) give the position of the point of departure C for curve c.

The curves plotted on Figs. 9 and 10 refer to the smallest transit time τ at which the first bunching takes place. But we must notice that (for a given ω_H) expression (46) is periodical in ψ, and takes the same value for ψ and $\psi+2\pi$, that is τ and $\tau+\pi/\omega_H$, hence Eq. (46) yields a curve like the one plotted on Fig. 11. Trajectories intercross at ψ_c, but they cross again and ψ_2, $\psi_c+2\pi$, $\psi_2+2\pi$, as shown on Fig. 12. All this, of course, rests upon the use of Llewellyn's formula, which cannot be trusted any more after trajectories first intercross at ψ_c. (See discussion in Section 1.) We noted, however, that in the case of *strong magnetic fields*, space-charge effects seem to play an unimportant role, and it is probable that they do not alter materially the shape of the curves in Fig. 12. One may foresee that trajectories should alternately cross each other, with periods of single and double stream motions separated by bunching. Such should be the general picture, at least for strong magnetic fields.

Wave Function for the Ground State of Lithium

KUN HUANG
Institute of Astronomy, Academia Sinica, and Department of Physics, National University of Peking, Kunming, China
(Received March 21, 1945)

A variational calculation of the ground state $1s^2 2s\,^1S$ of Li is carried out with the wave function

$$\Psi = \exp(-\alpha k r_3/2)\exp[-k(r_1+r_2)/2][a+bkr_{12}+ck^2(r_1-r_2)^2+dkr_3] - \exp(-\alpha k r_2/2)\exp[-k(r_1+r_3)/2][a+bkr_{13}+ck^2(r_1-r_3)^2+dkr_{12}].$$

The energy comes out to be -14.914 Rh, compared with the value -14.838 Rh obtained by the best wave function not containing terms like r_{12} and r_{13}, and the spectrocopic value -14.956 Rh.

THE ground state of the lithium-like ions was studied by several investigators with the method of variation of parameters.[1] Their attempts have been restricted to the use of combinations of single-electron wave functions. Despite the increasing number of parameters employed in their wave functions, the calculated energy values were improved rather slowly as compared with the results obtained with the simplest functions. These results all fall short of the experimental value for the total energy by about one percent. The discrepancy is considerably larger than results of similar methods applied to cases with two electrons not in the same sub-shell. In the light of Hylleraas' work on the helium atom,[2] it is clear that these facts show that their single-electron wave functions cannot satisfactorily take account of the close interaction between the two $1s$ electrons. As their improvements were made entirely on the wave function of the outer electron alone which in its simplest form is already quite good, this explains the slow improvement of the energy value. Although this fact was certainly realized, no step was however taken towards taking account of this effect, probably because of the rather large amount of numerical work any such attempt would necessitate. A projected investigation of the stability of the negative ion of helium has led the present writer to seek for an accurate trial wave function for the lowest state of a 3-electron ion, and the present attempt is made to use a wave function with a hydrogenic function for the $2s$ electron and to take care of the $1s$ electrons in the manner in which Hylleraas treated the helium atom. As the analytical part of the work is common to all such ions, we start in this paper by applying it to the lithium atom, partly to find out the accuracy of the trial function and partly because of the interest afforded by the problem itself.

We shall employ an antisymmetric wave function built up out of a core function similar to Hylleraas' function for two electrons with opposite spins plus a hydrogen-like $3s$ function for the third electron. Since the spin-dependent terms of the Hamiltonian will be omitted, the energy will be independent of the spin assigned to the $3s$ electron; we shall call this spin $(-)$ for the sake of definiteness.

For the $1s$ factors grouped together, we have used the simplest Hylleraas function

$$\exp[-\tfrac{1}{2}k(r_1+r_2)][a+b(kr_{12}) + ck^2(r_1-r_2)^2]\sigma^+(1)\sigma^-(2).$$

For the $2s$ electron, we have used the simple hydrogenic function with adjustable parameters:

$$\exp[-\tfrac{1}{2}\alpha(kr_3)](a+br_3)\sigma^-(3).$$

However, in view of the great advantage in using linear parameters for the numerical calculations and to bring the problem within reasonable length, we have omitted the product of the variable terms of the $1s$ and $2s$ factors and have taken as our trial function

$$\psi^{+--}(1,2,3) = \exp[-\tfrac{1}{2}k(r_1+r_2)-\tfrac{1}{2}\alpha(kr_3)] \times[a+bkr_{12}+ck^2(r_1-r_2)^2+dkr_3] \times\sigma^+(1)\sigma^-(2)\sigma^-(3).$$

[1] V. Guillemin and C. Zener, Zeits. f. Physik **61**, 199 (1930); C. Zener, Phys. Rev. **36**, 51 (1930); E. B. Wilson, J. Chem. Phys. **1**, 210 (1933).
[2] E. A. Hylleraas, Zeits. f. Physik **54**, 347 (1929).

This function is not properly antisymmetric. We must minimize the energy expression

$$\lambda=\int\Psi H\Psi\Big/\int\Psi\Psi,$$

using an antisymmetric function which we shall take in the form

$$\Psi=(1/N!)^{\frac{1}{2}}\sum_P(-1)^p P\psi^{+--}(1,2,3),$$

using the notation of Condon and Shortley,[3] in which P represents a permutation of the electrons 1, 2, 3, and p has the parity of P.

With this function,

$$\int\Psi H\Psi=(1/N!)\sum_P\sum_{P'}(-1)^{p+p'}\times\int P\psi^{+--}(1,2,3)HP'\psi^{+--}(1,2,3).$$

Since the Hamiltonian operator H is symmetric in the coordinates of the three electrons and does not involve the spins, the integral will vanish if P and P' assign the $+$ spin to two differently numbered electrons, for then one of the electrons will have a spin function σ^+ in P and σ^- in P' and these functions are orthogonal. Hence, for any given permutation

$$P:\quad 1,2,3\rightarrow a,b,c.$$

There are only two non-vanishing terms in the summation over P', namely those for

$$P':\quad 1,2,3\rightarrow a,b,c\qquad(p'=p)$$

and

$$P':\quad 1,2,3\rightarrow a,c,b.\quad(p'=p+1)$$

Because of the symmetry of the operator H, the summation over P merely introduces a factor $N!$ and we have finally

$$\int\Psi H\Psi=\int\psi^{+--}(1,2,3)H\psi^{+--}(1,2,3)-\int\psi^{+--}(1,2,3)H\psi^{+--}(1,3,2).$$

Similarly,

$$\int\Psi\Psi=\int\psi^{+--}(1,2,3)\psi^{+--}(1,2,3)-\int\psi^{+--}(1,2,3)\psi^{+--}(1,3,2).$$

It is easy to verify that when the distances $r_1, r_2, r_3, r_{23}, r_{13}, r_{12}$ are used in the expression of the kinetic energy and the scalar factor k taken out of the integrals in the usual manner, the total energy is given by

$$\lambda=(k^2M+kL)/N$$

where M, L, N corresponding, respectively, to the kinetic energy, potential energy, and the normalization factor, are given by the integrals:

$$M=\int\int\int\Big\{\Big(\frac{\partial\Phi}{\partial r_1}\Big)^2+\Big(\frac{\partial\Phi}{\partial r_2}\Big)^2+\Big(\frac{\partial\Phi}{\partial r_3}\Big)^2+2\Big(\frac{\partial\Phi}{\partial r_{12}}\Big)^2+2\Big(\frac{\partial\Phi}{\partial r_{13}}\Big)^2+\frac{r_1^2+r_{12}^2-r_2^2}{r_1r_{12}}\Big(\frac{\partial\Phi}{\partial r_1}\Big)\Big(\frac{\partial\Phi}{\partial r_{12}}\Big)$$
$$+\frac{r_1^2+r_{13}^2-r_3^2}{r_1r_{13}}\Big(\frac{\partial\Phi}{\partial r_1}\Big)\Big(\frac{\partial\Phi}{\partial r_{13}}\Big)+\frac{r_2^2+r_{12}^2-r_1^2}{r_2r_{12}}\Big(\frac{\partial\Phi}{\partial r_2}\Big)\Big(\frac{\partial\Phi}{\partial r_{12}}\Big)+\frac{r_3^2+r_{13}^2-r_1^2}{r_3r_{13}}\Big(\frac{\partial\Phi}{\partial r_3}\Big)\Big(\frac{\partial\Phi}{\partial r_{13}}\Big)$$
$$+\frac{r_{12}^2+r_{13}^2-r_{23}^2}{r_{12}r_{13}}\Big(\frac{\partial\Phi}{\partial r_{12}}\Big)\Big(\frac{\partial\Phi}{\partial r_{13}}\Big)\Big\}d\tau_1d\tau_2d\tau_3;$$

$$L=2\int\int\int\Big\{\frac{1}{r_{12}}+\frac{1}{r_{13}}+\frac{1}{r_{23}}-\frac{3}{r_1}-\frac{3}{r_2}-\frac{3}{r_3}\Big\}\Phi^2d\tau_1d\tau_2d\tau_3;$$

$$N=\int\int\int\Phi^2d\tau_1d\tau_2d\tau_3$$

[3] E. U. Condon and G. H. Shortley, *The Theory of Atomic Spectra*, pp. 164, 174 (1935).

where

$$\Phi=\exp\left(-\frac{\alpha r_3}{2}\right)\exp\left(-\frac{r_1+r_2}{2}\right)[a+br_{12}+c(r_1-r_2)^2+dr_3]$$

$$-\exp\left(-\frac{\alpha r_2}{2}\right)\exp\left(-\frac{r_1+r_3}{2}\right)[a+br_{13}+c(r_1-r_3)^2+dr_2].$$

Atomic units are used for the lengths and λ, the energy is in units of Rydbergs.

In the integrands involved, except a single term which we shall consider separately, all terms involve no more than five of the six distances, namely, r_1, r_2, r_3 and two of the electronic separations r_{12}, r_{13}, r_{23}. For the integration of these terms, it is convenient to use the explicitly appearing coordinates directly as the integration variables. The volume element in these variables is easily obtained. Consider for definiteness the variables r_1, r_2, r_3, r_{12}, r_{13}. Take the direction taken up by the position vector of the electron 1 as the polar axis of the polar coordinates of the two other electrons. Then the integrations over the azimuthal angles of the two electrons about the axis may be directly performed giving a factor $4\pi^2$. To pass over from the polar angles of the two electrons 2 and 3 into the variables r_{12} and r_{13}, it is only necessary to make the usual transformations from plane polar coordinates to bipolar coordinates twice separately, once for each electron, both times with the positions of the nucleus and electron 3 as the poles. A further integration over the angular coordinates of electron 1 reduces the number of integration variables to five and the volume has the form:

$$16\pi^2\int_0^\infty dr_1\int_0^\infty r_2dr_2\int_0^\infty r_3dr_3\int_{|r_1-r_2|}^{r_1+r_2} r_{12}dr_{12}\int_{|r_1-r_3|}^{r_1+r_2} r_{13}dr_{13}.$$

In these coordinates all the integrals may be put in the form of a general expression:

$$A\int_0^\infty dr_1\int_0^\infty dr_2\int_0^\infty dr_3\int_{|r_1-r_2|}^{r_1+r_2} dr_{12}\int_{|r_1-r_3|}^{r_1+r_2} dr_{13}r_1{}^l r_2{}^m r_3{}^n r_{12}{}^p r_{13}{}^q \exp\left[-(\alpha r_1+\beta r_2+\gamma r_3)\right]$$

the integration of which in the various cases causes no essential difficulty. It may however be mentioned that on a few occasions there occur integrals of the following type:

$$\int_0^\infty \frac{\exp(-\alpha r_1)}{r_1}dr_1\int_0^{r_1}\exp(-\beta r_2)r_2{}^l dr_2\int_0^{r_1}\exp(-\gamma r_3)r_3{}^m dr_3, \quad l,\, m\geqslant 1$$

which may be integrated by introducing

$$I(\mu)=\int_0^\infty \frac{\exp(-\alpha r_1)}{r_1}dr_1\int_0^{\mu r_1}\exp(-\beta r_2)r_2{}^l dr_2\int_0^{r_1} e^{-\gamma r_3}r_3{}^m dr_3$$

and obtained as

$$I(1)=\int_0^1 (dI/d\mu)d\mu.$$

We return now to consider the integral that involves all the six distances. The integral, apart from a numerical factor, has the form:

$$\iiint \exp(-r_1)\exp\left[-\frac{(1+\alpha)}{2}\right](r_2+r_3)\frac{r_{12}r_{13}}{r_{23}}d\tau_1 d\tau_2 d\tau_3.$$

It is not helpful to use these coordinates as the integration variables in this case, for both the volume

element and the limits of integration of the sixth coordinate become extremely complicated expressions, and it appears it cannot be integrated in a closed expression. To evaluate its value approximately, we have expanded the integrand into a series and have used spherical polar coordinates for the integration. It is somewhat simpler for the integration first to integrate over the angular coordinates of one of the electrons. This may be done in a manner similar to our considerations of the case with five coordinates. We take any direction taken up by the position vector of this electron as the polar axis for the polar coordinates of the two other electrons, and perform the integration over all such directions first. The integral has then the form:

$$4\pi^2\int_0^\infty r_1^2dr_1\int_0^\infty r_2^2dr_2\int_0^\infty r_3^2dr_3\int_0^\pi \sin\theta_2d\theta_2\int_0^{2\pi}d\varphi_2\int_0^\pi \sin\theta_3d\theta_3$$
$$\times\int_0^{2\pi}d\varphi_3\frac{r_{12}r_{13}}{r_{23}}\exp(-r_1)\exp\left[-\frac{1+\alpha}{2}(r_2+r_3)\right].$$

The integrand may then be expanded with the help of the well-known expansions:[3]

$$\frac{1}{r_{12}}=\sum_{l=0}^{\infty}\left(\frac{r_<^l}{r_>^{l+1}}\right)_{12}P_l(\cos\theta_2),\quad\text{etc.}$$

With the help of the addition formula:[4]

$$P_n(\cos\theta_{23})=P_n(\cos\theta_2)P_n(\cos\theta_3)+2\sum_{m=1}^{n}(-)^m\frac{(n-m)!}{(n+m)!}P_n(\cos\theta_2)P_n^m(\cos\theta_3)\cos m(\varphi_2-\varphi_3)$$

and the recurrence formula:[5]

$$(2n+1)\cos\theta P_n(\cos\theta)=(n+1)P_{n+1}(\cos\theta)+nP_{n-1}(\cos\theta),$$

the integrations over the various angular coordinates may be performed without difficulty. The integral is reduced to:

$$128\pi^3\sum_{k=0}^{\infty}\frac{1}{(2k+1)^2}\int_0^\infty r_3^2\exp\left(-\frac{1+\alpha}{2}r_3\right)dr_3\int_0^{r_3}r_2^2\exp\left(-\frac{1+\alpha}{2}r_2\right)dr_2\int_0^\infty r_1^2\exp(-r_1)\left(\frac{r_<^k}{r_>^{k+1}}\right)_{23}$$
$$\times\left\{\frac{1}{(2k+3)^2}\left(\frac{r_<^{k+2}}{r_>^{k+1}}\right)_{13}\left(\frac{r_<^{k+2}}{r_>^{k+1}}\right)_{12}-\frac{1}{(2k-1)(2k+3)}\left(\frac{r_<^{k+2}}{r_>^{k+1}}\right)_{12}\left(\frac{r_<^k}{r_>^{k+1}}\right)_{13}\right.$$
$$\left.-\frac{1}{(2k-1)(2k+3)}\left(\frac{r_<^k}{r_>^{k-1}}\right)_{12}\left(\frac{r_<^{k+2}}{r_>^{k+1}}\right)_{13}+\frac{1}{(2k-1)^2}\left(\frac{r_<^k}{r_>^{k-1}}\right)_{12}\left(\frac{r_<^k}{r_>^{k-1}}\right)_{13}\right\}dr_1.$$

Since the separate integrals, apart from the numerical factors, must always decrease with increasing k, as the integrands everywhere decrease, we see that:

first term for $k=1$ drops to a value $<(1/25)$ its value for $k=0$;
second term for $k=1$ drops to a value $<(1/15)$ its value for $k=0$;
third term for $k=1$ drops to a value $<(1/15)$ its value for $k=0$;
fourth term for $k=2$ drops to a value $<(1/225)$ its value for $k=0$.

[4] E. T. Whittaker and G. N. Watson, *A Course of Modern Analysis* (1927), p. 326.
[5] E. T. Whittaker and G. N. Watson, reference 4, p. 308.

As all the terms for $k=0$ and the fourth term for $k=1$ have positive signs we have,

$$\iiint \exp(-r_1)\exp\left[-\frac{1+\alpha}{2}(r_2+r_3)\right]\frac{r_{12}r_{13}}{r_{23}}d\tau_1 d\tau_2 d\tau_3$$

$$\cong 128\pi^3\int_0^\infty r_3^2\exp\left(-\frac{1+\alpha}{2}r_3\right)dr_3\int_0^{r_3} r_2^2\exp\left(-\frac{1+\alpha}{2}r_2\right)dr_2\int_0^\infty r_1^2\exp(-r_1)dr_1$$

$$\times\left\{\frac{1}{9}\left(\frac{1}{r_>}\right)_{23}\left(\frac{r_<^2}{r_>}\right)_{13}\left(\frac{r_<^2}{r_>}\right)_{12}+\frac{1}{3}\left(\frac{1}{r_>}\right)_{23}(r_>)_{13}\left(\frac{r_<^2}{r_>}\right)_{12}+\frac{1}{3}\left(\frac{1}{r_>}\right)_{23}\left(\frac{r_<^2}{r_>}\right)_{13}(r_>)_{12}\right.$$

$$\left.+\left(\frac{1}{r_>}\right)_{23}(r_>)_{12}(r_>)_{13}+\frac{1}{9}\left(\frac{r_<}{r_>^2}\right)_{23}(r_<)_{13}(r_<)_{12}\right\},$$

which is correct safely within 1/15 the true value.

The expressions of M, L, N as functions of the various parameters are given at the end of this paper.

When a trial value is assigned to α, M, L, N may be expressed as quadratic forms in the linear parameters a, b, c, d. With a suitable value chosen for k the minimum of λ and the ratios of the linear parameters may be determined in terms of the solution of a secular equation after the manner in which Hylleraas treated the helium problem. The method is sufficiently well known, so we shall not stop to go into its details. With these parameters so determined, the values of M, L, N may be calculated. If then k alone is allowed to vary, the minimum of λ is given by

$$L^2/4MN \text{ corresponding to } k=L/2M.$$

We have taken this value to be the minimum of λ corresponding to the assigned value of α. This procedure is to be repeated for various values of α and the minimum of the series of minima $L^2/4MN$ is then located.

It is known from results of usual calculations with the method of variation of parameters that the screening constants of the core electrons are not appreciably affected by the presence of electrons in an outer shell. In our calculation, we have used for k the value 5.64, which is the value corresponding to the minimum energy of Li^+ calculated with the function:

$$\exp\left[-\tfrac{1}{2}k(r_1+r_2)\right][a+bkr_{12}+ck^2(r_1-r_2)^2].$$

As it is believed that the wave functions for the 2s electron in former works are sufficiently good, as a guide to the value of α, we have used Guillemin and Zener's value[6] 1.26 for $k\alpha$. A few trials with values of α in this neighborhood have shown that the minimum is actually near their value for $k\alpha$, and that the minimum is so flat that with the energy calculated to the fifth place, α cannot be determined within 0.01. We may note that the exact minimum calculated with a trial function is without any particular significance. It depends largely on the form of the function we have chosen in particular, as is clearly demonstrated by the great change in the values of the parameters brought about by the introduction of a new term in the trial function. In fact, for the accuracy of the function we rely solely upon the closeness of the calculated energy to the true value, which guarantees the components in the higher states to be small. In view of this fact and the laborious task of calculating M, L, N for each new value of α, we shall take as our result what we start with, corresponding to the Guillemin and Zener's value for the screening constant. The values of the energy and the various parameters are given below:

$$\lambda=-14.914\pm0.001;\ \alpha=0.222,\ k=5.57;$$

$$a=1,\ b=-0.55642,\ c=-0.05710,\ d=-0.89063.$$

The uncertainty of 0.001 in the energy is caused by the part we have cut off from the series considered above. We give below the experimental value for the energy and two values calculated

[6] V. Guillemin, Jr. and C. Zener, Zeits. f. Physik 61, 199 (1930).

by previous investigators:

exp[7] −14.956; Guillemin and Zener[8] −14.837; Wilson[8] −14.838.

We see that the improvement in the energy value is considerable. The percentage error is reduced almost by a factor 3. Yet it is not as good as one might have expected, for the result still falls short of the accuracy obtained with the simplest Hylleraas functions for two-electron problems. And previous results with $1s2s$ configurations also show that the use of the simple $2s$ function cannot be wholly responsible for the discrepancy. So the inaccuracy is caused probably by the way we have omitted the products of the variable terms in constructing the trial wave function. It is uncertain if it can be improved in such a way as not to add materially to the labor of calculation.

In conclusion it is a pleasure to thank Professor Ta-you Wu for his interest and encouragement during the course of this work.

[7] Bacher and Goudsmit, *Atomic Energy States.*
[8] Condon and Shortley, *The Theory of Atomic Spectra* (1935), p. 352.

PHYSICAL REVIEW VOLUME 70, NUMBERS 3 AND 4 AUGUST 1 AND 15, 1946

Induction Effects in Terrestrial Magnetism*

Part II. The Secular Variation**

WALTER M. ELSASSER
RCA *Laboratories, Princeton, New Jersey*
(Received March 22, 1946)

In Part I a method has been developed for the integration of the electromagnetic field equations in the presence of fluid motions in a spherical conductor. This analysis is here applied to an interpretation of the secular geomagnetic variations. A very brief survey of some of the observed features of the secular variation is first given. It is pointed out that not only the phases but also the magnitudes of the harmonic components, including the main dipole, are subject to large changes at the present time. There follows a brief study of the skin effect which indicates that the observed variations of the dipole terms originate in a layer adjacent to the core's boundary several hundred kilometers deep; those of the higher terms originate in a layer no more than 200 km deep. Next, the "coupling matrix" introduced in Part I is evaluated in form of a table of all matrix elements that contain vectors of dipole and quadrupole type but no higher harmonics. It is shown that a zonal fluid motion (zonal toroidal flow in the terminology adopted here) produces rotation of the tesseral magnetic dipole terms and also oscillatory changes in amplitude of these terms. There is one and only one type of matrix element that represents an interaction of the main magnetic dipole with itself; the corresponding fluid motion is a meridional flow (poloidal flow) of quadrupole symmetry. With this term amplification or de-amplification occurs, depending on the sign of the velocity. The theory thus can account for all the observed components of the secular variation.

IN Part I of this paper the mathematical treatment was brought close to the point where a comparison with observational data is feasible. We shall now first give a brief glance to some of the observed features of the secular magnetic variation.

OBSERVATIONAL DATA

There is no need for a complete review at this place since a few years ago two extensive reference works[1,2] have appeared in short succession. The reader is referred to these for all details.

It is always possible to separate the fields of internal and external origin, and in this paper we consider only the part of the field of internal origin. The separation of the two fields can be carried out by a straightforward mathematical procedure based on the principles of potential theory; but the external field is so small that its contribution to the first few harmonics is negli-

* The completion of this work which was begun prior to the writer's joining the RCA Laboratories, has been delayed because of the war.
** Part I of this paper: W. M. Elsasser, Phys. Rev. 60, 876 (1941).

[1] J. A. Fleming, ed. *Terrestrial Magnetism and Electricity* (McGraw-Hill Book Company, Inc., New York, 1939).
[2] S. Chapman and J. Bartels, *Geomagnetism* (Clarendon Press, Oxford, 1940), 2 volumes.

gible for most purposes, especially if the external field is averaged over the short period fluctuations of the order of a few hours to a few days.

In Part I we used sets of fundamental vectors expressed in terms of spherical harmonics. While this development is convenient as a mathematical tool, the observed distribution of the magnetic field does not lend itself readily to the same type of analysis. The observational data are in general summarized in the form of magnetic maps, and rightly so since the spherical harmonic series for the actual field converges very slowly. It can therefore hardly replace the maps in practice even for the broad outlines of the field. Moreover, an accurate determination of spherical harmonic coefficients from observation would presuppose data available from all over the globe while in practice data originating in latitudes above 60° are extremely scarce. This fact does not preclude the formal determination of spherical harmonic coefficients from observations, but it introduces a considerable degree of inaccuracy into these coefficients. If nevertheless we have used the method of spherical harmonics in this paper, it is mainly on account of its mathematical convenience.

There exist two extensive analyses of the field in terms of spherical harmonics, that of Schmidt[3] for the year 1880 and that of Dyson and Furner[4] for the year 1922. Both include coefficients up to $n=6$, but the sixth-order terms involve too large errors to be significant. The distribution in magnitude of these coefficients is apparently random except for an over-all decrease with increasing n. It can be shown that a rather regular convergence obtains for the series whose coefficients are the root-mean-square values of all the coefficients having the same zonal index n. If we assume that there are no important sources of the magnetic field above the boundary of the core, it may be concluded from the convergence of this series that the bulk of the sources of the higher harmonics (quadrupoles and above) is most probably located in the top strata of the core.[5]

Although the two analyses quoted are some 40 years apart, it is not advisable to use them for the purpose of finding the secular variation of individual components except for a few leading terms, because of the errors inherent in this method. The material available for the dipole terms alone is somewhat more ample.[6,7] In Fig. 1 are plotted the relative magnitudes of the dipole terms parallel and perpendicular to the earth's axis, from eight separate determinations. The large scatter of the points is indicative of the inaccuracies of the method of computation, but the general trend is unmistakable. The relative values have been adjusted so that both coefficients are unity in the year 1900; the straight lines have been drawn from a visual estimate. The slope of the parallel dipole term represents a variation of -4.3 percent per century, that of the perpendicular dipole term, -3.6 percent per century. Similarly, the phase of the perpendicular dipole can be plotted against time. The resulting points scatter somewhat like those of Fig. 1; a mean curve corresponds to a rotation of the dipole, in the same sense as the earth itself, at a rate of 4.5 degrees per century, corresponding to a period of revolution of 8000 years. This is one of the slower components of the secular variation.

The objection may be raised that the primary data vary in time with the progressively greater

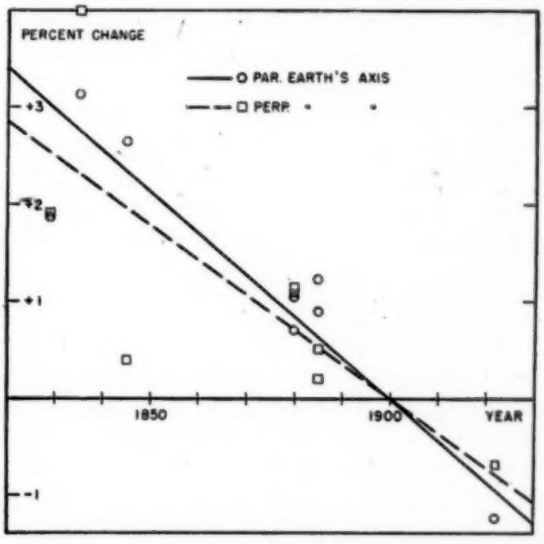

FIG. 1. Relative magnitude of dipole terms from eight different determinations.

[3] Ad. Schmidt, Abh. Bayer. Akad. Munich 19, 1 (1895).
[4] F. W. Dyson and H. Furner, M.N.R.A.S., Geophys. Suppl. 1, 76 (1923).
[5] W. M. Elsasser, Phys. Rev. 60, 876 (1941).
[6] See the article by McNish in reference 1.
[7] See Chapter 18 of reference 2.

extent of the observations, and that nearly simultaneous observations, although made by different authors, are likely to be based on nearly the same material, thus introducing a systematic error into the results. This is probably true to a certain extent, but only a fraction of the observed decrease of the dipole field could be attributed to this cause.*

The data found in the literature[6,7] indicate that for the quadrupole and higher terms the rates of relative change and the corresponding rates of rotation are even larger and that periods of the order of a thousand years or less are not uncommon. As has been pointed out before, the spherical harmonic series is not well adapted to the evaluation of the more detailed variations. Instead, a glance upon charts showing lines of constant annual secular variation[8,9] is instructive. Most of these lines consist of several closed curves that surround some seven or eight principal "foci" of geomagnetic activity. The regions of intense change around the foci have diameters of several thousand kilometers, so that their appearance on the surface of the earth is well compatible with the assumption that the sources of these variations are located at or below the boundary of the core which is 2900 km beneath the earth's surface. The rate of change of the field in such regions is of the order of $0.5\text{–}1.5\times10^{-3}$ gauss per year, as compared to an absolute magnitude of the field of 0.3–0.5 gauss (both values referring to the earth's surface). Hence Fourier components with periods of the order of several hundred to a few thousand years are indicated.

The regional distribution of the field variations and of their secular change seems to be capable of, at least, a semiquantitative simple interpretation. McNish[10] has shown that the instantaneous non-dipole part of the field can be represented with some accuracy by means of 14 elementary dipoles of suitable intensities located at a depth of one-half of the earth's radius, that is, slightly below the boundary of the core. The same author indicates that the regional secular variations can similarly be represented by a set of dipoles at this depth whose intensities change at certain given rates.

THE FIELD EQUATIONS

Resuming now our mathematical analysis we return for a moment to the electromagnetic field equations. In the presence of fluid motions in the conductor they are, by (1) and (31) of Part I:

$$\nabla\times\mathbf{B}-\mu\sigma\mathbf{E}=\mu\sigma\mathbf{v}\times\mathbf{B}, \tag{1}$$

$$\nabla\times\mathbf{E}+\partial\mathbf{B}/\partial t=0, \quad \nabla\cdot\mathbf{B}=0. \tag{2}$$

On taking the curl of (1) and substituting from (2) we obtain

$$-\nabla^2\mathbf{B}+\mu\sigma\partial\mathbf{B}/\partial t=\mu\sigma\nabla\times(\mathbf{v}\times\mathbf{B}). \tag{3}$$

Subsequently we shall assume, in addition

$$\nabla\cdot\mathbf{v}=0. \tag{4}$$

On using (4) and the second equation (2), the right-hand side of (3) can be transformed by a known vector identity into:

$$\partial\mathbf{B}/\partial t=(\mu\sigma)^{-1}\nabla^2\mathbf{B}-(\mathbf{v}\cdot\nabla)\mathbf{B}+(\mathbf{B}\cdot\nabla)\mathbf{v}. \tag{5}$$

If in this equation we put $\mathbf{v}=0$, we are left with an equation for the magnetic vector which has the form of a diffusion equation. This equation describes the gradual march of the field across a conductor and gives rise to the familiar phenomenon of the skin effect. It should be pointed out that the analogy with diffusion is rather limited since the boundary conditions at the surface of a conductor are different from the boundary conditions of a diffusion problem; the analogy with diffusion applies, therefore, mainly in the interior of an extensive conductor where the effect of the boundaries is small.

Assume now, in the second instance, that the velocities are very large so that the "diffusion" term can be neglected. The second term on the right hand side of (5) represents the convection of the field with the fluid. The field equations can now be written

$$d\mathbf{B}/dt=(\mathbf{B}\cdot\nabla)\mathbf{v}, \tag{6}$$

where the total derivative has the usual significance, indicating the rate of change of the field with respect to a moving particle.

* *Note added in proof:* A harmonic analysis of the field for the year 1942 which has just appeared corroborates the general decrease of the dipole field as expressed in Fig. 1: V. I. Afanasieva, Terr. Mag. **51**, 19 (1946).

[8] See the article by Fleming in reference 1.

[9] See chapter 3 of reference 2.

[10] A. G. McNish, Trans. Am. Geophys. Union **2**, 287 (1940).

The term, finally, which appears on the right-hand side of (6), represents the induction effects proper. Equation (6) is capable of a simple kinematical interpretation. Introduce a cartesian system of coordinates whose x axis has the direction of $\mathbf{B}$ at a given point and instant. We then have, by (4),

$$\frac{d\mathbf{B}}{dt}=-B\left(\frac{\partial \mathbf{v}}{\partial y}+\frac{\partial \mathbf{v}}{\partial z}\right). \tag{7}$$

Hence the rate of change of $\mathbf{B}$ for a fluid particle is equal to the instantaneous two-dimensional *convergence* of the velocity in a plane normal to the direction of $\mathbf{B}$.

Following now the analysis of Part I further, we set

$$\mathbf{B}=\nabla\times\mathbf{A}=\nabla\times(\textstyle\sum_\gamma c_\gamma \mathbf{T}(\gamma)), \tag{8}$$

and for the velocity

$$\mathbf{v}=\textstyle\sum_\alpha (v_\alpha \mathbf{S}(\alpha)+w_\alpha \mathbf{T}(\alpha)). \tag{9}$$

By standard procedures we arrive at the system of differential equations:

$$dc_\gamma/dt+\Lambda_\gamma c_\gamma=\textstyle\sum_{\alpha\beta} c_\beta R^{-1}(v_\alpha[\mathbf{T}_\alpha\cdot\mathbf{S}_\beta\times\mathbf{T}_\gamma{}^*] +w_\alpha[\mathbf{S}_\alpha\cdot\mathbf{S}_\beta\times\mathbf{T}_\gamma{}^*]), \tag{10}$$

where by (36), Part I, a square bracket stands as an abbreviation for the integral over the volume of the conducting sphere. The Λ's, which in Part I have been identified as the coefficients of free decay, arise from the "diffusion" term of Eq. (5). The "diffusion" effects will now be dealt with in a form appropriate to our special problem.

SKIN EFFECT

On applying to the currents flowing in the core harmonic analysis, both in time and in space, we are able to confine our attention to a system of currents with the following properties: It varies in time as $\exp(-i\omega t)$, and it is two-dimensional, the currents flowing in a spherical surface of radius r_0 where they are defined by the following toroidal vector field[11]

$$\mathbf{\Pi}_{(\vartheta)}=\frac{f}{\sin\theta}\frac{\partial Y_n{}^m}{\partial\varphi},\quad \mathbf{\Pi}_{(\varphi)}=-f\frac{\partial Y_n{}^m}{\partial\vartheta}, \tag{11}$$

where f is a constant. Apart from this surface the magnetic field fulfills the equation

$$\nabla^2\mathbf{B}+i\omega\mu\sigma\mathbf{B}=0,$$

and the same equation applies to the generating scalar, ψ:

$$\nabla^2\psi+iq^2\psi=0,\quad q=(\omega\mu\sigma)^{\frac{1}{2}}. \tag{12}$$

A particular solution of (12) is

$$\psi=\text{const.}\ r^{-\frac{1}{2}}J_{n+\frac{1}{2}}(i^{\frac{1}{2}}qr)\,Y_n{}^m(\vartheta,\varphi).$$

Now for values of ω corresponding to periods of several thousand years or less the argument qr of the Bessel function is numerically large except for points near the center of the sphere. Hence in the upper strata of the core we may replace the Bessel function by its asymptotic expansion. We now set, as a solution for the interior region, $r\leqq r_0$, valid everywhere except near the center,

$$\psi^{(i)}=ar^{-1}\exp(i^{-\frac{1}{2}}qr)\,Y_n{}^m,$$

where a is a constant. In the region intermediate between the current-bearing surface and the outer boundary of the core we must use a combination of two linearly independent solutions of the Bessel differential equation. Introducing at once the asymptotic expressions, we may use two conveniently chosen linearly independent solutions without reference to the special cylinder functions from which they originate. We thus set in the middle region, $r_0\leqq r\leqq R$

$$\psi^{(m)}=r^{-1}[b\cdot\exp(i^{-\frac{1}{2}}qr)+c\cdot\exp(-i^{-\frac{1}{2}}qr)]\,Y_n{}^m,$$

and for the external space, $r\geqq R$, we set

$$\psi^{(a)}=dr^{-n-1}Y_n{}^m,$$

where b, c, d are constants.

From the generating function ψ the field vectors are derived by differentiation. The field equations are fulfilled if

$$\mathbf{A}=\mathbf{T},\quad \mathbf{E}=i\omega\mathbf{T},\quad \mathbf{B}=R^{-1}\mathbf{S}.$$

Equations (10)–(14) of Part I give the explicit expressions for these vectors. The boundary conditions are as follows. At the inner boundary, $r=r_0$, we require continuity of $\mathbf{E}$ and $\mathbf{B}_{(r)}$, and further,

$$\mathbf{B}_{(\vartheta)}{}^{(m)}-\mathbf{B}_{(\vartheta)}{}^{(i)}=\mu\mathbf{\Pi}_{(\varphi)},$$

$$\mathbf{B}_{(\varphi)}{}^{(m)}-\mathbf{B}_{(\varphi)}{}^{(i)}=-\mu\mathbf{\Pi}_{(\vartheta)}.$$

[11] According to the discussion in Part I the magnetic field is purely poloidal, hence the electric field and current density are purely toroidal.

At the outer boundary, $r=R$, we require

continuity of $\mathbf{E}$ and of $\mathbf{B}_{(r)}$, and
continuity of $\mathbf{B}_{(\vartheta)}/\mu$ and $\mathbf{B}_{(\varphi)}/\mu$.

As before, μ will be assumed constant throughout space, so that the latter boundary conditions reduce to the requirement of continuity for both field vectors. The boundary conditions lead in the usual way to a system of linear equations among the coefficients, a, b, c, d, f. If the first three coefficients are eliminated one obtains the following relation for the strength of the field in the external space expressed by the intensity of the two-dimensional currents:

$$d=(n+i^{-\frac{1}{2}}qR)^{-1}R^{n+1}r_0\mu f\cdot\exp\left[-i^{-\frac{1}{2}}q(R-r_0)\right].$$

We may evaluate this expression by comparing it with the strength of the field that would be produced by the same system of surface currents in empty space, that is if we had $\sigma=0$ everywhere, apart from the current-bearing surface. The generating scalar of this field in the external space is given by

$$\psi=d_0r^{-n-1}Y_n^m,$$

where, after some simple calculations, we find

$$d_0=(2n+1)^{-1}r_0^{n+2}\mu f.$$

Therefore, finally,

$$\frac{d}{d_0}=\frac{2n+1}{n+i^{-\frac{1}{2}}qR}\left(\frac{R}{r_0}\right)^{n+1}\exp\left[-i^{-\frac{1}{2}}q(R-r_0)\right]. \quad (13)$$

If n is not too large the behavior of (13) is swamped by the real part of the exponential, which is

$$\exp\left[-(\tfrac{1}{2}\omega\mu\sigma)^{\frac{1}{2}}(R-r_0)\right].$$

The factor under the square root is known from the usual theory of the skin effect. Assuming $\omega=2.5\cdot10^{-11}$, corresponding to a frequency of one cycle per 8000 years we obtain a "skin depth" of

$$(\tfrac{1}{2}\omega\mu\sigma)^{-\frac{1}{2}}=250 \text{ km}.$$

It may safely be concluded that the secular variations of the dipole terms originate within the upper fifth of the core. Any constant part of the field may, of course, come from greater depth. The regional variations, having periods of the order of a thousand years or so, must possess sources that lie entirely in the top strata of the core, no lower than about 200 km below the boundary.

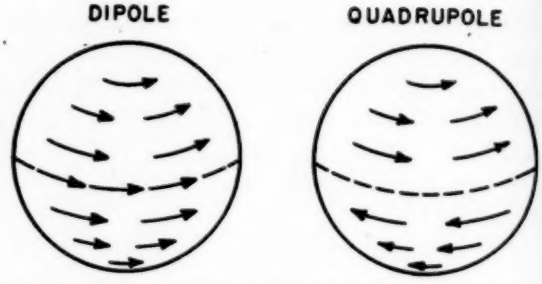

FIG. 2. A toroidal dipole and quadrupole, in perspective.

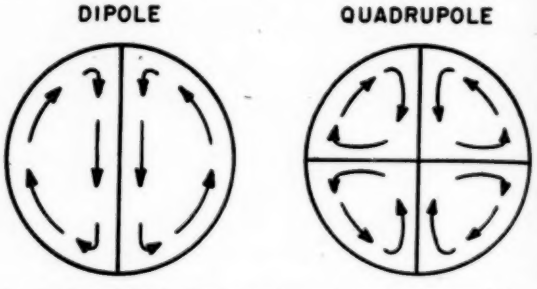

FIG. 3. A poloidal dipole and quadrupole, in meridional cross section, for $s=1$.

A TABLE OF MATRIX ELEMENTS

We pass now to the integration of the equations of motion (10) in simple cases. Below are given explicit expressions for all matrix elements which contain dipoles and quadrupoles but no higher spherical harmonics. The table is divided into two parts according to whether the velocity vector is toroidal or poloidal. In order to enable the reader to visualize readily the geometry of these vector fields some simple patterns are shown in Figs. 2 and 3. The fields shown are of the zonal type, i.e., $m=0$. Figure 2 represents in a perspectivic drawing a toroidal dipole and quadrupole field as it appears on the surface of the sphere. Figure 3 shows in meridional cross section types of flow which have the symmetry of a poloidal dipole and quadrupole. The character of these vector fields may be described as follows. If the zonal index is n there are n "belts" of zonal toroidal flow of alternating directions. In the poloidal case there are, in the meridional plane, n "vortices" along a meridional strip extending from the north to the south pole.

Thus in the dipole case the vortex shown extends from the north to the south pole; in the quadrupole case there are two vortices, each extending from a pole to the equator; and in the octupole case there would be two adjacent vortices in each hemisphere, separated by a null at 45°.

Similarly, the radial index, s, determines the number of reversals of the vectors between the center and the boundary of the sphere. Thus, in the toroidal case, there would be s belts of flow of alternating direction superposed upon each other on going from the center to the boundary at any given angle θ. For the poloidal case our Fig. 3 corresponds to $s=1$; for higher values of s there would be s vortices of alternating sense of circulation superposed upon each other between the center and the boundary, in any one sector of angular width π/n.

As illustrated by Figs. 2 and 3 for $m=0$, toroidal vector fields are symmetrical with respect to the equatorial plane when n is odd, more generally, when $n-m$ is odd; they are antisymmetrical with respect to the equatorial plane when $n-m$ is even. Poloidal vector fields are symmetrical with respect to the equatorial plane when $n-m$ is even and antisymmetrical when $n-m$ is odd. In a first approximation, disregarding turbulence, the fluid motion should be symmetrical about the equatorial plane and should therefore only contain odd toroidal and even poloidal terms.

The following are the matrix elements that involve vectors of toroidal flow:

$$
\begin{aligned}
[\mathbf{T}_1 \cdot \mathbf{S}_1^1 \times \mathbf{T}_1^{-1}] &= 4\pi i(2/3)NF,\\
[\mathbf{T}_1^1 \cdot \mathbf{S}_1 \times \mathbf{T}_1^{-1}] &= -4\pi i(2/3)NF,\\
[\mathbf{T}_1 \cdot \mathbf{S}_2^1 \times \mathbf{T}_2^{-1}] &= 4\pi i(6/5)NF,\\
[\mathbf{T}_1 \cdot \mathbf{S}_2^2 \times \mathbf{T}_2^{-2}] &= 4\pi i(12/5)NF,\\
[\mathbf{T}_1^1 \cdot \mathbf{S}_2^{-1} \times \mathbf{T}_2] &= 4\pi i(6/5)NF,\\
[\mathbf{T}_1^1 \cdot \mathbf{S}_2 \times \mathbf{T}_2^{-1}] &= -4\pi i(6/5)NF,\\
[\mathbf{T}_1^1 \cdot \mathbf{S}_2^1 \times \mathbf{T}_2^{-2}] &= -4\pi i(6/5)NF,\\
[\mathbf{T}_1^1 \cdot \mathbf{S}_2^{-2} \times \mathbf{T}_2^1] &= 4\pi i(6/5)NF,\\
[\mathbf{T}_2 \cdot \mathbf{S}_1^1 \times \mathbf{T}_2^{-1}] &= 4\pi i(2/5)NF,\\
[\mathbf{T}_2^1 \cdot \mathbf{S}_1 \times \mathbf{T}_2^{-1}] &= -4\pi i(2/5)NF,\\
[\mathbf{T}_2^1 \cdot \mathbf{S}_1^1 \times \mathbf{T}_2^{-2}] &= 4\pi i(2/5)NF,\\
[\mathbf{T}_2^2 \cdot \mathbf{S}_1 \times \mathbf{T}_2^{-2}] &= -4\pi i(4/5)NF.
\end{aligned}
$$

Here, N stands as an abbreviation for the product of the normalization factors

$$N=N(\alpha)N(\beta)N(\gamma),$$

where $N(\alpha)$, etc., is the normalization factor given by the square root in (22), Part I. F stands for the integral over the radial functions as given by (39), Part I.[12] F is a function of n and of indices, s, of the radial functions; the sundry indices, n and s, of each individual F have been omitted for the sake of simplicity.

The matrix elements of poloidal flow are:

$$
\begin{aligned}
[\mathbf{S}_1 \cdot \mathbf{S}_1 \times \mathbf{T}_2] &= 4\pi(4/5)NG^-,\\
[\mathbf{S}_1^1 \cdot \mathbf{S}_1 \times \mathbf{T}_2^{-1}] &= 4\pi(2/5)NG^-,\\
[\mathbf{S}_1^1 \cdot \mathbf{S}_1^{-1} \times \mathbf{T}_2] &= -4\pi(2/5)NG^-,\\
[\mathbf{S}_1^1 \cdot \mathbf{S}_1^1 \times \mathbf{T}_2^{-2}] &= 4\pi(2/5)NG^-,\\
[\mathbf{S}_2 \cdot \mathbf{S}_1 \times \mathbf{T}_1] &= 4\pi(4/5)NG^+,\\
[\mathbf{S}_2 \cdot \mathbf{S}_1^1 \times \mathbf{T}_1^{-1}] &= -4\pi(2/5)NG^+,\\
[\mathbf{S}_2 \cdot \mathbf{S}_2 \times \mathbf{T}_2] &= 4\pi(36/35)NG^-,\\
[\mathbf{S}_2 \cdot \mathbf{S}_2^1 \times \mathbf{T}_2^{-1}] &= 4\pi(18/35)NG^-,\\
[\mathbf{S}_2 \cdot \mathbf{S}_2^2 \times \mathbf{T}_2^{-2}] &= -4\pi(36/35)NG^-,\\
[\mathbf{S}_2^1 \cdot \mathbf{S}_1 \times \mathbf{T}_1^{-1}] &= 4\pi(6/5)NG^+,\\
[\mathbf{S}_2^1 \cdot \mathbf{S}_1^{-1} \times \mathbf{T}_1] &= 4\pi(6/5)NG^+,\\
[\mathbf{S}_2^1 \cdot \mathbf{S}_2^{-1} \times \mathbf{T}_2] &= 4\pi(18/35)NG^-,\\
[\mathbf{S}_2^1 \cdot \mathbf{S}_2^1 \times \mathbf{T}_2^{-2}] &= 4\pi(54/35)NG^-,\\
[\mathbf{S}_2^2 \cdot \mathbf{S}_1^{-1} \times \mathbf{T}_1^{-1}] &= 4\pi(12/5)NG^+,\\
[\mathbf{S}_2^2 \cdot \mathbf{S}_2^{-2} \times \mathbf{T}_2] &= -4\pi(36/35)NG^-\\
[\mathbf{S}_2^2 \cdot \mathbf{S}_2^{-1} \times \mathbf{T}_2^{-1}] &= 4\pi(36/35)NG^-.
\end{aligned}
$$

Here, N has the same significance as before, and

$$
\begin{aligned}
G^+ &= G_\alpha + G_\beta,\\
G^- &= G_\alpha - G_\beta,
\end{aligned}
$$

where G_α is the integral over the radial functions given by (43), Part I. The sundry indices, n and s, of the individual G's have again been omitted.

In using these formulas it might be remembered that

$$P_n^{-m}(\cos\vartheta)=\frac{(n-m)!}{(n+m)!}P_n^m(\cos\vartheta).$$

[12] In this formula read rdr in place of r^2dr. Other corrections: In formula (41) the right-hand side should be negative. In formula (44) insert a factor G_α in front of the second integral.

For the *normalized* vectors, however, we find readily $(\mathbf{T}_n^m)^* = \mathbf{T}_n^{-m}$ and similarly for the vectors **S**.

There are twelve elements in the first table and sixteen in the second. From these, additional matrix elements are derived by the following two operations: First, permutation of any two or three of the vectors in the bracket, on giving the bracket the positive or negative sign according to whether the permutation is of even or odd order. Secondly, a change of sign of all the upper indices in any one bracket. The total number of matrix elements of toroidal flow thus obtained is forty, that of elements of poloidal flow is forty-six. There are, in addition, forty-six matrix elements of scaloidal flow which differ from those of poloidal flow only in the form of the integrals over the radial functions. All matrix elements involving dipole and quadrupole vectors only which are not contained in this extended table, vanish in accordance with the selection rules derived in Part I.

MAGNETIC DIPOLE INTERACTIONS

In order to analyze the physical effects corresponding to the individual matrix elements we may classify the various vectors according to their order of magnitude. This is readily done for the magnetic field, that is for the "primary" magnetic vector of the matrix elements. The zonal dipole term is dominant, next comes the tesseral dipole term whose magnitude is about 20 percent of the former. The quadrupole terms are much smaller; the root-mean-square value of their potential over the earth's surface amounts to about 3.7 percent of the zonal dipole;[5] the fraction at the boundary of the core is about 6.5 percent.

It is much more difficult to estimate the relative magnitude of the components of the fluid motion. We must distinguish between the mean motion obtained from the time-average over the large scale turbulent deviations on the one hand, and the instantaneous pattern of the motion on the other. As far as the *mean* motion is concerned it may safely be assumed, on general principles of geophysical and astrophysical hydrodynamics, that the toroidal terms are predominant; they must be odd, $\mathbf{T}_1$, $\mathbf{T}_3$, $\mathbf{T}_5$, etc. and they represent a flow directed along the circles of latitude. Such a mean motion must, however, be accompanied by a subsidiary mean motion of the poloidal type; these vectors must be even, $\mathbf{S}_2$, $\mathbf{S}_4$, $\mathbf{S}_6$, etc. and they represent circulations with streamlines confined to the meridional planes. The magnitude of this meridional circulation may safely be assumed to be smaller than that of the zonal toroidal flow.

If we consider the instantaneous motion, including large-scale turbulence, it is still probable that the zonal flow predominates, but the turbulent velocities might occasionally be of comparable magnitude. As far as the harmonic components of the turbulent motion other than $\mathbf{T}_1$, $\mathbf{T}_3$, $\mathbf{T}_5$, etc. are concerned, it is difficult to make general statements, except that most of them are probably of about the same order of magnitude and that the development of the turbulent velocity field in terms of spherical harmonics converges extremely slowly.

We shall now assume that the "primary" magnetic field appearing in the matrix elements is given by the dipole terms, $\mathbf{S}_1$ and $\mathbf{S}_1^1$, $\mathbf{S}_1^{-1}$ alone. For any given term of the "secondary" magnetic field we can then find a number of matrix elements in the above table by which this term of the secondary field is produced through the action of specific components of the fluid motion. In the following discussion we shall limit ourselves to those cases where the secondary magnetic field is also a dipole. The preceding tables contain seven matrix elements in which both the primary and the secondary field are dipoles.

We begin with the first element in the table of toroidal flow; it represents an interaction of the tesseral dipole with itself.[13] The velocity vector, $\mathbf{T}_1$, appearing in this matrix element is presumably the largest term of the mean fluid motion. Consider now a fluid motion which contains this term only. Even in this case there is still an infinite set of such matrix elements distinguished from each other by the index, s, of the radial eigenfunction of the primary field and by the corresponding index of the secondary field. As far as the radial function of the fluid motion is concerned, we have pointed out in

[13] It should be remembered that the last vector in the bracket is conjugate complex to the component actually appearing in the secondary field.

Part I that there is no need for a development into orthogonal components, and we may, therefore, assume that there is only one radial eigenfunction of the velocity vector under the radial integrals.

As has been shown in Part I, the coupling matrix of toroidal flow is anti-symmetrical with respect to the primary and secondary field. It may readily be shown that this particular anti-symmetry comes about by the interchange of the indices n, m alone and that the coupling matrix is symmetrical with respect to an exchange of s_β and s_γ. We may therefore now assume that the matrix has been brought to its diagonal form with respect to the index s, and we can select a single diagonal element for which the equations of motion (10) become

$$\begin{aligned} dc_1^1/dt &= (8\pi/3)^{-\frac{1}{2}}(w_1 F/R)ic_1^1, \\ c_1^1 &= \text{const. } \exp\left[(8\pi/3)^{-\frac{1}{2}}(w_1 F/R)it\right]. \end{aligned} \tag{14}$$

The integration is performed here under the assumption of stationary fluid motion. The constant, w_1, has the dimension of a velocity and is the coefficient of $\mathbf{T}_1$ in the development (9) of the velocity field. F is the radial integral, of the form (39), Part I, which contains those linear combinations of the radial eigenfunctions of the field that make the matrix diagonal with respect to the index s. The motion of the tesseral dipole described by (14) is a rotation about the earth's axis. On assuming for this rotation the value of 4.5 degrees per century quoted before we can compute the velocity, w_1. We need only estimate F; this, being an integral over normalized functions, cannot exceed unity. On putting $F=0.3$ we find[14]

$$w_1 \sim 0.01 \text{ cm/sec.}$$

Next, we consider the coupling between the zonal and tesseral dipole terms. One such interaction is obtained from the first matrix element of the table of toroidal flow by a transposition, namely

$$[\mathbf{T}_1^{-1} \cdot \mathbf{S}_1^1 \times \mathbf{T}_1] = -4\pi(2/3)NF,$$

and the inverse action is given by the second element of the table. On performing again the reduction to diagonal form with respect to the radial index, s, we arrive at the following set of equations

$$\begin{aligned} dc_1/dt &= -(8\pi/3)^{-\frac{1}{2}}(w_1^{-1}F_1^{-1}/R)ic_1^1, \\ dc_1^1/dt &= -(8\pi/3)^{-\frac{1}{2}}(w_1^1 F_1^1/R)ic_1, \end{aligned} \tag{15}$$

where, for instance $F_1^{-1} = F(_1{}^{-1}{}_1{}^1{}_1{}^0)$ and similarly for F_1^1. The solutions are harmonic functions of the time; they are of opposite phase for the two coefficients. The existence of the effect depents on the presence of the components $\mathbf{T}_1^1$ and $\mathbf{T}_1^{-1}$ in the fluid motion; the simplest way of producing these components is to let the fluid rotate about an axis different from that of the earth. As indicated in the appendix, there exist some rather serious reasons against the casual assumption of a change in the rotational axis of the fluid, so that one would not dare draw any further conclusions without a more far-reaching hydrodynamical basis.

The interactions just analyzed exhaust the dipole couplings caused by toroidal flow. On going now to the second table, of poloidal flow, we find there the element, fifth in the list

$$Q = [\mathbf{S}_2 \cdot \mathbf{S}_1 \times \mathbf{T}_1], \tag{16}$$

representing a coupling of the main, zonal dipole with itself. This matrix element is the only one in which both the primary and the secondary field are equal to the main dipole. To show this, note first that the fluid motion in such a matrix element must obviously have rotational symmetry, that is, $m=0$. If now the velocity vector were toroidal, the corresponding matrix elements would vanish because $\mathbf{T}_n \times \mathbf{T}_m = 0$, identically for any two zonal toroidal vectors. Again, if the velocity vector is poloidal, the matrix elements involving higher harmonics, $\mathbf{S}_4$, $\mathbf{S}_6$, etc., vanish by virtue of the selection rules. Hence we are left with the matrix elements of the type (16) as the only one expressing an interaction of the main dipole with itself.

There is, in reality, again a twofold infinity of such matrix elements labeled by the radial indices s_β and s_γ, but now the matrix is no longer simply symmetrical or simply anti-symmetrical with respect to these two indices, as may be seen from the form of the radial integrals given by

[14] Erratum: On the lower right-hand side of page 111, Part I, read $v \sim 2$ mm/hour, and at the end of this paragraph read: "of the order of several decimeters per hour."

(43), Part I. The equations of motion (10) may now be written, if we set $s_\beta = s$, $s_\gamma = s'$

$$dc_s/dt + \Lambda_s c_s = v_2 R^{-1} \sum_{s'} Q(s, s') c_{s'}, \qquad (17)$$

where v_2 is the coefficient of $\mathbf{T}_2$ in the development (9) of the velocity field. The matrix elements, $Q(s, s')$ are all real quantities; therefore the coefficients c_s vary in magnitude, roughly speaking, in an exponential manner. Since the matrix in (17) cannot, in general, be reduced to diagonal form, a stationary mechanism of amplification cannot be assumed to exist, as has already been stated at the end of Part I. Instead, it must be assumed that the representative point of the system describes an irregular curve in the multi-dimensional space subtended by the coefficients c_s. This irregularity of the magnetic amplification or de-amplification is superposed upon the statistical behavior arising out of the turbulent character of the fluid motion. There might also exist a stratification of the fluid near the boundary so that the velocity pattern changes appreciably with increasing depth. If this condition holds the secular variation of the dipole terms shown in Fig. 1 might be attributed to a transient flow pattern in the topmost layer. The numerical values of the velocity to be computed from this type of interaction will be of the same general order of magnitude as given before for toroidal flow.

We now proceed to the next matrix element that involves an interaction between magnetic dipole terms. This is the sixth in the list of matrix elements of poloidal flow and describes an interaction of the perpendicular dipole with itself. This element contains the same component of the velocity, $\mathbf{S}_2$, as the preceding one; it differs from the latter only in so far as the coefficients of the radial eigenfunctions of the perpendicular dipole field may be different from those of the parallel dipole field. If these coefficients are alike, the two sets of matrix elements are equal in magnitude and opposite in sign. This action will tend to de-amplify the perpendicular dipole when the parallel dipole is amplified. In order to account for the presence of a perpendicular dipole one must rely on other interaction terms, a conclusion which seems obvious from the rotational symmetry of the velocity vector $\mathbf{S}_2$ appearing in these matrix elements.

There are two more matrix elements in the table of poloidal flow that represent dipole interactions. The tenth element of this table has the main dipole for its primary and a perpendicular dipole for its secondary field. The eleventh element represents the reverse interaction. Both couplings are produced by the velocity component $\mathbf{S}_2^1$. Finally, the third element from the bottom of the list describes an interaction of the perpendicular magnetic dipole with itself, engendered by the velocity component $\mathbf{S}_2^2$.

LIMIT OF AMPLIFICATION

In what precedes we have been concerned with an interpretation of the secular variation in terms of fluid motions. The question arises naturally of whether the amplifying mechanism which we have shown to exist is of such a nature that it could maintain the earth's field over an interval of time long compared with the periods of free decay. From the mathematical viewpoint this question is connected with the symmetry of the coupling matrix, as we have seen in Part I. If the coupling matrix is antisymmetrical the field decays; if the coupling matrix were symmetrical, on the other hand, a mechanism of indefinite amplification could at once be constructed. Now we have seen that the actual coupling matrix is in no case purely symmetrical. It seems difficult to demonstrate whether the symmetry of the coupling matrix is not only sufficient, but also a necessary condition of indefinite amplification.

Some further study makes it highly probable, however, that the amount of amplification is in any case limited,* so that the field would decay in the average over a long time. So long as the free decay is neglected the relative amplification can be estimated from Eq. (7) which shows it to be equal to the convergence of the flow normal to the magnetic lines of force. The changes in field intensity, therefore, represent a compression or expansion, as the case may be, of the magnetic flux rather than a creation of new flux. Thus, the

* This has been pointed out by Dr. T. G. Cowling to whom the author is greatly indebted for the communication of his results. This note and the above remarks have been added in proof.

problem of the long term maintenance of the earth's magnetic field involves phenomena different from the amplification mechanism studied here; we hope to return to this question in a future paper.

It is interesting to remark that there exists a limit of amplification which is quite independent of the mechanism of amplification itself; it is found in the magneto-mechanical forces exerted by the field upon the fluid. These forces become significant when they are comparable in magnitude with the purely mechanical forces which engender or control the fluid motion; in the earth's core this condition is nearly fulfilled. It is well known that the magneto-mechanical forces are directed so that they will tend to counteract the amplification of the field. Thus, for a sufficiently strong field, these forces will slow down and eventually prohibit further amplification. Whether or not this effect is significant for the earth can hardly be said at present, but it will be of interest to carry out the numerical estimate which is simple. The mechanical force produced by the field is given by the formula

$$\mathbf{F}=\mathbf{J}\times\mathbf{B}.$$

Here, $\mathbf{J}$ is the current density which can be written

$$\mathbf{J}=\sigma\mathbf{v}\times\mathbf{B}-\sigma\partial\mathbf{A}/\partial t.$$

We may confine ourselves to the first term on the right-hand side for an estimate of the order of magnitude. Thus, apart from numerical factors the mechanical force is of the order

$$F\sim\sigma vB^2,$$

where the italics stand for the magnitude of the corresponding vectors. We can expect that the magnetic field approaches a limiting value when this force becomes comparable to the forces in the fluid which engender the motions. As explained in the appendix these forces are in absolute magnitude very nearly equal to the Coriolis force,

$$F_c\sim 2\omega\rho v.$$

On equating the two expressions for the forces we obtain for this critical field strength

$$B_{\text{crit}}=(2\omega\rho/\sigma)^{\frac{1}{2}},$$

and numerically,

$$B_{\text{crit}}\sim 12 \text{ gauss}.$$

APPENDIX

In this appendix a few physical data on the earth's core which have immediate significance for our problem are collected. These include density, pressure, temperature, and electric conductivity. Last, not least, some elementary applications of hydrodynamics to motions in the core must be considered.

The direct information about the earth's core comes from seismology.[15,16] There seems to be fairly general agreement about the fluidity of the core, based upon the fact that transverse seismic waves are never transmitted by the core. There is, however, accessory evidence for the fluidity derived from the analysis of the tides of the solid earth.[17] Not so long ago Bullen[18] has made exhaustive determinations of the variation of density, pressure, and compressibility in the core. These are based on a critical analysis of seismological data by Jeffreys.[19]

The core has a radius, R, equal to 0.55 of the earth's radius, and the discontinuity of seismic velocity at the boundary of the core is perhaps the most outstanding single result of seismological observation. According to Bullen the density of the core at its boundary is 9.43 g/cm³; from there it increases steadily and smoothly to 11.54 g/cm³ at $0.40R$. Below $0.40R$ the density begins to increase very rapidly, and there appears to be a surface of discontinuity at $0.36R$ where the density changes from 14.2 to 16.8; thereafter it increases very slowly to about 17.2 at the earth's center. It is believed that the data for the upper half of the core are accurate to within a few percent while those for the central part of the earth are much less reliable. The hydrostatic pressure in the core is 1.37×10^{12} dyne/cm² (1.4×10^{6} atmospheres) at the boundary, increasing to 3.17×10^{12} dyne/cm² at $0.40R$.

We shall pass without discussion over the various arguments propounded by chemists to the effect that the predominant chemical component of the core is metallic iron, perhaps with a slight admixture of nickel. The internal structure of the core as revealed by the work of Jeffreys and Bullen makes it more probable that the main constituents of the upper part of the core, between R and $0.40R$, are the metals of the iron group. If the density curve as found between these limits is extrapolated to lower pressures it passes smoothly into the density curve for iron at high laboratory pressures measured by Bridgman.[20] If the

[15] See reference 1 of Part I.
[16] H. Jeffreys, *The Earth* (The Macmillan Company, New York, 1929), second edition.
[17] H. Jeffreys, M.N.R.A.S., Geophys. Suppl. 1, 376 (1926).
[18] K. E. Bullen, Bull. Am. Seismol. Soc. **32**, 19 (1942).
[19] H. Jeffreys, M.N.R.A.S. Geophys. Suppl. **4**, 594 (1939).
[20] P. W. Bridgman, Proc. Nat. Acad. Sci. **8**, 361 (1922); Proc. Am. Acad. Sci. **58**, 163 (1923).

curve is extrapolated to the side of high pressures it passes into a theoretical curve for extremely compressed iron computed by Jensen.[21]

The temperature of the core is not known, but we have two independent estimates of an upper limit. Jeffreys[22] states that the temperature at the core's boundary cannot exceed the melting point of the overlying solid; on estimating the latter he arrives at a temperature of 10,000° abs. for the boundary. Eucken[23] points out that separation of the solid and liquid phases in the earth would not have taken place unless the temperature of the mixture was less than the critical temperature of the liquid which he estimates, for iron, as 9000° abs., the critical pressure being 7300 atmos.

The electrical conductivity of the core, more precisely of the upper part, between R and $0.40R$, may be estimated as follows, assuming the matter to be mostly iron. According to the theory of electronic conductivity, σ is inversely proportional to the absolute temperature, T, and directly proportional to the square of the Debye temperature, Θ. The latter, in turn, is, apart from a slowly varying factor, proportional to the velocity of sound, known from seismic observations to be about twice as large as in ordinary iron. Taking $T=30T_0$ and $\Theta=2\Theta_0$ where the index 0 refers to laboratory conditions we have, apart from some other slowly varying factors that are difficult to evaluate, $\sigma=0.133\sigma_0$ which is slightly larger than the value, $\sigma=0.1\sigma_0$, adopted here. Since this value is relatively small as electronic conductivities go, it may be assumed that such impurities as are present have a relatively minor effect on the conductivity. It might be noted here that Cowling[24] has recently calculated the electric conductivity of the sun's interior; his figures are, very crudely, of the same general order as ours, larger for the central part and smaller for the upper strata of the sun.

Next we shall deal with motions in the core. Considering first pure inertial effects, we must mention an important paper by Poincaré.[25] The problem studied by him is whether the fluid of the core lags behind the precession of the earth's solid body which, as is well known, has a period of 11,000 years. Poincaré succeeds in showing that there should be no lag. If the fluid is enclosed in an ellipsoidal vessel the degree of lag depends on the numerical excentricity of the boundary. If the latter number is large compared to the ratio of the frequency of precession to the frequency of revolution, the fluid follows the precession of the vessel as if it was a rigid body. Now it is known from the theory of the earth's figure that the eccentricity of the core's boundary is not much less than the eccentricity at the earth's surface, whence Poincaré's result follows. In its derivation the assumption is made that the fluid is incompressible, but this should hardly be too serious a restriction.

The hydrodynamical equations for the fluid in the core are

$$d\mathbf{v}/dt+2\boldsymbol{\omega}\times\mathbf{v}=\rho^{-1}(\mathbf{F}-\nabla p),$$

where $\boldsymbol{\omega}$ is the vectorial angular velocity of the earth, p the pressure, ρ the density, and $\mathbf{F}$ the combined gravitational and centrifugal forces. Now consider small deviations from equilibrium and put

$$p=p_0+p_1 \text{ where } \mathbf{F}=\nabla p_0.$$

The equations of motion then become

$$d\mathbf{v}/dt+2\boldsymbol{\omega}\times\mathbf{v}=-\rho^{-1}\nabla p_1.$$

The first term on the left-hand side, representing the accelerations, is small compared to the second term, the Coriolis term. The methods by which this is proved are extensively discussed in textbooks on dynamic meteorology or oceanography. The hydrodynamical conditions in the core resemble somewhat those in the ocean; the densities differ by a factor of ten and the molecular viscosities should be of the same general order of magnitude if the core consists of liquid metal. We now have the approximate equation

$$2\boldsymbol{\omega}\times\mathbf{v}=-\rho^{-1}\nabla p_1 \qquad (18)$$

as the condition of quasi-stationary flow. From this relation we may estimate the magnitude of the deviations from equilibrium pressure. For two points at a distance L from each other we get

$$\Delta p_1\sim 2\omega v\rho L.$$

Taking $v=0.03$ cm/sec. and $L=3.10^8$ cm,

$$\Delta p_1\sim 1.3\times 10^4 \text{ dyne/cm}^2.$$

This is a pressure difference of only about 1 cm of mercury, or one part in 10^6 of the total hydrostatic pressure. These deviations from hydrostatic equilibrium are so minute that it seems of little use to speculate at present about their possible causes. The smallness of these pressure differences is a direct expression of the prevalence of the gyroscopic forces; the fluid reacts upon disturbances of its static equilibrium by setting up a flow pattern that balances these disturbances through the action of the Coriolis force.

In deriving the preceding relationships we have ignored the action of the magneto-mechanical force on the fluid motion. So long as this force is neglected our argument is in complete analogy to the conventional analysis for meteorological and oceanographical problems of this type. The magneto-mechanical force gives rise to an additional term on the left-hand side of (18) which is linear in the velocity. We have previously shown that with the magnitude of the field actually found in the core this term is comparable in magnitude to the Coriolis term. It follows that the estimated order of magnitude of the deviations from hydrostatic equilibrium pressure remains substantially the same in the presence of this term.

---

[21] H. Jensen, Zeits. f. Physik **111**, 373 (1938).
[22] H. Jeffreys, M.N.R.A.S., Geophys. Suppl. **3**, 6 (1932).
[23] A. Eucken, Nach. Gött. Akad. 1944, No. 1; Naturwiss. **32**, 112 (1944).
[24] T. G. Cowling, M.N.R.A.S. **105**, 166 (1945).
[25] See H. Lamb, *Hydrodynamics* (Cambridge University Press, England, 1932), sixth edition, Sec. 384.

The Inversion Spectrum of Ammonia*

WILLIAM E. GOOD
Westinghouse Research Laboratories and the University of Pittsburgh, Pittsburgh, Pennsylvania
(Received May 27, 1946)

Ammonia gas is known to exhibit a strong absorption in the region of 0.8 cm^{-1}. By sweeping the frequency of a continuous wave oscillator and using a balanced wave guide system with one arm of the wave guide serving as an absorption chamber, thirty lines of the fine structure, as predicted by Sheng, Barker, and Dennison, have been observed in this region. Their intensities and frequencies have been measured for two different temperatures and an empirical expression for the frequencies of the lines in terms of their rotational quantum numbers is given. At pressures of 5×10^{-1} mm Hg and below, the lines are very well resolved. At pressures of 10^{-2} mm Hg and below, a definite hyperfine structure appears. The Stark effect is also observed when a d.c. field is applied to the absorbing gas.

I. INTRODUCTION

AMMONIA gas affords an interesting subject of investigation because it is possible to study one of its molecular transitions by using radiofrequency techniques. In 1934 Cleeton and Williams[1] found that ammonia gas gave a strong absorption line at 0.8 cm^{-1} (1.25-cm wave-length or 24,000 mc/sec.). With the equipment that is now available in the one-centimeter region, it is possible to carry their work much further.

The ammonia molecule can be considered to be a regular pyramid with the nitrogen atom at the apex and the three hydrogen atoms in a triangle forming the base (see Fig. 1). Dennison and Hardy[2] and Dennison and Uhlenbeck[3] have shown that the vibrational energy levels are split into pairs[4] because of the two positions of equilibrium for the nitrogen atom. The energy difference between the two levels of the lowest pair is the energy difference which Cleeton and Williams investigated and the one in which we are interested. This "inside-out" effect or "inversion" of the molecule also gives rise to a doubling of the far infra-red absorption lines of ammonia[5] and Herzberg[6] has called it "inversion doubling." It follows that the absorption spectrum in the 0.8 cm^{-1} region could be called the "inversion spectrum." It is this inversion spectrum that is investigated in this paper.

Unpublished work by Howe[7] and others showed that as the pressure of the ammonia gas is reduced, this main absorption line becomes narrower. Sheng, Barker, and Dennison[8] have predicted a fine structure for this line, which should be observable providing the pressure can be reduced sufficiently to make possible the resolution of the individual lines.

This paper is primarily concerned with the measurement and the interpretation of this fine structure. Thirty absorption lines have been observed and their frequencies and intensities measured.

II. EXPERIMENTAL

The frequency source used in this investigation is a continuous wave oscillator tube. It is of the type that can be tuned continuously over a broad frequency region and it may be swept

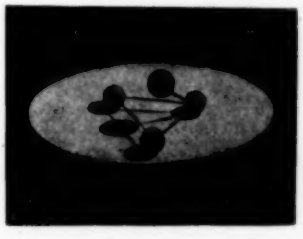

FIG. 1. The NH_3 molecule.

* Submitted to the Graduate School of the University of Pittsburgh in partial fulfillment of the requirements for the degree of Doctor of Philosophy.

[1] C. E. Cleeton and N. H. Williams, Phys. Rev. **45**, 234 (1934).

[2] D. M. Dennison and J. P. Hardy, Phys. Rev. **39**, 938 (1932).

[3] D. M. Dennison and G. E. Uhlenbeck, Phys. Rev. **41**, 313 (1932).

[4] G. Herzberg, *Infrared and Raman Spectra* (D. Van Nostrand Company, New York, 1945), pp. 221–224.

[5] N. Wright and H. M. Randall, Phys. Rev. **44**, 391 (1933).

[6] Reference 4, p. 27.

[7] H. S. Howe, Doctorate Thesis, University of Michigan (1940).

[8] Sheng, Barker, and Dennison, Phys. Rev. **60**, 786 (1941).

rapidly in frequency by applying a varying voltage to one of its electrodes.

A wave guide system is used, one section of which (about two meters long) is sealed at the ends with a thin dielectric tape so as to make it pressure tight. This section is the absorption cell and is connected to a vacuum pump and gas filling apparatus. A crystal detector is used to detect the radiofrequency power after it passes through the absorption cell. A block diagram of the apparatus is shown in Fig. 2. The radio waves leave the oscillator and travel down the wave guide past the first variable attenuator (used to adjust the power level in the rest of the system) to the "T" section in the center of the diagram. Here the energy splits and half of it passes through the absorption cell on the right and thus to the right-hand crystal, the other half proceeds down the left wave guide past the various attenuators to the left-hand crystal detector. The rectified currents from the two crystal detectors are passed through two equal resistances (R) to ground. A galvanometer is connected across the two resistors. This arrangement permits the system to be balanced by adjusting the variable attenuator in the left-hand arm to give zero galvanometer current. Once this is done fluctuations in the oscillator power will cause approximately equal fluctuations in the two crystal currents and are thus balanced out. This balanced system is particularly useful when measuring small attenuations. To make an absorption measurement the gas cell is evacuated and the left-hand variable attenuator is adjusted to give zero galvanometer current. The gas is then introduced into the gas cell. The unbalance caused by the absorbing gas is corrected by adjusting the calibrated attenuator so that the galvanometer is returned to zero. The attenuation of the gas is read directly from the calibrated attenuator. To measure the absorption of the gas *vs.* frequency, it is necessary to change the frequency step by step and repeat the above for each frequency. When the absorption lines are sufficiently sharp, it is easier to observe a particular line by sweeping the frequency of the oscillator over the frequency range of the line. This can be done by applying a sawtooth voltage to one of its electrodes. This same sawtooth voltage is applied to the horizontal deflection plates of an oscilloscope tube, thus making the horizontal scale a frequency scale, because the oscillator frequency and the oscilloscope spot are being swept in synchronism. A balanced amplifier serves to amplify the difference voltage that is developed across the two resistors and apply it to the vertical deflection plates of the oscilloscope. Thus, if there is no gas in the absorbing cell the trace on the scope should remain flat, as the frequency of the oscillator is swept. However, if the gas that is introduced absorbs energy in a part of the frequency region that is being swept, the system will be unbalanced and the scope trace will be deflected by an amount proportional to the magnitude of the absorption (see Figs. 3 and 4). The scope is connected so that the absorption is positive upwards.

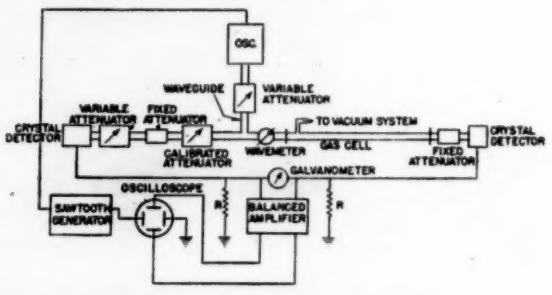

FIG. 2. Block diagram of apparatus.

The cavity type wavemeter that is coupled to the right-hand wave guide has the same effect as the absorbing gas. As the oscillator frequency sweeps through the frequency to which the wave meter is tuned, the wavemeter absorbs energy and its resonance curve is traced out on the scope. Its shape and appearance are very similar to the NH_3 absorption lines shown in Fig. 3. To measure the frequency of an absorption line, it is only necessary to superpose the wavemeter "pip" on the absorption line and read the wavemeter dial. The wavemeter was calibrated by using the harmonics from an oscillator that was synchronized with the standard frequency from the Bureau of Standard's station WWV. The calibrated attenuator was calibrated using a thermister type bolometer in a bridge circuit.

The inversion spectrum fine structure was found to be very well resolved at pressures below 0.5 mm of Hg. Further reduction of pressure caused the individual lines to become sharper as shown in Figs. 3 and 4. The width and shape

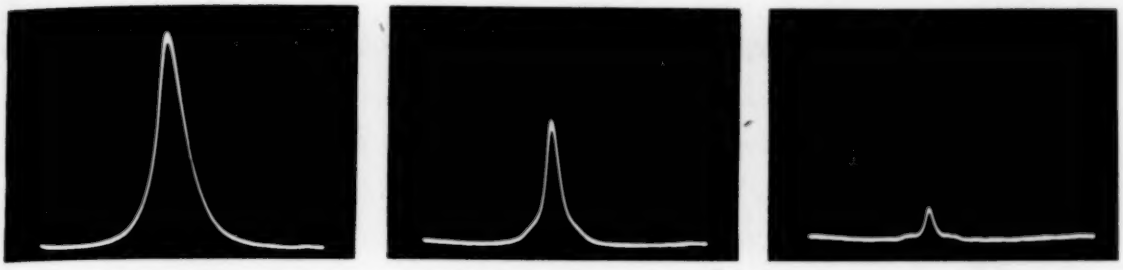

(a) $p=5\times10^{-2}$ mm Hg (b) $p=2.5\times10^{-2}$ mm Hg (c) $p=9\times10^{-3}$ mm Hg

FIG. 3. Oscilloscope picture of absorption *vs.* frequency for one line of the fine structure for different pressures. $J=3$, $K=3$; full scale 22 mc/sec.; $T=297°$K.

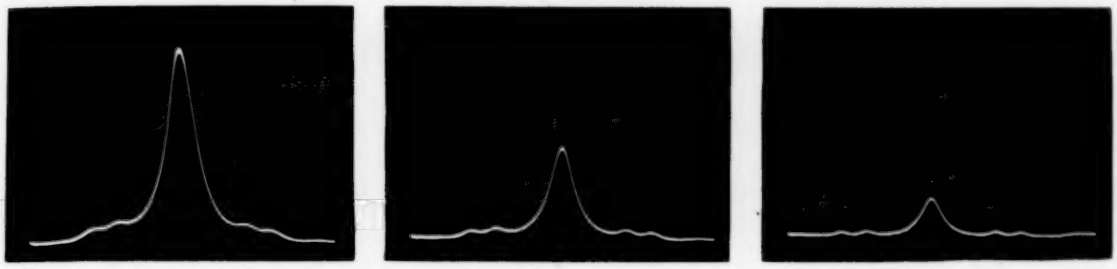

(a) $p=1.5\times10^{-2}$ mm Hg (b) $p=9\times10^{-3}$ mm Hg (c) $p=5\times10^{-3}$ mm Hg

FIG. 4. Oscilloscope picture of absorption *vs.* frequency for one line of the fine structure for different pressures showing the hyperfine structure. $J=3$, $K=3$; full scale 8.6 mc/sec.; $T=297°$K. Note difference in frequency scale between Figs. 3 and 4.

of the line shown is entirely caused by the gas itself and is not affected particularly by this method of observation. This is true because the natural width of the oscillator tube spectrum is extremely small compared to the width of the line being observed.

Two sets of data have been taken. The frequencies and the intensities of the inversion spectrum fine structure have been measured for two different temperatures but approximately the same pressures. These data are plotted in Figs. 5 and 6. To insure the same pressure for a series of measurements the gas was introduced into the absorption cell and left there during the whole run. To obtain a zero balance for each line the frequency of the oscillator was set to one side of the line and the system was balanced. Then the frequency was shifted the few megacycles needed to bring it to the peak of the absorption line (maximum galvanometer deflection) and the calibrated attenuator was adjusted for balance and read.

The measurement of the frequencies is accurate to about ±5 megacycles. The measurement of attenuation is accurate to about ±10 percent.

Because of the fact that the wave guide wavelength is different from the free space wavelength, a correction factor $\lambda/\lambda g$ must be applied to each value of intensity to correct it to the value it would have if it were measured in free space. This correction has been applied to all of the data in this report.

III. DISCUSSION

As mentioned before, the transition that gives rise to the inversion spectrum is the one between the two levels of the split vibrational ground state. The splitting can be explained by the fact that the nitrogen atom has two positions of equilibrium—one on either side of the plane of the hydrogen atoms. The nitrogen atom may pass through the potential hill, which exists in the region of the plane of the hydrogen atoms, by a tunneling process.[9] The amount of the splitting of the vibrational levels is a sensitive function of the height and breadth of this potential barrier. It is reasonable to expect that the shape of the potential barrier will be a function of the rotational level that a molecule is in.

[9] Reference 4, pp. 221–224.

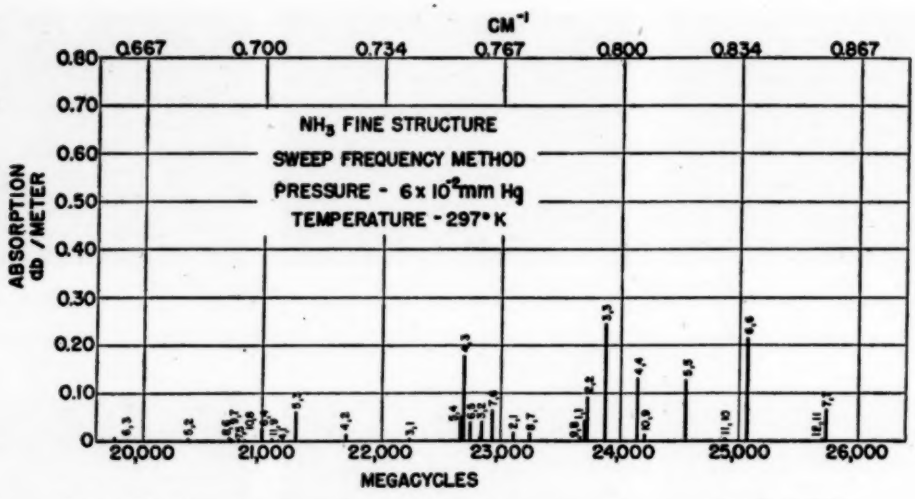

FIG. 5. The inversion absorption spectrum fine structure for ammonia. $T=297°K$.

Indeed, Sheng, Barker, and Dennison[10] explain this absorption fine structure in terms of the different degrees of centrifugal distortion caused by the various molecules being in different rotational states. With each rotational state, there is associated a definite splitting and thus a definite spectrum line. The two quantum numbers J and K are used to indicate the rotational level of a particular molecule. K is the number of units of angular momentum about the symmetry axis while J is the total rotational quantum number. Sheng, Barker, and Dennison calculate that the wave numbers of the lines in the inversion fine structure can be represented by

$$\frac{\nu}{hc}(\text{cm}^{-1})=\frac{\nu_0}{hc}-0.0011(J^2+J)+0.0016K^2. \quad (1)$$

The expression that is obtained from the measured frequencies is

$$\frac{\nu}{hc}(\text{cm}^{-1})=0.79347-0.005048(J^2+J)$$
$$+0.007040K^2+0.00001546(J^2+J)^2$$
$$-0.00004260(J^2+J)K^2+0.00002920K^4. \quad (2)$$

The average deviation of the measured lines from the above expression (2) is about 0.01 percent. The difference between the two expressions seems to indicate that the theoretical model needs some modification. The numbers indicated above the lines in Figs. 5 and 6 are the J and K values for that line.

The intensities of the lines should be a function of the number of molecules in each rotational level and their transition probabilities. The number of molecules in a given level depends on the distribution of thermal energies and the statistical weights. The statistical weights depend on the value of J and the nuclear spin of the hydrogen atoms.[11] For this case the levels for $K=0$, 3, 6, 9, etc. will have twice the statistical weight of those for $K=1$, 2, 4, 5, 7, etc. Note the increased intensities of the lines for $K=3$ and 6 in Figs. 5–8. Because of the symmetry properties,[12] levels for $K=0$ are not split but merely displaced so that no inversion line should exist. No lines having $K=0$ were found.

Figure 7 shows a plot of the experimental intensities *vs.* frequency for separate K values. Figure 8 (a) shows the observed intensities for the strongest lines of different J values, while Fig. 8 (b) shows the relative intensities which were calculated following the suggestions in Herzberg.[13] Note the uniform distribution that would be obtained if the lines for $K=3$, 6, and 9 were reduced by a factor of two.

The low temperature data were taken to see if the effect of the thermal distribution "moving

[10] Sheng, Barker, and Dennison, Phys. Rev. 60, 786 (1941).

[11] Reference 4, pp. 27, 413.
[12] Reference 4, p. 413.
[13] Reference 4, pp. 27, 29, 422.

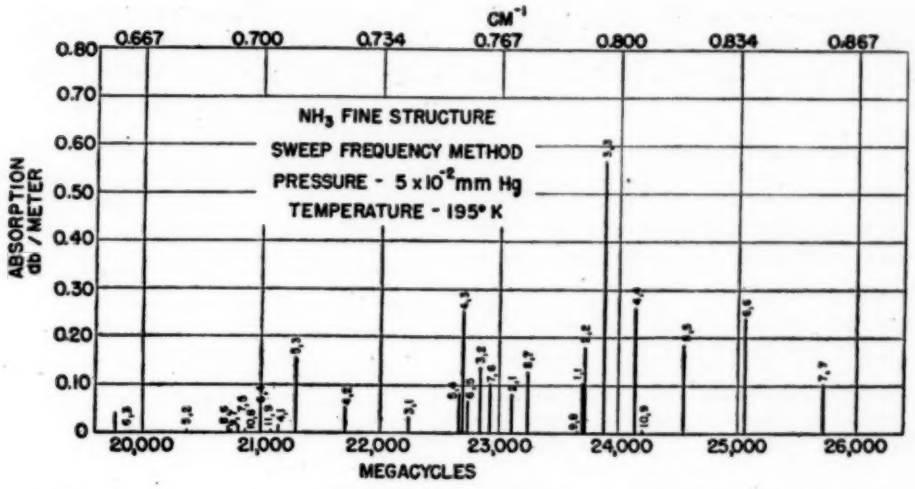

FIG. 6. The inversion absorption spectrum fine structure for ammonia. $T = 195°K$.

over" could be noticed. It was expected that the intensities of lines having lower values of J and K would increase and that of lines having higher values of J and K would decrease. This effect is apparent on careful examination of Figs. 5 and 6 but it is obscured by two other effects. First, for a temperature reduction of 300°K to 200°K there will be an increase of $\frac{3}{2}$ in the number of molecules, providing the pressure remains constant. Second, the average velocity of the molecules will be reduced by the lower temperature, therefore increasing the time between collisions which causes the lines to be sharper and thus relatively more intense. However, the pressure was reduced by 20 percent, so for direct comparison of Figs. 5 and 6 the magnitudes of the lines in Fig. 6 should be decreased by about $\frac{1}{3}$.

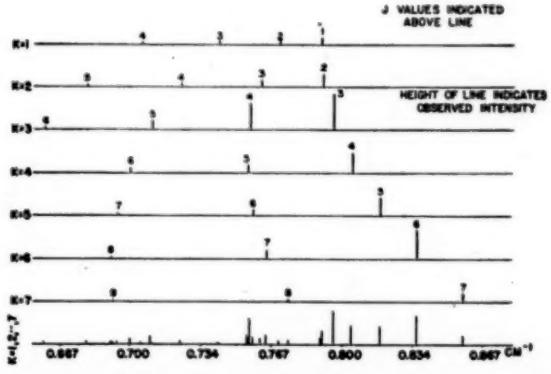

FIG. 7. The NH_3 inversion spectrum for different values of the rotational quantum number K. Composite spectrum shown on bottom line.

This collision broadening effect for diminishing pressure is shown graphically in Figs. 3 and 4. The collision broadening process is one of interruption of the absorbed wavetrain by a collision with another molecule. As the number of molecules is reduced, the time between collisions increases, the length of the absorbed wavetrain increases, and the absorption "line" becomes sharper. At a pressure of about 10^{-2} mm Hg the mean free path of the molecules should be about the same as the narrow dimension of the wave guide so that it would be expected that the line breadth would be more or less constant below this pressure.

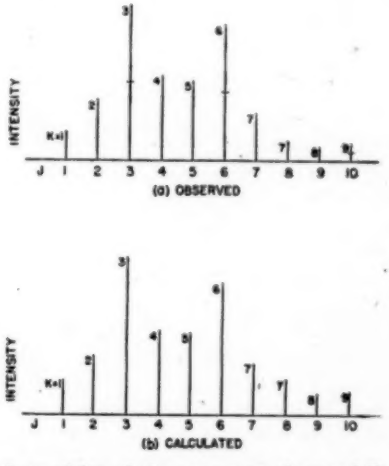

FIG. 8. Intensities of the strongest observed lines of the fine structure of NH_3 ($T = 300°K$). (a) Observed relative intensities; (b) Calculated relative intensities. Note the symmetrical distribution that would result providing the lines for $K = 3$, 6, and 9 were divided by two.

The above explanation would also give weight to the assumption that most of the absorbed energy finally appears as kinetic energy of the gas.

IV. CONCLUSIONS

Thirty absorption lines in the fine structure of the inversion spectrum of ammonia gas have been observed and identified with their rotational quantum numbers.[14] An empirical expression has been found which represents the wave numbers of the lines in terms of their J and K values. The intensities at room temperature compare well with those calculated from the thermal distribution of the rotational levels and the transition probabilities. The intensities at reduced temperature behave as expected and the variation of line breadth with pressure was demonstrated.

Figure 4 shows a definite hyperfine structure for the line $J=3$, $K=3$. Other lines show the same type of symmetrical structure but with different separations of the components.

A definite frequency shift (Stark effect) of the various lines was observed when a d.c. field was applied to the absorbing gas.

[14] This identification agrees with that of B. Bleaney and R. P. Penrose which is given in their letter to the editor in Nature **157**, 339 (1946).

Letters to the Editor

PROMPT publication of brief reports of important discoveries in physics may be secured by addressing them to this department. The closing date for this department is the third of the month. Because of the late closing date for the section no proof can be shown to authors. The Board of Editors does not hold itself responsible for the opinions expressed by the correspondents. Communications should not in general exceed 600 words in length.

Conductivity of Sodium-Ammonia Solutions

J. G. DAUNT, M. DÉSIRANT, AND K. MENDELSSOHN
Clarendon Laboratory, Oxford, England
AND
A. J. BIRCH
Dyson Perrins Laboratory, Oxford, England
July 5, 1946

RECENTLY Richard A. Ogg[1] has reported the occurrence of superconductivity in quickly frozen solutions of sodium in ammonia. In view of the fact that all other superconductors have transition points of the order of 5°K, corresponding to an excitation energy of 5×10^{-4} ev, the appearance of superconductivity at very much higher temperatures (about 200°K) is somewhat unexpected.

We have repeated Ogg's conductivity experiment on a number of concentrations ranging from $0.7N$ to $2N$ and noted in agreement with his work that the resistance drops very appreciably on freezing. However by making a current and potential measurement we found that the small residual resistance was caused by the solution itself, and not as Ogg suggests by a contact resistance at the electrodes.

It might be mentioned that Ogg's interpretation of the observed magnetic moment in a ring is not necessarily as conclusive as may appear at first sight. If a ring is frozen in a magnetic field and the field subsequently switched off, a magnetic moment due to paramagnetic regions within the material which have lost their ability to reorientate themselves could be mistaken for a persistent current. A more conclusive test is to freeze a ring in zero magnetic field and to attempt to induce a current by switching on and off a strong magnetic field. However, in a considerable number of experiments on rings with the concentration range stated above, we were unable to observe a residual magnetic moment with either technique of inducing a persistent current.

[1] Richard A. Ogg, Phys. Rev. 69, 243 and 544 (1946

The Mass of the Neutron

DONALD J. HUGHES
Argonne National Laboratory, P.O. Box 5207, Chicago 80, Illinois
July 11, 1946

IN a recent Letter to the Editor on the above subject, K. Sun[1] has pointed out that if Bethe's[2] calculation of the mass of the neutron is repeated, using Mattauch's[3] more recent values for the H_2^1-D mass difference and the H^1 mass, a slightly lower neutron mass results. The value he obtains is 1.008 92±0.000 04 as compared to Bethe's 1.008 93±0.000 05. In the calculation, however, Sun used the same value as Bethe for the deuteron binding energy, namely 2.17±0.04 Mev, the uncertainty in this quantity being the main source of uncertainty in the neutron mass.

The binding energy of the deuteron is now known more accurately than the above figure indicates and the more recent results should be used in the calculation. Wiedenbeck and Marhoefer[4] give 2.185±0.006 Mev for the deuteron binding energy. This latter value, together with Mattauch's 0.001 539±0.000 0021 mass unit for the H_2^1-D difference, give the neutron-proton mass difference directly as 0.000 807±0.000 0068 or 751±6.3 Kev. Using the H^1 mass of Mattauch (1.008 130±0.000 0033), we then get a neutron mass of 1.008 937±0.000 0075. Thus the final mass, instead of being about 9 Kev lower than Bethe's value, and with an uncertainty of 37 Kev, is 6.5 Kev higher, with an uncertainty of only 7 Kev.

[1] K. Sun, Phys. Rev. 69, 240 (1946).
[2] H. Bethe, Phys. Rev. 53, 314 (1938).
[3] J. Mattauch, Phys. Rev. 57, 1155 (1940).
[4] M. L. Wiedenbeck and C. J. Marhoefer, Phys. Rev. 67, 54 (1945).

Transmission of Light by Superconducting Lead Films

AARON WEXLER
Department of Chemistry, The Johns Hopkins University, Baltimore, Maryland
July 16, 1946

AMONG the properties of a substance which might be expected to undergo a change at the superconducting transition temperature are the optical properties. Hirschlaff[1] found, for visible light, no appreciable change in the reflectivity of tantalum and lead mirrors, as these passed reversibly through the superconducting transition. Daunt, Keeley, and Mendelssohn[2] showed that there is no measurable difference in the absorption of infra-red radiation in the region of 10μ at temperatures above and below the superconducting transitions of lead and tin.

Inasmuch as the foregoing results depended upon the interaction of the radiation with the surface layers, it was deemed worth while to check the light transmission of superconducting films. Lead films were evaporated at room temperature, upon polished fused quartz plates, and electrical leads were provided for resistance measurements. A representative square film had a resistance of 9.182 ohms at 300°K, 3.317 ohms at 80°K, 1.722 ohms at 20.4°K, 1.492 ohms at 10.1°K, and 0.000 ohm at 7.2°K. The light transmission was observed by two methods. (a) The films were uniformly illuminated by an incandescent bulb at such an intensity that the light transmitted was just visible. (b) The films were illuminated with light from a high pressure mercury arc, and the transmitted spectra was recorded photographically. The transmission was found to remain constant from 300°K to 5.1°K, i.e., down to 2° below the measured transition temperature.

As was to be expected from the work of Picard and Duffendack,[3] of Arni,[4] and of others, photomicrographs showed that the films were granular. It should be inter-

esting to study the light transmission, over a large frequency range, of films prepared by the techniques of Appleyard and Misener[5] and of Shalnikov,[6] i.e., of films, deposited at sub-liquid air temperatures, for which there is no possibility of agglomeration.

[1] E. Hirschlaff, Proc. Camb. Phil. Soc. **33**, 140 (1937).
[2] J. G. Daunt, T. C. Keeley, and K. Mendelssohn, Phil. Mag. **23**, 264 (1937).
[3] R. G. Picard and O. S. Duffendack, J. App. Phys. **14**, 291–305 (1943).
[4] E. L. Arni, Phys. Rev. **63**, 451–4 (1943).
[5] E. T. S. Appleyard and A. D. Misener, Nature **142**, 474 (1938).
[6] A. Shalnikov, Nature **143**, 74 (1938).

Viscosity of Glass as Affected by Dissolved Gases

W. A. Graff and A. E. Badger
University of Illinois, Urbana, Illinois
July 18, 1946

WHEN ordinary glasses of commercial types are melted and subjected to a vacuum, large quantities of dissolved gases are liberated causing considerable foaming of the molten glass. Although numerous investigations have been concerned with the composition of these gases, which consist of SO_2, O_2, H_2O, CO_2, and N_2 in amounts depending on the glass batch used, the effects of dissolved gases on the properties of the glasses have not been studied thoroughly.

We have made preliminary experiments dealing with the effect of dissolved gases on the viscosity of glass, the general method of attack being to melt the glass in vacuum in order to obtain gas-free glass and then to saturate different samples of this glass with various gases. The latter procedure consisted in melting the glass in a platinum crucible and bubbling the test gas through the melt by means of a platinum tube immersed in the molten glass.

Viscosity measurements by the fiber-elongation method indicate that the presence of CO_2 and H_2O decreased slightly the viscosity of a commercial soda-lime-silica glass at the annealing and strain points, as shown below. The precision of these measurements is ±2°F (Table I).

Table I.

	Softening pt. °F	Annealing pt. °F	Strain pt. °F
Glass melted in vacuum	1341	1018	960
Glass treated with CO_2	1344	1008	950
Glass treated with H_2O	1336	1004	949

The softening, annealing, and strain points correspond to viscosity of $\log \eta = 7.65$, 13.4, and 14.6, respectively.

Additional tests on viscosities of glasses made at temperatures up to 2500°F with a Bureau of Mines design of viscometer have not been conclusive. In these experiments the viscosity of a gas-free glass contained in a platinum cylindrical crucible was measured in an atmosphere of CO_2 or air containing water vapor. It was thought that the slow solution of the test gas in the glass would produce a change in viscosity.

Within experimental error no change in viscosity of the molten glass was noted, although the glass was held at these high temperatures for a period of two weeks. Whether the glass viscosity at high temperatures is unchanged by dissolved gases or whether the rate of solution of gas in glass under these conditions is insignificant has not been proven.

R-F Heating Cyclotron Filaments

Albert E. Hayes, Jr.
57 Severskv Court, Baltimore 21, Maryland
July 9, 1946

IN the construction and operation of radiofrequency generators as a source of power for the heating of the filaments of cyclotrons, it is customary to locate the radiofrequency oscillator itself at the control position to facilitate adjustment. This requires the use of a long transmission line between the oscillator and the cyclotron ion source and a consequent loss of energy due to the high currents flowing therein. It is suggested that the oscillator frequency be selected so that the transmission line may be made one quarter wave-length in length at the mean operating frequency of the oscillator. By this expedient the impedance looking into the transmission line from the oscillator will be very nearly a pure resistance of value equal to Z_0^2/Z_f where Z_f is the impedance of the cyclotron filament itself, and Z_0 is the characteristic or iterative impedance of the transmission line. By having a pure resistance load connected to the oscillator, the effects of slight changes in impedance of the ion source filament during operation will not affect the oscillator nearly as much as when it is operating into a random length of line and feeding a reactive load. The losses in such a system will be much less than those in present-day arrangements due to the elimination of wasteful reactive currents in the line. It will also be easier to couple efficiently from the oscillator to the line due to the use of the higher load impedance on the oscillator.

On the Possible Use of Brownian Motion for Low Temperature Thermometry

A. W. Lawson and Earl A. Long
Institute for the Study of Metals, University of Chicago, Chicago, Illinois
July 23, 1946

THE thermodynamic scale of temperature below 1°K is at present based on a combination of calorimetric and magnetic measurements[1] which, although rigorous, requires elaborate time-consuming techniques. For this reason, it appears worth while to consider alternative possibilities of establishing a thermodynamic scale which may prove to be experimentally somewhat more adaptable.

In principle at least, one may use the Johnson noise developed by a resistor R at temperature T. Nyquist[2] has shown that the mean square fluctuation voltage developed by such a resistor is given by

$$\langle V^2 \rangle_{Av} = 4kTR\Delta f, \qquad (1)$$

where k is Boltzmann's constant and Δf is the frequency range of the voltage fluctuations admitted to the detector. Unfortunately, a practical limit to the use of Eq. (1) is set by interference with the measurement, arising from shot noise in the grid and plate of the first amplifier tube. The shot noise arising from plate current is equivalent to the Johnson noise from a resistor of approximately $3r_p/\mu$ ohms at 300°K in the grid circuit. The shot noise from the grid current is given by

$$\langle V^2\rangle_{Av}=2eI_gR_g^2\Delta f. \tag{2}$$

If we assume that Johnson noise must be at least as large as the extraneous shot noise, the lowest temperatures measurable with amplifiers employing ordinary commercial tubes are of the order of a few degrees Kelvin. However, if the first stage of the amplifier uses a Western Electric D-96475 electrometer tube, for which $r_p \leqq 25{,}000$ ohms, $\mu \leqq 3$, and $I_g \leqq 10^{-15}$ ampere, then by using a grid resistance of 10^9 ohms as a source of thermal noise, one may estimate that the lowest temperatures measurable are of the order of 0.01°K. With an input capacity of $30\mu\mu$f (probably a practical minimum), a grid resistance of 10^9 ohms yields a band width in the input circuit of about 5 cycles/sec. Thus, if the noise is integrated over 20 seconds, an accuracy of about 10 percent is attainable, using an amplifier with a pass band from about 2 to 3 cycles/sec. and a sensitivity of about 10^{-7} volt. Although such amplifiers have been built, they are rather expensive and require considerable care in adjustment and use. Furthermore, a grid resistance of 10^9 ohms implies the use of a semi-conductor such as carbon, and will therefore have an exponential temperature coefficient of resistance at the temperatures of interest. This circumstance introduces additional experimental difficulties which, although surmountable, lead one to consider alternative possibilities.

A comparatively simple thermometer based on the detection of Brownian motion appears to be provided by a quartz crystal bar. Consider one mode of mechanical vibration of such a bar, say, for simplicity, the fundamental mode of extensional vibrations parallel to the long dimension a, which we shall assume to be along the X axis of the crystal. By the equipartition law, the potential energy of vibration stored in this mode as a result of Brownian motion must equal $\frac{1}{2}kT$. Thus, denoting by s_{11} the elastic modulus and by b and c the other two dimensions of the crystal, we find for the mean square fluctuation in stress

$$\langle X_x^2\rangle_{Av}=(2kT/abc)(1/s_{11}). \tag{3}$$

Owing to the piezoelectric properties of quartz, a mean square fluctuation in voltage will be generated between the faces of the bar normal to the Y axis of the crystal, given by

$$\langle V^2\rangle_{Av}=\frac{32\pi^2}{ab}\frac{c}{\epsilon^2}\frac{d_{12}^2}{s_{11}}kT, \tag{4}$$

where d_{12} is the appropriate piezoelectric modulus and ϵ^2 is the dielectric constant. Equation (4) is based on the assumption that $h\nu \ll kT$. This condition, however, is not violated at 10^{-4} °K if ν is less than 10^7 cycles/sec. Taking $s_{11}=1.3\times10^{-12}$ cm²/dyne, $d_{12}=6.9\times10^{-8}$ e.s.u., $a=5$ cm, $b=0.1$ cm, $c=1.0$ cm, and $\epsilon=4.5$, one obtains

$$\langle V^2\rangle_{Av}=1.4\times10^{-12}T, \tag{5}$$

where V is in volts and T is in degrees Kelvin.

The operation of this device is based on the high Q (low damping capacity) of a quartz vibrator, since then all the energy in a particular mode will be concentrated in a very narrow range of frequency in the neighborhood of 50 kc. For instance, reasonable precautions ensure Q's of the order of 5×10^4 for such bars. With such a Q, the internal resistance of the quartz is only a few thousand ohms, so that an input resistance of 10^8 ohms is adequate. Thus, a sharply tuned amplifier with a band width of a few cycles and an input resistance of 10^8 ohms should, according to Eq. (1) and Eq. (2), permit the measurement in a few seconds of temperatures of the order of 0.001 °K with a precison better than one percent. With careful design of the input stage and selection of low noise input tubes, measurement of temperatures as low as 0.0001°K may be possible.

Several remarks should be added. Since both $\partial s_{11}/\partial T$ and $\partial d_{12}/\partial T$ must vanish at $T=0$, a negligible error should be introduced by calibrating the thermometer at the boiling point of helium and then extrapolating. This procedure avoids the necessity of measuring s_{11} and d_{12} at each temperature which, though simple, is time consuming.

The principal experimental difficulty with the thermometer will be to insure good thermal contact without decreasing the Q of the oscillator. One feasible procedure would be to isolate the crystal mechanically (and thus thermally) for the short period necessary to measure $\langle V^2\rangle_{Av}$ after achieving equilibrium. There appears to be some possibility of preparing a crystal which is both paramagnetic and piezoelectric (e.g., $NiSO_4\cdot7H_2O$, a poor example), and using the thermometer itself as a bath.

The values inserted in Eq. (4) were room temperature values. At lower temperatures these values will be somewhat different but should not change sufficiently to invalidate the main result.[3]

Unfortunately, the facilities required for an experimental test of the proposed device are not at present available to us. However, the preliminary considerations presented here seem sufficiently promising to warrant the consideration of active cryogenic investigators.

[1] Cf. H. B. G. Casimir, *Magnetism and Very Low Temperatures* (The Cambridge University Press, New York, 1940), pp. 41–44.
[2] H. Nyquist, Phys. Rev. **32**, 110 (1928).
[3] Cf. W. G. Cady, *Piezoelectricity* (McGraw-Hill Book Company, Inc., New York, 1946), pp. 221–223.

The Power Spectrum of the Cosmic-Ray Cascade Component

EDWARD P. NEY
Rouss Physical Laboratory, University of Virginia
Charlottesville, Virginia
July 18, 1946

SEVERAL components of the cosmic radiation have been shown to follow at their point of origin a power law of the form $F(E)=\text{const.}\ E^{-1.8}$, where $F(E)$ is the number of the particles of energy greater than E.[1,2] If one

assumes that the *cascade* component can be expressed in the form

$$F(E, l)=F(l)E^{-s}, \tag{1a}$$

$$G(E, l)=G(l)E^{-s}, \tag{1b}$$

where $F(E, l)$ and $G(E, l)$ are the number of electrons and quanta, respectively, with energies greater than E at a distance l (measured in radiation units); and considers the problem as a boundary value problem with the single boundary condition that the energy content of the cascade as a whole cannot be infinite, then it follows that $1<s<2$. The demonstration proceeds along the following lines.

1. To show that $s>1$

Define new functions $f(E, l)$ and $g(E, l)$ such that

$f(E, l)dE$ = number of electrons at l with energies between E and $E+dE$,

$g(E, l)dE$ = number of quanta at l with energies between E and $E+dE$.

Then

$$f(E, l)dE=-\frac{\partial F(E, l)}{\partial E}dE, \tag{2a}$$

$$g(E, l)dE=-\frac{\partial G(E, l)}{\partial E}dE. \tag{2b}$$

The energy content of the cascade as a whole $\bar{E}$ can be expressed as

$$\bar{E}=\int_{E_j}^{\infty}[f(E, l)+g(E, l)]EdE, \tag{3a}$$

where E_j is the "crossover" energy between the shower mechanisms of collisions with nuclei (i.e., twin birth and radiative collision) and the classical mechanisms of energy loss by collisions with electrons (i.e., Compton effect and ionization).

Substituting (1) and (2) in (3) results in

$$\bar{E}=\beta(l)s\int_{E_j}E^{-s}dE. \tag{3b}$$

Integration and examination of (3b) leads to the conclusion that for $\bar{E}$ to be finite s must be greater than one. This has been pointed out by Heisenberg.[2]

It is even more important to know how fast the energy spectrum can fall off.

2. To show that $s<2$.

On integrating out Eq. (3b) for $s>1$ there results

$$\bar{E}=\beta(l)\frac{s}{s-1}\frac{1}{E_j^{s-1}}. \tag{3c}$$

The definition of E_j is that it is the energy of an electron at which it will lose on the average all of its energy in the next radiation unit of distance by collisions with electrons. That is, $E_j=X_0(dE/dx)_I$ where X_0 is the length of the radiation unit in centimeters[1]

$$\left(\frac{1}{X_0}=4N\frac{Z^2e^2}{\hbar c}\left(\frac{e^2}{mc^2}\right)^2\log\frac{183}{Z^{\frac{1}{3}}}\right),$$

and $(dE/dx)_I$ is the rate of energy loss by ionization. In the definition of $1/X_0$, N is the number of nuclei of charge Ze per cubic centimeter. Because of the very slow variation of $1/X_0$ with $\log Z^{-\frac{1}{3}}$, X_0 can be assumed to vary inversely as the product of Z^2 by N. The term $(dE/dX)_I$ is proportional to the number of extra nuclear electrons and thus to N times Z. Therefore E_j is proportional to $1/Z$. Utilizing this fact (3c) can be written

$$\bar{E}=\gamma(l)\frac{s}{s-1}Z^{s-1}. \tag{3d}$$

Equation (3d) means that the energy content of a cascade increases with the Z of the material in which the cascade is formed. The physical reason for this is that the energy at which ionization losses become important is much higher in lead than in water for example, and while a 50-Mev particle would be a cascade particle in lead it would not be in water ($E_j=10$ Mev for lead and $E_j=100$ Mev for water). While it is allowable for the energy content to increase with Z, this increase must stop as Z approaches infinity or the cascade will not have a finite energy content. This means that $d\bar{E}/dZ$ must go to zero when Z approaches infinity if not before. The limiting condition is

$$\lim_{Z\to\infty}(d\bar{E}/dZ)=\lim_{Z\to\infty}(\gamma(l)sZ^{s-2})=0. \tag{4}$$

In order for (4) to be satisfied the exponent of Z must be negative and the quantity s must be less than 2. Observations on the cascade component [1]lead to a value for the exponent "s" of 1.8 ± 0.17. This falls in the range prescribed by the foregoing that $1<s<2$.

[1] H. Euler, Zeits f. Physik **116**, 73 (1940).
[2] W. Heisenberg, *Cosmic Radiation* (lectures given at Max Planck Institute). Translated by T. H. Johnson (Princeton University Press, New Jersey).

The Vibrational Levels of an Anharmonic Oscillator

D. TER HAAR
Institute for Theoretical Physics, University of Copenhagen, Denmark
July 2, 1946

MORSE[1] has given an equation for the potential energy function of a diatomic molecule as a function of the distance apart of the nuclei which allows (for S-states) an exact solution. The potential has the following form:

$$U(r)=D\cdot(\exp[-2a(r-r_0)]-2\exp[-a(r-r_0)]), \tag{1}$$

where D is the dissociation energy and r_0 the equilibrium distance of the two nuclei. Morse concludes now that the energy levels are given *rigorously* by the equation:

$$E=-D+\frac{2\sqrt{D}}{A}(n+\tfrac{1}{2})-\frac{(n+\frac{1}{2})^2}{A^2}, \tag{2}$$

where

$$A=(2\mu)^{\frac{1}{2}}/a\cdot\hbar \quad (\mu\text{: reduces mass}). \tag{3}$$

Since Morse's conclusion has been quoted in many textbooks,[2] it is perhaps useful to point out that Eq. (2) is only an approximation, although in every practical case of diatomic molecules a very good approximation, as we shall see in the following.

The Schrödinger equation has the form:

$$\Delta\psi+\frac{2\mu}{\hbar^2}(E-U(r))\psi=0. \tag{4}$$

Introducing polar coordinates we get in the usual way:

$$\psi = P_l^m(\vartheta, x)\cdot\varphi(r)/r, \tag{5}$$

where $\varphi(r)$ has to be solved from the following equation (restricting ourselves to S-states):

$$\frac{d^2\varphi}{dr^2}+\frac{2\mu}{\hbar^2}(E-U(r))\varphi=0. \tag{6}$$

We look for a solution of (6) satisfying the following boundary conditions:

$$\varphi=0 \quad \text{for} \quad r=0, \tag{7a}$$

$$\varphi=0 \quad \text{for} \quad r=\infty. \tag{7b}$$

(At this point Morse introduces a different boundary condition: $\varphi=0$ for $r=-\infty$ instead of (7a); since r is a polar coordinate it will, however, never take negative values. Furthermore, Morse remarks himself that φ should be equal to zero for $r=0$ but he adds that for the eigenvalues of E, which he finds, $\varphi(0)$ is very small. This last fact corresponds just to the outcome that Eq. (2) is such a good approximation for the energy levels.)

Introducing expression (1) for $U(r)$ into Eq. (6) and applying condition (7b) we get the following solution for φ:

$$\varphi(r)=N\cdot z^{Ap}\cdot e^{-z}\cdot M(Ap+\tfrac{1}{2}-A\sqrt{D},\, 2Ap+1;\, 2z), \tag{8}$$

where

$$z=A\sqrt{D}\cdot\exp\left[-a(r-r_0)\right], \tag{9}$$

and $p=(-E)^{\frac{1}{2}}$, N a normalizing factor while $M(\alpha,\beta;x)$ is the confluent hypergeometric series, satisfying:[3]

$$x\frac{d^2M}{dx^2}+(\beta-x)\frac{dM}{dx}-\alpha M=0. \tag{10}$$

Applying now condition (7a) and using (9) we find the energy levels of the closed stationary states from the equation:

$$M(Ap+\tfrac{1}{2}-A\sqrt{D},\, 2Ap+1;\, 2A\sqrt{D}\exp(ar_0)). \tag{11}$$

In all applications to diatomic molecules $2A\sqrt{D}\cdot\exp(ar_0)$ is large so that we can use the asymptotic expression for M:[3]

$$M(\alpha,\beta;x)\sim\frac{\Gamma(\beta)}{\Gamma(\beta-\alpha)}(-x)^{-\alpha}\left(1-\alpha\cdot\frac{\alpha-\beta+1}{x}+\cdots\right)$$
$$+\frac{\Gamma(\beta)}{\Gamma(\alpha)}e^x x^{\alpha-\beta}\left(1+\frac{(1-\alpha)(\beta-\alpha)}{x}+\cdots\right) \tag{12}$$

and even:

$$M(\alpha,\beta;x)\sim\frac{\Gamma(\beta)}{\Gamma(\alpha)}e^x x^{\alpha-\beta}, \tag{13}$$

which gives the following zero points:

$$\Gamma(\alpha)=\infty \quad \text{or} \quad \alpha=-n, \quad n=0,1,2,\cdots. \tag{14}$$

Comparing this with (11) we get:

$$p=\sqrt{D}-\frac{n+\frac{1}{2}}{A}, \tag{15}$$

which gives with $p=(-E)^{\frac{1}{2}}$ just Eq. (2). We see, however, that this is an *approximation* and not the rigorous solution. The deviations are, however, so small as to be negligible in every case of diatomic molecules. From (12) it is easily seen that these deviations are only beginning to be appreciable if:

$$\left.\begin{aligned} &A\sqrt{D}\cdot(\exp(ar_0)-ar_0-1)\lesssim 1 \quad (r_0\neq 0)\\ \text{or}\quad &A\sqrt{D}\lesssim 1 \quad (r_0=0).\end{aligned}\right\} \tag{16}$$

Morse, Fisk, and Schiff[4] have used the potential (1) for the interaction between two nucleons and in this case (16) is satisfied and they use indeed Eq. (11) to determine the relation between E and D; they do not, however, refer to Morse's original paper[1] and they do not point out the fact that for all cases of diatomic molecules Eq. (2) is the solution of Eq. (11). In Table I we have collected for different values of r_0 and $A(-E)^{\frac{1}{2}}$ the solution of $A\sqrt{D}$ from (11) according to Morse, Fisk, and Schiff[4] and the solution of $A\sqrt{D}$ from (2) (between brackets). As should be expected, the deviations decrease for increasing $A\sqrt{D}$ and ar_0.

TABLE I. Values of $A\sqrt{D}$.

ar_0 \ $A\sqrt{-E}$	0		0.5		1.0	
0	0.90	(0.50)	1.48	(1.00)	2.03	(1.50)
0.5	0.73	(0.50)	1.23	(1.00)	1.71	(1.50)
1.0	0.61	(0.50)	1.07	(1.00)	1.54	(1.50)

Finally we may add that a similar point arises for the potential introduced by Rosen and Morse.[5] The boundary conditions in this case should be (using their notation):

$F=0$ for $u\to 1$ and for $u=\frac{1}{2}$ (and not for $u=0$).

I want to express my sincere thanks to Professor N. Bohr and Professor C. Møller for the interest shown in this note and to the Rask-Ørsted-Foundation for a grant which has enabled me to stay in Copenhagen.

[1] P. M. Morse, Phys. Rev. **34**, 57 (1929).
[2] E.g., H. Hellmann, *Einführung in die Quantenchemie* (Leipzig-Wien, 1937), p. 294; G. Herzberg, *Molecular Spectra and Molecular Structure* (New York, 1939), Vol. I, p. 109. (Herzberg gives Eq. (2) and adds: *without* any higher powers of $n+\frac{1}{2}$ (italics of Herzberg).)
[3] See e.g., E. Jahnke and F. Emde, *Tables of Functions* (New York, 1945), Chap. X.
[4] P. M. Morse, J. B. Fisk, and L. I. Schiff, Phys. Rev. **50**, 748 (1936).
[5] N. Rosen and P. M. Morse, Phys. Rev. **42**, 210 (1932).

Cosmic Radiation Above 40 Miles

S. E. GOLIAN, E. H. KRAUSE, AND G. J. PERLOW
U. S. Naval Research Laboratory, Washington, D. C.
July 15, 1946

WE have obtained cosmic-ray data above the earth's atmosphere by means of an apparatus contained in a German V-2 rocket. The rocket was fired by the Ordnance Department, United States Army on June 28, 1946 in connection with a series of tests being made by the Army at its White Sands, New Mexico, proving grounds.

Data were transmitted back to a receiving station on the ground by means of a multi-channel radio equipment. Difficulties which developed in this and accompanying electronic circuits prevented satisfactory records below 200,000 feet. Forty-one seconds of data were obtainable after this time, all of it on ascent. Maximum altitude obtained was 350,000 feet.

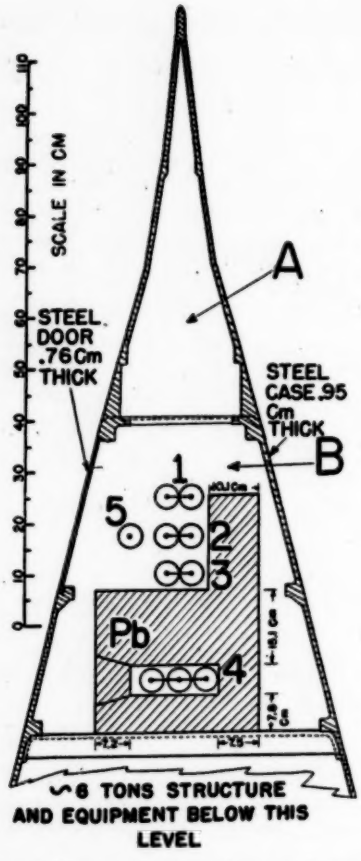

FIG. 1. Arrangement of cosmic-ray equipment as mounted in the warhead.

Figure 1 is a schematic drawing of the cosmic-ray equipment as mounted in the warhead. Chamber *A* above the cosmic-ray chamber had a total weight, including contents, of 100 pounds, which was almost entirely steel. If this is considered spread uniformly across the top of chamber *B*, it is equivalent to about 7.8 centimeters of iron. Single counts in counters 1, 5, and 4 were transmitted, as well as coincidences (1, 2, 3), (2, 3, 4), (3, 5), and (1, 3, 5). In addition, coincidence between each of these various data could be read off the record on the ground. Coincidence resolving times in the rocket were 20×10^{-6} sec., while the resolving time for inter-channel coincidences on the ground was 5×10^{-3} sec. The cosmic-ray counters were fastened in a light aluminum rack which could be removed from the lead for solid angle calibration. A series of calibration runs was made both at Washington and at White Sands, (altitude 4000 feet, geomagnetic latitude 42°N).

Considering first the data from the single counters, counters 1 showed an increase in rate above 200,000 feet over the rate on the ground of 21.3 ± 1.0 times. Counter 5 showed an increase of 20.7 ± 1.2 times. Counters 4 gave 34.9 ± 1.7 for this ratio. In a separate experiment on the ground at White Sands with a vertical telescope, it was determined that the ratio of hard count to total count was 0.651 ± 0.024. If the primary rays are all hard, then the shielded counters (4) should have a ratio of counting rate in flight to ground rate higher than that for the unshielded counters by the ratio 1 to 0.651. Reduction of the shielded counting rate by the reciprocal of this factor gives 22.7 ± 1.4, which agrees with the ratios for the other counters within probable error. Probable errors are determined from statistics only. Counting rates in flight were 36.2/sec., 22.0/sec., and 39.2/sec. for counters 1, 5, and 4, respectively.

The data from the coincidence channels were as follows: (1, 2, 3) increased by a factor of 56 over the ground rate, (3, 5) by a factor of 150, and (1, 3, 5) by a factor of 420. Channel (2, 3, 4) developed an electronic defect and furnished no usable data. Of the 61 counts observed in 28.6 sec. in the shower channel (1, 3, 5) 49, or 80 percent, accompanied coincidences (1, 2, 3). The latter channel in this time had 103 counts. Thus, 49/103 or 48 percent of the counts in (1, 2, 3) were accompanied by showers. This presumably accounts for the higher increase in counting rate than the single counter results indicate.

The effect of the warhead structure as determined in the ground calibration was to increase the soft part of the count in (1, 2, 3) by a factor of 2.2 over the rate without warhead. At the same time, a shower in (1, 3, 5) was recorded for each 6.6 soft counts recorded in (1, 2, 3) with the warhead in place. The high shower to total count ratio in flight probably indicates therefore, that showers of many particles are produced at high altitudes in the structure adjacent to the counters.

Further experimental work is being undertaken for future flights. The present data are perhaps best regarded as provisional pending subsequent corroboration. In particular, whatever effect the high shower count may have had on the single counters has not been completely determined.

The writers are indebted to their colleagues in the Rocket Sonde Section, Naval Research Laboratory, and to M. Schein for suggestions concerning the problem.

Single Scattering and Annihilation of Positrons

HO ZAH-WEI
Laboratoire de Chimie Nucleaire, College de France, Paris
July 26, 1946

I

IN the process of collisions between electrons, it is impossible to distinguish, after the collision, between the recoil electron track and that of the incident β-particle. One cannot, therefore, separate the cases of strong energy exchange (large angle of scattering, θ) from those of weak energy exchange ($\sim\frac{1}{2}\pi-\theta$). But in the case of collisions between positrons and electrons, if one investigates them in a cloud chamber with a magnetic field, one can distinguish the particles easily according to the sense of their curvatures, which permits one to study the problem of single scattering more in detail. But until now, as we know, such kind of collision has not yet been reported.

In the course of the writer's study on the β^+-spectrum of $_{25}Mn^{52}$, a great number of such collisions (single scattering) have been observed, which allowed her to make a first comparison with the theory.[1] The experimental conditions are as follows: Cloud chamber was filled with air at an initial pressure of about 1.9 atmos. and the magnetic field was about 900 gauss. The source, $_{25}Mn^{52}$ prepared by the reaction of $_{26}Fe^{54}(d, \alpha)_{25}Mn^{52}$, was mounted in the center of the chamber. The trajectories were photographed stereoscopically. Measurements were carried out by means of the same objectives as in the original photography; by such arrangement, a natural size image of the track in space was produced at a position corresponding to that in the cloud chamber. Of a total length of 240-m trajectories (reduced to normal conditions) from 2774 positrons (the energy of which extends from 25 to 800 kev with maximum intensity at about 200 kev), 178 single scatterings with energy exchange $A \geq 10$ percent have been observed ($A = E^-/E_0^+$, where E_0^+ and E^- are the energy of the initial positron and that of the recoil electron, respectively). Some of such collisions are shown in Fig. 1. Within the limit of experimental error, it seems that the principle of conservation of energy holds in the collisions of positrons with electrons.

A comparison of the experimental results on the frequency of single scatterings with the theory, which was developed independently by Bhabha[2] and Bothe is shown in Fig. 2. In the first approximation, there is a general agreement between the theoretical and the experimental curves. But it is noticeable, that, in the case of strong energy exchange ($A > 0.5$) where the experimental accuracies are much higher, the experimental values are much higher then the theoretical ones. Just in such cases, the distance of approach between the positrons and the electrons is of the order of magnitude of the classical radius of electron and one may expect some deviations from the Coulomb's interactions. Further investigations are necessary in order to clarify these anomalies.

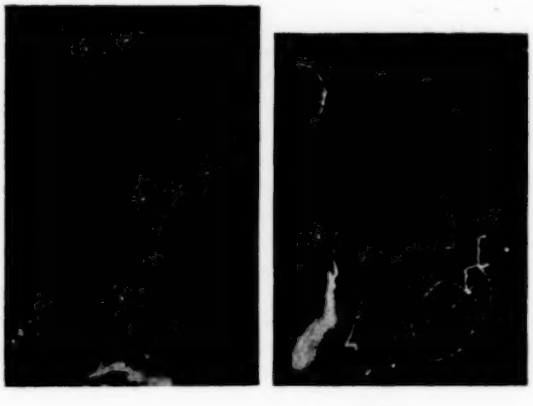

a b

FIG. 1. Some close collisions between positrons and electrons.
a. $A = 0.89$. $E_0^+ = 175$ kev; b. $A = 0.31$. $E_0^+ = 230$ kev.

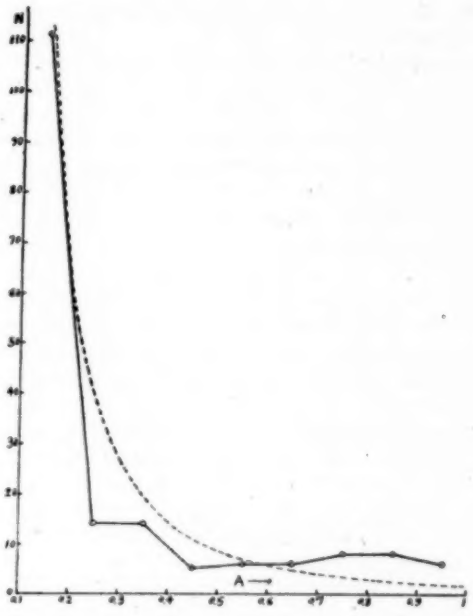

FIG. 2. Comparison of theory and experiment on frequency of single scattering. N is the number of single scatterings; A is E^-/E_0^+. The circles indicate experimental results. The dotted curve is from theory.

II

There have been many experimental works which gave sufficient evidence for the existence of annihilation of fast positrons, but it seems, as we know, there is still no direct proof (for example, by means of cloud chamber). In the course of the present experiment, from 240 meters of β^+-trajectories, 3 annihilations of positron still in motion were observed, i.e., the trajectories stopped suddenly in the illuminated part of the cloud chamber. (By means of the stereoscopical photographs, we can identify them without doubt.) Their energies are 92, 245, and 352 kev, respectively. According to Bethe's calculation,[3] based on Dirac's theory of positron, the expected value of annihilation for a total length of 240-m trajectories of positrons with the corresponding energy range is 2.8. The agreement between the theory and the experiment may be considered as satisfactory.

[1] Ho Zah-wei, Comptes rendus **222**, 1168 (1946). One of such close collision photographs has been projected in the cosmic-rays conference held at Bristol, England, Sept. 1945, as reported in Nature **156**, 543 (1945).
[2] H. J. Bhabha, Proc. Roy. Soc. **154**, 195 (1936).
[3] H. A. Bethe, Proc. Roy. Soc. **150**, 129 (1935).

A Thermodynamic Criterion for the Fracture of Metals—A Criticism

CLARENCE ZENER
Institute for the Study of Metals, University of Chicago, Chicago, Illinois
July 20, 1946

A THERMODYNAMICAL criterion for the fracture of metals has recently been proposed.[1] The purpose of this letter is to point out that this proposed criterion is

in contradiction to certain well-established principles regarding fracture.

The proposed criterion is

$$U = L, \tag{1}$$

where U is the "strain energy" at fracture, i.e., the work per unit volume which has been performed upon the metal just prior to fracture, and L is a function of certain thermodynamical variables, the form of which is irrelevant to the criticism herein presented.

The first principle contradicted by Eq. (1) is that in most metals the strain energy absorbed prior to fracture is dependent upon the conditions of test, e.g., upon stress system, temperature, and rate of deformation. Thus according to the proposed criterion the left member of Eq. (1) is a function of the conditions of test while the right member is independent of these conditions. As one example of the effect of stress system, a comparison will be made with deformation by a uniaxial tension with deformation by torsion. It is well recognized[2] that more strain energy is absorbed under the latter conditions. In fact, tool steels fracture in tension with essentially no prior plastic deformation, and hence with an extremely small strain energy, while they suffer considerable plastic deformation in torsion. As a second example, tensile experiments under high hydrostatic pressure will be quoted. Bridgman[3] has demonstrated that the flow stress ($\bar{\sigma}$ in Saibel's notation) is essentially independent of hydrostatic pressure, while the strain at fracture, and hence the strain energy at fracture, can be increased many fold by hydrostatic pressure.

The second principle contradicted by Eq. (1) is that, under constant test conditions, the strain energy at fracture is very structure sensitive. According to the proposed criterion the left-hand side of Eq. (1) is therefore structure sensitive, while the right-hand side is not. As a common example, temper brittleness[4] of steel will be mentioned. Two steels, one of which is temper brittle, the other not, may have precisely the same flow stress (Saibel's $\bar{\sigma}$), and yet under severe test conditions the ductility, and hence the strain energy at fracture, of the latter will be many times that of the former under the same severe test conditions.

[1] E. Saibel, Phys. Rev. **69**, 667 (1946).
[2] M. Gensamer, *Strength of Metals Under Combined Stresses* (ASM, 1940).
[3] P. W. Bridgman, Rev. Mod. Phys. **17**, 3 (1945).
[4] J. H. Holloman, "Temper-brittleness," Am. Soc. Metals, to be published.

Homogeneous Perturbations in Band Spectrum of AgH Molecule

R. F. Schmid and L. Gerö
Physical Institute of the Royal Hungarian University of Technical and Economic Sciences, Budapest, Hungary
November 15, 1943

MORE than 60 bands of the well-known $^1\Sigma - {}^1\Sigma$ AgH band system were photographed with great intensity and dispersion in our laboratory and a rotational analysis was carried to rather high rotational quantum numbers. Twenty-seven bands of this system were formerly analyzed by Bengtsson and Olsson[1] but only to much lower rotational levels. The upper states of the bands are unusually violently perturbed. As the perturbations are of the "homogeneous" type, they are caused by another $^1\Sigma$ electron term, lying some thousand cm^{-1}-units above the perturbed one and having considerably lower rotational constants. The mutual influence of the perturbing $^1\Sigma$ states is shown schematically in Fig. 1. As can be seen on this figure, the successions of the upper rotational levels of the bands do not belong to one or another of the "unperturbed" $^1\Sigma$ states, but go over alternately in the consecutive vibrational levels of both electron states. Therefore, the initial vibrational quantum number changes gradually with increasing rotation in each rotational level series and consequently the corresponding line intensities and isotope shifts do also, both being functions of this quantum number. In this way the anomalous intensity distributions and isotope shifts can be explained completely.

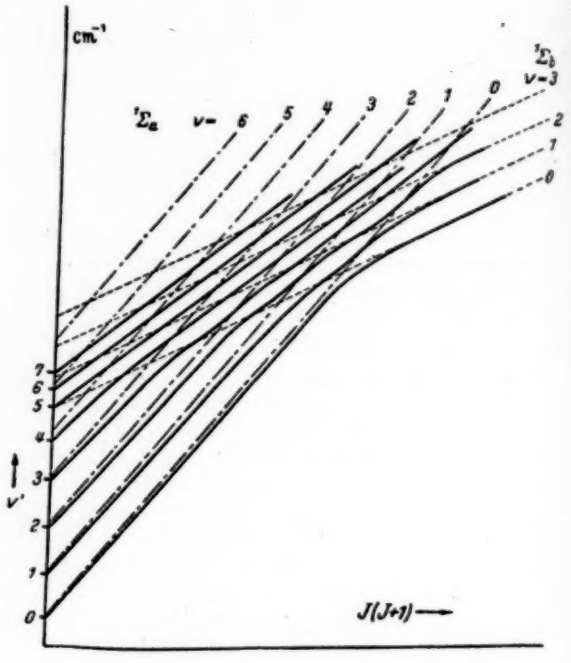

FIG. 1. Mutual influence of perturbing $^1\Sigma$ states.

In the case of homogeneous perturbations, as is well known, the rotational levels with $J=0$ are perturbed in the same way as the others; consequently they may not be regarded as "the vibrational levels" of any electron state, because their mutual positions in the term scheme are quite accidental, as much so as the positions of levels with any other J. Similarly a "rotational constant" calculated at $J=0$ is merely the direction of the level series at this point and is in no way typical for the whole vibrational state. It has, therefore, little meaning to draw these "vibrational and rotational constants," determined at $J=0$, as functions of v and to conclude from them to term convergence (as in the case of C_2) or to avoidance of potential curves.

The complete rotational analysis and the explanation of perturbations, anomalous intensity distributions, and isotope shifts were published in detail in the dissertations of I. Doktorits, R. Gáspár, and K. Mészáros, respectively, and in papers of the authors.[2]

[1] E. Bengtsson and E. Olsson, Zeits. f. Physik **72**, 163 (1931).
[2] L. Gerö and R. Schmid, Zeits. f. Physik **121**, 459 (1943); Naturwiss. **30**, 751 (1942).

Possibility of Observing a Transverse Doppler Effect

P. H. Abelson and A. V. Maskeit
Naval Research Laboratory, Washington, D. C.
and
Nathan Rosen
University of North Carolina, Chapel Hill, North Carolina
July 27, 1946

THE slowing down of a moving clock predicted in relativity theory both for linear[1] and rotational[2] motions is of great significance. In the case of atoms regarded as clocks, the wave-length of radiation emitted from moving atoms will be increased in second-order terms (transverse Doppler effect) by an amount

$$\Delta\lambda = \lambda v^2/2c^2,$$

where λ is the wave-length from a "stationary" atom, v is the velocity of the moving atom, and c that of light. Ives and Stillwell[3] have demonstrated the existence of this effect by determining the mean displacement of wave-lengths emitted by hydrogen atoms (canal rays) in the forward and backward directions along their motion. However, it seems desirable to obtain this effect more directly.

Berenda[2] has suggested the use of radioactive atoms in a cyclotron to show the slowing down of a moving clock. His proposal involved a comparison of the specific activity of radioactive material that had been rotated in the cyclotron with that of similar material kept at rest. However, this procedure would involve a number of serious difficulties, such as the following:

The time spent in accelerating a particle in the cyclotron is about 10^{-4} second. Taking a current of 100μa, one has at any instant about 6×10^{10} particles in the process of being accelerated at all radii. If the electric field were removed, the beam would supposedly continue to move in a circular path in the magnetic field. In a cyclotron there is in general a pressure of at least 10^{-6} mm of mercury. On the assumption of a mean free path of 10^4 cm, a particle of the beam, having a velocity of 10^9-10^{10} cm/sec., would undergo something of the order of 10^6 collisions per second, which would tend to knock the particle out of the beam. On the other hand, in order to establish an effect, the beam would have to be maintained for at least some minutes. Once the "ions at the limiting radius were brought to rest," the problem of determining the specific activity of 6×10^{10} particles, or 10^{-12} gram, would be considerable. Moreover, in addition to such practical difficulties, there is also a difficulty of principle: a particle circling in the magnetic field and undergoing a radioactive change in charge or mass would in general be thrown out of its original orbit.

What appears to be a more practical possibility lies in a direct measurement of the transverse Doppler effect in the collimated beam of high energy protons from a cyclotron or a Van de Graaf generator, passing down a long tube containing helium or some other gas at low pressure. The wave-length shift is nearly proportional to the acquired energy and for hydrogen atoms with energies of 4 Mev should be of the order of 20A for the Hβ line. With the second-order effect not much smaller than the first-order Doppler effect, the necessity for observing the radiation at exactly 90° to the direction of the beam is no longer very critical. The difficulties expected in such an experiment would be associated with line broadening arising from collisions and inhomogeneity in energy, weak intensity, and fogging of the photographic plates by stray radiation, so that carefully planned experimental conditions would be required.

[1] A. Einstein, Ann. d. Physik **17**, 891 (1905).
[2] C. W. Berenda, Phys. Rev. **62**, 280 (1942).
[3] H. E. Ives and G. R. Stillwell, J. Opt. Soc. Am. **31**, 369 (1941).

Gamma-Ray Anomaly Following the Atomic Bomb Test of July 1, 1946

G. Herzog
Houston, Texas
July 22, 1946

IN order to determine possible after-effects of the atomic bomb test on Bikini Islands of July the first (June 30 Houston time), a recording gamma-ray meter of high sensitivity was installed on June 29th. An all-metal gamma-ray detector of 3″ diameter and of 26½″ length is used. The detector is of special construction which has been developed by The Texas Company in its Geophysical Laboratory and which results in high efficiency for the detection of gamma-rays. After amplification, the pulses from the counter are integrated in a circuit with a time constant of 20 seconds. The resulting d.c. voltage is measured with a balanced electronic voltmeter and it is recorded on an L. & N. recorder.

The device is set up on the second floor in a brick house in the residential section of Houston. The location was chosen in order to assure the least interference from commercial radium users such as laboratories and medical institutions.

Starting on June 29th the recorder chart gives a straight line corresponding to 56.5 cts/sec. This continues until July 4th at approximately 8 P.M. There a gradual increase in counting rate sets in. It reaches a maximum of 102 cts/sec. at 3 A.M. on July 5th. The intensity then decreases and reaches its normal value at about 7 P.M. on July 5th. (Because of the statistical fluctuations and the assymptotical approach to the normal value, the time for the beginning and end of the anomaly cannot be exactly determined). From there on until July 15th the base line remains straight and constant.

On July 7th the equipment was carefully checked and no defects could be found. This together with the slow build-up of the anomaly makes it quite assuring that the observed effect is connected with the release of radioactive substances during the bomb test. (Air temperature, barometric pressure, and wind velocities were normal during the anomaly.)

The maximum observed increase in gamma-ray intensity is 77 percent. The half-width of the anomaly is 5 hours. The maximum occurs 108 hours after the bomb explosion. This corresponds to a travelling speed of the radioactive material in excess of 60 miles per hour.

Volt-Ampere Characteristics for the Flow of Ions or Electrons Between Concentric Cylinders in Gases at Atmospheric Pressure

CHESTER W. RICE
General Electric Company, Schenectady, New York
July 18, 1946

THE following equations give the volt-ampere characteristics for the flow of current from a cylindrical emitter of radius r_1 to a surrounding coaxial collector of radius r_2, before ionization by collision begins. The emitter may be either a positive ion or electron source. The mean free path in the gas between the electrodes is assumed to be small compared with the electrode spacing.

The similar case for parallel planes was treated by J. J. Thomson[1] and we here apply his method to the case of concentric cylinders.

Poissons' equation in cylindrical coordinates may be written

$$\frac{1}{r}\frac{d}{dr}(Xr)=4\pi\rho, \tag{1}$$

where r equals the radius, X equals the potential gradient dV/dr, and ρ is the space-charge density.

The second equation that we assume is

$$i=2\pi r\rho\mu X, \tag{2}$$

where i is the current per unit length of cylinder and μ is the positive ion or electron mobility (i.e., velocity for unit potential gradient) all in c.g.s. electrostatic units.

We first substitute the value of ρ from (2) in (1), then separate the variables and integrate to obtain

$$X=\pm\left(\frac{2i}{\mu}+\frac{C}{r^2}\right)^{\frac{1}{2}}, \tag{3}$$

where C is the constant of integration. We determine C as follows. We have

$$\rho=ne, \tag{4}$$

where n equals the number of ions or electrons per unit volume and e the charge per ion or electron. If we substitute this value of ρ and the value of X from (3) in (2) we obtain

$$n=\frac{i}{2\pi re\mu(2i/\mu+C/r^2)^{\frac{1}{2}}}. \tag{5}$$

If we let n_1 equal the value of n at the surface of the emitter r_1, we have from (5)

$$n_1=\frac{i}{2\pi r_1 e\mu(2i/\mu+C/r_1^2)^{\frac{1}{2}}}. \tag{6}$$

A second equation from n_1 which we will derive below is

$$n_1=\frac{(6\pi)^{\frac{1}{2}}(I-i)}{2\pi r_1 ce}, \tag{7}$$

where I is the saturation current per unit length of emitter and c is the r.m.s. velocity of the ion or electron at the emitter temperature.

Equating (6) and (7) and solving for C, we obtain

$$C=\frac{r_1^2c^2}{6\pi\mu^2}\left(\frac{i}{I-i}\right)^2-\frac{2ir_1^2}{\mu}. \tag{8}$$

To save space, we write

$$a^2=\frac{c^2}{6\pi\mu^2}\left(\frac{i}{I-i}\right)^2, \tag{9}$$

and

$$b=2i/\mu. \tag{10}$$

Hence,

$$C=r_1^2a^2-r_1^2b. \tag{11}$$

If we substitute (11) back in (3), we obtain the general solution for the potential gradient

$$X=\frac{b^{\frac{1}{2}}(r^2+[r_1^2a^2-r_1^2b]/b)^{\frac{1}{2}}}{r}. \tag{12}$$

Before integrating this expression to obtain the volt-ampere characteristics, we will go back and derive Eq. (7). Here we assume that the net current i leaving the emitter is equal to the saturation current I of the emitter minus the back diffusion current i_b, that is

$$i=I-i_b. \tag{A}$$

From the kinetic theory of gases we have

$$i_b=2\pi r_1 n_1 ce/(6\pi)^{\frac{1}{2}}, \tag{B}$$

where the r.m.s. velocity c equals $(3kT/m)^{\frac{1}{2}}$, k equals 1.37×10^{-16} Boltzmann's constant, T the absolute temperature of the emitter, and m the mass of the ion or electron.

Substituting (B) in (A) and solving for n_1 we obtain the desired Eq. (7).

We now integrate Eq. (12) and obtain solutions which are suitable for calculating the volt-ampere characteristic for different conditions. No single solution appears to be suitable to cover the whole volt-ampere characteristic under all conditions.

In general,

$$V|_1^2=\int_{r_1}^{r_2}X\,dr=b^{\frac{1}{2}}\int_{r_1}^{r_2}\frac{[r^2+(r_1^2a^2-r_1^2b)/b]^{\frac{1}{2}}}{r}dr. \tag{13}$$

Peirce[2] Eq. (130) gives for the full equation

$$V|_1^2=[r_1^2a^2+b(r_2^2-r_1^2)]^{\frac{1}{2}}-r_1a+[r_1^2a^2-r_1^2b]^{\frac{1}{2}}\times\log_e\frac{r_2}{r_1}\frac{[r_1^2a^2-r_1^2b]^{\frac{1}{2}}+r_1a}{[r_1^2a^2-r_1^2b]^{\frac{1}{2}}+[r_1^2a^2+b(r_2^2-r_1^2)]^{\frac{1}{2}}}. \tag{14}$$

The above equation is only good when $r_1^2a^2$ is greater than r_1^2b.

Case A. When $r_1^2a^2$ is small compared with br_1^2 we have the full space-charge condition and (13) reduces to

$$V|_1^2 = b^{\frac{1}{2}} \int_{r_1}^{r_2} \frac{(r^2 - r_1^2)^{\frac{1}{2}}}{r} dr. \quad (15)$$

Peirce[2] Eq. (131) gives

$$V|_1^2 = b^{\frac{1}{2}}([r_2^2 - r_1^2]^{\frac{1}{2}} - r_1 \cos^{-1}[r_1/r_2]). \quad (16)$$

Case B. When $r_1^2a^2$ is large compared with br_1^2 we have a transition equation from the full space-charge condition to no space charge. Here (13) reduces to

$$V|_1^2 = b^{\frac{1}{2}} \int_{r_1}^{r_2} \frac{(r^2 + r_1^2 a/b)^{\frac{1}{2}}}{r} dr. \quad (17)$$

Peirce[2] Eq. (130) gives

$$V|_1^2 = (r_1^2a^2 + br_2^2)^{\frac{1}{2}} - (r_1^2a^2 + br_1^2)^{\frac{1}{2}} + r_1 a \log_e \frac{r_2}{r_1} \frac{r_1 a + (r_1^2a^2 + br_1^2)^{\frac{1}{2}}}{r_1 a + (r_1^2a^2 + br_2^2)^{\frac{1}{2}}}. \quad (18)$$

Case C. When $r_1^2a^2$ is large compared with both br_1^2 and br_2^2. In this case the current is limited by back diffusion only and Eq. (18) reduces to

$$V|_1^2 = r_1 a \log_e r_2/r_1. \quad (19)$$

As previously stated, the above equations are all in c.g.s. electrostatic units. For calculation we will want to use cm, gram, second, volts, amperes per cm, length, and mobility in cm/sec./volt/cm. In that case a remains

$$a = \frac{e}{(6\pi)^{\frac{1}{2}}\mu}\left(\frac{i}{I-i}\right), \quad (20)$$

and b becomes

$$b = 0.903 \times 10^{12}\, 2i/\mu. \quad (21)$$

It was interesting to find experimentally that these equations which are based on a constant mobility gave a good fit to the experimental volt-ampere characteristics, under a wide variety of conditions, for both electron and lithium positive ion emitters in air at atmospheric pressure.

[1] J. J. Thomson, *Conduction of Electricity through Gases* (The Cambridge University Press, New York), second edition, p. 267.
[2] B. O. Peirce, *A Short Table of Integrals* (Ginn and Company, New York).

Note on Thickness of Quartz Wafers for Observed Surface Phenomena

D. D'EUSTACHIO
Bliley Manufacturing Corporation, Erie, Pennsylvania
July 16, 1946

THE writer and his co-workers have reported some effects occurring on thin crystals.[1-3] In this work the critical thickness has been given as 25–30 microns. These figures for thickness do not take into account the depth of the etch pits developed on the surface. Examination of the cross sections of some of the plates, and more recent work with smoother surfaces indicate that the thickness is ~10 microns.

[1] D. D'Eustachio and S. B. Brody, Phys. Rev. **69**, 256 (1946).
[2] D. D'Eustachio, Paper presented at the Cambridge Meeting of the Am. Phys. Soc., April, 1946.
[3] D. D'Eustachio and S. Greenwald, Phys. Rev. **69**, 532 (1946).

Spontaneous Emission of Neutrons from Uranium*

G. SCHARFF-GOLDHABER AND G. S. KLAIBER
Department of Physics, University of Illinois, Urbana, Illinois
May 18, 1942

FLEROV and Petrzhak[1] have established the existence of spontaneous fission in uranium by recording the heavy fission fragments with a uranium-coated ionization chamber. The partial decay constant of the "average uranium atom" calculated from their data lies between 2×10^{-25} and 2×10^{-24} sec.$^{-1}$ for this process. It seemed possible that the mechanism of spontaneous fission might be different from that of induced fission, in particular that no neutrons might be split off in the former process. Libby[2] had previously made an unsuccessful attempt to find spontaneous fission neutrons with the help of a boron counter. His results indicated an upper limit for the partial disintegration constant of 2×10^{-22} sec.$^{-1}$ for spontaneous fission with neutron emission. We have now carried out an experiment with a more sensitive calibrated arrangement, using a hydrogen-filled ionization chamber which allowed us to record neutrons of an energy higher than about 100 kev.[3] Spontaneous emission of neutrons from uranium was observed. Several sources of error were excluded by check experiments and simple considerations. From the number of counts obtained we estimate the partial decay constant for spontaneous fission for the "average uranium atom" to be of the order of 7×10^{-24} sec.$^{-1}$ under the assumption that one neutron is emitted per fission. Neutrons with energies up to 800 kev have been observed.

* This paper was received for publication on the date indicated, but was voluntarily withheld from publication until the end of the war.
[1] G. N. Flerov and K. A. Petrzhak, J. Phys. U.S.S.R. **3**, 275 (1940).
[2] W. F. Libby, Phys. Rev. **55**, 1269 (1939).
[3] G. S. Klaiber and G. Scharff-Goldhaber, Phys. Rev. **61**, 733 (A) (1942).

On the Production of Penetrating Ionizing Particles by the Non-Ionizing Component of Cosmic Radiation

P. J. G. DE VOS
Mercusky Instituut vir Fisika, Universiteit van Stellenbosch, Stellenbosch, South Africa
AND
S. J. DU TOIT
Departement vir Natuurkunde, Universiteitskollege vir C. H. O., Potchefstroom, South Africa
Jnly 22, 1946

EXPERIMENTS of the type using a vertical coincidence set of two or more counter tubes, in which an absorber is placed either above the whole system, or between the two top counters, have been reported by various authors.[1-6] All these experiments are in agreement in that they give an increased coincidence rate with the absorber in the first position as compared to that with the absorber in between the counters.

In all these experiments, except those of Froman and Stearns,[5] the material shifted during the experiment was either iron or lead, and the increase in counting rate was found to be relatively small. Rossi *et al.*,[7] using the anti-coincidence method, have shown conclusively that the

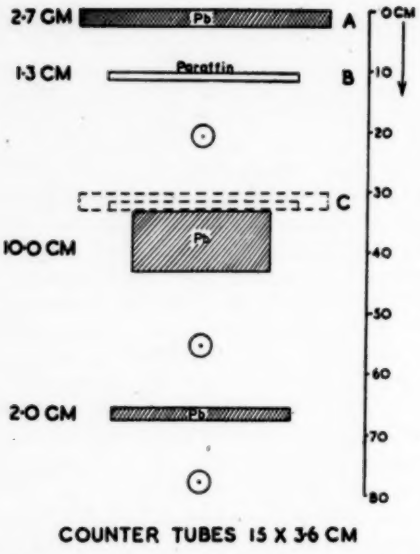

FIG. 1. Threefold coincidence set-up showing the arrangement of lead and paraffin absorbers. Drawn to scale.

increase in counting rate caused by shifting lead absorber relative to the coincidence set is not to any appreciable extent caused by the production of ionizing particles (penetrating or soft) by the non-ionizing component of cosmic radiation, but can be accounted for by spurious effects such as knock-on showers, scattering and side-showers. This holds for experiments made at low altitudes. The large increase found by Schein and Wilson at 25,000 feet seems to be real enough.

Froman and Stearns used paraffin in their experiments and found the very interesting result that paraffin, in relatively thin layers, caused a larger increase in counting rate when so shifted, than a layer of lead of approximately the same thickness.

In order to try to confirm this result a series of coincidence measurements were made in the Merensky Physics Institute at Stellenbosch, i.e., practically at sea level. The experimental set-up was as shown in Fig. 1, which has been drawn to scale. Threefold coincidences were recorded with (a) lead in position *A* and paraffin in *B* or *C* and (b) paraffin kept in position *B* and lead placed alternately in positions *A* and *C*. The results obtained are collected in Table I.

The Geiger-Müller counters used in this experiment were made according to a technique previously described,[8] and the set has now given eighteen months' continuous service without one becoming defective. The resolving time of the recording circuit was reduced to a minimum by using very small coupling condensers (50 micromicrofarads) between the tubes and their amplifiers, as well as relatively small leak resistors.

As Table I shows, shifting the lead scatterer from *A* to *C* makes very little difference to the threefold coincidence counting rate. The fact that the rates are equal must be regarded as accidental as can be seen from the probable mean error, but the results show that the effect, if any, is very small.

TABLE I. Threefold coincidence rate[7] or various positions of lead and paraffin scatterers

Series	Lead position	Paraffin position	Counts	Time in hours	counts/hour
(a)1	*A*	*B*	25503	821.9	31.0±0.2
2	*A*	*C*	24773	821.2	30.2±0.2
(b)1	*A*	*B*	35701	1147.4	31.1±0.2
2	*C*	*B*	31103	999.4	31.1±0.2

Shifting the layer of paraffin scatterer however, causes a change in counting rate substantially greater than the probable mean error. If spurious effects were responsible for the change in counting rate between (a) 1 and (a) 2, it is to be expected that these same effects would also cause a change between (b) 1 and (b) 2, for one would expect lead to be a better scatterer and producer of knock-on showers than the far less dense paraffin. We therefore come to the same conclusion as that reached by Froman and Stearns, that the effect is real.

The fact that a light substance like paraffin is so effective in producing this effect gives ground for the hypothesis that the neutral component of cosmic radiation responsible for the phenomenon might be fast neutrons, and the penetrating secondaries might be mesotrons, or even protons. It may be remarked in this connection that Jánossy and Rochester[9] have already come to the conclusion that cosmic-ray neutrons might be responsible for an appreciable part of the penetrating showers observed at sea level. Anti-coincidence experiments are now under way at Potchefstroom to measure the penetrating power of the primary neutral radiation, and of the secondary ionizing particles.

One of us (S. J. du T.) wishes to express his sincere indebtedness to the Council of Industrial and Scientific Research of the Union of South Africa for a liberal grant.

[1] B. Rossi, Zeits. f. Physik **68**, 64 (1931).
[2] D. S. Hsiung, Phys. Rev. **46**, 653 (1934).
[3] H. Maass, Ann. d. Physik **27**, 507 (1936).
[4] M. Schein and V. C. Wilson, Phys. Rev. **54**, 304 (1938).
[5] D. K. Froman and J. C. Stearns, Phys. Rev. **54**, 969 (1938).
[6] F. R. Shonka, Phys. Rev. **55**, 24 (1939).
[7] B. Rossi, L. Jánossy, G. D. Rochester, and M. Bound, Phys. Rev. **58**, 761 (1940).
[8] P. J. G. de Vos and S. J. du Toit, Rev. Sci. Inst. **16**, 270 (1945).
[9] L. Jánossy and G. D. Rochester, Proc. Roy. Soc. **A182**, 180 (1943).

Successive Multiple Production of Penetrating Particles

W. B. FRETTER AND W. E. HAZEN
University of California, Berkeley, California
July 19, 1946

THE production of mesotrons by protons in successive nuclear collisions has been predicted by Hamilton, Heitler, and Peng[1] but Janossy subsequently showed[2] that one would expect a multiple process in the case of collision with a nucleus containing many protons and neutrons. Several observers[2,3] have reported some 90 penetrating particle showers in some of which mesotrons are identifiable. There has, however, been no previous direct observation of successive production centers for penetrating particles, with the possible exception of a photograph by Shutt,[3] in which heavily ionizing particles are ejected from a plate that was traversed by a penetrating particle shower.

Rochester[3] observed showers in which the penetrating particles came from different directions with no common intersection and concluded that a cascade process had probably occurred.

Evidence for the production of "mesotrons" in successive events has been obtained with a stereoscopic photograph in a counter-controlled cloud chamber. The chamber was 16 inches in diameter, nine inches deep, and contained eight ½-inch thick lead plates. The depth of the illuminated region was five inches. Slanted tracks were separated into positive and negative ion columns by a residual clearing field. The relative ages of the tracks could be accurately determined by the separation of the ion clusters in either the slanting or the vertical tracks.

Among 2100 photographs, 11 showed penetrating particle showers. All of the showers occurred among the latter two-thirds of the pictures when there was a 30-cm block of lead about 100 cm above the chamber. In each of six showers there was apparently a common origin in the lead block above the chamber; in the others, no common origin seemed possible but it should be kept in mind that the strong scattering observed for mesotrons might lead to confusion. In contrast with penetrating particle showers observed at 10,000- and 14,000-foot elevations, most of the present showers were associated with cascade radiation (electrons, etc.) to a greater or lesser extent. Two of the showers seemed to show additional production of heavily ionizing particles from new centers just as in the case of Shutt's observation.

One of the showers (Fig. 1) gives unmistakable evidence for three separate centers, which probably were in cascade, from each of which penetrating particles were emitted. Three particles from the first center (probably in the 30-cm block of lead) penetrated all eight lead plates and are similar to the "mesotron shower" particles that have often been observed. Additional nuclear collisions occurred in both the first and third lead plates. In the first plate, two heavily ionizing particles were produced that stop in the second plate. A particle that penetrated the second and third plates at an angle was also produced, as well as a particle that was projected downward through four or more plates. In the third plate, a third collision occurred with one particle ejected upward at an angle through one or more plates and two ejected downward through two or more plates and out of the illuminated region. Other diverging particles that stopped in the fourth plate were also produced. The tracks were clearly identified with a stereoscopic viewer by means of which relative depths could be observed.

The shower from the first lead plate might have been initiated by a particle that ionized strongly in the top compartment. This particle, however, was not in the same direction as the general trend of the showers and hence may have been a result rather than the cause of the shower from the top plate. Such a shower could have been produced by a neutron or γ-ray, the latter being unlikely since there was no evidence for other soft radiation in the vicinity. The shower from the third plate appears to have been initiated either by one of the penetrating particles produced in the first plate or by the same particle that produced the shower in the first plate.

[1] J. Hamilton, W. Heitler, and H. W. Peng, Phys. Rev. **64**, 78 (1943)
[2] L. Janossy, Phys. Rev. **64**, 345 (1943).
[3] W. M. Powell, Phys. Rev. **69**, 385 (1946); R. P. Shutt, Phys. Rev. **69**, 261 (1946); G. D. Rochester, Nature **154**, 399 (1944); W. E. Hazen, Phys. Rev. **65**, 67 (1944).

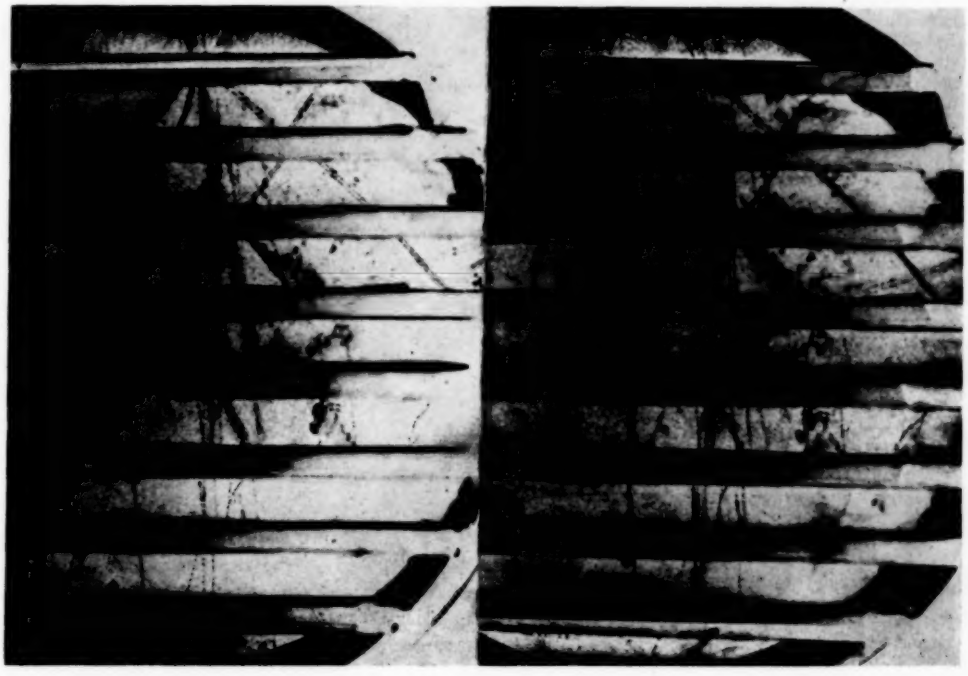

FIG. 1. Cloud-chamber photograph showing multiple production of penetrating particles in three separate successive events.

Mass Assignment of 2.6 *h* Ni^{65} *

J. A. SWARTOUT AND G. E. BOYD
Clinton Engineer Works, Monsanto Chemical Company, Clinton Laboratories, Oak Ridge, Tennessee
AND
A. E. CAMERON, C. P. KEIM, AND C. E. LARSON
Clinton Engineer Works, Tennessee Eastman Corporation, Oak Ridge, Tennessee
July 31, 1946

THE assignment of the 2.6 *h* Ni activity to a definite mass number was complicated in the past by the ambiguity of reactions by which it was produced. Assignment to a mass of 63 was made primarily on the basis of the higher yield obtained by bomardment of nickel in a field of fast neutrons than in a field of slow neutrons which was interpreted to be indicative of its formation by an $(n, 2n)$ reaction on Ni^{64}.[1-4] The availability of enriched copper isotopes in the Manhattan Project has now made possible a positive assignment of the 2.6 *h* Ni isotope to a mass number of 65. This reassignment brings the stability characteristics of this radioactive isotope into agreement with predictions based upon the Bohr-Wheeler theory.

Approximately 100 mg of each of two copper samples enriched in Cu^{65} and in Cu^{63} by the calutron were obtained from the magnetic separation plant operated by the Tennessee Eastman Corporation. The enriched samples were purified chemically by three electrolyses from a H_2SO_4-HNO_3 electrolyte using platinum electrodes and then dissolved in purified nitric acid and conductivity water. Mass-spectrographic analyses indicated the following isotopic abundances in the samples:

Sample 1: 93.1±0.5 percent Cu^{65}, 6.9±0.5 percent Cu^{63},
Sample 2: 3±1 percent Cu^{65}, 97±1 percent Cu^{63}.

In order to establish the mass of the 2.6 *h* Ni isotope, comparisons were made of intensities of the nickel activity obtained from (n, p) reactions on each of the enriched copper samples placed in the neutron field of the chain-reacting uranium pile. Because of the low activation cross section expected for the (n, p) reaction compared with that for an (n, γ) reaction, it was necessary to eliminate the possibility of traces of nickel impurity in the copper. Assurance of freedom from nickel contamination was obtained by repeated bombardments in the pile at constant neutron flux of the same copper samples followed by chemical isolation of nickel after each bombardment. Attainment of a constant specific activity of the 2.6 *h* Ni isotope was considered to be evidence for its production only by an (n, p) reaction with copper.

TABLE I. Evidence for the production of 2.6 *h* Ni by the reaction: Cu^{65} (n,p) Ni^{65}.

	Sample 1	Sample 2
Weight of enriched Cu sample bombarded (mg)	48.8	27.4
Weight of Cu^{65}—(based on mass-spectrograph analysis)	45.2 to 45.7 mg	0.55 to 1.1 mg
Total 2.6 *h* beta-activity—(c/m at 100% geom.)	1.5×10^{3}	1.7×10^{4}
Specific activity—(c/m/mg Cu^{65} at 100% geom.)	3.4 to 3.3×10^{4}	3.1 to 1.5×10^{4}

The chemical separation of nickel from the bombarded copper samples consisted of a copper sulfide precipitation from 0.5*N* HCl solution in the absence of nickel carrier (this precipitate was then converted to copper oxide for rebombardment in the pile), two copper sulfide precipitations in the presence of nickel carrier, addition of cobalt carrier and precipitation with α-nitroso-β-naphthol to remove any cobalt activity produced by an (n, γ) reaction on cobalt impurity or by (n, α) on copper, and finally three or four nickel dimethylglyoxime precipitations.

The apparent specific beta-activities of the 2.6 *h* Ni obtained from the first one or two bombardments were erratic, due probably to nickel impurity in the copper and to the presence of longer lived beta-activities, believed to be from Pt^{197}, which resulted in complex decay and absorption curves. However, in the nickel fractions from subsequent bombardments, the amount of the 2.6 *h* Ni beta-activity was proportional to the amount of Cu^{65} bombarded, as is illustrated by data from one bombardment of enriched Cu^{63} and enriched Cu^{65}. (Table I.)

The characteristics of the beta-activity agreed with those previously reported[3] in that the half-life was within the limits of 2.5 to 2.7 *h*, and the energy as determined by Feather analysis was 1.9 to 2.0 Mev.

The possibility of a mix-up in the two enriched copper samples prior to or during these experiments was eliminated by the following precautions: (1) the mass-spectrographic analyses were confirmed within limits of experimental error by radiochemical methods based upon the relative amounts of 12.8 *h* Cu^{64} and 5 *m* Cu^{66} produced by neutron bombardment; (2) the weights of the two copper samples which were bombarded were sufficiently different in magnitude to permit detection of any change in the subsequent bombardment; (3) the relative activities of the two copper sulfide precipitates measured three days after the final bombardment when essentially all of the activity would be caused by the 12.8 *h* Cu^{64} agreed with the relative amounts of Cu^{63} present in the samples; and (4) the identity of the enriched Cu^{65} sample was confirmed after the last bombardment by mass-spectrographic analysis.

* This paper is based on the results of research performed under contract W-35-058-eng-71 with the Manhattan Project at the Clinton Laboratories, Oak Ridge, Tennessee.
[1] E. A. Oeser and J. L. Tuck, Nature **139**, 1110 (1937).
[2] F. A. Heyn, Physica **4**, 1224 (1937).
[3] J. J. Livingood and G. T. Seaborg, Phys. Rev. **53**, 765 (1938).
[4] M. E. Nelson, M. L. Pool, and J. D. Kurbatov, Phys. Rev. **61**, 428 (1942).

Properties of Radar Echoes from Shell Splashes

HERBERT GOLDSTEIN*
Department of Physics, Harvard University, Cambridge, Massachusetts
July 31, 1946

BACK scattering from spray drops has frequently been proposed as the explanation of phenomenon of sea echo on microwave radar. Although many of the characteristics of the echo are in accord with this hypothesis, measurements on the frequency dependence are in violent disagreement with the theoretical prediction.[1] It has been suggested that the study of the echo from a target known

to contain spray, such as the splash thrown up by a shell striking water, might provide further information on the matter.

Through the cooperation of the Army authorities at Ft. Wright, Fishers Island, New York, measurements have been made on echoes from splashes set up by inert 90-mm anti-aircraft shells fired at ranges up to 8000 yd. from the gun, corresponding to distances up to 6800 yd. from the radars. Accurate measurements of the location, dimensions, and duration of each splash were obtained from motion pictures taken with a cine-theodolite. The radar systems used were three experimental truckborne sets developed by the Propagation Group, Radiation Laboratory, Massachusetts Institute of Technology, operating on wave-lengths of 9.2, 3.2, and 1.25 cm, respectively. The outputs from any two of the systems could be presented on two special high intensity A-scopes which were simultaneously photographed by a high speed camera,[2] providing a record of each successive sweep. The pulse recurrence frequency, about 200 c.p.s., was crystal controlled and furnished an accurate time scale. The absolute power of the received echo on each sweep could be determined by reference to a pulse from a signal generator injected into the system at a known r-f level and displayed on the scopes. (The dynamic characteristics of the receiver were determined by separate calibration with a signal generator.)

The outstanding features common to all the echoes measured are most strikingly shown in the comparison between the 9.2- and 1.25-cm records with horizontal polarization. On both wave-lengths the echo fluctuated violently because of interference effects, there being little correlation between successive pulses. In order to exhibit the general rise and decay of the echo, the fluctuations were smoothed somewhat by averaging over successive intervals of 0.12 sec. From the constants of the system, and assuming perfect reflection from a flat sea, the apparent radar cross section of the splash was then calculated for each time interval and for both wave-lengths. (The error of the absolute calibration is estimated at not more than 2 db on 9.2 cm or 4 db on 1.25 cm.) The two lower curves of Fig. 1 are plots of the cross sections so calculated as time from the start of the splash. A similar plot of the ratio of the two cross sections, in db, is shown by the top curve. The proper interpretation of these curves depends on some of the characteristics of the splash. Despite the flat trajectory (all the shells ricocheted) the splash was almost entirely vertical. Initially the splash rose rapidly in height, attaining 80 percent of its 50 ft. maximum by the end of 0.5 sec. Thereafter its dimensions changed only slowly, but the original column of water rapidly disintegrated into spray. The motion pictures clearly show that this pillar of spray, though progressively thinning in density, retained almost its maximum height up to the very end. Most of the time, therefore, the splash covered many of the interference lobes, even at the longer wave-length. The separate parts of the initial column of water should scatter coherently. From the magnitude of the cross sections and the

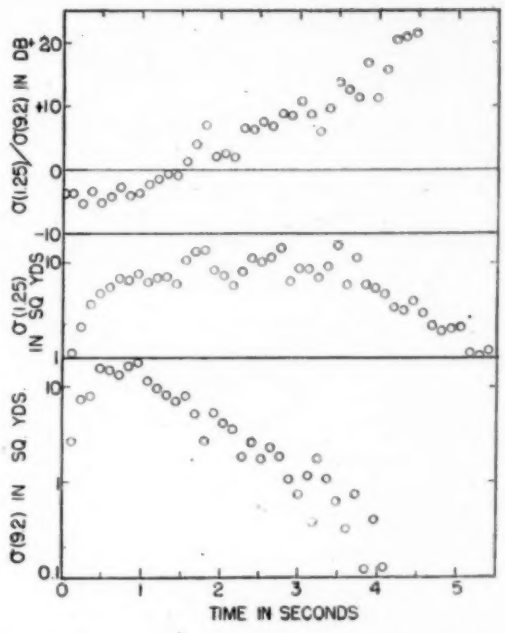

FIG. 1. The lowest curve is a plot of the radar cross section of a typical shell splash on 9.2 cm as a function of time. The corresponding plot at a wave-length of 1.25 cm is shown in the middle curve, while the ratio of the two cross sections is plotted in the top curve.

geometry it is clear that the main back-scattered beam misses the radar which receives only the side lobes, which at constant angle increase in intensity with increasing wave-lengths. The echo is therefore stronger on 9.2 cm at the start, but as the splash changes into spray and the scattering becomes incoherent, the balance swings to the shorter wave-length. Even after the splash has reached its maximum height, the echo on 1.25 cm is still increasing and attains its peak long after the 9.2-cm echo has started to decay. Toward the end, when the spray has become finely divided, the 1.25-cm echo is still appreciable when the echo on 9.2 cm has completely disappeared. The ratio of the cross sections ideally should approach the +35 db figure predicted for very small drops by the Rayleigh λ^{-4} law. The maximum value measured is much lower (about +20 db) probably because of the drops not being sufficiently small. It is still much greater than the ratio observed for sea echo, +8 db, confirming the conclusion that sea echo cannot arise from the small drops of spray.

It is a pleasure to acknowledge the aid and cooperation of the personnel of the Mt. Prospect Field Station, Radiation Laboratory, M.I.T., and of the members of the Propagation Group, especially Miss Margaret Harwood who performed most of the tedious film analysis.

* The work reported on was performed while at the Radiation Laboratory, M. I. T.

[1] Herbert Goldstein, Phys. Rev. 69, 695A (1946), and paper in preparation.

[2] The photographic techniques have been described by H. Goldstein and P. D. Bales, Rev. Sci. Inst. 17, 89 (1946).